

**THE DARK MATTER PROBLEM IN ROTATIONALLY
SUPPORTED GALAXIES**

by
PENGFEI LI

Submitted in partial fulfillment of the requirements for the degree of
Doctor of Philosophy

Department of Astronomy
Dissertation Adviser: Dr. Stacy McGaugh & Federico Lelli

CASE WESTERN RESERVE UNIVERSITY

August, 2020

**CASE WESTERN RESERVE UNIVERSITY
SCHOOL OF GRADUATE STUDIES**

We hereby approve the dissertation of

Pengfei Li

candidate for the degree of **Doctor of Philosophy**.

Committee Chair

Stacy McGaugh

Committee Member

Federico Lelli

Committee Member

Earle Luck

Committee Member

Christopher Mihos

Committee Member

Benjamin Monreal

Dissertation Defense

June 19, 2020

Dedicated to those who love me and I love.

Contents

Title	1
Signature Sheet	ii
Table of Contents	iii
List of Tables	vii
List of Figures	viii
Preface	x
Acknowledgements	xi
Abstract	xiii
1 Introduction	1
1.1 Observational Evidence of the Mass Discrepancy Problem	2
1.2 Dark Matter Being the Solution and Its Challenges	5
1.3 Modified Dynamics Being the Solution and Its Challenges	16
1.4 The SPARC Database	24
1.5 The Aims and Structure of This Dissertation	26
2 A Comprehensive Catalog of Dark Matter Halo Models for SPARC Galaxies	29
2.1 Abstract	29
2.2 Introduction	30
2.3 Data, models and method	30
2.3.1 The SPARC sample	30
2.3.2 Dark matter halo profiles	31
2.3.3 MCMC simulations	36
2.4 Results	38
2.5 Conclusion	41

3	A Constant Characteristic Volume Density of Dark Matter Haloes from SPARC	46
	Rotation Curve Fits	
3.1	Abstract	46
3.2	Introduction	47
3.3	Method	48
	3.3.1 SPARC database	48
	3.3.2 Halo models	49
	3.3.3 Bayesian analysis	51
3.4	Results	54
	3.4.1 Individual fits	54
	3.4.2 Fit goodness	54
	3.4.3 Correlations between halo and disc properties	55
3.5	Comparison with previous work	60
3.6	Conclusions	62
3.7	Appendix: Checking the distributions of galactic parameters and Λ CDM priors	62
	3.7.1 Distributions of galactic parameters	62
	3.7.2 Priors of halo parameters	65
4	The Halo Mass Function of Late-type Galaxies from H I kinematics	79
4.1	Abstract	79
4.2	Introduction	80
4.3	Data	81
	4.3.1 The HIPASS Galaxy Sample	81
	4.3.2 SPARC Rotation Curve Fits	81
	4.3.3 The Single-Dish H I Line Widths	82
4.4	Results	83
	4.4.1 The Halo Mass–Line Width Correlation	83
	4.4.2 Stellar Mass Function	83
	4.4.3 Halo Mass Function	86
4.5	Discussion and conclusion	89
4.6	Appendix A: Optical inclinations vs. kinematic inclinations	91
4.7	Appendix B: Comparing the measured halo mass functions with IllustrisTNG simulations	93
5	Adiabatic Compression of Dark Matter Halos	97
5.1	Abstract	97
5.2	Introduction	98
5.3	Compression code and input	99
	5.3.1 The compression algorithm	99
	5.3.2 Input of compression	101
5.4	Results	102
	5.4.1 Compressing the static, best-fit NFW halos	102

5.4.2	Fitting compressed halos	105
5.5	Conclusion	108
6	Fitting the Radial Acceleration Relation to Individual SPARC Galaxies	109
6.1	Abstract	109
6.2	Introduction	110
6.3	Method	111
6.3.1	Parameter dependence	111
6.3.2	MCMC simulation	113
6.4	Fitting individual galaxies	114
6.4.1	Fit results	114
6.4.2	Distributions of adjusted parameters	118
6.5	Galaxy scaling relations	119
6.5.1	Radial acceleration relation	119
6.5.2	Baryonic Tully-Fisher relation	120
6.6	Does the critical acceleration scale g_{\ddagger} vary?	123
6.7	Discussion and conclusion	125
6.8	Appendix A: Flat priors vs. physically motivated priors in MCMC simulations	128
6.9	Appendix B: Rotation curve fits and best-fit parameters	131
7	Summary and Outlook	142
7.1	Summarizing major results	142
7.2	Prospective work	145

List of Tables

2.1	The best-fit parameters for galaxy IC2574.	43
3.1	The slopes of the fitted linear relations for R_d , r_s and $\rho_s \cdot r_s$ against galaxy luminosity $L_{[3,6]}$ in log space.	57
3.2	The best-fit values of halo parameters and fit goodness for the Einasto profile with both Λ CDM priors and flat priors	69
3.3	Same as Table 3.2, but for the DC14 profile	74
4.1	The best-fit parameters of the modified Schechter function for the NFW, Einasto and DC14 profiles.	87
6.1	BTFR: The fitted parameters and scatter.	122
6.2	Maximum posterior parameters and reduced χ^2 of individual rotation curve fits to the RAR	132

List of Figures

1.1	The merger of galaxies using 3-body and N-body simulations	7
1.2	The core-cusp problem	8
1.3	The missing satellite problem in the Milky Way	9
1.4	The “Too-Big-To-Fail” problem	11
1.5	Plane and corotation of satellites	12
1.6	The landscape of dark matter candidates	14
1.7	Direct, indirect and collider detections of dark matter particles	15
1.8	Tree diagram of the theories of modified gravity	17
1.9	The Stellar and Baryonic Tully-Fisher relations	18
1.10	The Radial Acceleration Relation of rotationally supported galaxies	20
1.11	The baryonic mass versus circular velocity	21
1.12	The power spectrum of CMB temperature fluctuations	22
1.13	The simulated structure formation	23
1.14	The effective surface brightness and luminosity of the SPARC galaxies	24
2.1	Cumulative distributions of the reduced χ^2_v for seven halo profiles	39
2.2	The relations between stellar masses and DM halo masses for the seven halo models	40
2.3	Concentrations of the SPARC galaxies against halo masses for the seven halo models	41
2.4	The rotation curve fits of the dwarf galaxy IC2574 using seven models	42
2.5	The posterior distributions of the fitting parameters for IC2574 using the Burkert profile	44
2.6	The best rotation-curve fits of 175 SPARC galaxies using the Burkert profile	45
3.1	Rotation curve fits and posterior distributions of fitting parameters for the dwarf galaxy IC2574 using Einasto and DC14 profiles	53
3.2	The cumulative distributions of χ^2_v for Einasto and DC14 models	54
3.3	Scaling relations between halo properties and galaxy 3.6 μm luminosity for Einasto and DC14 profiles	56
3.4	Histograms of the best-fit values of ρ_s for Einasto and DC14 profiles	57
3.5	The product $\rho_0 \cdot r_s$ vs. galaxy luminosity for Einasto and DC14 profiles when imposing flat priors	58

3.6	Characteristic volume density ρ_s vs. scale radius r_s for the Einasto and DC14 profiles	59
3.7	Same as Figure 3.5 but for pISO profile with the maximum disc method	61
3.8	Distributions of optimized galactic parameters for the Einasto model	63
3.9	Distributions of optimized galactic parameters for the DC14 model	64
3.10	Halo mass-concentration relation and stellar mass-halo mass relation for Einasto and DC14	66
3.11	The shape parameter α_ϵ of the Einasto model versus $L_{[3.6]}$ and M_{halo}	67
4.1	Correlations between halo mass and inclination corrected H I-line widths for SPARC galaxies	84
4.2	Correlations between stellar mass and inclination corrected H I-line widths for SPARC galaxies, and the stellar mass function	85
4.3	The halo mass functions measured using the HIPASS galaxies for the NFW, Einasto and DC14 profiles	88
4.4	The eccentricity and surface brightness profiles for two example galaxies, UGC05918 and UGC06787	92
4.5	Optical inclinations vs. kinematic inclinations for the SPARC galaxies	93
4.6	The $\log M_{200}$ - $\log W_{P50}^i/2$ relation and the measured HMF with $W_{P50}^i/2$ corrected for kinematic inclinations	94
4.7	The halo mass function measured using the HIPASS galaxies for the DC14 profile compared with the prediction of simulations	96
5.1	Example galaxies NGC2903 and UGC06786 with compressed halos	103
5.2	The reduced χ_v^2 after compression are plotted against their values prior to compressions	104
5.3	Same as Figure 5.1 but with $M_s = 4\pi\rho_s r_s^3$ optimized	106
5.4	The optimal $M_s = 4\pi\rho_s r_s^3$ are plotted against their original values	107
6.1	Example of MCMC fits and the corresponding posterior distribution for NGC 2841	114
6.2	Same as Figure 6.2 but for the gas-dominated dwarf galaxy IC 2574	115
6.3	Distributions of fitted parameters	117
6.4	RAR and the residuals with Υ_* , D , and i optimized	120
6.5	Baryonic Tully-Fisher relation with Υ_* , D , and i optimized	121
6.6	Cumulative distributions of reduced χ^2 for fixed g_{\dagger} fits and variable g_{\dagger} fits	124
6.7	Distribution of optimal g_{\dagger} imposing a flat and Gaussian prior	125
6.8	Cumulative distributions of reduced χ^2 for fixed G_N fits and variable G_N fits	129
6.9	Distribution of optimal G_N imposing a flat and Gaussian prior	130
6.10	Rotation curve fits of 175 SPARC galaxies using the radial acceleration relation	141

Preface

In this dissertation, I present the cumulative work I have done during the past four years in the Department of Astronomy. Chapter 2, 3, 4, 6 have been published previously as

1. Chapter 2: Li, Lelli, McGaugh, Schombert (2020), “A Comprehensive Catalog of Dark Matter Halo Models for SPARC Galaxies”, *ApJS*, 247, 31;
2. Chapter 3: Li, Lelli, McGaugh, Starkman, Schombert (2019), “A Constant Characteristic Volume Density of Dark Matter Halos from SPARC Rotation Curve Fits”, *MNRAS*, 482, 5106;
3. Chapter 4: Li, Lelli, McGaugh, Pawlowski, Zwaan, Schombert (2019), “The Halo Mass Function of Late-type Galaxies from H I Kinematics”, *ApJL*, 886, L11;
4. Chapter 6: Li, Lelli, McGaugh, Schombert (2018), “Fitting the Radial Acceleration Relation to Individual SPARC Galaxies”, *A&A*, 615, A3.

Acknowledgements

Although I am the only listed author, many people have contributed to this dissertation directly or indirectly. To date, four years ago, Stacy McGaugh opened the door of Astronomy to me, so that I can pursue my favorite scientific career. Since then, Stacy has been closely advising me in research, scientific talk, as well as English. I have been impressed by how knowledgeable he is, since every time I raised a random question or idea, he could always tell me the story behind, and point some references to me. I also want to mention that, with his support, I attended three conferences during my four-year PhD. This is a very rare case for a graduate student. His continuous support has been the key for the success of my PhD.

Federico Lelli is my co-advisor. He proposed (or co-proposed) four out of the five projects I did during my PhD period. He has provided me extensive help in research, English writing, and career development. I am impressed by his quick work. He often provided feedbacks within 12 hours after I sent new results or new paper drafts. This greatly speeds up my progress. Otherwise I would not be able to finish my PhD within 4 years.

Marcel Pawlowski is actually my first instructor in Astronomy. I worked with him during my first half year here in this department, and learned many basic astronomical knowledge from him. Data play an essential role in astronomical research, so I would like to thank James Schombert for building the SPARC database, which made my entire PhD project possible.

I got great help in learning astronomical courses from Chris Mihos, Earle Luck, Heather Morrison, and Paul Harding. Chatting with them also significantly boosts my understanding in Astronomy. Charles Knox and Bill Janesh have been helping me in all computer-related problems. Agnes Torontali has been saving me from miscellaneous work so that I

can concentrate on research. I benefit from the friendly environment created by Jay Franck, Aaron Watkins, Joe Curro, Ray Garner, John Crooke, Tiffany Visgaitis, Wei Du, Emily Safron, as well as many good friends in Physics and other Departments.

I also want to express my gratitude to my former advisors in Physics, Claudia de Rham and Huichao Song. Thanks for their inspirations in research. Those precious experiences are still helping me.

Finally, I would like to thank my parents, all my relatives and friends in China. Thanks for their continuous love and support, as clearly manifested during this pandemic.

The Dark Matter Problem in Rotationally Supported Galaxies

Abstract

by

PENGFEEI LI

Different lines of evidence suggest that the observed dynamics of galaxies, galaxy clusters, and the Universe as a whole cannot be explained by the visible, baryonic matter when applying the standard laws of Gravity. Two competing solutions have been proposed and hotly debated in the past decades: introduce dark matter (DM) or modify the laws of gravity. In this dissertation, I present a systematic investigation of these two hypothesis using 175 late-type galaxies from the Spitzer Photometry & Accurate Rotation Curves (SPARC) database.

On the DM front, I fit the SPARC rotation curves testing seven different halo profiles. Based on these fits, I explore the correlations between DM halos and stellar disks, and find that the characteristic volume density of DM halos is remarkably constant over 5 decades in galaxy luminosity. This serves as a testing bed for galaxy formation models. Using the correlation between DM halo masses and HI line widths, I measure for the first time the DM halo mass function (HMF). The measured HMF agrees with the prediction of DM-only simulations at intermediate and low halo masses, but differs significantly at high mass end. Finally I compute the effect of adiabatic compression on the DM halos due to the baryonic gravitational potential, and find that compressed halos contribute more to rotation curves, exacerbating the core-cusp problem over the whole range of galaxy masses.

On the modified gravity front, I test the statistically established radial acceleration relation (RAR) which indicates a strong link between the baryonic mass distribution and the observed dynamics of galaxies. The vast majority of the SPARC galaxies can be well described by the RAR. The best-fit RAR has an rms scatter of 0.057 dex, comparable to the observational uncertainties on rotation curves. This leaves little room for intrinsic scatter if

any. I check the critical acceleration scale in the RAR is universal among late-type galaxies, marking no difference between the RAR and the Modified Newtonian Dynamics.

Overall, Modified Newtonian Dynamics can describe disk galaxies with less problems than DM models, but a comprehensive evaluation requires the systematic investigations on galaxy-cluster and cosmological scales.

Chapter 1

Introduction

What is the Universe made of? How does the Universe work? These two fundamental questions have been the core of physical science. On macroscopic scales, the evolution of the Universe is largely driven by Gravity. To date, the most general and best tested description of Gravity is represented by Einstein's theory of General Relativity, extending and generalizing Newton's Gravitational law. Newton explains the surface acceleration of the Earth and the orbits of the solar planets using a single law of gravity, although these two systems differ significantly in terms of acceleration scales (the gravitational acceleration on the Earth is about 10 m/s^2 while the centripetal acceleration of Neptune is about $6 \times 10^{-6} \text{ m/s}^2$) and sizes (the size of the Earth is around 10^4 km while the size of the solar system is about 10^{13} km or 60 AU). This confirms the universality of Newtonian gravity from planetary scales to the solar-system scale. At higher speed and stronger gravitational fields, Newtonian gravity breaks down and one needs General Relativity to explain observed phenomena such as the advance of Mercury's perihelion, the dynamics of compact objects (neutron stars and black holes), and light bending (gravitational lensing).

On microscopic scales, high-energy experiments have revealed that 61 fundamental particles (18 quarks and antiquarks, 3 leptons and antileptons, 3 neutrinos and antineutrinos, photon, 8 gluons, W^\pm bosons, Z^0 boson, Higgs boson) comprise all the matter we have seen, and 3 fundamental interactions (electro-magnetic interaction, weak and strong interactions) explains all the laws of nature at and beyond the scale of fm , i.e. 10^{-15} m , the minimum scale that physics have ever reached, but below the scale at which gravity starts dominating. Therefore, it seems that the 61 fundamental particles and 4 fundamental

interactions are the answers to the two questions mentioned at the beginning at size scales ranging from fm to the solar system and beyond the acceleration scale of 10^{-6} m/s^2 .

However, things become problematic at larger size scales, such as galactic scale, galaxy-cluster scale and cosmological scale. At these size scales, the acceleration scale is also far below 10^{-6} m/s^2 . One example is the dynamical studies of spiral galaxies (e.g. see Bosma 1978; Rubin et al. 1978). Since baryons (comprised of three quarks) are overwhelmingly more massive than other stable particles due to the considerable potential energy of the strong interaction, their total mass is essentially a good approximation to galaxy mass, and can be effectively estimated through photometry. Spiral galaxies present stable rotating disks. The rotation velocities give the centripetal acceleration. The bridge connecting centripetal acceleration and mass distribution is the law of gravity. In the case of weak field and low speed, the law is believed to be Newtonian gravity. However, the mass required by the observed rotation velocities, according to Newtonian gravity, is significantly larger than the observed mass through photometry. This is the mass discrepancy problem. It reveals that either there exists some invisible matter that has not been observed via photometry or the assumed law of gravity does not apply at this low acceleration. Therefore, two competing paradigms have been proposed, extensively researched and hotly debated: introducing dark matter or modifying gravity. Since the dark matter paradigm has gained most of the attentions, the mass discrepancy problem is often cited as the dark matter problem.

In this Chapter, I will first review the observational evidence of the mass discrepancy problem, and then discuss the successes and challenges of the two candidate solutions. I will also introduce the SPARC galaxy database, followed by the introduction of the aims and structure of the dissertation.

1.1 Observational Evidence of the Mass Discrepancy Problem

Galactic scale The mass discrepancy problem was first identified in dynamical studies of the Milky Way. The Milky Way possesses a thin disk of gas and stars, where the solar system resides at $\sim 8 \text{ kpc}$ from the center. Oort (1932) studied the motions of stars in the solar neighborhood along the direction perpendicular to the disk. Their vertical velocity

dispersion reflects the gravitational potential and hence the required total mass density of the disk. However, the measured velocity dispersion of stars implies a surface density of $\sim 74 M_{\odot} \text{ pc}^{-2}$, significantly higher than the summation of the observed gas ($\sim 14 M_{\odot} \text{ pc}^{-2}$) and stellar ($\sim 38 M_{\odot} \text{ pc}^{-2}$) surface densities. This is also called the Oort discrepancy.

When observations reached extragalactic scale, the measurements of rotation curves for nearby galaxies became possible. Babcock (1939) measured the rotation curve of the Andromeda Galaxy. He found that the stellar mass-to-light ratio has to increase radially (up to $62 M_{\odot}/L_{\odot}$ in the outskirts) in order to reproduce the observed rotation curve. With greater accuracy, Rubin et al. (1978) reported the extended rotation curves of ten high-luminosity spiral galaxies with Hubble type ranging from Sa to Sc using optical spectra. They found all rotation curves are approximately flat at large radii (up to 50 kpc). This is contradictory to the observed luminosity profiles of stellar disks, which decrease exponentially from the center to the outskirts.

In the mean time, radio astronomers started measuring galaxy rotation curves using the 21 cm line of atomic hydrogen (H I). This method allows rotation curves to be traced to much larger radii, since H I gas is often more extended than stellar disks. Bosma (1978) studied the rotation curves of seven galaxies. Similarly, expected Keplerian decline was not found. They confirmed the flatness of the rotation curves at large radii is a common feature for most spiral galaxies.

Galaxy-cluster scale The same problem appeared in galaxy clusters when Zwicky (1937) used the virial theorem to estimate the total mass of the Coma Cluster. He equally distributed the total mass to roughly 1000 nebulae in the clusters, giving a mean nebula mass greater than $4.5 \times 10^{10} M_{\odot}$. He hence derived the value of mass-to-light ratio of $\gamma \sim 500$. Zwicky (1937) compared the result to that of the local Kapteyn stellar system, i.e. the stellar system of the closest halo star to the solar system. The local Kapteyn stellar system has a mass-to-light ratio of $\gamma \sim 30$, which is much larger than our solar system but still significantly smaller than his estimate for the Coma Cluster.

Later studies using gravitational lensing further confirmed the huge mass discrepancy in galaxy clusters. Galaxy clusters are massive enough to bend light from the sources behind them. The background objects are hence distorted and magnified. By measuring the magnification of a background galaxy population, one can measure the dynamical masses of

galaxy clusters (e.g. see Taylor et al. 1998). Strong lensing can lead to multiple images for a single background source. Analyzing the distribution of these images provide a solid way to determine the distribution of dynamical mass (Natarajan et al. 2017). Weak lensing can only cause minute distortions to the images of galaxies. But the apparent shear deformation appeared in the background galaxies can still be used to derive the distribution of the total mass of galaxy clusters (Refregier 2003). All these studies revealed the dynamical mass of galaxy clusters overwhelm the observed X-ray gas mass and galaxy mass, indicating a huge mass discrepancy.

Cosmological scale Unlike galactic and galaxy-cluster scales at which the mass discrepancy problem shows up directly from two independent measurements of the masses (dynamics and photometry), the problem at cosmological scale comes from different reasonings and depends on assumed cosmological models.

The early inspiration of introducing dark matter in cosmology is to explain structure formation. In the standard cosmology, the present structure of the Universe results from the gravitational collapse of the primordial baryonic overdensities. Since baryons were strongly coupled with photons via Thomson scattering before the epoch of recombination, the fluctuations in the CMB temperature map reveals that the overdensity of baryonic matter was $\frac{\delta\rho}{\rho} \sim 10^{-5}$ at recombination. Under the expanding background, the overdensities grow linearly with the cosmological scale factor, $\frac{\delta\rho}{\rho} \sim a$, so that the present overdensity should have been 10^{-2} , which is seriously contradictory to the observed overdensities of galaxies ($\frac{\delta\rho}{\rho} \sim 10^6$) and galaxy clusters ($\frac{\delta\rho}{\rho} \sim 50$). This implies that either there is additional matter which does not interact with photons via electro-magnetic interaction (e.g. non-baryonic cold dark matter) but provides extra gravitational potentials, or the gravity needs to be stronger to speed up the gravitational collapse against the expanding background.

Later observations that result in the concordance cosmology (Kowalski et al. 2008) establish dark matter as an essential component of the standard cosmology. The observed cosmic microwave background (CMB) radiation is explained as the relic radiation of the early Universe decoupled from baryonic matter at the recombination epoch. The observed tiny temperature anisotropies in the CMB spectrum hence reveals the density fluctuations in the early Universe, which can be decomposed into a series of harmonic oscillations. The coefficient of each component describes the strength of the oscillation, and the strengths

of all the components are assembled into the power spectrum function. The position of the first peak in the power spectrum is determined by the geometry of the Universe in the standard cosmology. The measured spectrum indicates a flat Universe, corresponding to the unity of the total mass-energy density fraction, i.e. $\Omega_{\text{tot}} = 1$ (e.g. see Hinshaw et al. 2009).

In the mean time, the distance measurements using Type Ia supernovae extends Hubble's law to redshift $z \sim 2$ (e.g. see Perlmutter et al. 1999), providing strong constraints on the values of dark energy density fraction (Ω_{Λ}) and matter density fraction (Ω_{m}). Together with the constraints from the CMB power spectrum, the total matter density fraction is determined as $\Omega_{\text{m}} = 0.276$ (Komatsu et al. 2009). This is consistent with the measurement using the baryonic acoustic oscillation (BAO, Eisenstein et al. 2005), leading to the concordance cosmology (Kowalski et al. 2008).

On the other hand, the Big Bang nucleosynthesis (BBN) model links the abundance of light elements to the baryon-to-photon ratio (see Cyburt et al. 2016). Observations of the primordial abundances of light elements such as Deuterium, Lithium, and Helium (Aver et al. 2015; Cooke et al. 2014; Aoki et al. 2009) hence provide strong constraints on the baryon-to-photon ratio. Given that the photon number is well determined by the CMB temperature, these observations and the BBN model give a solid estimation of the value of baryonic mass density, $\Omega_{\text{b}} \sim 0.05$ (Cyburt et al. 2016). The derived baryonic mass density is significantly lower than the total mass density, revealing a huge mass deficit.

1.2 Dark Matter Being the Solution and Its Challenges

Reproducing the cosmological observations A direct idea towards the mass discrepancy problem is to introduce some invisible matter, i.e. dark matter. In order to solves the dilemma of $\Omega_{\text{m}} > \Omega_{\text{b}}$, dark matter has to be non-baryonic. In the early Universe, baryonic matter was ionized and strongly coupled with photons. Dark matter, instead, is transparent to radiation, and hence decoupled earlier than baryonic matter. Therefore, the overdensities of dark matter and baryonic matter evolve differently with cosmic time leaving different imprints on the CMB. With the introduction of dark matter, the observed CMB power spectrum is well reproduced (e.g. see Planck Collaboration et al. 2016). The third peak is most

sensitive to dark matter density. If there is no dark matter, the third peak would be lower than the second one due to the absence of gravitational compression against photon pressure. The observed third peak is comparable to the second in height, indicating dark matter provides significant gravitational potential wells.

Adding dark matter can also reproduce the observed baryonic acoustic oscillation (BAO, Eisenstein et al. 2005). According to the standard cosmology, photons were coupled with charged particles before recombination, and the overdensities of the coupled baryon/photon fluid provide gravitational potential against photon pressure due to Thompson scattering. This sets up oscillating density waves. At recombination, photons diffused out leaving the standing waves of baryons. Since the overdensities are suppressed within small scales during radiation-dominated era, if there is no dark matter, the radiation-dominated era would end so late that the small-scale overdensities would have enough time to grow to large scale. This leads to more large-scale power and so large BAO amplitude. By adjusting the dark matter density, one can easily reproduce the observed BAO amplitude.

The dark matter model has a strong argument in structure formation. The additional mass provide extra gravitational potential wells. Since they do not interact with photons, the overdensity of dark matter can grow up to $\frac{\delta_D}{\rho_D} \sim 10^{-3}$ at recombination, providing potential wells much stronger than that of baryons. The potential wells then speed up the baryonic collapse to form the structure we observe at the present time.

Since the dark-matter model explains all the observations at cosmological scale with the same Ω_{CDM} , it has become the standard and most accepted explanation for mass discrepancies.

Challenges at small scales Inspite of the success at large scale, the dark matter paradigm faces a number of challenges at small scales (see Bullock & Boylan-Kolchin 2017, for a review). According to the dark matter model, the observed cosmic structure results from the primordial adiabatic fluctuations, which evolve and grow under gravitational instability. Depending on the property of dark matter particles, there are two different possible paths to form structures: top down structure formation and bottom up structure formation. For hot dark matter, which has low mass and moves at relativistic speed, only the most massive overdensities can survive, since smaller overdensities cannot provide strong enough gravitational potential to prevent dark matter particles from streaming away. Therefore, the most

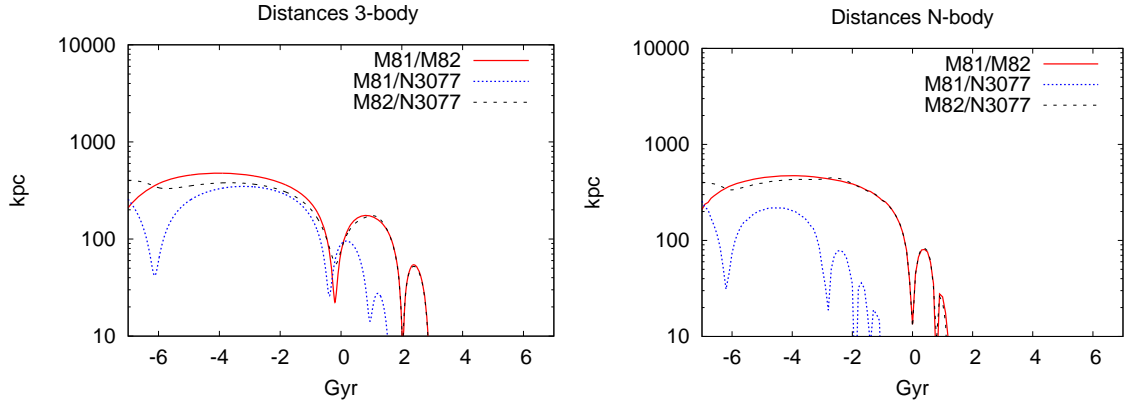


Figure 1.1 The merger of galaxies using 3-body (left) and N-body (right) simulations (from Oehm et al. 2017). The 3-body simulations assume the NFW halos of the three galaxies are as rigid as three single particles, while the N-body simulations use millions of particles to represent their halo profiles and trace the entire evolutions. The distances between two merging galaxies are plotted against time. The evolutionary process depends on the initial conditions. The plots showed here correspond to the condition leading to the shortest merging time.

massive object such as superclusters form first. Less massive objects such as groups and galaxies forms later through fragmentation and collapse. If dark matter particles are massive and slow-moving, i.e. cold dark matter (CDM), fluctuations on all scales can survive. Since less massive fluctuations collapse faster than massive overdensities, small objects such galaxies form first. More massive objects form through hierarchical merger (Press & Schechter 1974a). The hierarchical structure formation model has gained more and more attention and now strongly favored over the top-down model. As a stage of the whole process, Oehm et al. (2017) simulated the mergers of the three member galaxies, M81, M82 and NGC 3077 in the nearby M81 group of galaxies. They found the merger of two galaxies takes several Gyr (see Figure 1.1). This is a big challenge to the hierarchical structure formation model, since superclusters are formed by many mergers which will take longer than the age of the Universe. Therefore, additional mechanism has to be introduced in order to form the observed structures within the cosmic time.

At galactic scale, dark matter is expected to make up the missing mass revealed by galaxy dynamics. In order to quantify how much CDM halos can contribute to the total mass distribution in galaxies, one needs to resolve the halo structure. This study was carried out by Navarro et al. (1996a) by simulating the formation of dark matter halos. They

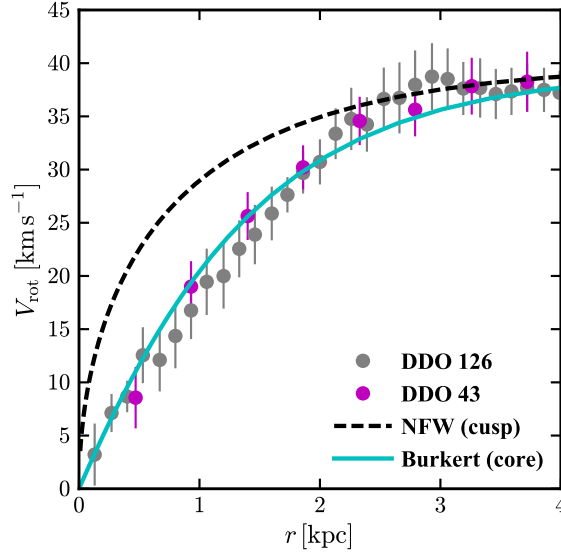


Figure 1.2 The core-cusp problem (from Bullock & Boylan-Kolchin 2017). The rotation curves of galaxy DDO 126 and DDO 43 from the LITTLE THINGS survey (Oh et al. 2015) are compared with the predictions of the NFW and Burkert profiles with $V_{\max} \sim 40 \text{ km s}^{-1}$. The NFW profile predicts a fast rising rotation curve at small radii in contrast to the observed ones. The Burkert profile, which has a core instead of a cusp in the center, provide a better description of the data.

found that though the halos could have very different masses, they can be described by the same profile with two parameters characterizing the overall density amplitude and the halo concentration, i.e. the Navarro-Frenk-White (NFW) profile. For disk galaxies, the expected rotation velocities would be the summation of the contributions of the NFW halos and baryonic disks. However, the NFW profile presents an steeply rising density profile, leading to a fast rising rotation curve at small radii (see Figure 1.2). This is in serious contrast with the rotation curves of many dwarf galaxies (e.g. see McGaugh et al. 2001; de Blok et al. 2008; Adams et al. 2014; Oh et al. 2015), known as the core-cusp problem (Flores & Primack 1994; Moore 1994). This problem has inspired many ideas such as baryonic feedback. Although the masses of galaxies are dominated by dark matter, the halo structure could be modified by repeating star formation (Read et al. 2016a) or supernova explosions (Governato et al. 2012; Di Cintio et al. 2014a). These processes can drive baryonic outflows, which in turn add additional outward gravitational pull onto DM particles. This effectively reduces the central density of DM halos. Other ideas include modifying the properties of dark matter, e.g. self-interacting dark matter (SIDM, Carlson et al. 1992;

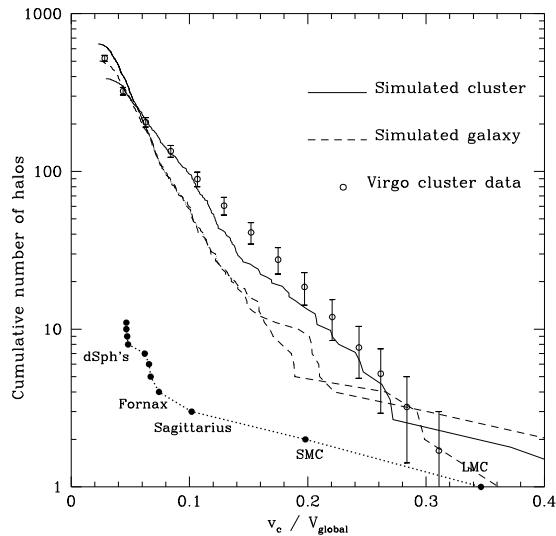


Figure 1.3 The missing satellite problem in the Milky Way (from Moore et al. 1999). The cumulative numbers of halos within the Milky Way (Mateo 1998) and Virgo Cluster (Binggeli et al. 1985) are plotted against circular velocity V_c normalized by the circular velocity of the host halo V_{global} , compared with the simulated results.

Spergel & Steinhardt 2000). The SIDM model introduces non-gravitational interaction between DM particles, so that elastic scattering events occur frequently within dark matter halos. The macroscopic result is a repulsive pressure, which causes the cusp to expand towards a core.

Since galaxies are formed from primordial fluctuations of dark matter, their abundance is predictable by the CDM model. Although the initial spectrum of density fluctuations experienced a complicated evolution, the transformed mass spectrum of collapsed objects can be derived using linear theory and spherical collapse (Gunn & Gott 1972; Press & Schechter 1974a; Sheth et al. 2001). Halo abundance is expressed as the derivative of dark matter halo number density over halo mass, i.e. dn/dM . Both simulations and analytic derivations suggest $dn/dM \sim M^{-1.9}$ at small and intermediate halo masses, while present an exponential decrease at the masses of typical galaxy clusters (e.g. see Sheth et al. 2001; Schechter 2002; Springel et al. 2008). This indicates that there should be more low-mass objects, such as satellite galaxies, than massive ones. Hundreds of satellites are hence expected in the Milky Way, but only ~ 50 of them have been observed (Drlica-Wagner et al. 2015). This big discrepancy is now known as “the Missing Satellite Problem” (Moore et al.

1999; Klypin et al. 1999, see Figure 1.3).

Later measurement of baryonic mass function (Read & Trentham 2005) shows that the Missing Satellite Problem is just part of the overall mismatch between the predicted and measured mass functions, assuming a linear relation between galaxy luminosity and total mass. The observed galaxy abundance is systematically lower than predicted at both low and high masses. Baryonic feedback is introduced to compensate this deviation. At high masses, the physical mechanism of active galactic nuclei (AGNs) is commonly invoked to suppress star formation by limiting black hole growth (Mihos & Hernquist 1996; Di Matteo et al. 2005; Springel et al. 2005; Hopkins et al. 2006; Debuhr et al. 2010; Choi et al. 2014; Emsellem et al. 2015). For low-mass halos, it is found that gas accretion is inefficient when there exists a strong photoionizing background (Ikeuchi 1986; Rees 1986; Babul & Rees 1992; Efstathiou 1992; Shapiro et al. 1994; Thoul & Weinberg 1996; Quinn et al. 1996). Therefore, star formation could be strongly suppressed after reionization, so that observed satellites must have been formed or accreted enough gas before that (Bullock et al. 2000; Kravtsov et al. 2004; Ricotti & Gnedin 2005; Koposov et al. 2009; Okamoto & Frenk 2009). This effectively reduces the number of predicted satellites in the Milky Way. It also predicts that the observed satellites must be among the most massive sub-halos in CDM simulations (Boylan-Kolchin et al. 2011). However, comparison with the Aquarius (Springel et al. 2008) and Via Lactea II (Diemand et al. 2008) simulations shows that there are many simulated subhalos more massive than the observed satellites both in the Milky Way (left panel in Figure 1.4) and in the field (right panel in Figure 1.4). This raises a problem since the more massive subhalos are too big to fail to form galaxies given that less massive satellites are observed (Boylan-Kolchin et al. 2011, 2012).

The problem associated with satellites is not only in the number, but also in how they are distributed and moving. In the CDM model, dark matter halos are quasi-spherical, and the subhalos within the host are expected to be randomly distributed and oriented (Pawlowski & McGaugh 2014). However, the satellites of the Milky Way appear to lie in a narrow plane perpendicular to the Galactic disk (Kunkel & Demers 1976; Lynden-Bell 1976; Kroupa et al. 2005) as shown in the left panel of Figure 1.5. This is inconsistent with isotropic or prolate substructure expected in the CDM model at the 99.5% level (Metz et al. 2007). Moreover, the motions of these satellites do not seem random but present an orbital

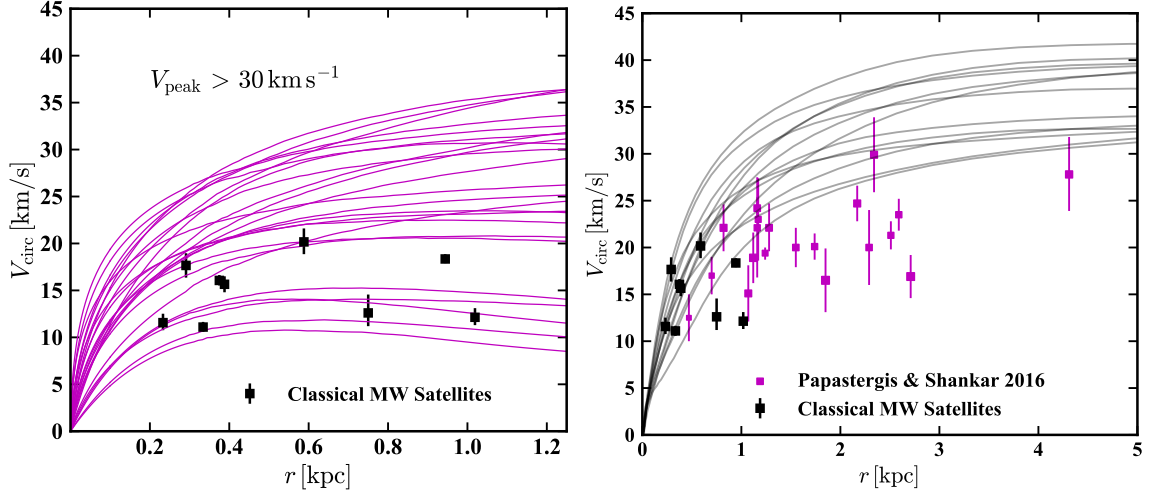


Figure 1.4 The “Too-Big-To-Fail” problem (from Bullock & Boylan-Kolchin 2017). The circular velocities of classical Milky-Way satellites (left) and field dwarfs (right) are plotted against their half-light radii. The magenta and gray lines show the predictions of the Aquarius simulations (Springel et al. 2008) for subhalos with peak maximum circular velocities $V_{\text{max}} > 30 \text{ km s}^{-1}$, and self-consistent hydrodynamic simulations (Fitts et al. 2017), respectively. There exist a large number of real Milky-Way satellites as well as dwarf galaxies with masses smaller than the predicted subhalos, so that the predicted halos must be massive enough to counteract the star-formation suppression by reionization, revealing the “Too-Big-To-Fail” problem in the Milky Way and in the field (Papastergis & Ponomareva 2017), respectively.

behavior (Pawlowski & Kroupa 2013). A similar configuration of satellite galaxies has been discovered in M31 (Metz et al. 2007), with 15 out of 27 dwarf galaxies lying in a thin plane and rotating around Andromeda (Conn et al. 2013; Ibata et al. 2013). A recent study (Müller et al. 2018) provides strong evidence that the satellite galaxies of the Centaurus A group present a whirling plane (see the right panel of Figure 1.5), which was suggested previously by Tully et al. (2015). These findings imply that the cosmological substructure components could not have been formed through near-isotropic infall, challenging the small-scale structure formation in the CDM paradigm.

Dark matter candidates Astronomical observations inspired the idea of introducing dark matter but do not predict what dark matter is. They do provide several important constraints on its properties.

- **Optically dark:** Dark matter particles are not observed, so that they can at most weakly interact with photons and charged particles. As a result, dark matter par-

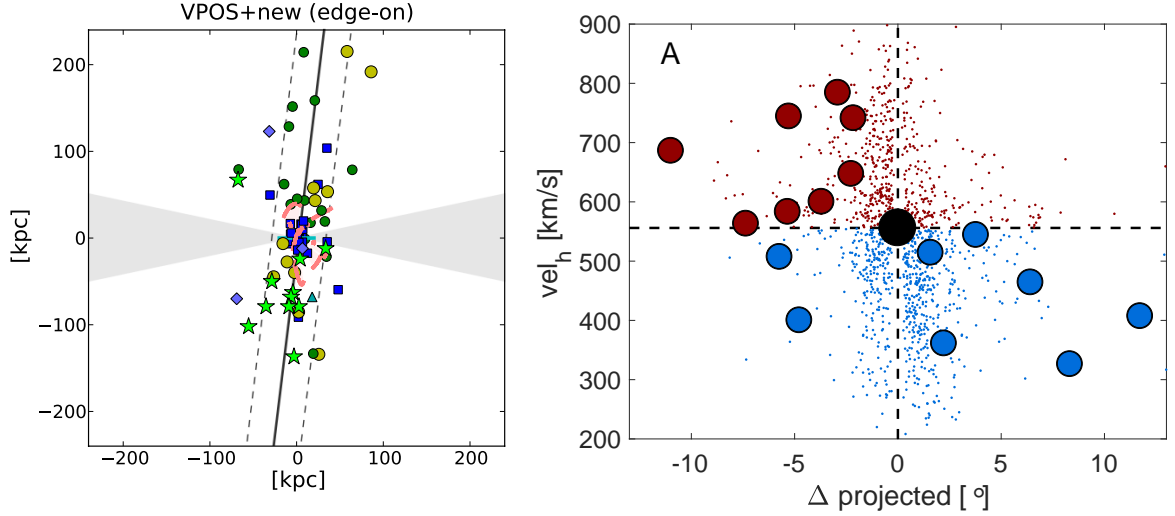


Figure 1.5 Plane and corotation of satellites. Left: Edge-on view of the Milky-Way satellite system taken from Pawlowski et al. (2015). Yellow circles, blue squares, and green triangles represent satellite galaxies, young halo globular clusters and star clusters, and unconfirmed objects (dwarfs or star clusters), respectively. Right: Heliocentric velocities versus angular distance for the satellite galaxies around Centaurus A taken from Müller et al. (2018). The black dot shows Centaurus A. Large and small points represent satellite galaxies and planetary nebula, with blue and red colors indicating approaching and receding, respectively.

ticles are nearly dissipationless and hence cannot cool down and collapse into the center of galaxies via emitting photons. But they can contribute to the background light via annihilation. Therefore, measuring the intensity of the cosmic background radiation from microwave to γ -ray bands can provide constraints on the cross section and mass of dark matter candidates (see Overduin & Wesson 2004, for review).

- Nearly collisionless: Frequent and strong collisions would make the distribution of dark matter particles round. The observations of the morphology of galaxy clusters (Mohr et al. 1995) and cluster collision (Clowe et al. 2006) hence constrain the strength of self-interaction of dark matter particles (e.g. see Hochberg et al. 2014; Hansen et al. 2015).
- Cold: The property “cold” means the DM particles are slow-moving (non-relativistic), as required by the structure formation theory. Dark matter particles have to be cold enough to form small-scale overdensities at the epoch of matter-radiation equality,

which seed observed objects such as galaxies. Cosmological simulations suggest that the mass of dark matter particles has to be above a few keV (Benson et al. 2013; Lovell et al. 2014; Kennedy et al. 2014).

- **Fluid-like:** Observations have not detected any discreteness of dark matter halos on galactic scale, so that the granularity of dark matter particle must be sufficiently small and fluid-like. If the mass of dark matter particles is as high as $\sim 10^6 M_\odot$, the granularity would heat galactic disks and disrupt globular clusters (Moore 1993; Rix & Lake 1993). Particles with mass $\lesssim 10^4 M_\odot$ could also introduce Poisson noise to the Ly α forest spectrum (Afshordi et al. 2003). These set up the upper limit of dark matter mass as $10^{3\sim 4} M_\odot$. Searches for massive astrophysical compact halo object (MACHO) (Alcock et al. 2000; Afonso et al. 2003; Tisserand et al. 2007; Wyrzykowski et al. 2011) using gravitational microlensing place further constraints on the mass of dark matter particle: less than 20% of the Milky-Way halo mass is made up by objects with mass between 10^{-7} and $10 M_\odot$. Therefore, the mass of dark matter particle must not lie in this range.
- **Classical (non-quantum):** Requiring dark matter particles to be classical is to avoid the occurrence of quantum behaviors, so that they can be well confined on galaxy scales. This sets up the lower limit for the mass of dark matter particle, since quantum nature would manifest only if the mass is sufficiently small. The specific lower limits depend on if the particle is Bosonic or Fermionic. For Bosonic dark matter, simply setting the de Broglie wavelength as galactic scale, saying 1 kpc, it gives $m \sim 10^{-22}$ eV (Hu et al. 2000). For Fermionic dark matter, Pauli exclusion principle dominates over quantum tunneling. Based on the phase space density from Tremaine & Gunn (1979), Baltz (2004) estimated the lower limit as $m \sim 25$ eV in order to confine dark matter within Milky-Way type galaxies.
- **Long-lived:** Dark matter particles have to be sufficiently stable, i.e. their lifetime must be longer than the age of the Universe, since they still exist at the present time. Some stronger constraints based on both observations and theoretical models require the lifetime to be an order of magnitude longer than Hubble time (e.g. see Queiroz & Sinha 2014; Audren et al. 2014; Mambrini et al. 2016; Baring et al. 2016; Lu &

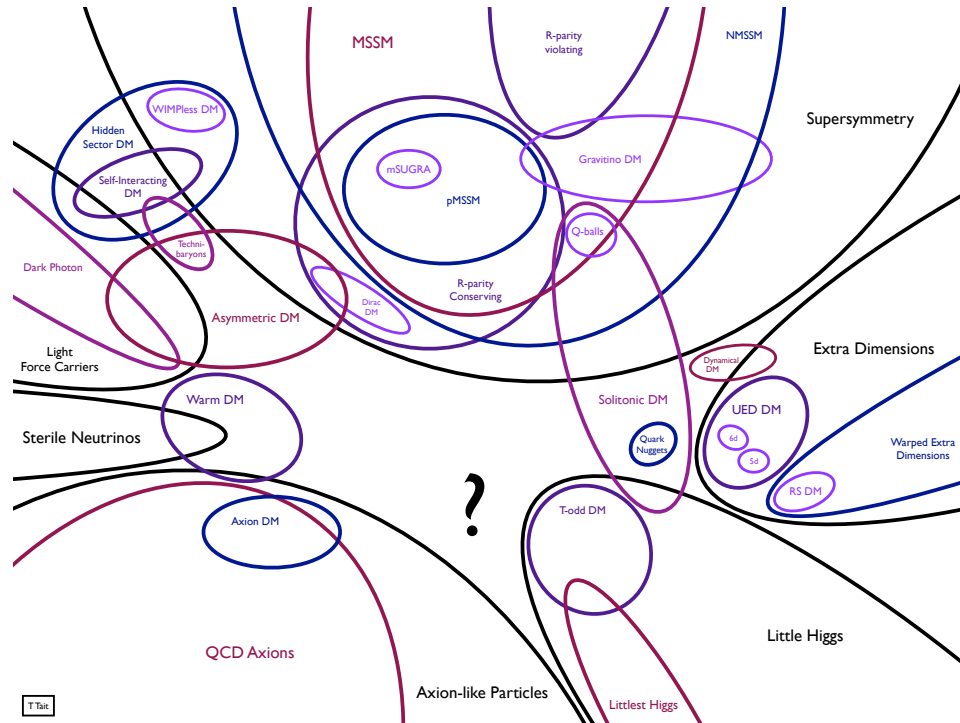


Figure 1.6 The landscape of dark matter candidates from Kusenko & Rosenberg (2013), image made by Timothy Tait.

Zong 2016; Slatyer & Wu 2017).

These constraints exclude a significant number of dark matter candidates. A landscape of dark matter candidates (see Kusenko & Rosenberg 2013) is shown in Figure 1.6. Baryonic dark matter such as brown dwarfs, black holes, cold gas, and warm dark matter such as neutrinos, which are not listed in the diagram, have been ruled out by these requirements. Another missing candidate is dark fluid (Zhao & Li 2010; Khoury 2015), which assumes that dark matter is fluid instead of particle, as described by scalar field, and can behave as both dark matter and dark energy. All the candidates listed in Figure 1.6 are from hypothesized extensions beyond the standard model of Particle Physics. For example, the sterile neutrino is proposed to generate neutrino mass. It is a gauge singlet fermion, and plays the role of right-handed neutrinos. As long as it is stable and provides the right amount of mass, it can be the dark matter. Another example is the axion, which is a new fundamental particle motivated by the strong CP problem in quantum chromodynamics (violation of CP symmetry, 't Hooft 1976). The axion is a pseudo-Goldstone boson. It is unstable, so that

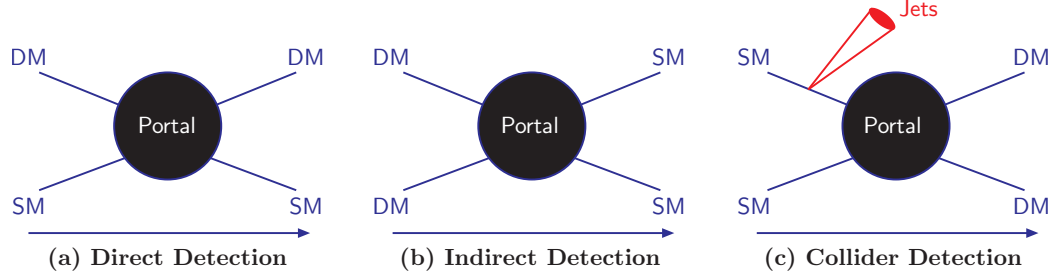


Figure 1.7 Direct, indirect and collider detections of dark matter particles making use of the interaction with standard-model particles (from Arcadi et al. 2018).

its small mass and weak coupling have to be tuned within a specific range in order to play the role of dark matter.

Among these candidates, the most compelling one for cosmologists is the weakly interacting massive particle (WIMP). WIMP is not a specific particle from a specific model, but represents a category of candidates which are massive and only interact through weak interaction and gravity. It can be a neutralino from the minimum supersymmetry standard model (MSSM), a Kaluza-Klein particle from the universal extra dimension (UED), or a T-odd particle from the little Higgs model. What makes it most favorable is the “WIMP miracle”. Assuming dark matter is a thermal relic and can annihilate into standard-model particles, the observed abundance of dark matter requires a self-annihilation cross section of $\langle \sigma v \rangle \simeq 3 \times 10^{-26} \text{ cm}^3 \text{ s}^{-1}$ (Feng 2010). This roughly matches the cross section expected for weakly interacting particles. Therefore, searches for WIMPs have been extensively carried out.

The detections of WIMPs make use of its weak interaction with standard-model particles, complementary to its gravity effect that manifests itself from astrophysical observations. Figure 1.7 illustrates the three WIMP detection strategies: direct detection, indirect detection, and collider detection. Direct detection seeks to measure the recoil of nuclei due to the scattering by WIMPs. The commonly used element is Xenon, e.g. the XENON100 experiment operated underground at the Italian Gran Sasso National Laboratory (Aprile et al. 2010, 2011a,b). The present measurement has not detected any excess scattering rate over the known background (e.g. see Tan et al. 2016; Aprile et al. 2017).

Indirect detection aims to detect the byproduct of WIMP annihilations, such as γ -rays. This method has been applied by the Fermi Gamma-Ray Space Telescope (Abdo et al.

2010; Ackermann et al. 2012, 2013). However, no excess γ -ray emission has been observed so far (Ackermann et al. 2015; Albert et al. 2017).

Collider detection attempts to produce WIMPs at the large hadron collider using proton-proton collisions (Bai et al. 2010; Goodman et al. 2010, 2011; Rajaraman et al. 2011). Since WIMPs are electrically neutral, they cannot leave imprints on the detector. But once produced, they will carry some energy and transverse momentum, which will be missing from the detector and possibly manifested in the form of a mono-jet. To date, the LHC has provided no evidence for WIMPs or other particles beyond the Standard Model. Now that space, ground and underground detections have not captured any signal of WIMPs despite tremendous efforts in the past decades, the most favorable candidate is losing its appeal.

1.3 Modified Dynamics Being the Solution and Its Challenges

Instead of extending particle species beyond the standard model of particle physics, one can modify the fundamental laws of how particles interact, i.e. gravity or inertia in this specific case. Introducing extra mass is equivalent to making gravity stronger mathematically, though the background physics is significantly different. There have been a number of theories of modified gravity as shown in Figure 1.8. These theories are proposed by adding new fields, extending the dimension of space-time, invoking non-local effects, or considering higher orders of the derivative of metric based on general relativity. Many models aim to address the cosmological constant problem (also known as the dark energy problem), such as Massive Gravity (de Rham & Gabadadze 2010; de Rham et al. 2011), and the Fab Four (Charmousis et al. 2012). Models that address the dark energy problem generally do not address the mass discrepancy problem. One of the theories that deal with the mass discrepancy problem is the Tensor-Vector-Scalar model (TeVeS Bekenstein 2004), a relativistic version of Modified Newtonian Dynamics (MOND, Milgrom 1983). At small scales, non-relativistic theory is sufficiently accurate in most cases given that the gravitational field is weak and the speed at which particles move is much smaller than light speed. Therefore, I will focus on the non-relativistic modified gravity in this section.

From the Tully-Fisher Relation to Modified Newtonian Dynamics

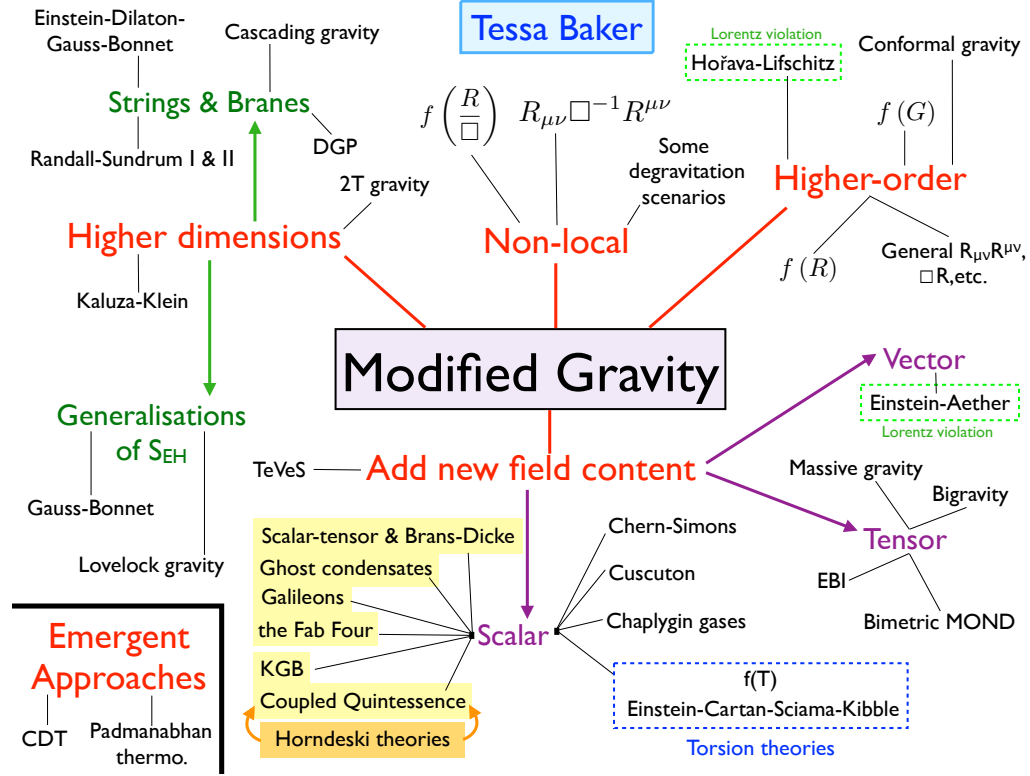


Figure 1.8 Tree diagram of the theories of modified gravity taken from Bull et al. (2016).

Combing spectroscopic measurements of H I line widths at 21 cm and optical photometry for disk galaxies, Tully & Fisher (1977) established a correlation between H I line width and galaxy luminosity, i.e. the well-known Tully-Fisher Relation, and suggested its potential usage as a distance indicator. As flat rotation curves had been extensively reported (Rubin et al. 1978; Bosma 1978), Milgrom (1983) proposed a modified theory of gravity, i.e. Modified Newtonian Dynamics (MOND). MOND reproduces the Tully-Fisher relation at large radii in galaxies, while recovering to Newtonian gravity at small radii where gravity is strong. However, what controls the transition between these two regions is not radius but acceleration, because different galaxies, though possibly significantly different in size, show consistency with a single Tully-Fisher relation. Thus, MOND predicts the existence of a critical acceleration scale, $a_0 \sim 10^{-10} \text{ m s}^{-2}$. Acceleration in MOND is related to Newtonian acceleration according to

$$g = g_N \mu(g_N/a_0), \quad (1.1)$$

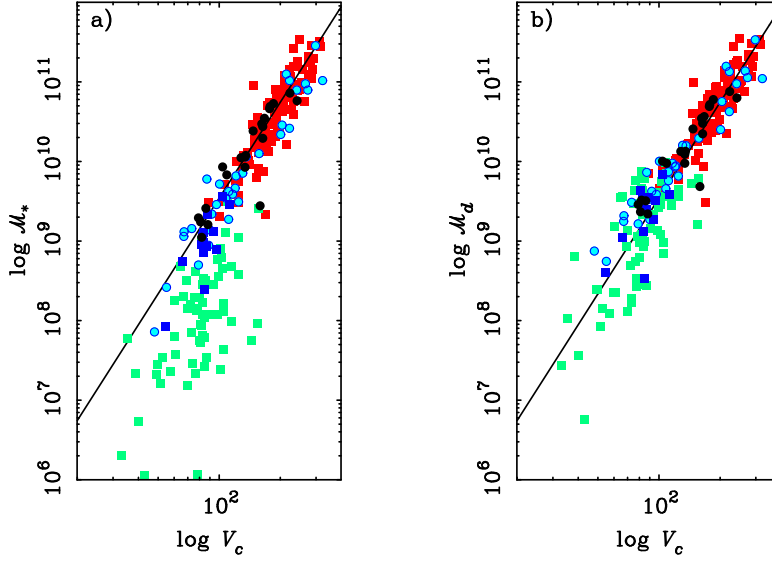


Figure 1.9 The Stellar (left) and Baryonic (right) Tully-Fisher relations (from McGaugh et al. 2000). Squares and circles represent galaxies with the circular velocity estimated from linewidth ($V_c = \frac{1}{2}V_{20}$) and resolved rotation curves ($V_c = V_{\text{flat}}$), respectively. Colors indicate the sources of the data: red from Bothun et al. (1985), black from Verheijen (1997), green from Pildis et al. (1997); Eder & Schombert (2000), light blue from McGaugh & de Blok (1998a), and dark blue from Matthews et al. (1998).

where $\mu(g_N/a_0)$ is an interpolation function, which goes as $\sqrt{g_N/a_0}$ when $g_N/a_0 \ll 1$ while returns to 1 when $g_N/a_0 \gg 1$. It can be interpreted as either modified inertial (Newton's second law), or modified gravity. In the case of rotating galaxies, it predicts

$$V_\infty^4 \propto MG a_0, \quad (1.2)$$

where V_∞ is the asymptotic rotation velocity and M is baryonic mass. This is essentially a baryonic version of Tully-Fisher relation, i.e. the correlation between total baryonic mass and flat rotation velocity. The Baryonic Tully-Fisher Relation (BTFR) was then established by McGaugh et al. (2000) as shown in Figure 1.9. When plotting stellar mass (m_*) against flat rotation velocity (V_{flat}), dwarf galaxies are systematically below the linear relation (see the left panel of Figure 1.9). After adding gas mass to the total baryonic mass ($M_b =$

$M_\star + M_{\text{gas}}$), they all move upward onto the expected line (see the right panel of Figure 1.9). This is because dwarf galaxies are gas rich. Considering only stellar mass will miss a significant fraction of the total baryonic mass. Verheijen (2001) found that the scatter of this relation went down when moving from B band to K band, since stellar mass-to-light ratio varies little at near infrared band. As a result, the BTFR has smaller scatter than the Tully-Fisher relation (McGaugh 2005; Lelli et al. 2016b), as expected in MOND.

The Radial Acceleration relation

Though MOND has clear asymptotic limits at high and low accelerations, it remains blank between these two acceleration scales. The commonly adopted method is to assume an interpolating function, such as the standard μ -function (Milgrom 1983) and the simple μ -function (Famaey & Binney 2005; Zhao & Famaey 2006). Theoretical works have not been able to work out a solid interpolating function. On the observational side, attention has been on the whole rotation curves rather than only the flat parts. By defining the mass discrepancy at each radii, $M_{\text{tot}}/M_{\text{bar}} \simeq V_{\text{obs}}^2/V_{\text{bar}}^2$, McGaugh (2004b) was able to investigate the common behaviors of many rotation curves. When plotting the mass discrepancy against acceleration, a clear relation, named the mass discrepancy-acceleration relation (MDAR), appeared. This relation not only incorporates the flat parts of rotation curves, but also describes the transition between high and low accelerations.

A potential defect of the MDAR is that the mass discrepancy and the centripetal acceleration are not independent observables, since both involve observational rotation velocities. It is hence unclear if this correlation results from the interconnection of these two observables by definition. Using a larger and more homogeneous sample of late-type galaxies (Lelli et al. 2016a), McGaugh et al. (2016b) plot $g_{\text{obs}} = \frac{V_{\text{obs}}^2}{R}$ against $g_{\text{bar}} = \frac{V_{\text{bar}}^2}{R}$ at each radius. These two observables are entirely independent, since g_{obs} is observed using spectroscopy while g_{bar} is determined by photometry. Despite entirely independent measurements, these two quantities are strongly correlated as manifested by the 2693 data points from 153 late-type galaxies (see Figure 1.10). This relation is the radial acceleration relation (RAR, also see Lelli et al. 2017b). It can be well fit by the function,

$$g_{\text{obs}} = \frac{g_{\text{bar}}}{1 - e^{-\sqrt{g_{\text{bar}}/g_{\ddagger}}}}, \quad (1.3)$$

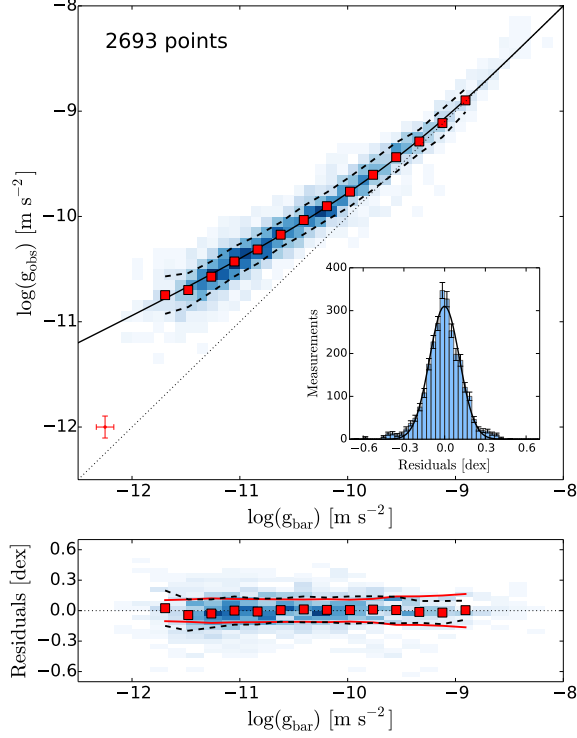


Figure 1.10 The Radial Acceleration Relation of rotationally supported galaxies from McGaugh et al. (2016a). The centripetal acceleration $g_{\text{obs}} = \frac{V_{\text{obs}}^2}{R}$ is calculated from rotation velocities, and the baryonic acceleration $g_{\text{bar}} = |\partial\Phi/\partial R|$ is derived from the distributions of stellar mass and gas mass. The total 2693 data points are plotted as a two-dimensional histogram. The solid, dashed and dotted lines are the best-fit relation, $1\text{-}\sigma$ ridges, and the line of unity, respectively. Red squares are the mean of binned data. The inset shows the distribution of the residuals, which is well fit by a Gaussian function with a standard deviation of 0.11 dex. The lower panel presents the distribution of the residuals as a function of g_{bar} , which shows no systematics.

where $g_{\ddagger} = 1.2 \times 10^{-10} \text{ m s}^{-2}$ is the only fitting parameter. The scatter around this relation is rather small, 0.13 dex, dominated by observational uncertainties on rotation curves, galaxy distance, disk inclination, as well as the variations of stellar mass-to-light ratio from galaxy to galaxy.

The RAR is an empirical law, established directly from the data and hence independent of any model. But it can be viewed as a realization of MOND, since it resembles all characteristics of MOND, such as the asymptotic BTFR at low acceleration and the existence of a characteristic acceleration scale g_{\ddagger} . The empirical relation indicates that rotation curves are solely determined by the distributions of baryonic mass. Dark matter, if exists, must be

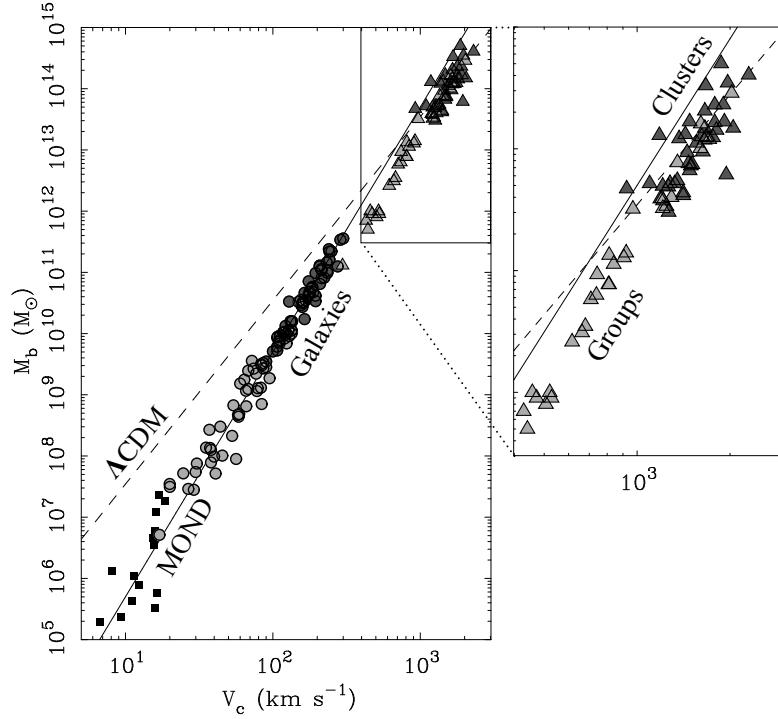


Figure 1.11 The baryonic mass versus circular velocity taken from McGaugh (2015). Squares, light gray circles, dark gray circles, light gray triangles, dark gray triangles represent dwarf spheroidals (McGaugh & Wolf 2010), gas rich spirals (McGaugh 2012), star-dominated spirals (McGaugh 2005), groups (Angus et al. 2008), and clusters of galaxies (Sanders 2003), respectively. The solid line is the prediction of MOND and the dashed line is the nominal expectation of Λ CDM assuming the cosmic baryonic fraction. Panel b is the expanded version of a portion of panel a. The data show that MOND is preferred by dwarfs and large spirals, while Λ CDM is preferred by groups and clusters of galaxies.

closely related to baryons and conspire to follow the radial acceleration relation. Therefore, it is difficult to naturally explain the RAR in the CDM paradigm.

Challenges in galaxy clusters and cosmology

The great success of MOND in galaxies motivated further investigations into groups, galaxy clusters, and the large scale structure of the Universe. Problems emerge in all these areas. Angus et al. (2008) studies 26 X-ray emitting systems on group scale, and found that their observed baryonic masses are systematically lower than the MOND predictions. Similarly, Sanders (2003) found that MOND, though provides stronger gravity, cannot completely remove the necessity of extra mass. The data of groups and galaxy clusters are shown in Figure 1.11, together with dwarf and spiral galaxies. The Λ CDM prediction is

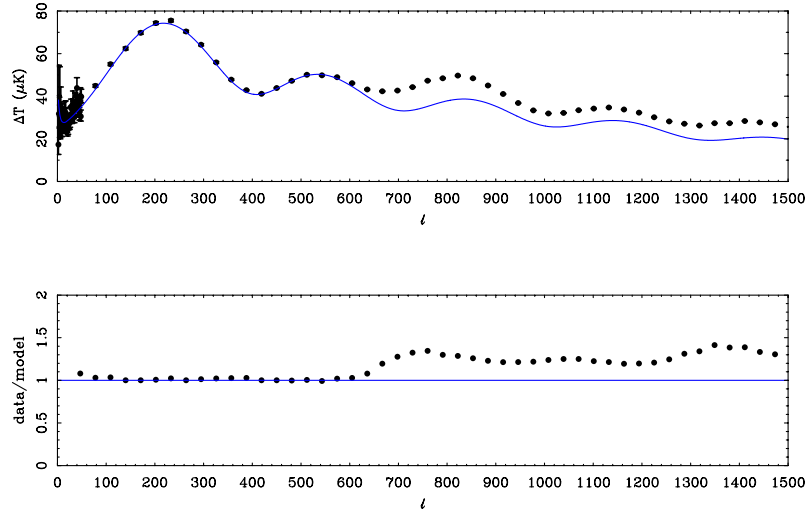


Figure 1.12 The power spectrum of CMB temperature fluctuations taken from McGaugh (2015). The measured spectrum by the Planck (Planck Collaboration et al. 2014) is compared to the prediction of the MOND-inspired no-CDM model (McGaugh 2004a).

made using the virial mass-virial velocity relation (McGaugh et al. 2010) with the cosmic baryon fraction $f_b = 0.17$ (Komatsu et al. 2011). Figure 1.11 suggests that galaxy clusters are better described by Λ CDM and groups are below the predictions of both MOND and Λ CDM. There is a “missing baryons” problem at group and cluster scales in MOND paradigm.

At cosmological scales, the observed CMB power spectrum is well reproduced in Λ CDM. Dark matter plays an essential role in explaining odd peaks by providing extra gravitational potential wells. The potential wells compress baryons and photons against rarefaction, leading to higher odd peaks. In a no-CDM model, baryonic damping is the dominated phenomenon. As a result, higher numbered peaks are also weaker in amplitude as shown in Figure 1.12. Though the first two peaks are reproduced perfectly, the third peak strongly disfavors a model without dark matter.

As mentioned earlier, dark matter has a strong argument in structure formation. Their density fluctuations provide extra gravitational wells, which help speed up baryonic collapses. In the MOND paradigm, matter density is baryon density. As a result, the epoch of matter-radiation equality occurs after recombination, at $z_{\text{eq}} \simeq 400$. Gas accretion is prevented by photon pressure until the decoupling of photons and baryons. This leads to the late start to structure formation. However, MOND predicts stronger gravitational interac-

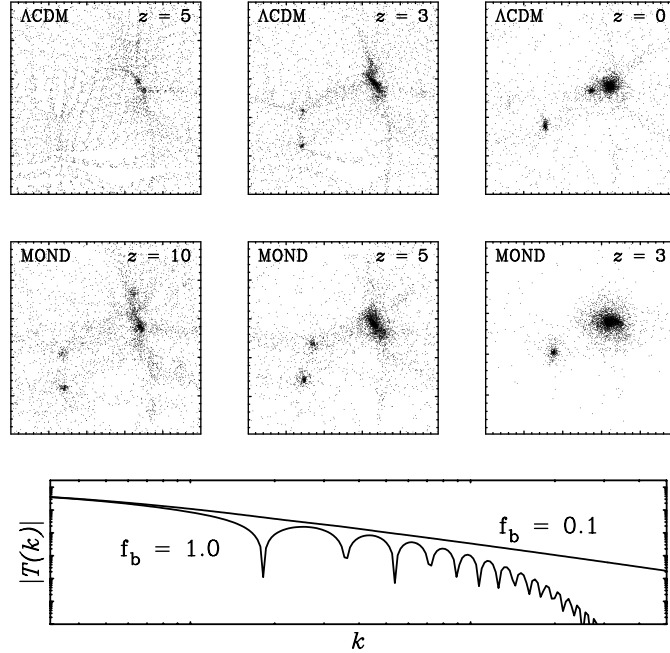


Figure 1.13 The simulated structure formation (from McGaugh 2015) using the MLAPM N -body code (Knebe & Gibson 2004). Top and middle panels show the predictions of Λ CDM and MOND, respectively. Panel g shows the transfer functions (Eisenstein & Hu 1998) in both models indicated by baryonic fraction f_b (0.1 for Λ CDM and 1.0 for MOND).

tions than Newtonian gravity at low acceleration, so that gas accretion proceeds significantly faster. N -body simulations (Knebe & Gibson 2004) show that large-scale structures are formed earlier in the MOND paradigm than in the Λ CDM model, though the later started earlier (see Figure 1.13). In short, massive galaxies, the cosmic web, and the first massive clusters are formed at $z \simeq 10$, $z \simeq 4$, and $z \simeq 2$, respectively, in the MOND paradigm (Sanders 1998, 2001). In addition, the large voids would have been swept empty at present time if the Universe was MONDian.

One of the big differences between a purely baryonic Universe and a dark-matter dominated Universe is the transfer functions. In Λ CDM, the initial baryonic acoustic oscillations are rearranged by dark matter fluctuations after recombination. This process effectively smoothed the transfer function. Therefore, the observed amplitude of the acoustic oscillations is significantly less profound in the CDM model than in a purely baryonic model (see the Panel g in Figure 1.13). This has been argued against MOND by (Dodelson 2011) assuming a linear growth of structure. However, MOND is a highly non-linear theory. It

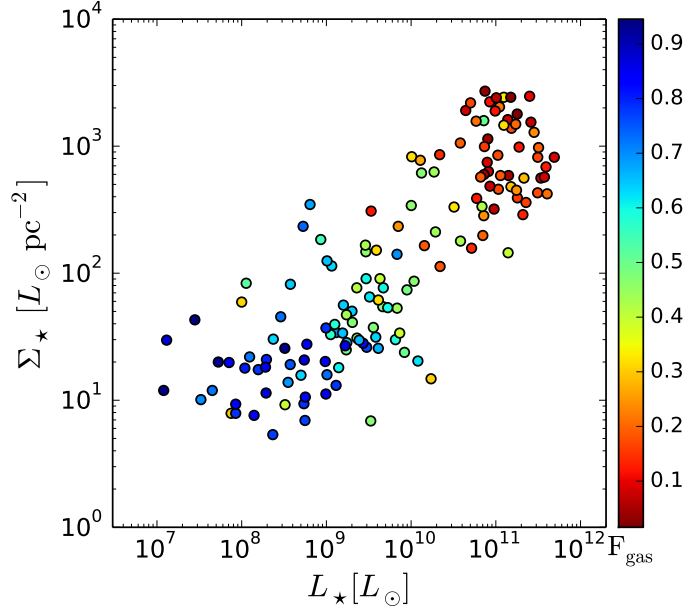


Figure 1.14 The effective surface brightness and luminosity of the SPARC galaxies (from McGaugh et al. 2016a). Galaxies are color-coded by gas fraction. The SPARC galaxies span ~ 5 dex in luminosity, ~ 3 dex in surface brightness, and range from gas-poor large spirals to gas-rich dwarf irregulars (see Lelli et al. 2016a, for details).

remains unclear if the initial baryonic acoustic oscillations can be smoothed in later non-linear evolution (McGaugh 1999).

1.4 The SPARC Database

In this thesis, I carry out a detailed and systematical investigation into the mass discrepancy problem using a large sample of late-type galaxies from the Spitzer Photometry & Accurate Rotation Curves (SPARC, Lelli et al. 2016a) database. The SPARC database¹ includes 175 late-type galaxies with high-quality HI/H α rotation curves and near-infrared Spitzer photometry. The HI measurements allow tracing the rotation velocity (V_{obs}) out to large radii providing strong constraints on the DM halo profiles. The Spitzer photometry has a key benefit: the stellar mass-to-light ratio has little scatter at $3.6 \mu\text{m}$ (e.g. McGaugh & Schombert 2014; Meidt et al. 2014; Schombert et al. 2019). This effectively helps breaking the disk-halo degeneracy (van Albada et al. 1985) when delineating the contributions of

¹astroweb.case.edu/SPARC

stellar disk and dark matter halo to the observed rotation curves. The mass models for the stellar disk and bulge (when present) are built by numerically solving the Poisson equation for the observed surface brightness profile at $3.6 \mu\text{m}$. Similarly, the mass contribution of the gas is derived from the observed HI surface density profile, scaled up to include Helium. The derived gravitational potentials of the baryonic components are represented by the circular velocities of test particles, tabulated as V_{disk} , V_{bul} , V_{gas} corresponding to the contributions of stellar disk, bulge and gas, respectively. For convenience, the stellar contributions in the SPARC database are tabulated using a mass-to-light ratio of unity in solar units, and need to be scaled down to more realistic values at $3.6 \mu\text{m}$ (Lelli et al. 2016a; Starkman et al. 2018).

SPARC is a large sample by the standard of HI interferometry. It includes all late-type galaxies from spirals to dwarf irregulars, and spans a large range in stellar mass (5 dex) and surface brightness (> 3 dex). This makes the SPARC sample ideal for model testing and exploring the properties of DM halos.

Galaxy distances in the SPARC database are measured via five different methods (see Lelli et al. 2016a, for details): (1) Hubble flow assuming $H_0 = 73 \text{ km s}^{-1} \text{ Mpc}^{-1}$ and correcting for Virgo-centric infall (97 galaxies). This is the least accurate method, since peculiar velocities could systematically affect the distance estimations. But it becomes more accurate for distant galaxies. Therefore, a distance-dependent scheme is adopted to estimate the uncertainties: 30% for $D \leq 20 \text{ Mpc}$, 25% for $20 < D \leq 40 \text{ Mpc}$, 20% for $40 < D \leq 60 \text{ Mpc}$, 15% for $60 < D \leq 80 \text{ Mpc}$, and 10% for $D > 80 \text{ Mpc}$. (2) Membership to the Ursa major cluster of galaxies. 28 galaxies are identified as the members of the Ursa major cluster (Verheijen & Sancisi 2001). Their distances are hence estimated as the mean value of the members, $18 \pm 0.9 \text{ Mpc}$ (Sorce et al. 2013). The uncertainty is dominated by the depth of the cluster, $\sim 2.3 \text{ Mpc}$. Adding the random error, the total uncertainty is 2.5 Mpc. (3) The tip magnitude of the red giant branch (TRGB). This method makes use of the fact that the brightest red-giant-branch stars have an I-band absolute magnitude of -4.0 ± 0.1 (Sakai 1999), which is insensitive to metallicity and age. The uncertainty of the TRGB method has two sources: systematic error in the empirical TRGB calibration, and statistic error on the size of star sample. This method provides distance estimations for 45 SPARC galaxies with uncertainties smaller than 10%. (4) The period-luminosity relation of Cepheids.

Cepheid variables are observed in three SPARC galaxies. Their pulsation periods are found to correlate with their luminosities. This strong, empirical relation established Cepheids as an accurate distance indicator. Its dependence on metallicity introduces some physical uncertainties. Observational uncertainties mainly result from the variations of the relation in different passbands, and photometric contamination, as well as some unknown extinction. These contribute to a total uncertainty $\sim 10\%$ for the three SPARC galaxies. (5) Type Ia supernovae. This method provides accurate distance estimations for two SPARC galaxies with uncertainties around 10% , dominated by the scatter around the luminosity-width relation that is used to standardize the candle.

Disk inclinations are determined when deriving rotation curves from the HI velocity fields using a tilted-ring model (Begeman 1987). This model assumes near-circular motions, and considers the warps of stellar disks by introducing radius dependent inclination. The final inclination angle is estimated as the mean value in the outer parts of the HI disk. Possible non-circular motions and the warps of disks contribute the major uncertainties. Considering the observational uncertainties, galaxy distance and disk inclination can be treated as fitting parameters when fitting rotation curves.

1.5 The Aims and Structure of This Dissertation

The mass discrepancy problem appears at many scales: the galactic scale, the galaxy-cluster scale, and the cosmological scale. The dark matter solution is successful at the cosmological scale, while facing many challenges at smaller scales. In contrast, the modified gravity solution does exactly the opposite. In this dissertation, I focus on galactic scales, and test both solutions using a large and homogeneous sample, the SPARC sample. Similar studies have been done in the past, but they mostly used small samples and did not succeed in breaking the disk-halo degeneracy. Taking advantage of the SPARC sample, I carry out a systematical study into the mass discrepancy problem. That includes testing the models by applying them to individual SPARC galaxies, investigating the predictions and the associated problems. To be specific, this dissertation is organized as follows.

In Chapter 2, I test seven dark-matter halo models (empirically or simulation motivated) by fitting the SPARC rotation curves. This provides an investigation into the core-

cusps problem since we fit both cored and cuspy halo profiles. As mentioned earlier, one of the solutions of this problem is to invoke baryonic feedback. This leads to modified halo profiles (e.g. see Di Cintio et al. 2014a; Read et al. 2016a). Fitting these profiles provides insights into the underlying physical processes. I provide a set of homogeneous rotation curve fits, and hence dark matter halo parametrizations. They can serve for model comparison and exploring halo properties.

In Chapter 3, I explore the correlations between dark matter halos and stellar disks using the SPARC rotation curve fits. Two simulation-motivated halo profiles, Einasto (Einasto 1965) and DC14 (Di Cintio et al. 2014a), are adopted, since they are well understood and provide satisfactory rotation curve fits. The derived scaling relations serve as test beds for galaxy formation models.

In Chapter 4, I measure for the first time the dark matter halo mass function using galaxies from the H I Parkes All Sky Survey catalog (Meyer et al. 2004; Zwaan et al. 2010). Using the SPARC rotation curve fits, I establish the correlation between H I line width and dark matter halo mass for disk-dominated galaxies. This relation enables me to derive the halo masses for the large HIPASS sample without fitting rotation curves, and hence measure the halo mass function. This provides a direct comparison with the N-body cosmological simulations.

In Chapter 5, I study the effect of adiabatic compression of DM halos resulting from the formation of stellar disks. The common method of fitting rotation curves treats stellar disks and dark matter halos as separate, independent, and static components. However, these two components are dynamically coupled. By simulating the evolution of dark matter halos, I investigate how the compression can affect the dark matter distribution for galaxies with a large variety in mass and hence the resultant rotation curves. I also develop a new method of fitting rotation curves that results in DM halos in dynamic equilibrium with embedded baryons.

In Chapter 6, I fit the radial acceleration relation to individual SPARC galaxies. This tests if the statistically established relation holds for individual galaxies. I check the resultant parameter distributions, such as stellar mass-to-light ratio, and investigate the intrinsic scatter of this relation. I also investigate if there is a universal acceleration scale in the fitted RAR, which marks the essential difference between an empirical law and a fundamental

theory. This is equivalent to testing the MOND paradigm in individual galaxies.

In Chapter 7, I summarize the results and discuss the future projects.

Chapter 2

A Comprehensive Catalog of Dark Matter Halo Models for SPARC Galaxies

2.1 Abstract

We present rotation curve fits to 175 late-type galaxies from the *Spitzer* Photometry and Accurate Rotation Curves (SPARC) database using seven dark matter (DM) halo profiles: pseudo-isothermal, Burkert, Navarro-Frenk-White (NFW), Einasto, Di Cintio et al. (2014a, hereafter DC14), cored-NFW, and a new semi-empirical profile named Lucky13. We marginalize over stellar mass-to-light ratio, galaxy distance, disk inclination, halo concentration and halo mass (and an additional shape parameter for Einasto) using a Markov Chain Monte Carlo method. We find that cored halo models such as the DC14 and Burkert profiles generally provide better fits to rotation curves than the cuspy NFW profile. The stellar mass-halo mass relation from abundance matching is recovered by all halo profiles once imposed as a Bayesian prior, whereas the halo mass-concentration relation is not reproduced in detail by any halo model. We provide an extensive set of figures as well as best-fit parameters in machine-readable tables to facilitate model comparison and the exploration of DM halo properties.

2.2 Introduction

Rotation curves reveal a discrepancy between dynamically determined and optically measured masses of galaxies (Rubin et al. 1978; Bosma 1981; van Albada et al. 1985). Together with other astrophysical evidences, this led to the introduction of dark matter. Since then, various DM halo profiles have been proposed, such as the pseudo-isothermal (pISO) and NFW (Navarro et al. 1996b) profiles.

Lelli et al. (2016a) built the Spitzer Photometry & Accurate Rotation Curves (SPARC) database including 175 late-type galaxies with extended H I/H α rotation curves and near-infrared surface photometry. This galaxy sample provides us the opportunity to make a comprehensive survey of halo models by fitting all the data in a homogeneous fashion.

A large amount of rotation curve fits can serve the purpose of exploring DM halo properties and potential correlations. For example, in Li et al. (2019), we fit two simulation-motivated profiles, the Einasto (Einasto 1965) and DC14 (Di Cintio et al. 2014a) profiles, to the SPARC galaxies, and find that the halo scale radius and surface density of the DM halo correlate with galaxy luminosity with a similar power law, while the characteristic volume density is a constant. This finding benefits from the wide ranges in stellar mass, surface brightness and gas fraction that the SPARC galaxies span.

In this paper, we provide rotation curve fits to 175 SPARC galaxies using seven halo models with/without Λ CDM motivated priors, depending on the availability of the priors for each profile. Summary tables and figures are organized by galaxy and by halo profile together with the best-fit parameters, so that readers can easily look up these fits for their own research. The results are made publicly available in the SPARC website.

2.3 Data, models and method

2.3.1 The SPARC sample

The SPARC database (Lelli et al. 2016a) includes 175 late-type galaxies with high-quality H I/H α rotation curves and near-infrared Spitzer photometry. The H I measurements allow tracing the rotation velocity (V_{obs}) out to large radii providing strong constraints on the DM halo profiles. The Spitzer photometry has a key benefit: the stellar

mass-to-light ratio has little scatter at $3.6 \mu\text{m}$ (e.g. McGaugh & Schombert 2014; Meidt et al. 2014; Schombert et al. 2019). This effectively helps breaking the disk-halo degeneracy (van Albada et al. 1985) when delineating the contributions of stellar disk and dark matter halo to the observed rotation curves. The mass models for the stellar disk and bulge (when present) are built by numerically solving the Poisson equation for the observed surface brightness profile at $3.6 \mu\text{m}$. Similarly, the mass contribution of the gas is derived from the observed H I surface density profile, scaled up to include Helium. The derived gravitational potentials of the baryonic components are represented by the circular velocities of test particles, tabulated as V_{disk} , V_{bul} , V_{gas} corresponding to the contributions of stellar disk, bulge and gas, respectively. For convenience, the stellar contributions in the SPARC database are tabulated using a mass-to-light ratio of unity in solar units, and need to be scaled down to more realistic values at $3.6 \mu\text{m}$ (Lelli et al. 2016a; Starkman et al. 2018).

SPARC is a large sample by the standard of H I interferometry. It includes all late-type galaxies from spirals to dwarf irregulars, and spans a large range in stellar mass (5 dex) and surface brightness (> 3 dex). This makes the SPARC sample ideal for model testing and exploring the properties of DM halos.

Galaxy distances in the SPARC database are measured via five different methods (see Lelli et al. 2016a, for details): Hubble flow assuming $H_0 = 73 \text{ km s}^{-1} \text{ Mpc}^{-1}$ and correcting for Virgo-centric infall, the tip magnitude of the red giant branch, the period-luminosity relation of Cepheids, membership to the Ursa major cluster of galaxies, and Type Ia supernovae. Disk inclinations are estimated kinematically. We treat distance and inclination as nuisance parameters, marginalizing over their uncertainty by imposing Gaussian priors with a standard deviation equal to their formal uncertainty.

2.3.2 Dark matter halo profiles

In this paper, we attempt to investigate all available DM profiles, including pseudo-isothermal (pISO), Burkert, NFW, Einasto, DC14, cored-NFW and a new semi-empirical profile that we call Lucky13. In general, each halo profile contains two fitting parameters: a scale radius r_s and a characteristic volume density ρ_s . For convenience, the free parameters

in our fits are the concentration C_{200} and the rotation velocity V_{200} , which are defined as

$$C_{200} = r_{200}/r_s; \quad V_{200} = 10 C_{200} r_s H_0, \quad (2.1)$$

where r_{200} is the radius inside of which the average halo density is 200 times the critical density of the universe. For consistency, we use these cosmologically motivated definitions also for purely empirical DM profiles, such as the pISO and Burkert models. In the following, we describe each halo model in detail.

pISO: Rotation curves of dwarf galaxies are found to be well fit by an empirical profile with a constant-density core, the pseudo-isothermal profile (see e.g. Adams et al. 2014; Oh et al. 2015),

$$\rho_{\text{pISO}} = \frac{\rho_s}{1 + (\frac{r}{r_s})^2}. \quad (2.2)$$

The enclosed mass profile is given by

$$M_{\text{pISO}} = 4\pi\rho_s r_s^3 \left[x - \arctan(x) \right], \quad (2.3)$$

where we have introduced the dimensionless parameter $x = r/r_s$. The corresponding rotation velocity profile is

$$\frac{V_{\text{pISO}}}{V_{200}} = \sqrt{\frac{1 - \arctan(x)/x}{1 - \arctan(C_{200})/C_{200}}}. \quad (2.4)$$

Burkert: The enclosed mass of the pISO profile quickly diverges at large radii (Eq. 3). Burkert (1995) proposed a modified version of the pISO profile that diverges more slowly,

$$\rho_{\text{Burkert}} = \frac{\rho_s}{(1 + \frac{r}{r_s})[1 + (\frac{r}{r_s})^2]}, \quad (2.5)$$

with an enclosed halo mass profile given by

$$M_{\text{Burkert}} = 2\pi\rho_s r_s^3 \left[\frac{1}{2} \ln(1 + x^2) + \ln(1 + x) - \arctan(x) \right]. \quad (2.6)$$

Its rotation velocity is then given by

$$\frac{V_{\text{Burkert}}}{V_{200}} = \frac{C_{200}}{x} \times \sqrt{\frac{\frac{1}{2} \ln(1+x^2) + \ln(1+x) - \arctan(x)}{\frac{1}{2} \ln(1+C_{200}^2) + \ln(1+C_{200}) - \arctan(C_{200})}}. \quad (2.7)$$

NFW: N-body DM-only simulations of structure formation predict a cuspy profile (Navarro et al. 1996b),

$$\rho_{\text{NFW}} = \frac{\rho_s}{\left(\frac{r}{r_s}\right)\left[1 + \left(\frac{r}{r_s}\right)\right]^2}, \quad (2.8)$$

which goes as $\rho \propto r^{-1}$ at small radii and $\rho \propto r^{-3}$ at large radii. Its enclosed mass profile is

$$M_{\text{NFW}} = 4\pi\rho_s r_s^3 \left[\ln(1+x) - \frac{x}{1+x} \right], \quad (2.9)$$

corresponding to the rotation velocity profile

$$\frac{V_{\text{NFW}}}{V_{200}} = \sqrt{\frac{C_{200}}{x} \frac{\ln(1+x) - x/(1+x)}{\ln(1+C_{200}) - C_{200}/(1+C_{200})}}. \quad (2.10)$$

Einasto: Using high-resolution DM-only simulations, Navarro et al. (2004) find that the simulated halos can be better described by the Einasto profile (Einasto 1965),

$$\rho_{\text{Einasto}} = \rho_s \exp \left\{ -\frac{2}{\alpha_\epsilon} \left[\left(\frac{r}{r_s} \right)^{\alpha_\epsilon} - 1 \right] \right\}, \quad (2.11)$$

which introduces an additional shape parameter α_ϵ . When $\alpha_\epsilon > 0$, the profile has a finite central density. Its enclosed mass profile (Mamon & Łokas 2005; Merritt et al. 2006) is

$$M_{\text{Einasto}} = 4\pi\rho_s r_s^3 \exp \left(\frac{2}{\alpha_\epsilon} \right) \left(\frac{2}{\alpha_\epsilon} \right)^{-\frac{3}{\alpha_\epsilon}} \frac{1}{\alpha_\epsilon} \Gamma \left(\frac{3}{\alpha_\epsilon}, \frac{2}{\alpha_\epsilon} x^{\alpha_\epsilon} \right), \quad (2.12)$$

where $\Gamma(a, x) = \int_0^x t^{a-1} e^{-t} dt$ is the incomplete Gamma function, and the velocity profile is given by

$$\frac{V_{\text{Einasto}}}{V_{200}} = \sqrt{\frac{C_{200}}{x} \frac{\Gamma \left(\frac{3}{\alpha_\epsilon}, \frac{2}{\alpha_\epsilon} x^{\alpha_\epsilon} \right)}{\Gamma \left(\frac{3}{\alpha_\epsilon}, \frac{2}{\alpha_\epsilon} C_{200}^{\alpha_\epsilon} \right)}}. \quad (2.13)$$

The shape parameter α_ϵ depends on halo mass (Dutton & Macciò 2014),

$$\alpha_\epsilon = 0.0095v^2 + 0.155, \quad (2.14)$$

where $\log v = -0.11 + 0.146m + 0.0138m^2 + 0.00123m^3$ and $m = \log(M_{\text{halo}}/10^{12}h^{-1}M_\odot)$. Simulated DM halos present a standard deviation of 0.16 dex around the mean relation. However, in real galaxies, the final distribution of α_ϵ differs significantly from this relation if we do not impose it as a Bayesian prior (Li et al. 2019). We hence include this relation as part of the Λ CDM priors (explained in Section 2.3).

DC14: According to cosmological simulations of galaxy formation, baryonic matter accreted within the halos could exert a feedback effect on the halo and hence modify its halo profiles. Di Cintio et al. (2014a) consider the baryonic feedback due to supernovae using a set of zoom-in, hydrodynamic simulations. They establish the DC14 model, whose profile is defined in terms of the model class (α, β, γ) (Hernquist 1990; Zhao 1996),

$$\rho_{\alpha\beta\gamma} = \frac{\rho_s}{\left(\frac{r}{r_s}\right)^\gamma \left[1 + \left(\frac{r}{r_s}\right)^\alpha\right]^{(\beta-\gamma)/\alpha}}, \quad (2.15)$$

where β and γ are, respectively, the inner and outer slopes, and α describes the transition between the inner and outer regions. The values of these parameters depend on the stellar-to-halo mass ratio (SHM),

$$\begin{aligned} \alpha &= 2.94 - \log[(10^{X+2.33})^{-1.08} + (10^{X+2.33})^{2.29}], \\ \beta &= 4.23 + 1.34X + 0.26X^2, \\ \gamma &= -0.06 + \log[(10^{X+2.56})^{-0.68} + 10^{X+2.56}], \end{aligned} \quad (2.16)$$

where $X = \log(M_\star/M_{\text{halo}})$ is the SHM ratio in logarithmic space. Its enclosed mass profile is given by

$$M_{\text{DC14}} = 4\pi r_s^3 \rho_s \frac{1}{\alpha} [B(a, b+1, \epsilon) + B(a+1, b, \epsilon)], \quad (2.17)$$

where $B(a, b, x) = \int_0^x t^{a-1}(1-t)^{b-1} dt$ is the incomplete Beta function, and we define $a = (3 - \gamma)/\alpha$, $b = (\beta - 3)/\alpha$ and $\epsilon = \frac{(r/r_s)^\alpha}{1+(r/r_s)^\alpha}$. Thus, its velocity profile is given by

$$\frac{V_{\text{DC14}}}{V_{200}} = \sqrt{\frac{C_{200}}{x} \frac{B(a, b + 1, \epsilon) + B(a + 1, b, \epsilon)}{B(a, b + 1, \epsilon_c) + B(a + 1, b, \epsilon_c)}}. \quad (2.18)$$

Equation 3.4 only works for the SHM ratio within $(-4.1, -1.3)$, since this is the range where the supernovae feedback is significant and dominant. At $X < -4.1$, the energy released by supernovae is insufficient to modify the initial cuspy profile, so that an NFW profile remains. At $X > -1.3$, feedback due to active galactic nuclei might start to dominate. We hence set $X = -1.3$ as the largest acceptable value, following Katz et al. (2017).

The fitting results for the Einasto and DC14 profiles are presented in Li et al. (2019). For completeness and comparison, we also include those fits in this paper.

coreNFW: More recently, Read et al. (2016a,b) investigate the evolution of isolated dwarf galaxies using high-resolution hydrodynamic simulations. They conclude that long-time evolution can transform an inner cusp into a finite central core through repeated bursts of star formation. They provide a general fitting function for the evolved DM profile in terms of the NFW profile,

$$M_{\text{coreNFW}}(< r) = M_{\text{NFW}}(< r) f^n, \quad (2.19)$$

where $f = \tanh(\frac{r}{r_c})$ acts to cancel the central cusp. The core size r_c is proportional to the stellar half-mass radius $R_{1/2}$, $r_c = \eta R_{1/2}$, where the proportional constant η is suggested to be 1.75. There could be some galaxy-to-galaxy scatter around this value of η , but we keep it fixed to minimize the number of free parameters in the fit.

How shallow the core becomes is controlled by the evolution parameter n ($0 < n < 1$). When $n = 1$, it is a complete core, while $n = 0$ corresponds to a cusp. Therefore, the evolution of the halo profile is traced by the value of n , which is given by

$$n = \tanh\left(\kappa \frac{t_{\text{SF}}}{t_{\text{dyn}}}\right), \quad (2.20)$$

where the so-called star-formation time t_{SF} is set to 14 Gyr since all SPARC galaxies are at $z=0$, the tuning parameter κ is set to 0.04 as suggested by the simulations of Read et al.

(2016a) and the dynamic time t_{dyn} is defined as

$$t_{\text{dyn}} = 2\pi \sqrt{\frac{r_s^3}{GM_{\text{NFW}}(r_s)}}. \quad (2.21)$$

For the SPARC galaxies, this gives values of n spanning the range 0.1 to 1.0. The resulting cored NFW (coreNFW) profile has a volume density profile given by

$$\rho_{\text{coreNFW}} = f^n \rho_{\text{NFW}} + \frac{nf^{n-1}(1-f^2)}{4\pi r^2 r_c} M_{\text{NFW}}. \quad (2.22)$$

Lucky13: We construct another cored profile from the (α, β, γ) models by considering the specific case $\gamma = 0$ to reach a finite core and $\beta = 3$ to get the same decreasing rate as the NFW profile at large radii. The transition parameter is simply set as $\alpha = 1$. This gives us the following profile

$$\rho_{130} = \frac{\rho_s}{[1 + (\frac{r}{r_s})]^3}, \quad (2.23)$$

which we call the Lucky13. Its enclosed mass profile is given by

$$M_{130} = 4\pi\rho_s r_s^3 \left[\ln(1+x) + \frac{2}{1+x} - \frac{1}{2(1+x)^2} - \frac{3}{2} \right], \quad (2.24)$$

corresponding to the velocity profile

$$\frac{V_{130}}{V_{200}} = \sqrt{\frac{C_{200}}{x} \frac{\ln(1+x) + \frac{2}{1+x} - \frac{1}{2(1+x)^2} - \frac{3}{2}}{\ln(1+C_{200}) + \frac{2}{1+C_{200}} - \frac{1}{2(1+C_{200})^2} - \frac{3}{2}}}. \quad (2.25)$$

2.3.3 MCMC simulations

We fit the observed rotation velocities by summing the contribution of each component,

$$V_{\text{tot}}^2 = V_{\text{DM}}^2 + \Upsilon_{\text{disk}} V_{\text{disk}}^2 + \Upsilon_{\text{bul}} V_{\text{bul}}^2 + V_{\text{gas}}^2. \quad (2.26)$$

In general, DM profiles have two free parameters V_{200} and C_{200} (the Einasto profile has an additional shape parameter α_ϵ). For the baryonic contributions, there are also three adjustable parameters: stellar mass-to-light ratio Υ_\star , galaxy distance D and disk inclination i . They comprise a five (six for Einasto) dimensional parameter space. To fit these

halo profiles, we map the posterior distributions of these fitting parameters using the open python package *emcee* (Foreman-Mackey et al. 2013). As in Li et al. (2019), we impose lognormal priors on Υ_\star around their fiducial values ($\Upsilon_{\text{disk}}=0.5$ and $\Upsilon_{\text{bul}}=0.7$ according to McGaugh et al. 2016b; Lelli et al. 2017b) with a standard deviation of 0.1 dex suggested by stellar population synthesis models (e.g., see Bell & de Jong 2001a; Portinari et al. 2004; Meidt et al. 2014; Schombert et al. 2019), and Gaussian priors on D and i around their mean values as tabulated in the SPARC database with standard deviations given by their uncertainties.

As for halo parameters, we set general loose boundaries for them: $10 < V_{200} < 500$ km s⁻¹, $0 < C_{200} < 1000$. Within these ranges, flat priors are imposed for all considered halo profiles. For the NFW, Einasto, DC14, coreNFW and Lucky13 profiles, we also impose the Λ CDM priors, which is comprised of the SHM relation (Moster et al. 2013) and the halo mass-concentration relation (Macciò et al. 2008). The multi-epoch abundance matching determines the relation between stellar and DM halo masses,

$$\frac{M_\star}{M_{200}} = 2N \left[\left(\frac{M_{200}}{M_1} \right)^{-\beta} + \left(\frac{M_{200}}{M_1} \right)^\gamma \right]^{-1}, \quad (2.27)$$

where $\log(M_1) = 11.59$, $N = 0.0351$, $\beta = 1.376$ and $\gamma = 0.608$. Moster et al. (2013) estimated the scatter to be $\sigma(\log M_\star) = 0.15$ dex around this relation. This prior, together with the lognormal prior on stellar mass-to-light ratios, robustly breaks the disk-halo degeneracy.

Macciò et al. (2008) show that the concentration and halo mass are correlated via a power law,

$$\log(C_{200}) = a - b \log(M_{200}/[10^{12} h^{-1} M_\odot]), \quad (2.28)$$

where the coefficients a and b depend on cosmology and halo profile. For the NFW, coreNFW and Lucky13 profiles, we use the values from the WMAP5 cosmology corresponding to $H_0 = 72$ km s⁻¹ Mpc⁻¹, close to the value adopted for the SPARC database,

$$a = 0.830, \quad b = -0.098. \quad (2.29)$$

Di Cintio et al. (2014a) show that the concentration for the DC14 profile is related to that

of NFW by

$$C_{200,DC14} = C_{200,NFW}(1.0 + e^{0.0001[3.4(X+4.5)]}). \quad (2.30)$$

For the Einasto profile, the coefficients as shown in Li et al. (2019) are

$$a = 0.977, \quad b = -0.130. \quad (2.31)$$

Equation 2.28 is the mean concentration-halo mass relation, and it has an intrinsic scatter of 0.11 dex.

We choose the likelihood function as $\exp(-\frac{1}{2}\chi^2)$, where χ^2 is defined as

$$\chi^2 = \sum_R \frac{[V_{\text{obs}}(R) - V_{\text{tot}}(R)]^2}{(\delta V_{\text{obs}})^2}, \quad (2.32)$$

where V_{obs} is the observed rotation velocity and δV_{obs} is the observational uncertainty. The final posterior probability is proportional to the product of the likelihood function and priors according to Bayes theorem.

We use the standard affine-invariant ensemble sampler in *emcee* as in Li et al. (2019). We initialize the MCMC chains with 200 random walkers and the size of stretch-move $a = 2$. We run 500 iterations for the burn-in period and then reset the sampler, before running another 2000 iterations. We check that the acceptance fractions for most galaxies are within 10% and 70%. There are a few galaxies with lower acceptance fractions, but their posterior distributions are well behaved. The parameter sets corresponding to the maximum probability are marked as the best-fit parameters. We estimate their uncertainties using the “std” output of GetDist, an open Python package for analysing Monte Carlo samples.

2.4 Results

In Figure 3.2, we plot the cumulative distribution function (CDF) of the reduced χ^2 ($\chi_v^2 = \frac{\chi^2}{N-f}$) for all the halo profiles. Among these profiles, the Einasto profile with flat priors on halo parameters has the best fit quality since it has the largest number of fitting parameters. In general, cored profiles such as Burkert, coreNFW, DC14, Einasto, pISO, provide better rotation curve fits than the cuspy NFW profile, no matter if we impose Λ CDM priors

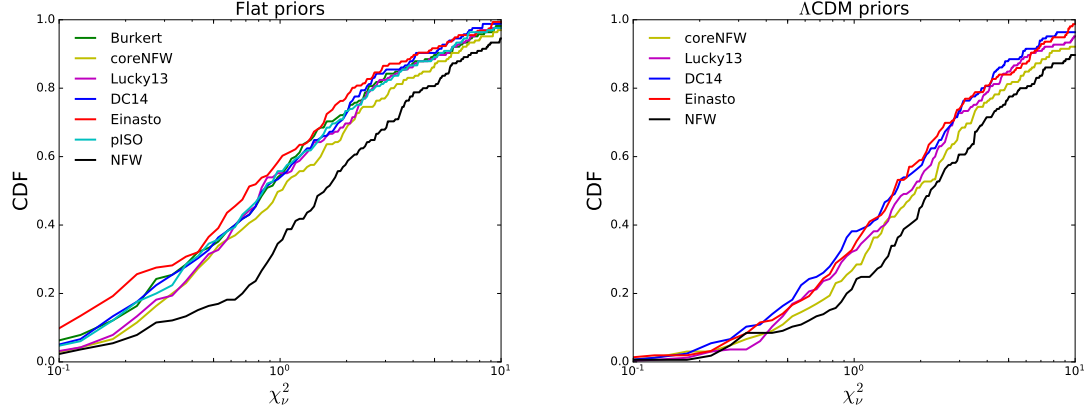


Figure 2.1 Cumulative distributions of the reduced χ_ν^2 for seven halo profiles with flat (left) and Λ CDM priors (right).

(the combination of the stellar-to-halo mass relation and halo mass-concentration relation, as well as equation 3.11 for the Einasto profile) or not. When imposing the Λ CDM priors, the fit quality decreases for all halo profiles, but the adherence to Λ CDM scaling relations drastically improve, as we now discuss.

We plot stellar versus halo masses in Figure 2.2. Stellar mass shows a positive correlation with halo mass for all the halo models. When imposing flat priors, the DC14 profile presents the closest match to the SHM relation, having the smallest standard deviation of 1.01 dex. The Lucky13 profile also shows a relation that matches the expected SHM relation well except for a few outliers, resulting in a standard deviation of 1.24 dex. On the other hand, the Einasto, NFW, and coreNFW profiles display much larger scatter, having standard deviations of 1.68 dex, 1.61 dex and 1.36 dex, respectively. Finally, the Burkert and pISO profiles show mean vertical shifts of 0.51 dex and -0.44 dex with respect to the expected SHM relation, giving systematically higher and lower stellar masses.

When we impose the Λ CDM priors, the expected SHM relation is well reproduced at low halo masses for all halo profiles. For massive galaxies, the DM halo masses are mostly smaller than the abundance-matching prediction. The extent to which this deviation is significant depends on halo models: the DC14 profile provides the best agreement, while the NFW, coreNFW, and Lucky13 profiles show larger discrepancies. The disagreement at high halo masses for the NFW profile has been pointed out by Posti et al. (2019a), who argued for a linear SHM relation for late-type galaxies. They imposed the mass-

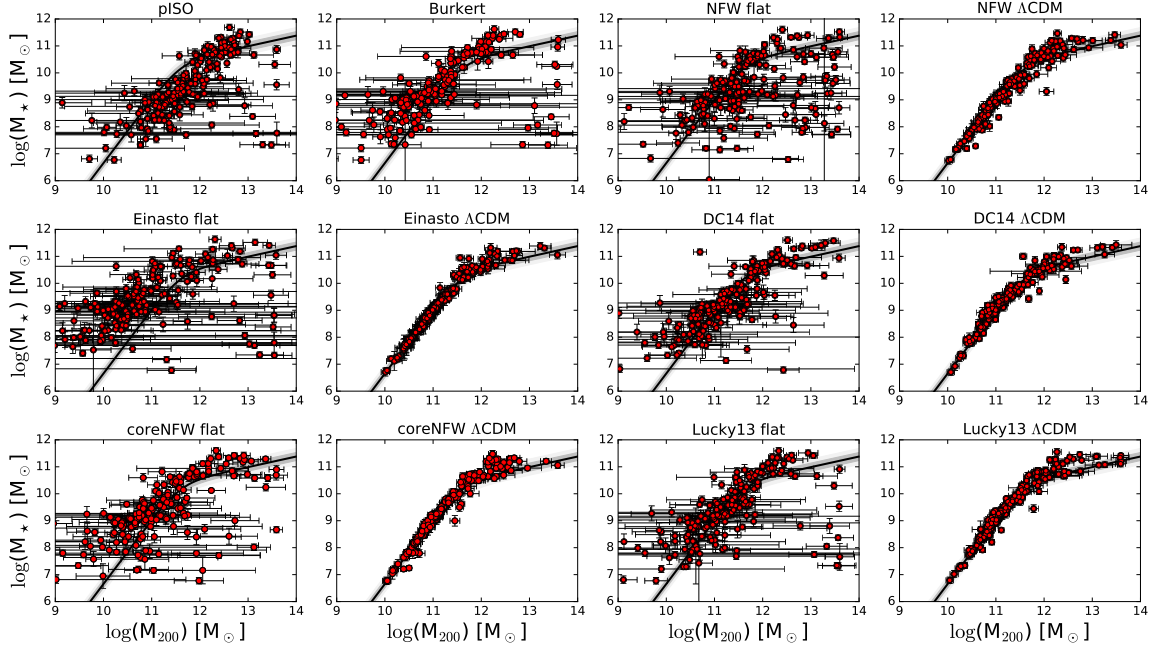


Figure 2.2 The relations between stellar masses and DM halo masses for the seven halo models. Solid lines show the expected stellar-halo mass relation (Moster et al. 2013), which is roughly recovered when the Λ CDM priors are imposed. Dark and light shadow regions correspond to 1σ and 2σ standard deviations, respectively.

concentration relation as a prior but did not impose the SHM relation. We here confirm that there exist some discrepancies at high halo masses for the NFW profile even when we impose the SHM relation as a prior (see also Katz et al. 2017).

We plot halo concentration against halo mass in Figure 2.3. When imposing flat priors, the pISO, Einasto, and Lucky13 profiles do not present clear trends between concentrations and halo masses, having Spearman’s correlation coefficients between -0.1 and -0.3 . The Burkert, NFW, DC14, and coreNFW profiles show marginal evidence for anti-correlations, having Spearman’s coefficients between -0.3 and -0.5 . Moreover, these putative anti-correlations seem steeper than expected from cosmology. The halo mass-concentration relation is not as well recovered as the SHM relation even if it is imposed as part of the Λ CDM priors. Remarkably, in such a case, the DC14 model is the only one to present a significant anti-correlation (Spearman’s coefficient of -0.5), but the relation appears systematically shifted towards higher concentrations. The other profiles (NFW, Einasto, coreNFW, and Lucky13) have Spearman’s coefficients between 0.0 and -0.2 indicative of no correla-

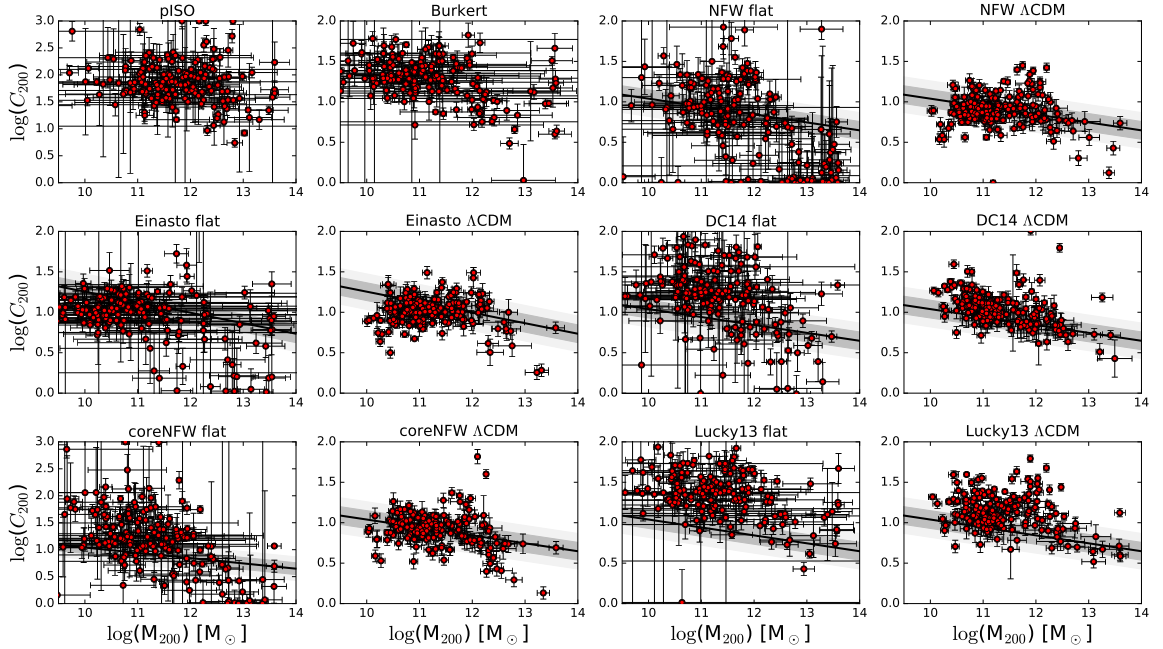


Figure 2.3 Concentrations of the SPARC galaxies against halo masses for the seven halo models. Solid lines are the expected relations from N -body simulations (Macciò et al. 2008), which are model dependent and not available for the pISO and Burkert profiles. Dark and light shadow regions represent 1σ and 2σ standard deviations, respectively. The concentrations for the DC14 profile have been converted to that for NFW in order to compare with the imposed relation.

tions, as evinced by the relatively flat distributions of concentrations versus halo masses.

In Figure 6.2, we show the fits for an example galaxy, IC2574, using all the models. We list the best-fit parameters in Table 1. In Figure 2.6, we show the fits of all SPARC galaxies using the Burkert profile. Similar figures and tables are available on the SPARC website for all 175 galaxies and all seven halo profiles.

2.5 Conclusion

In this paper, we provide the community with a homogeneous catalog of DM halo parameters for 175 galaxies from the SPARC database, considering seven different halo models. Homogeneity is an important guarantee for fair comparisons of models, as Korsaga et al. (2019b) find that different fitting procedures can lead to significantly different fitting results. The halo parameters are derived performing MCMC fits to H I/H α rotation curves.

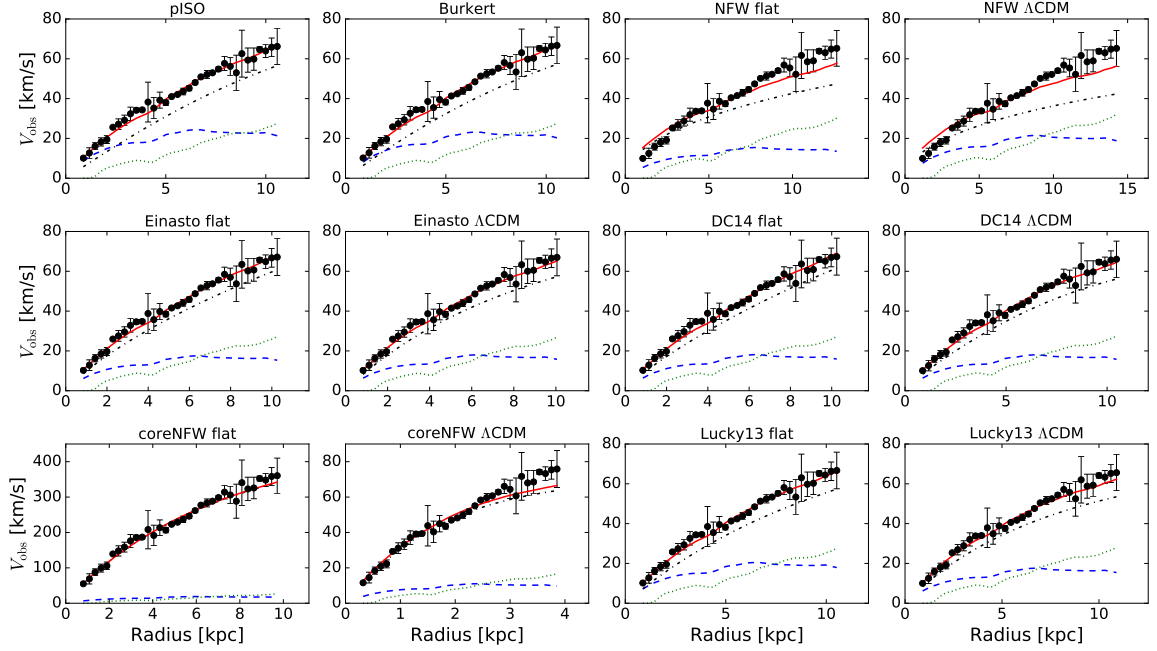


Figure 2.4 Example galaxy: The best-fit rotation curves of the dwarf galaxy IC2574 using seven models with/without Λ CDM priors. Blue, green, purple and black lines represent disk, gas, bulge (if present) and dark matter contributions, respectively. Solid red lines are the total rotation curves, and the shadow regions reflect 1σ (dark) and 2σ (light) confidence levels. The complete figure set (175 images) is available in the online journal.

We impose flat priors on the halo parameters, Gaussian priors on galaxy distance and disk inclination, and lognormal prior on stellar mass-to-light ratio. For five DM halo models, we also present rotation-curve fits imposing basic Λ CDM priors: the stellar mass-halo mass relation from abundance matching and the mass-concentration relation from cosmological simulations. In general, cored DM profiles provide better fits than the cuspy NFW. Moreover, while the stellar mass-halo mass relation is generally recovered by all halo models when imposed as a prior, the mass-concentration relation is not reproduced in detail by any halo model. All the fit results are publicly available on the SPARC database in the form of machine-readable tables and summary figures.

Table 2.1. The best-fit parameters for galaxy IC2574.

Model	Y_{disk} (M_{\odot}/L_{\odot})	Y_{bul} (M_{\odot}/L_{\odot})	Distance (Mpc)	Inclination (deg.)	V_{200} (km/s)	C_{200}	r_s (kpc)	$\log \rho_s$ [M_{\odot}/pc^3]	$\log(M_{200})$ [M_{\odot}]	α	χ^2_{ν}
pISO-Flat	0.77 ± 0.09	...	4.04 ± 0.20	80.0 ± 5.5	119.39 ± 57.47	14.76 ± 1.32	11.08 ± 5.43	-2.62 ± 0.90	11.73 ± 0.63	0.00 ± 0.00	2.51
Burkert-Flat	0.69 ± 0.09	...	4.03 ± 0.19	77.8 ± 5.6	85.83 ± 44.24	7.49 ± 0.57	15.69 ± 8.17	-2.52 ± 0.96	11.30 ± 0.67	0.00 ± 0.00	2.41
NFW-Flat	0.26 ± 0.05	...	4.83 ± 0.19	87.4 ± 2.1	105.03 ± 5.57	1.00 ± 0.01	143.87 ± 7.74	-4.29 ± 0.10	11.57 ± 0.07	0.00 ± 0.00	36.55
NFW-LCDM	0.44 ± 0.05	...	5.45 ± 0.16	88.4 ± 1.8	78.56 ± 2.99	1.00 ± 0.01	107.59 ± 4.36	-4.29 ± 0.07	11.19 ± 0.05	0.00 ± 0.00	36.30
Einasto-Flat	0.41 ± 0.10	...	3.92 ± 0.20	76.2 ± 6.4	275.92 ± 98.58	1.64 ± 0.81	230.07 ± 140.20	-4.49 ± 0.95	12.83 ± 0.47	0.33 ± 0.10	36.30
Einasto-LCDM	0.44 ± 0.09	...	3.84 ± 0.20	76.8 ± 5.9	63.18 ± 3.50	4.71 ± 0.25	18.39 ± 1.42	-3.33 ± 0.13	10.90 ± 0.07	0.76 ± 0.06	36.30
DC14-Flat	0.44 ± 0.10	...	3.92 ± 0.20	75.4 ± 6.4	123.50 ± 11.53	7.68 ± 0.79	22.03 ± 3.05	-2.83 ± 0.18	11.78 ± 0.12	0.00 ± 0.00	2.17
DC14-LCDM	0.42 ± 0.05	...	4.00 ± 0.19	80.8 ± 4.8	67.56 ± 3.12	9.53 ± 0.59	9.72 ± 0.75	-2.68 ± 0.10	10.99 ± 0.06	0.00 ± 0.00	2.43
coreNFW-Flat	0.50 ± 0.12	...	3.71 ± 0.20	10.4 ± 0.9	495.74 ± 49.16	11.69 ± 0.62	58.11 ± 6.54	-2.01 ± 0.20	13.59 ± 0.13	0.00 ± 0.00	3.08
coreNFW-LCDM	0.43 ± 0.09	...	1.47 ± 0.20	59.3 ± 8.8	54.70 ± 4.82	14.65 ± 0.80	5.12 ± 0.53	-1.77 ± 0.18	10.72 ± 0.11	0.00 ± 0.00	6.22
Lucky13-Flat	0.54 ± 0.11	...	4.02 ± 0.20	77.9 ± 5.7	105.99 ± 32.05	7.09 ± 0.73	20.49 ± 6.54	-2.37 ± 0.57	11.58 ± 0.39	0.00 ± 0.00	2.27
Lucky13-LCDM	0.39 ± 0.06	...	4.17 ± 0.19	83.7 ± 3.9	74.04 ± 3.07	7.99 ± 0.47	12.70 ± 0.92	-2.26 ± 0.11	11.11 ± 0.05	0.00 ± 0.00	2.70

Note. — Table 1 is published in its entirety in the machine-readable format. A portion is shown here for guidance regarding its form and content.

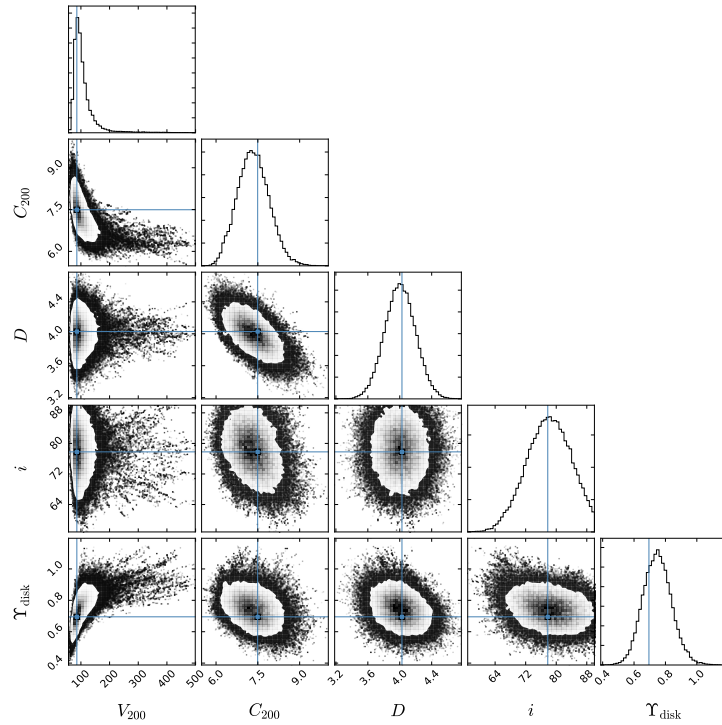


Figure 2.5 The posterior distributions of the fitting parameters for the example galaxy IC2574 using the Burkert profile. The complete figure set for 175 SPARC galaxies using all the models (175×12 images) is available in the SPARC website. Also available are the corresponding Monte Carlo samples in the format required by the open Python package GetDist.

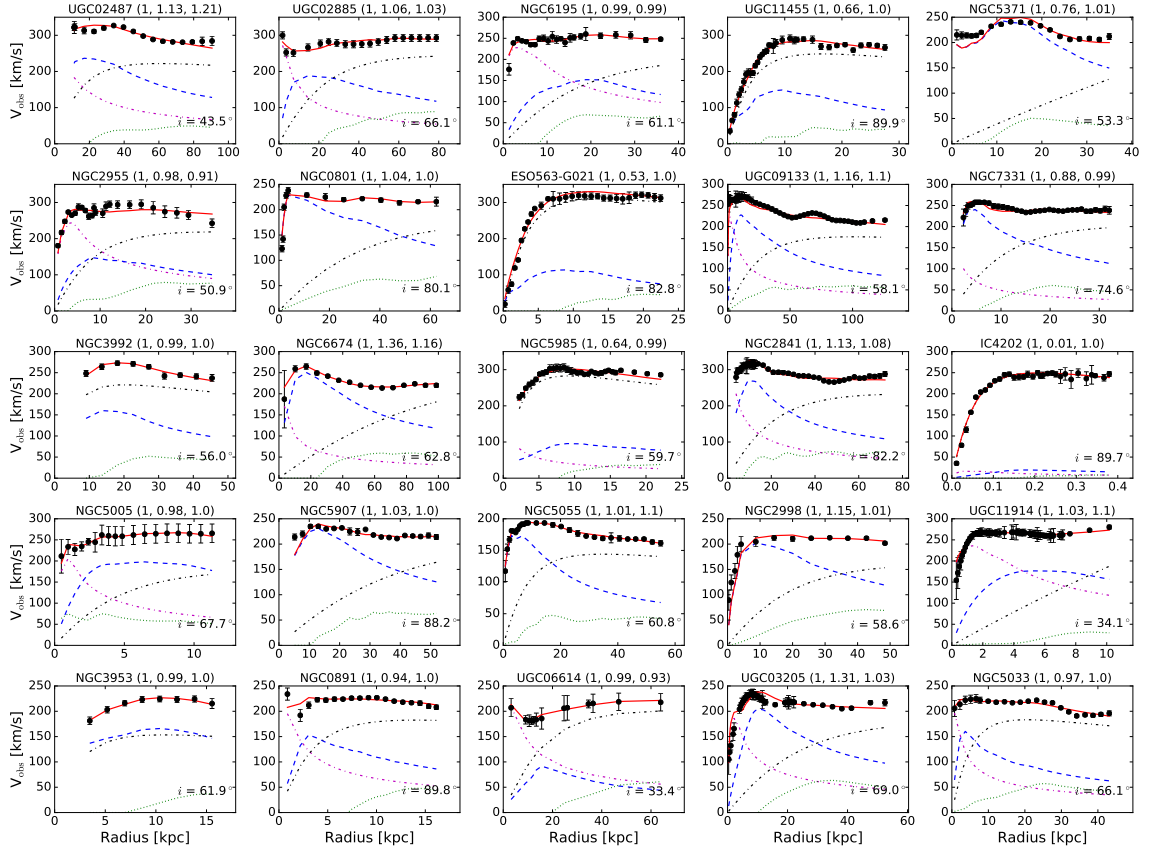


Figure 2.6 Example model: The best rotation-curve fits of 175 SPARC galaxies using the Burkert profile. Lines are the same as those in Figure 6.2. The three numbers in the parentheses of the subtitles are the quality flag Q (for details see Lelli et al. 2016a) and the ratios of the best-fit distances and inclinations to their original values, respectively. Best-fit inclination is shown within each panel. Galaxies are ordered by decreasing quality and luminosity. The complete figure set for all the halo models (7×12 images) is available in the online journal.

Chapter 3

A Constant Characteristic Volume Density of Dark Matter Haloes from SPARC Rotation Curve Fits

3.1 Abstract

We study the scaling relations between dark matter (DM) haloes and galaxy discs using 175 galaxies from the SPARC database. We explore two cosmologically motivated DM halo profiles: the Einasto profile from DM-only simulations and the DC14 profile from hydrodynamic simulations. We fit the observed rotation curves using a Markov Chain Monte Carlo method and break the disc-halo degeneracy using near-infrared photometry and Λ CDM-motivated priors. We find that the characteristic volume density ρ_s of DM haloes is nearly constant over ~ 5 decades in galaxy luminosity. The scale radius r_s and the characteristic surface density $\rho_s \cdot r_s$, instead, correlate with galaxy luminosity. These scaling relations provide an empirical benchmark to cosmological simulations of galaxy formation.

3.2 Introduction

In the cold dark matter (CDM) paradigm, the observed flat rotation curves of disc galaxies (Bosma 1978; Rubin et al. 1978) are attributed to DM haloes. The scaling relations between DM haloes and baryonic discs provide strong constraints to galaxy formation models and have been extensively explored (e.g. van Albada et al. 1985; Kent 1987; de Blok & McGaugh 1997). In particular, Kormendy & Freeman (2004, 2016) collected tens of rotation curve fits with nonsingular isothermal halo profiles and found that the halo central density ρ_0 and core radius r_c are correlated with galaxy luminosity, while their product $\rho_0 \cdot r_c$ is nearly a constant. The constancy of $\rho_0 \cdot r_c$ was also found by Spano et al. (2008) and Donato et al. (2009) using different cored DM halo profiles.

A well-known problem in fitting rotation curves is the disc-halo degeneracy (van Albada et al. 1985): the DM halo parameters are strongly degenerated with the assumed stellar mass-to-light ratio (Υ_\star). This can bias the resultant correlations if one does not properly delineate disc and halo contributions to the total rotation curves. In order to break the degeneracy, Kormendy & Freeman (2016) used the maximum disc method, which is a sensible assumption for high-mass, high-surface-brightness galaxies but could lead to unreasonably high Υ_\star for low-luminosity, low-surface-brightness galaxies (e.g. Starkman et al. 2018).

The cored DM profiles used in these works are empirically motivated: they often provide good fits to the observed rotation curves. DM-only simulations, however, suggest different profiles. Early N-body simulated haloes were found to be well fit by the NFW profile (Navarro et al. 1996a) which has an inner cusp. This profile, however, does a poor job in fitting the rotation curves of low-luminosity and low-surface-brightness galaxies (e.g. de Blok et al. 2001; de Blok & Bosma 2002; de Blok et al. 2008; Katz et al. 2017). Later simulations with higher resolution showed that the Einasto profile (Einasto 1965) can describe the simulated haloes better than NFW (Navarro et al. 2004; Merritt et al. 2005). This profile, however, has one more parameter and does not consider any baryonic process such as star formation and supernovae feedback which are believed to modify the initial DM distributions (Governato et al. 2010, 2012).

Di Cintio et al. (2014a) analysed zoom-in hydrodynamic simulations from the MUGS (Stinson et al. 2010), which consider gas cooling, star formation, and supernovae feed-

back. They found that the resulting DM density profile at $z=0$ (hereafter DC14 profile) systematically depends on the stellar-to-halo mass (SHM) ratio. Thus, simulations with and without baryonic process suggest different halo profiles. It is then of interest to explore the empirical scaling laws for these simulation-based DM profiles.

Katz et al. (2017) use 147 late-type galaxies from the SPARC database (Lelli et al. 2016a) to show that the DC14 profile gives better fits to rotation curves than the NFW profile (Navarro et al. 1996b). Here we consider the Einasto and DC14 profiles to study scaling laws between DM haloes and baryonic properties of galaxies. Since we consider two cosmologically motivated DM profiles, we can impose Λ CDM priors on halo parameters: the SHM correlation from multi-epoch abundance matching and the mass-concentration (c-M) relation from simulations. The SHM relation can help break the disc-halo degeneracy and the c-M relation breaks the degeneracy between halo parameters. We use homogeneous mass models for 175 galaxies with Spitzer photometry at $3.6 \mu\text{m}$, which further help to break the disc-halo degeneracy since Υ_\star is almost constant in the near infrared (e.g., McGaugh & Schombert 2014; Meidt et al. 2014).

In Section 2, we introduce the SPARC database, the two halo profiles, and the Bayesian analysis along with the corresponding priors. In Section 3, we show fits of DC14 and Einasto profiles and then present the correlations between DM haloes and galaxy discs. For comparison to Kormendy & Freeman (2016), we also apply the maximum disc method to the pseudo-isothermal profile. We discuss our results in Section 4.

3.3 Method

3.3.1 SPARC database

The SPARC database (Lelli et al. 2016a) includes 175 late-type galaxies spanning a wide range in surface brightness (4 dex) and luminosity (5 dex). Their luminosity profiles are well traced by Spitzer photometry at $3.6 \mu\text{m}$. According to stellar population synthesis models, Υ_\star varies little with star formation history of galaxies in near infrared bands (e.g., McGaugh & Schombert 2014; Meidt et al. 2014). As such, the stellar mass distributions are well determined by Spitzer photometry, providing a physically motivated way to break the disc-halo degeneracy. The wide range in galaxy luminosity, Spitzer photometry in the

near infrared band, accurate rotation curves, and relatively large sample make SPARC ideal to explore the properties of DM haloes and their relations to galactic discs.

3.3.2 Halo models

We explore two halo profiles, Einasto and DC14. The Einasto density profile (Navarro et al. 2004) is given by

$$\rho_{\text{EIN}}(r) = \rho_s \exp\left\{-\frac{2}{\alpha_\epsilon}\left[\left(\frac{r}{r_s}\right)^{\alpha_\epsilon} - 1\right]\right\}, \quad (3.1)$$

with r_s the scale radius, ρ_s the characteristic density and α_ϵ describing the rate at which the logarithmic slope decreases towards the center. Its enclosed mass profile (Mamon & Łokas 2005; Merritt et al. 2006) is given by

$$M(r) = 4\pi\rho_s \exp\left(\frac{2}{\alpha_\epsilon}\right)r_s^3\left(\frac{2}{\alpha_\epsilon}\right)^{-\frac{3}{\alpha_\epsilon}}\frac{1}{\alpha_\epsilon}\Gamma\left(\frac{3}{\alpha_\epsilon}, \frac{2}{\alpha_\epsilon}\left(\frac{r}{r_s}\right)^{\alpha_\epsilon}\right), \quad (3.2)$$

where $\Gamma(a, x) = \int_0^x t^{a-1} e^{-t} dt$ is the incomplete Gamma function.

The DC14 profile is in the form of the (α, β, γ) model (Hernquist 1990; Zhao 1996),

$$\rho(r) = \frac{\rho_s}{\left(\frac{r}{r_s}\right)^\gamma [1 + \left(\frac{r}{r_s}\right)^\alpha]^{(\beta-\gamma)/\alpha}}, \quad (3.3)$$

where β defines the outer slope, γ the inner slope, and α measures the width of the transition region. The values of these parameters depend on the SHM ratio:

$$\begin{aligned} \alpha &= 2.94 - \log[(10^{X+2.33})^{-1.08} + (10^{X+2.33})^{2.29}], \\ \beta &= 4.23 + 1.34X + 0.26X^2, \\ \gamma &= -0.06 + \log[(10^{X+2.56})^{-0.68} + 10^{X+2.56}], \end{aligned} \quad (3.4)$$

where $X = \log(M_\star/M_{\text{halo}})$ is the logarithmic SHM ratio, M_\star is the stellar mass, and M_{halo} is the total halo mass. For $X < -4.1$, the profile returns to the NFW form since there is not enough energy from supernovae to substantially modify the halo profile. For $X > -1.3$, feedback from active galactic nuclei is expected to be important and the DC14 profile may not be an effective description any more since it takes only stellar feedback into account.

Following Katz et al. (2017), we consider $X = -1.3$ as the highest possible value for SPARC galaxies. With the constraints of equation 3.4, the DC14 halo has only two free parameters. Its enclosed mass within radius r can be calculated by changing the variable from r to

$$\epsilon = \frac{(r/r_s)^\alpha}{1 + (r/r_s)^\alpha} \quad (3.5)$$

so that

$$M(r) = 4\pi r_s^3 \rho_s \frac{1}{\alpha} [B(a, b + 1, \epsilon) + B(a + 1, b, \epsilon)], \quad (3.6)$$

where $B(a, b, x) = \int_0^x t^{a-1} (1-t)^{b-1} dt$ is the incomplete Beta function, $a = (3 - \gamma)/\alpha$ and $b = (\beta - 3)/\alpha$.

We define the dimensionless radius $x = r/r_s$ and adopt the virial radius r_{200} inside of which the average density is 200 times the critical density of the universe ($\rho_{\text{crit}} = \frac{3H_0^2}{8\pi G}$). We also define M_{halo} as the total mass within their virial radius. The concentration C_{200} and the rotation velocity V_{200} at the virial radius are then given by

$$C_{200} = r_{200}/r_s, \quad V_{200} = 10 C_{200} r_s H_0, \quad (3.7)$$

where H_0 is the Hubble constant ($73 \text{ km s}^{-1} \text{ Mpc}^{-1}$ in this paper).

With these notations, the rotation velocity from DM haloes is given by

$$\frac{V_{\text{Ein}}}{V_{200}} = \sqrt{\frac{C_{200}}{x} \frac{\Gamma(\frac{3}{\alpha_\epsilon}, \frac{2}{\alpha_\epsilon} x^{\alpha_\epsilon})}{\Gamma(\frac{3}{\alpha_\epsilon}, \frac{2}{\alpha_\epsilon} C_{200}^{\alpha_\epsilon})}}, \quad (3.8)$$

$$\frac{V_{\text{DC14}}}{V_{200}} = \sqrt{\frac{C_{200}}{x} \frac{B(a, b + 1, \epsilon) + B(a + 1, b, \epsilon)}{B(a, b + 1, \epsilon_c) + B(a + 1, b, \epsilon_c)}}, \quad (3.9)$$

where $\epsilon_c = \frac{C_{200}^\alpha}{1 + C_{200}^\alpha}$. The total rotational velocity is given by

$$V_{\text{tot}}^2 = V_{\text{DM}}^2 + \Upsilon_{\text{disc}} V_{\text{disc}}^2 + \Upsilon_{\text{bul}} V_{\text{bul}}^2 + V_{\text{gas}}^2, \quad (3.10)$$

where V_{disc} , V_{bul} and V_{gas} are the contributions of disc, bulge and gas, respectively, as tabulated in the SPARC database (Lelli et al. 2016a). Υ_{disc} and Υ_{bul} are the stellar mass-to-light ratios of disc and bulge with fiducial values of 0.5 and 0.7, respectively.

As described in Li et al. (2018), galaxy distance (D) and disc inclination (i) affect the stellar components and the total observed rotational velocities (V_{obs}), respectively. They transform as

$$V'_k = V_k \sqrt{\frac{D'}{D}}, \quad V'_{\text{obs}} = V_{\text{obs}} \frac{\sin(i)}{\sin(i')}, \quad (3.11)$$

where k denotes disc, bulge or gas, respectively. We allow D and i to vary by imposing Gaussian priors with standard deviations given by the observational errors. Thus, the free parameters in our fits are totally fixed by Υ_\star , D , i , V_{200} , C_{200} and additionally α_ϵ for the Einasto model.

3.3.3 Bayesian analysis

For both Einasto and DC14 models, we map the posterior distributions of halo parameters, as well as the three galactic parameters (Υ_\star , D , i) using the open source Python package *emcee* (Foreman-Mackey et al. 2013). In Bayesian analysis, posterior distributions are determined by priors and likelihood functions. The latter is chosen as $\exp(-\frac{1}{2}\chi^2)$ in which χ^2 is defined in terms of rotational velocities,

$$\chi^2 = \sum_R \frac{[V_{\text{obs}}(R) - V_{\text{tot}}(R)]^2}{(\delta V_{\text{obs}})^2}, \quad (3.12)$$

where δV_{obs} is the uncertainty on rotational velocities. We impose the same priors on galactic parameter as in Li et al. (2018): Gaussian priors on D and i around their tabulated values in the SPARC database with standard deviations given by the observational errors; lognormal prior on Υ_\star around their fiducial values $\Upsilon_{\text{disc}} = 0.5$ and $\Upsilon_{\text{bul}} = 0.7$ with a standard deviation of 0.1 dex suggested by stellar population synthesis models (McGaugh et al. 2016b; Lelli et al. 2017b).

We set loose boundaries on halo parameters: $10 < V_{200} < 500$ km/s, $0 < C_{200} < 100$ for Einasto and DC14 models, and $0 < \alpha_\epsilon < 2$ for Einasto. We obtain one set of fits with flat priors on halo parameters and another one with Λ CDM priors, comprising the SHM and mass-concentration relations.

The SHM relation (Moster et al. 2013) presents a lognormal distribution around the

mean relation,

$$\frac{M_{\star}}{M_{\text{halo}}} = 2N \left[\left(\frac{M_{\text{halo}}}{M_1} \right)^{-\beta} + \left(\frac{M_{\text{halo}}}{M_1} \right)^{\gamma} \right]^{-1}, \quad (3.13)$$

with a scatter of $\sigma(\log M_{\star}) = 0.15$ dex. The parameters in the equation are fixed by multi-epoch abundance matching: $\log(M_1) = 11.59$, $N = 0.0351$, $\beta = 1.376$ and $\gamma = 0.608$.

Halo concentrations and halo masses are found to follow a power law (Macciò et al. 2008),

$$\log(C_{200}) = a - b \log(M_{\text{halo}}/[10^{12}h^{-1}M_{\odot}]), \quad (3.14)$$

with an intrinsic scatter of 0.11 dex. The parameter a and b depend on cosmology and adopted DM profiles. Macciò et al. (2008) gives specific relations in different cosmologies. We adopt the values corresponding to the *WMAP5* cosmology (equation 10 in Macciò et al. 2008), which gives $a = 0.830$ and $b = -0.098$ for DC14. For the Einasto model, the only available results are for the *Planck* cosmology (Dutton & Macciò 2014): $a = 0.977$ and $b = -0.130$. In the SPARC database, the distances of some galaxies are estimated with flow models assuming $H_0 = 73 \text{ km s}^{-1} \text{ Mpc}^{-1}$. This is consistent with the local distance scale (Tully et al. 2016; Riess et al. 2016) but is not entirely consistent with either cosmology. Flow distances have large errors, so this small inconsistency plays a very minor role and only affect the final values of the best-fit distances.

For the extra parameter α_{ϵ} in the Einasto model, Dutton & Macciò (2014) shows that its value depends on halo mass,

$$\alpha = 0.0095v^2 + 0.155, \quad (3.15)$$

where $\log v = -0.11 + 0.146m + 0.0138m^2 + 0.00123m^3$ and $m = \log(M_{\text{halo}}/10^{12}h^{-1}M_{\odot})$. The measured standard deviation in their simulation is 0.16 dex around the above relation. This constraint is important. Left free, α can mimic a constant density core. This can provide good fits to rotation curves, but is not consistent with Λ CDM (Chemin et al. 2011).

The above relations compose the Λ CDM priors. We then use the standard affine-invariant ensemble sampler in *emcee* to map the posterior distributions based on the above likelihood function for both flat and Λ CDM priors.

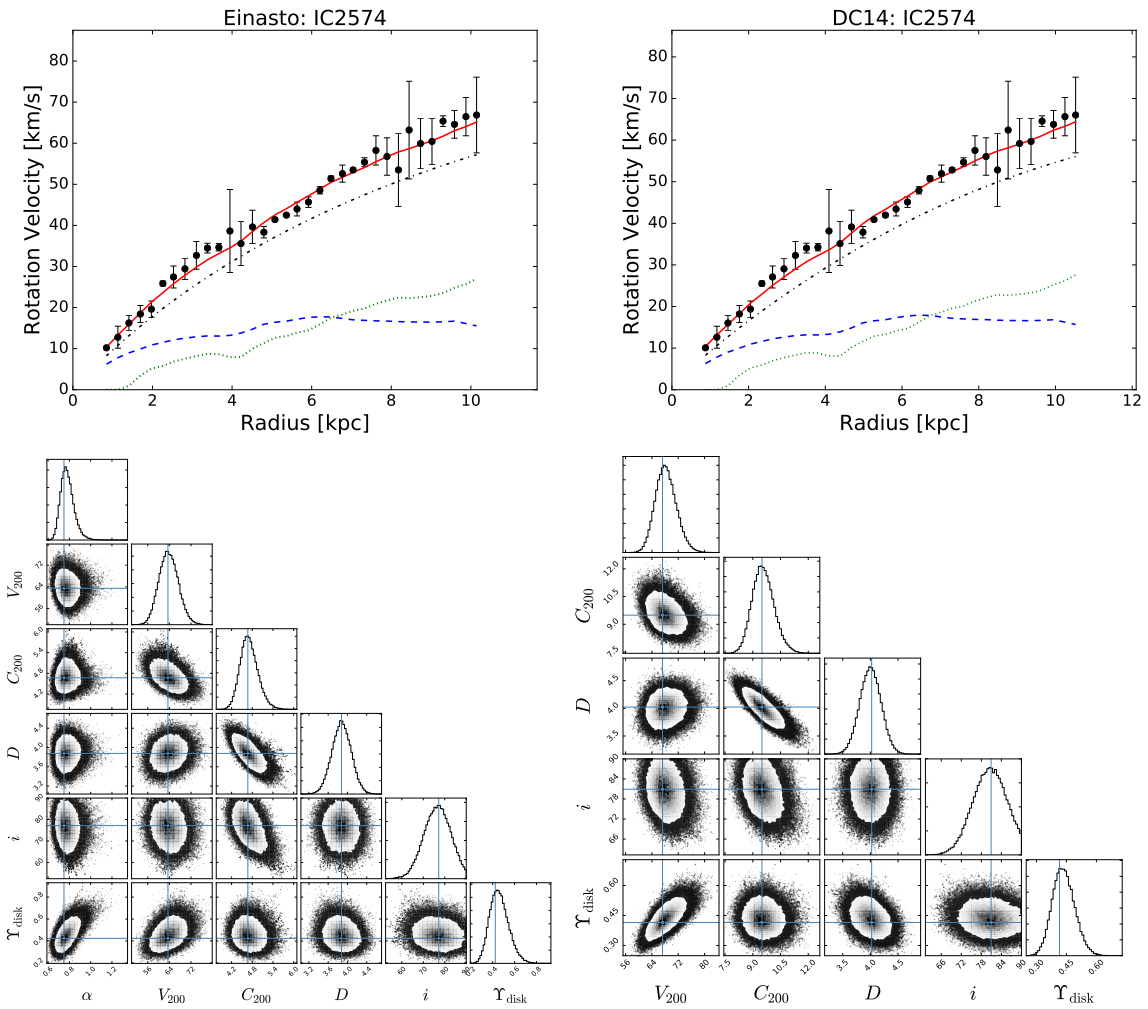


Figure 3.1 Rotation curve fits and posterior distributions of fitting parameters for the dwarf galaxy IC2574 using Einasto (left) and DC14 (right) profiles. Green, blue and black lines show the contributions of gas, disc and dark matter, respectively. Red lines represent the total fitted rotation curves. The complete figure set of 175 images is available at the SPARC website.

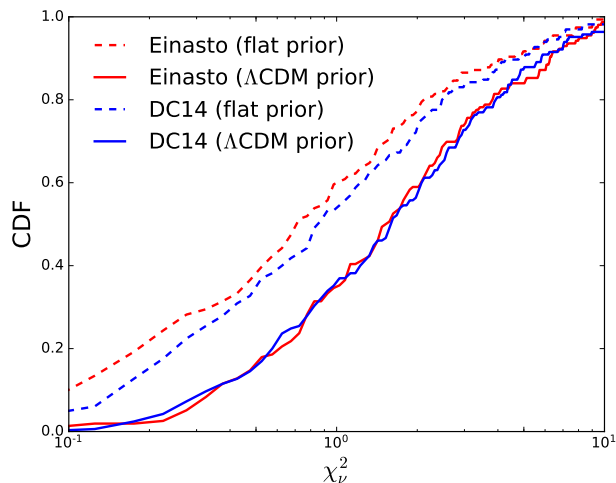


Figure 3.2 The cumulative distributions of χ_ν^2 for Einasto (red lines) and DC14 (blue lines) models imposing flat priors (solid lines) and Λ CDM priors (dashed lines).

3.4 Results

3.4.1 Individual fits

In Figure 3.1, we show an example fit for a gas-dominated dwarf galaxy (IC 2574). The best-fit parameters of these two profiles are close, except that Einasto prefers a smaller concentration than does DC14. This is a general trend for SPARC galaxies, which is due to the large values of α_ϵ as shown in Figure 3.11. For IC2574, $\alpha_\epsilon = 0.76$. This is larger than the expectation of the imposed Λ CDM prior. This is a manifestation of the cusp-core problem: the fits frequently prefer α_ϵ that are more consistent with a cored DM halo profile.

3.4.2 Fit goodness

To check the fit quality of Einasto and DC14 models, we inspect the cumulative distribution functions (CDF) of their χ_ν^2 for both flat and Λ CDM priors (Figure 3.2). Flat priors give better fits than Λ CDM priors due to the weaker constraints on the free parameters. The resulting best-fit values, however, do not necessarily agree with the expectations from Λ CDM cosmological simulations. For example, for flat priors, although the Einasto profile gives better fits to SPARC galaxies than DC14, its shape parameter α_ϵ is systematically higher than expected (see Figure 3.11). In general, we explore flat priors just to check the

maximum ability of a model to fit real galaxies.

When the Λ CDM priors are imposed, Einasto and DC14 models show comparable fit quality, but Einasto is making use of an additional parameter. In the appendix, we show the distributions of galactic parameters and check how well the Λ CDM priors are recovered. We also check that the SHM ratios for both models are in the range of [-3.5, -0.5] for SPARC galaxies, thereby allowing sufficient stellar feedback. The resultant χ^2_ν do not correlate with SHM ratios, indicating neither model introduces any systematics. Since both profiles can describe the data comparably well, we proceed to explore possible disc-halo correlations.

3.4.3 Correlations between halo and disc properties

In Figure 3.3, we plot r_s (top panels), ρ_s (middle panels) and $\rho_s \cdot r_s$ (bottom panels) against the observed luminosity at [3.6] when imposing Λ CDM priors. In the top panels, we also show the relation with the disc scale length R_d , which is obtained by fitting an exponential profile to the outer parts of the [3.6] luminosity profile (see Lelli et al. 2016 for details). Both galaxy luminosity and disc scale length from the SPARC database are converted to the new best-fit distances. The uncertainty in R_d is dominated by the error in distance. The uncertainty in $L_{[3.6]}$ is the quadratic sum of errors on distances and flux as tabulated in SPARC. We calculate errors on r_s and $\rho_s \cdot r_s$ by error propagation based on the uncertainties in the fitting parameters.

In the top panels, both r_s and R_d show an apparent correlation with galaxy luminosity. To quantify the strength of these correlations, we calculate their Pearson r coefficient and find, $r(r_s) = 0.65$, $r(R_d) = 0.81$ for Einasto and $r(r_s) = r(R_d) = 0.77$ for DC14, indicating strong correlations. We fit the data to a linear relation in log-space:

$$\log r_s = (0.18 \pm 0.02) \log L_{[3.6]} - (0.67 \pm 0.15), \quad \log R_d = (0.26 \pm 0.01) \log L_{[3.6]} - (2.24 \pm 0.14) \quad (3.16)$$

for Einasto and

$$\log r_s = (0.27 \pm 0.02) \log L_{[3.6]} - (1.6 \pm 0.17), \quad \log R_d = (0.25 \pm 0.02) \log L_{[3.6]} - (2.05 \pm 0.15) \quad (3.17)$$

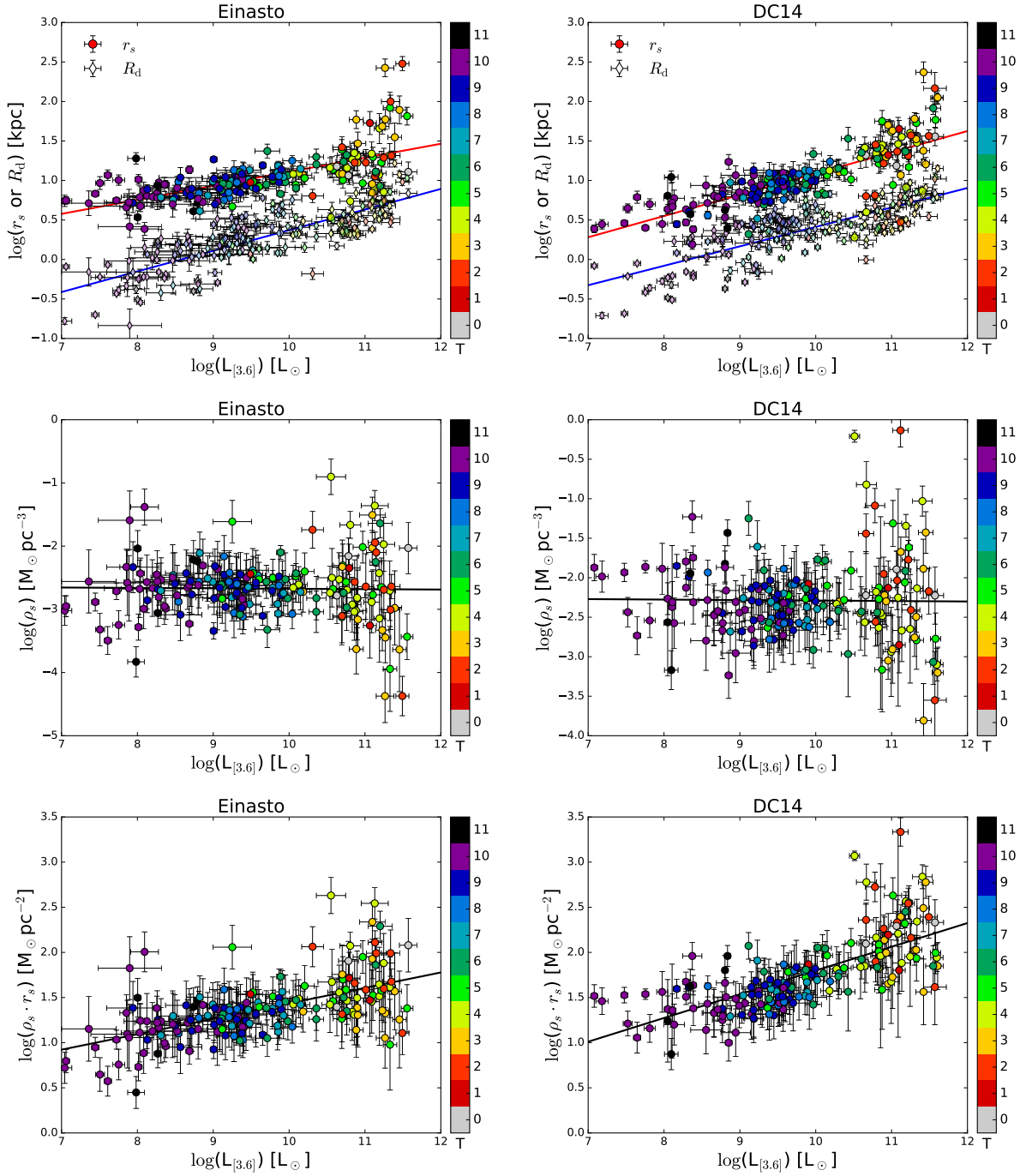


Figure 3.3 Scaling relations between halo properties and galaxy [3.6] luminosity for Einasto (left) and DC14 (right) profiles when imposing Λ CDM priors. Top: halo scale radius and disc scale length. Middle: halo characteristic volume density ρ_s . Bottom: halo characteristic surface density $\rho_s \cdot r_s$. Galaxies are colour-coded by Hubble type with numbers from 0 to 11 corresponding to S0, Sa, Sab, Sb, Sbc, Sc, Scd, Sd, Sdm, Sm, Im, BCD, respectively. In all panels, solid lines show linear fits.

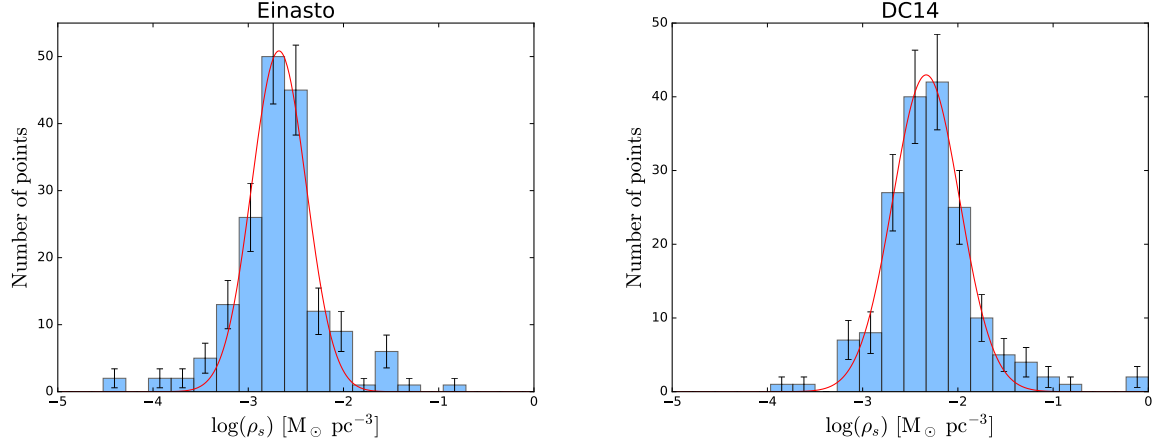


Figure 3.4 Histograms of the best-fit values of ρ_s for Einasto and DC14 profiles. Red lines are fitted Gaussian functions.

Table 3.1 The slopes of the fitted linear relations for R_d , r_s and $\rho_s \cdot r_s$ against galaxy luminosity $L_{[3.6]}$ in log space.

Model	R_d	r_s	$\rho_s \cdot r_s$
Einasto	0.26 ± 0.01	0.18 ± 0.02	0.17 ± 0.02
DC14	0.25 ± 0.02	0.27 ± 0.02	0.26 ± 0.02

for DC14 as shown in Table 3.2 and 3.3. Although Einasto and DC14 show different power laws in halo scale radius, they almost share the same correlation between R_d and $L_{[3.6]}$. Lelli et al. (2016a) show the correlation between the original values of R_d and $L_{[3.6]}$ (their Figure 2). We check the power index is about 0.25, consistent with our results.

The bottom panels of Figure 3.3 shows that $\rho_s \cdot r_s$ correlates with galaxy luminosity: their Pearson r values for Einasto and DC14 are 0.59 and 0.70, respectively. The fitted power laws are

$$\log \rho_s \cdot r_s = (0.17 \pm 0.02) \log L_{[3.6]} - (0.28 \pm 0.17) \quad (3.18)$$

for Einasto and

$$\log \rho_s \cdot r_s = (0.26 \pm 0.02) \log L_{[3.6]} - (0.83 \pm 0.20) \quad (3.19)$$

for DC14. These strong correlations are in contrast with what Kormendy & Freeman (2016) found: a roughly constant central surface density, $\rho_0 \cdot r_c \propto L_B^{0.058 \pm 0.067}$. We note, however, that the product $\rho_s \cdot r_s$ has a different meaning from $\rho_0 \cdot r_c$ in Kormendy & Freeman (2016) as

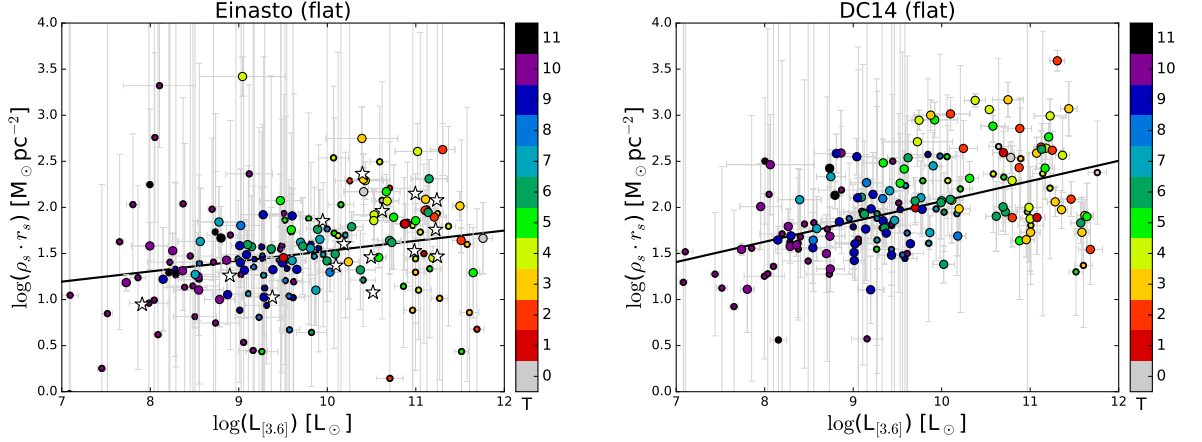


Figure 3.5 The product $\rho_0 \cdot r_s$ vs. galaxy luminosity for both profiles when imposing flat priors. Galaxies are colour-coded by Hubble type. Solid lines are the best-fit linear relations. Large and small points represent galaxies with uncertainties on r_s smaller and larger than 20%, respectively. White stars on the left panel are the fit results from Chemin et al. (2011) using the same halo profile.

they use a different halo model. The constant central density of their non-singular isothermal halo contrasts with the variable inner density profile of the Einasto and DC14 halo models. This issue is further discussed in the next Section.

Remarkably, r_s and $\rho_s \cdot r_s$ correlate with galaxy luminosity with the same power law for both halo profiles. This suggests that the characteristic volume density ρ_s is almost constant. This is evident from the middle panels of Figure 3.3. The Pearson r products indeed are negligible (~ -0.01) for both profiles. The best-fit relations are almost flat with $\log(\rho_s) = -2.7 \pm 0.3 [M_\odot \text{pc}^{-3}]$ for Einasto and $\log(\rho_s) = -2.3 \pm 0.1 [M_\odot \text{pc}^{-3}]$ for DC14. Since our fits recover a tight stellar-to-halo mass relation (see Figure 3.10), it is clear that ρ_s does not correlate with halo mass either.

We colour-code galaxies by Hubble type in all panels of Figure 3.3. The well-known correlation of galaxy type with luminosity is obvious. We see no evidence for a dependence of halo parameters on morphological type beyond the variation with luminosity (cf. Korsaga et al. 2019a, 2018).

Figure 3.4 shows the histograms of the volume density parameter ρ_s for both profiles. Despite the limited statistics, they roughly show Gaussian shapes. We fit their distributions to Gaussian functions (red lines). The fitted Gaussian profiles have mean values of -2.7 and

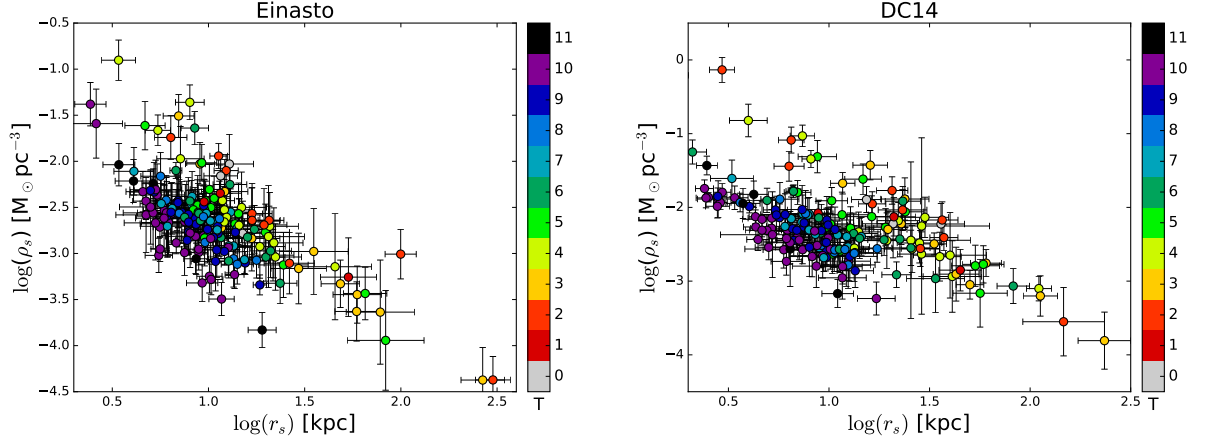


Figure 3.6 Characteristic volume density ρ_s is plotted against scale radius r_s in log space for the Einasto (left) and DC14 (right) profiles when imposing Λ CDM priors. Galaxies are color-coded by Hubble type.

-2.3 for Einasto and DC14, respectively, consistent with the fitted linear relations. Their corresponding standard deviations are $\sigma(\text{Einasto}) = 0.29 \pm 0.02$ dex and $\sigma(\text{DC14}) = 0.35 \pm 0.01$ dex. These are smaller than the rms scatter (0.48 dex for Einasto and 0.50 dex for DC14) due to outliers.

In Figure 3.5, we plot $\rho_s \cdot r_s$ against galaxy luminosity when imposing a flat rather than Gaussian prior. The fitted solid lines for both profiles still show correlations with galaxy luminosity, but with significantly larger scatter. The degeneracy between ρ_s and r_s increases the uncertainties on $\rho_s \cdot r_s$ dramatically for both models. Thus, before we can make claims about the constancy (or lack thereof) of the product $\rho_s \cdot r_s$, the degeneracy must be broken.

A detailed study of the Einasto profile was performed by Chemin et al. (2011) fitting 17 rotation curves from the THINGS survey (Walter et al. 2008; de Blok et al. 2008). When using a Kroupa IMF (Kroupa 2001), their values of Υ_* are around 0.5, which is consistent with our stellar population synthesis prior. In the left panel of Figure 3.5, we overplot their results (from their Table 2) as white stars. The SPARC sample is about one order of magnitude larger than that in Chemin et al. (2011), so our scaling relations are better defined.

The relation between the halo parameters ρ_s and r_s themselves are shown in Figure 3.6. Similar relations were explored before using smaller galaxy samples (e.g., Chemin et al. 2011; Kormendy & Freeman 2016). Figure 3.6 shows that late-type and early-type disc

galaxies cover distinct regions in the $r_s - \rho_s$ plane: late-type galaxies (Sd to Im) tend to have lower halo densities at a given r_s than early-type spirals (S0 to Sc). Late-type galaxies have, on average, lower surface brightness than early-type galaxies (e.g. Lelli et al. 2016a), so Figure 3.6 suggests that low-surface-brightness galaxies may inhabit lower density haloes than high-surface-brightness galaxies (de Blok & McGaugh 1996; McGaugh & de Blok 1998b). The data are consistent with a trend of increasing r_s with decreasing ρ_s , but we refrain from fitting power-laws because the trend is driven by a few extreme objects, and may depend systematically on morphological type. For the Einasto profile, we also investigated the relations between α_ϵ and the other halo parameters, finding no significant correlation with either ρ_s or r_s .

3.5 Comparison with previous work

The correlation between $\rho_s \cdot r_s$ and galaxy luminosity seems to contradict the constant $\rho_0 \cdot r_c$ found in previous studies (Spano et al. 2008; Donato et al. 2009; Kormendy & Freeman 2016). However, these two quantities are not exactly the same, since ρ_0 is the central volume density of cored DM halo profiles, while ρ_s is the characteristic volume density of the Einasto or DC14 profiles. Moreover, we use different analysis methods.

To break the disc-halo degeneracy, Spano et al. (2008) assume constant Υ_\star at R band, but stellar population synthesis models predict strong variation of Υ_\star in optical bands (e.g. McGaugh & Schombert 2014). Donato et al. (2009) delineated stellar contributions using a mixture of methods such as fitting the universal rotation curve (Persic et al. 1996) and adopting spectro-photometric galaxy models. Thus, the contributions of each component strongly depend on the efficacy of the modelling. Kormendy & Freeman (2016) adopt the maximum disc method, which may be unphysical for low-mass and low surface-brightness galaxies (e.g. Starkman et al. 2018). Moreover, all these studies assume flat priors on the halo parameters. As we showed in the previous Section, flat priors can significantly blur the $\rho_s \cdot r_s$ correlation with galaxy luminosity. In the following, we show that the method to break the disc-halo degeneracy also makes a big difference.

To understand the origin of these different results, we employ the maximum disc method

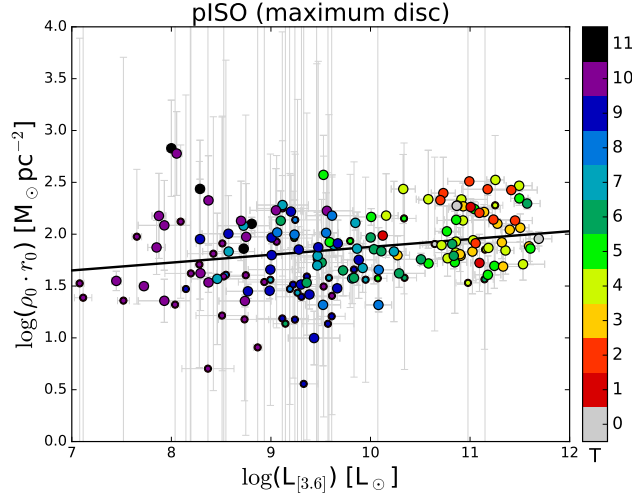


Figure 3.7 Same as Figure 3.5 but for pISO profile with the maximum disc method.

and fit the pseudo-isothermal (pISO) profile,

$$\rho(r) = \rho_0 [1 + (r/r_0)^2]^{-1} \quad (3.20)$$

where $\rho_0 \cdot r_0$ has the meaning of central surface density. To implement the maximum disc method, we adopt the maximum disc values of Υ_* from Starkman et al. (2018). For consistency, we fix galaxy distances and disc inclinations to the original values from the SPARC database. Therefore, the only fitting parameters are those on DM haloes. For better comparison with Kormendy & Freeman (2016), we impose flat priors on halo parameters.

The resultant $\rho_0 \cdot r_0$ against galaxy luminosity is shown in Figure 3.7. The correlation between $\rho_0 \cdot r_0$ and galaxy luminosity is pretty weak: its Pearson r value is 0.16. The fitted line has a slope of 0.075 ± 0.035 , consistent with that of Kormendy & Freeman (2016). Thus, we obtain the same result when we make comparable assumptions about the disc and halo.

The maximum disc method gives a different result from our population synthesis result. According to the correlations shown in the previous section, more luminous galaxies tend to have larger r_s and $\rho_s \cdot r_s$ while leaving ρ_s almost constant. However, the maximum disc method makes stellar discs to contribute as much as they can, which compensates the contribution from DM haloes. It hence leads to a constant central surface density ($\rho_0 \cdot r_0$)

of dark matter. Our result differs because of the different prior on Υ_{disc} , not because of any conflict in the data. The maximum disc method pushes the Υ_{disc} for low-mass galaxies to unreasonably high values, so this prior seems less physical than the population synthesis prior.

3.6 Conclusions

In this paper, we fit SPARC galaxy rotation curves with two simulation-motivated profiles (Einasto and DC14) and show that the properties of DM haloes and stellar discs are strongly correlated. However, the characteristic volume density ρ_s is constant over 5 dex in luminosity for both profiles. Although different galaxies show quite different rotation curves, they consistently require constant ρ_s .

The constant volume density provides new insights into galaxy formation. It indicates that halo volume density is unrelated to galaxy luminosity. In the Λ CDM context, more luminous galaxies must be hosted in bigger haloes, but the halo size and mass must progressively increase in order to keep the characteristic volume density constant. It would be interesting to see whether this phenomenology is reproduced in cosmological simulations of galaxy formation. Presumably, the characteristic volume density of DM haloes depend on the implementation of baryonic physics (star formation, stellar feedback, etc.), so our scaling relations provide crucial benchmarks for theories of galaxy formation.

3.7 Appendix: Checking the distributions of galactic parameters and Λ CDM priors

3.7.1 Distributions of galactic parameters

We plot the distributions of optimized galactic parameters for Einasto and DC14 models in Figure 3.8 and 3.9, respectively. The distributions of Υ_{\star} are shown in the top panels for both models. Red dashed lines indicate their fiducial values ($\Upsilon_{\text{disc}} = 0.5$ and $\Upsilon_{\text{bul}} = 0.7$ according to McGaugh et al. 2016b). We check that the median values of the optimized Υ_{disc} for Einasto and DC14 are close to the fiducial value: 0.49 for Einasto and 0.52 for

Einasto

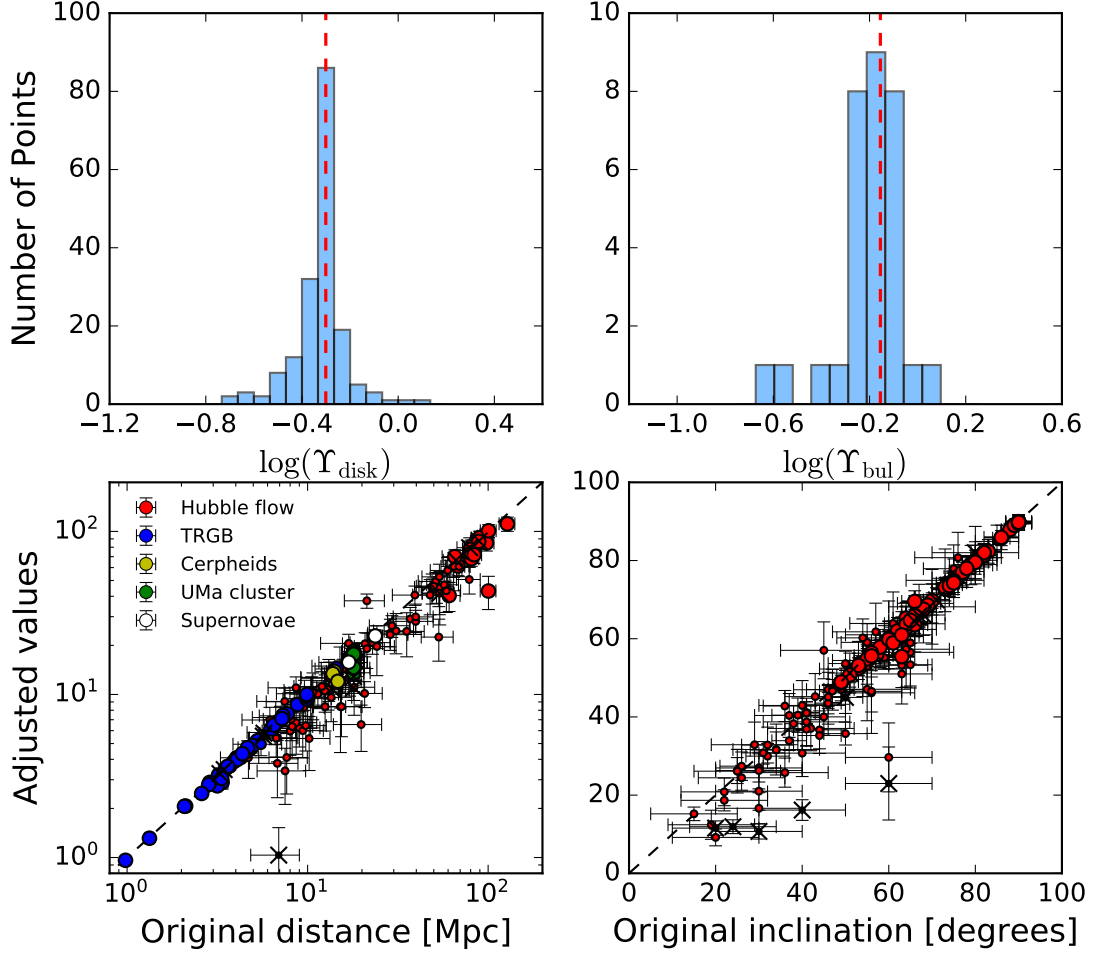


Figure 3.8 Distributions of optimized galactic parameters for Einasto model. Top panels show the histograms of stellar mass-to-light ratio for discs (top-left) and bulges (top-right). Red dashed lines indicate their fiducial values according to Lelli et al. (2016a). In the bottom panels, we plot the optimized galaxy distances and disc inclinations against their original values. Different methods of measuring galaxy distances are represented by different colors. Large and small points represent galaxies with observational errors larger and smaller than 15% for distances and 5% for inclinations, respectively. Galaxies with low-quality flag ($Q=3$, see Lelli et al. 2016a) are marked as black crosses. Black dashed lines are line of unity.

DC14

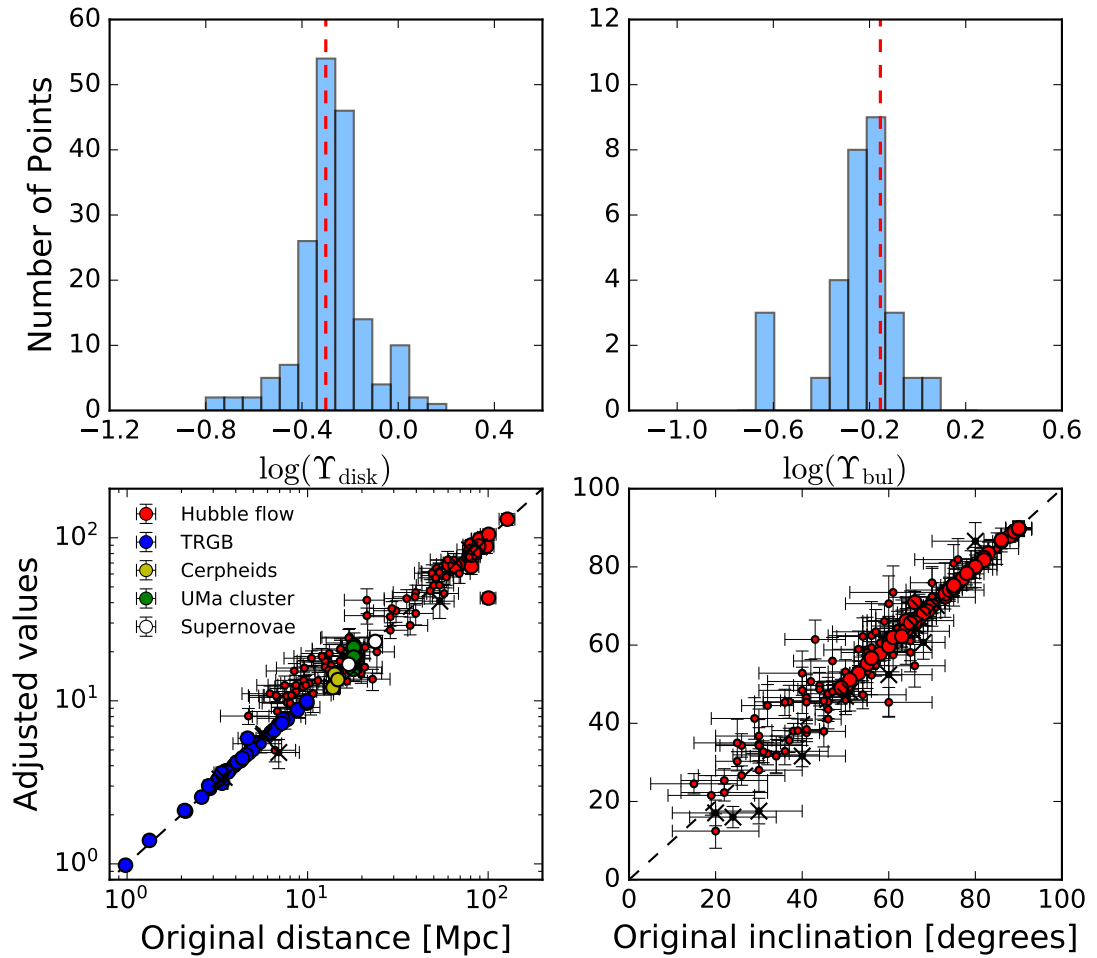


Figure 3.9 Same as Figure 3.8 but for DC14 model.

DC14. Einasto clearly shows a tighter distribution than DC14. There are 32 galaxies in the SPARC database hosting a bulge and the distributions of their optimized Υ_{bul} are shown in top-right panels. Their median values for both models are slightly smaller than the fiducial value: 0.63 for Einasto and 0.58 for DC14.

In the bottom panels, adjusted distances and inclinations are plotted against their original values as tabulated in the SPARC database. Errors on the adjusted values are calculated by the output of ‘std’ in the open software ‘GetDist’. Distances of SPARC galaxies are measured with five different methods: the Hubble flow corrected for Virgo-centric infall, the tip of the red giant branch (TRGB) method, the magnitude-period relation of Cepheids,

membership to the Ursa Major cluster of galaxies (UMa cluster), and supernovae (SN) light curves. Hubble flow is the least accurate method, hence the corresponding distances present large scatter for both models, while the distances from other methods mostly stay on the line of unity. There are systematic discrepancies in the distributions of distances and inclinations for both models: Einasto prefers smaller distances and inclinations, while DC14 prefer larger values.

Interestingly, Einasto and DC14 show opposite systematics. Smaller D corresponds to a smaller contribution of baryonic matter, while smaller inclinations lead to an increase in the amplitude of rotation velocities. This suggests that Einasto haloes provide a systematically larger contribution to the total rotation velocities than DC14 haloes.

3.7.2 Priors of halo parameters

To check whether the Λ CDM priors we impose are recovered, we plot the SHM and mass-concentration relations for both models in Figure 3.10. Both models show tight SHM relations. Most galaxies are well within the 2σ region of the fiducial abundance-matching scatter. The Einasto model gives a slightly tighter SHM relation than does DC14. However, the resultant mass-concentration relations show large discrepancies for both models. There are 26.3% and 30.3% of the total galaxies outside 2σ regions for Einasto and DC14 profiles, respectively. The fractions are larger than the expectation of the 2σ confidence region (5%). Again, Einasto and DC14 show opposite systematics: smaller and larger concentrations are preferred for Einasto and DC14 models, respectively. Recalling that the Einasto profile requires smaller contributions from baryonic distributions and larger observational rotational velocities compared to the DC14 profile, it seems contradictory that it still prefers smaller concentrations than DC14.

This effect is due to the exponential decrease of halo density in Einasto model at large radii. If the shape parameter $\alpha_\epsilon > 0.2$, the density decrease of Einasto halo is faster than an NFW profile (see Figure 2 in Dutton & Macciò 2014). For the same total halo mass (M_{halo}), Einasto model with $\alpha_\epsilon > 0.2$ places more mass closer to the center. Although this may make outer DM distribution insufficient to support a flat rotation curve, it would not contradict the data since rotation curves are not available at large radii. Therefore, when fitting rotation curves, MCMC enlarges the total rotation velocities by decreasing

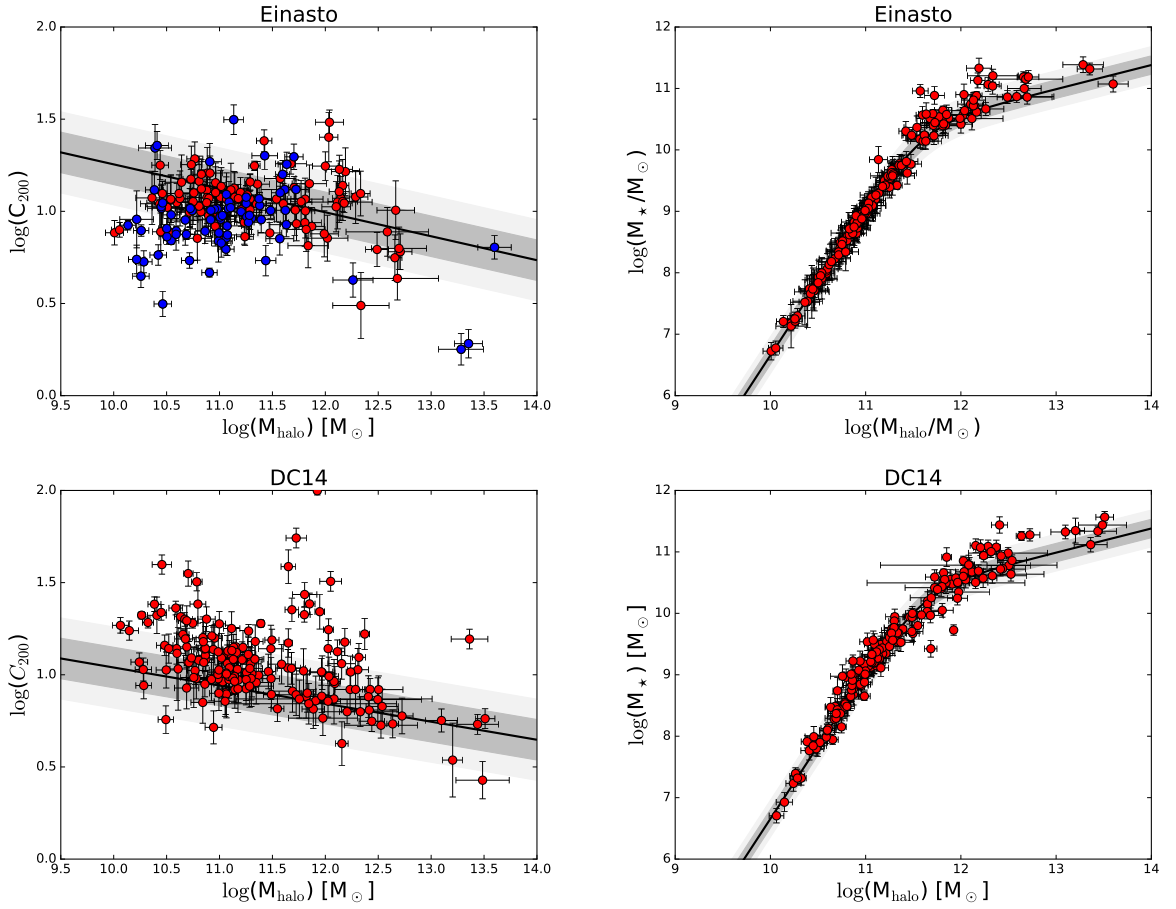


Figure 3.10 Halo mass-concentration relation (left) and stellar mass-halo mass relation (right) for Einasto (top) and DC14 (bottom) when Λ CDM priors are imposed. Solid lines show the expected mean relation from cosmological simulations; dark and light bands show 1σ and 2σ confidence regions, respectively. Blue points represent galaxies with $\alpha_{\epsilon} > 0.3$ in the Einasto profile. This is the manifestation of the cusp-core problem, as these galaxies violate the Λ CDM expectation for α_{ϵ} even if they fall within the range expected for the mass-concentration relation.

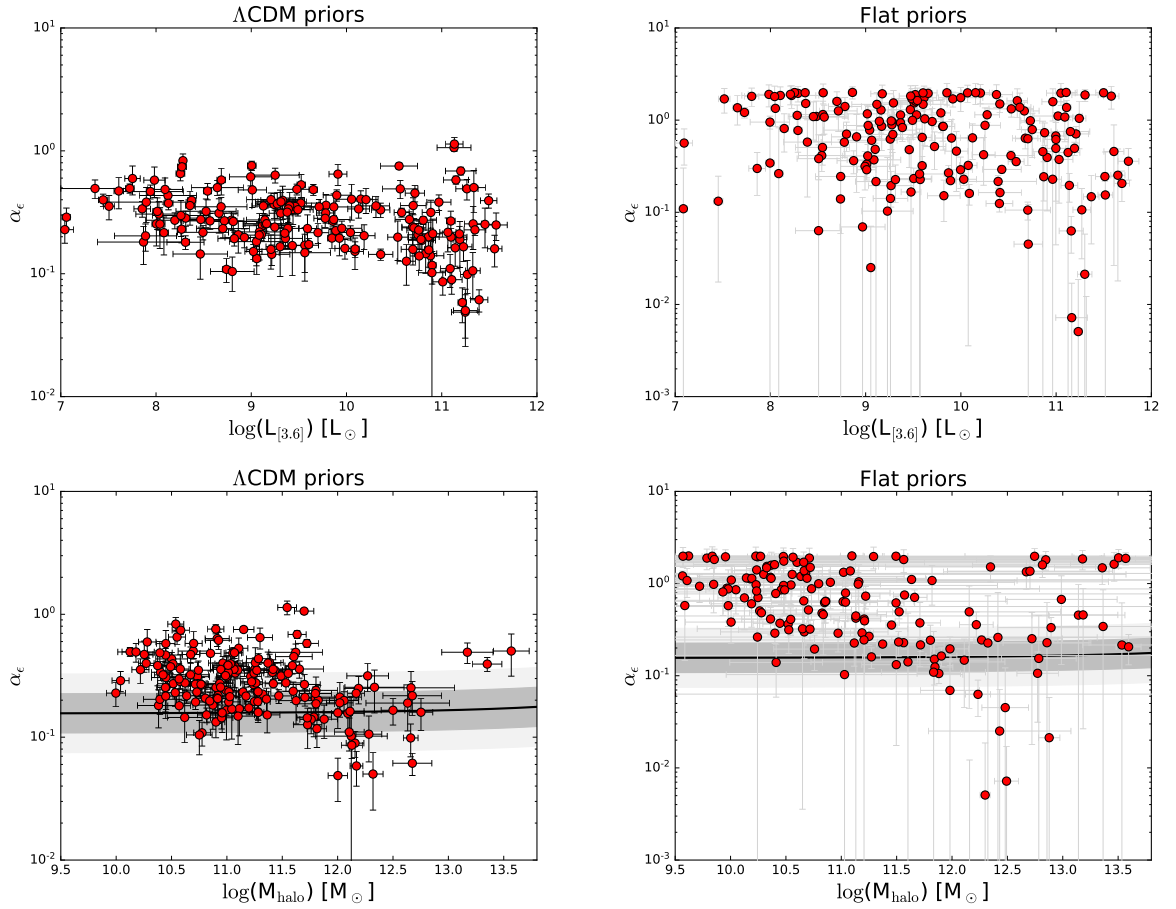


Figure 3.11 The shape parameter α_ϵ of the Einasto model versus $L_{[3.6]}$ (top panels) and M_{halo} (bottom panels), when imposing ΛCDM priors (left) and flat priors (right). The solid line in the bottom panels is the median relation expected from cosmological simulations and the dark and light regions correspond to 1σ and 2σ standard deviations, respectively. The cusp-core problem manifests itself by driving α_ϵ to larger values than expected in ΛCDM . Note that this problem sometimes occurs at high as well as low mass.

inclination. In the meantime, decreasing concentration could also decrease the inner mass and hence reduce halo contributions. To check this, we use blue colour to mark those galaxies with $\alpha_\epsilon > 0.3$ (instead of 0.2 for better illustration) in Figure 3.10. Consequently, blue points apparently represent those galaxies with smaller concentration than expected.

In Figure 3.11, we plot the values of α_ϵ against galaxy luminosity and halo mass for both Λ CDM priors (left) and flat priors (right). In the case of Λ CDM priors, α_ϵ is constant with galaxy luminosity but larger than expected for galaxies with halo mass smaller than $10^{11.5} M_\odot$. These galaxies are typically dwarf galaxies with slowly-rising rotation curves. Large values of α_ϵ reduce the central density and give better fits to the rotation curves. In the case of flat priors, the distribution of α_ϵ shows a significantly larger scatter. Most galaxies have a value of α_ϵ larger than 0.3. This is qualitatively consistent with the finding in Chemin et al. (2011) while in clear contrast to Λ CDM simulations. Navarro et al. (2004, 2010) show that the simulated DM haloes for dwarf galaxies, large spirals and clusters are consistently better fit by the Einasto profile with α_ϵ in the range of [0.1, 0.2]. Tissera et al. (2010) add baryons into their simulation and consider the feedbacks in galaxy formation. The resultant values of α_ϵ remain in the same range. Thus, although the simulation-motivated Einasto profile can well describe the rotation curves of late-type galaxies, the shape parameter presents a considerable discrepancy from what simulations predict.

Table 3.2: The best-fit values of halo parameters and fit goodness for the Einasto profile with both Λ CDM priors (left panel) and flat priors (right panel). Some galaxies have more fitting parameters than the data points in their observed rotation curves, so their χ^2_v are blank.

SPARC ID	Galaxy Name	α_ϵ	r_s kpc	$\log \rho_s$ [$M_\odot \text{pc}^{-3}$]	χ^2_v	α_ϵ	r_s kpc	$\log \rho_s$ [$M_\odot \text{pc}^{-3}$]	χ^2_v
001	UGC02487	0.25 ± 0.06	12.84 ± 3.70	-2.03 ± 0.41	6.427	0.36 ± 0.13	26.66 ± 10.42	-2.76 ± 0.54	5.769
002	UGC02885	0.16 ± 0.05	65.25 ± 16.89	-3.43 ± 0.36	1.095	0.25 ± 0.23	79.61 ± 35.25	-3.61 ± 0.66	1.036
003	NGC6195	0.25 ± 0.09	78.15 ± 31.84	-3.64 ± 0.67	2.169	1.82 ± 0.51	24.04 ± 23.32	-2.78 ± 1.76	1.844
004	UGC11455	0.69 ± 0.05	8.49 ± 1.39	-1.64 ± 0.23	2.040	0.75 ± 0.06	7.99 ± 1.67	-1.59 ± 0.29	2.076
005	NGC5371	0.05 ± 0.02	7.15 ± 2.03	-1.97 ± 0.43	2.459	0.00 ± 0.01	16.05 ± 28.16	-3 ± 185191	1.629
006	NGC2955	0.06 ± 0.01	35.26 ± 14.55	-2.98 ± 0.59	2.874	1.98 ± 0.19	14.06 ± 1.85	-2.13 ± 0.20	2.857
007	NGC0801	0.25 ± 0.10	83.35 ± 38.28	-3.94 ± 0.67	8.062	0.15 ± 0.30	701 ± 1516	-5.41 ± 3.11	7.686
008	ESO563-G021	1.06 ± 0.06	8.00 ± 1.37	-1.36 ± 0.24	9.000	1.11 ± 0.06	7.02 ± 2.18	-1.24 ± 0.43	9.037
009	UGC09133	0.05 ± 0.02	19.44 ± 5.32	-2.69 ± 0.46	7.042	0.01 ± 0.01	3.04 ± 0.85	-1.00 ± 0.40	6.444
010	UGC02953	0.23 ± 0.02	20.67 ± 2.73	-2.64 ± 0.19	5.712	0.24 ± 0.03	25.22 ± 3.22	-2.76 ± 0.18	5.701
011	NGC7331	0.17 ± 0.04	48.50 ± 11.20	-3.33 ± 0.33	0.746	0.11 ± 0.07	136.3 ± 121.0	-4.12 ± 1.23	0.736
012	NGC3992	0.11 ± 0.04	20.82 ± 7.12	-2.71 ± 0.47	1.378	0.15 ± 0.10	13.69 ± 16.19	-2.34 ± 1.59	0.913
013	NGC6674	0.49 ± 0.09	266.24 ± 69.08	-4.37 ± 0.42	1.781	0.46 ± 0.43	473.3 ± 407.2	-4.82 ± 1.27	1.618
014	NGC5985	0.20 ± 0.04	7.00 ± 1.29	-1.51 ± 0.28	2.423	0.22 ± 0.03	2.98 ± 0.89	-0.73 ± 0.45	2.133
015	NGC2841	0.10 ± 0.03	59.30 ± 17.15	-3.45 ± 0.40	1.470	0.02 ± 0.04	3297 ± 55365	-6.76 ± 23.36	1.367
016	IC4202	0.75 ± 0.04	3.41 ± 0.69	-0.90 ± 0.28	7.304	0.78 ± 0.04	0.59 ± 0.11	0.65 ± 0.27	5.993
017	NGC5005	0.19 ± 0.08	45.49 ± 19.92	-3.14 ± 0.69	0.100	1.05 ± 0.56	8.63 ± 15.19	-2.00 ± 3.22	0.118
018	NGC5907	0.06 ± 0.02	16.82 ± 5.58	-2.65 ± 0.46	4.133	0.01 ± 0.01	116 ± 1393	-4.33 ± 16.51	3.527
019	UGC05253	0.58 ± 0.04	12.36 ± 1.78	-2.10 ± 0.22	0.775	0.71 ± 0.15	13.99 ± 2.44	-2.25 ± 0.26	0.769
020	NGC5055	0.21 ± 0.03	11.81 ± 1.71	-2.43 ± 0.20	2.846	0.49 ± 0.08	17.28 ± 1.85	-2.78 ± 0.16	2.748
021	NGC2998	0.09 ± 0.02	19.77 ± 5.69	-2.77 ± 0.40	1.201	0.06 ± 0.03	30.11 ± 22.94	-3.14 ± 1.04	1.103
022	UGC11914	0.50 ± 0.19	99.77 ± 18.59	-3.01 ± 0.31	0.747	1.88 ± 0.28	74.65 ± 14.65	-2.25 ± 0.34	0.527
023	NGC3953	0.11 ± 0.03	21.86 ± 7.63	-2.88 ± 0.49	1.571	0.45 ± 0.56	5.59 ± 9.57	-1.76 ± 2.88	0.563
024	UGC12506	0.16 ± 0.05	12.93 ± 2.61	-2.25 ± 0.30	0.211	0.20 ± 0.07	10.59 ± 2.65	-2.08 ± 0.39	0.167
025	NGC0891	0.27 ± 0.05	9.03 ± 1.55	-2.03 ± 0.28	4.047	1.37 ± 0.27	7.22 ± 0.62	-1.77 ± 0.13	1.280
026	UGC06614	0.22 ± 0.07	53.38 ± 17.87	-3.26 ± 0.52	0.432	1.08 ± 0.50	30.84 ± 20.53	-2.99 ± 1.17	0.099
027	UGC02916	1.14 ± 0.14	11.29 ± 1.18	-1.94 ± 0.16	9.816	2.00 ± 0.11	9.41 ± 1.19	-2.01 ± 0.19	9.183
028	UGC03205	0.09 ± 0.02	16.85 ± 6.41	-2.64 ± 0.52	3.091	0.11 ± 0.02	4.73 ± 2.46	-1.47 ± 0.72	2.934
029	NGC5033	0.38 ± 0.06	9.22 ± 1.66	-2.02 ± 0.25	2.507	0.62 ± 0.11	11.41 ± 2.07	-2.20 ± 0.26	2.220
030	NGC4088	0.20 ± 0.06	22.29 ± 6.97	-3.04 ± 0.45	0.789	0.67 ± 0.54	111.66 ± 57.94	-3.61 ± 0.86	0.728
031	NGC4157	0.21 ± 0.07	29.42 ± 9.75	-3.16 ± 0.48	0.670	0.49 ± 0.45	44.99 ± 33.04	-3.36 ± 1.28	0.457
032	UGC03546	0.19 ± 0.04	11.52 ± 2.94	-2.35 ± 0.38	1.102	0.73 ± 0.20	9.27 ± 1.54	-2.15 ± 0.27	0.747
033	UGC06787	0.39 ± 0.05	300.91 ± 62.55	-4.37 ± 0.31	18.308	0.21 ± 0.07	1756 ± 2083	-5.57 ± 1.74	17.897
034	NGC4051	0.15 ± 0.04	18.50 ± 5.62	-2.93 ± 0.43	4.150	1.58 ± 0.61	4.60 ± 11.92	-1.86 ± 4.20	1.499
035	NGC4217	0.36 ± 0.06	12.15 ± 3.36	-2.33 ± 0.42	3.191	1.50 ± 0.29	3.81 ± 1.07	-1.28 ± 0.39	1.373
036	NGC3521	0.10 ± 0.11	20.51 ± 8.81	-2.82 ± 0.67	0.324	1.96 ± 0.52	15.41 ± 21.55	-2.46 ± 2.56	0.179
037	NGC2903	0.27 ± 0.02	5.46 ± 0.83	-1.66 ± 0.21	6.308	0.29 ± 0.03	3.35 ± 0.64	-1.23 ± 0.28	6.191
038	NGC2683	0.12 ± 0.03	16.79 ± 5.64	-2.84 ± 0.46	3.066	0.39 ± 0.29	6.85 ± 3.93	-2.00 ± 0.85	1.705
039	NGC4013	0.32 ± 0.08	58.90 ± 15.32	-3.63 ± 0.39	0.918	0.23 ± 0.39	223.5 ± 206.9	-4.47 ± 1.34	0.830
040	NGC7814	0.16 ± 0.04	16.84 ± 4.05	-2.57 ± 0.35	0.604	0.24 ± 0.11	11.17 ± 4.29	-2.23 ± 0.63	0.593
041	UGC06786	0.19 ± 0.03	11.57 ± 2.32	-2.16 ± 0.29	0.665	0.16 ± 0.04	6.49 ± 1.61	-1.64 ± 0.36	0.542

Table 3.2 – Continued

SPARC ID	Galaxy Name	α_ϵ	r_s kpc	$\log \rho_s$ [$M_\odot \text{pc}^{-3}$]	χ^2_v	α_ϵ	r_s kpc	$\log \rho_s$ [$M_\odot \text{pc}^{-3}$]	χ^2_v
042	NGC3877	0.24 ± 0.04	10.11 ± 2.32	-2.31 ± 0.34	6.521	1.26 ± 0.31	3.49 ± 0.59	-1.37 ± 0.25	2.685
043	NGC0289	0.14 ± 0.04	21.65 ± 5.42	-3.02 ± 0.35	2.205	0.37 ± 0.25	31.51 ± 17.31	-3.40 ± 0.76	2.033
044	NGC1090	0.28 ± 0.04	12.10 ± 3.68	-2.53 ± 0.42	2.419	0.41 ± 0.05	6.83 ± 2.43	-1.98 ± 0.49	1.808
045	NGC3726	0.24 ± 0.07	24.53 ± 7.25	-3.12 ± 0.44	3.939	0.45 ± 0.52	206.3 ± 112.7	-4.17 ± 0.85	2.871
046	UGC09037	0.45 ± 0.07	17.33 ± 3.41	-2.74 ± 0.31	1.327	0.99 ± 0.33	12.07 ± 2.42	-2.46 ± 0.34	1.143
047	NGC6946	0.23 ± 0.04	21.02 ± 5.24	-2.97 ± 0.36	1.753	0.63 ± 0.31	8.70 ± 2.34	-2.30 ± 0.45	1.566
048	NGC4100	0.14 ± 0.03	14.41 ± 3.86	-2.69 ± 0.37	1.370	0.64 ± 0.15	5.21 ± 0.99	-1.65 ± 0.29	0.419
049	NGC3893	0.21 ± 0.05	14.33 ± 4.10	-2.57 ± 0.42	1.614	0.79 ± 0.40	7.13 ± 3.03	-1.96 ± 0.70	0.522
050	UGC06973	0.36 ± 0.07	6.37 ± 1.23	-1.74 ± 0.29	2.494	0.88 ± 0.48	3.30 ± 5.31	-1.23 ± 2.94	2.568
051	ESO079-G014	0.49 ± 0.08	14.86 ± 4.43	-2.50 ± 0.46	2.861	1.33 ± 0.25	8.09 ± 2.15	-1.99 ± 0.37	0.962
052	UGC08699	0.16 ± 0.04	26.35 ± 7.97	-3.11 ± 0.42	0.787	0.05 ± 0.08	707 ± 5541	-5.70 ± 10.94	0.691
053	NGC4138	0.13 ± 0.05	15.07 ± 4.85	-2.78 ± 0.45		1.38 ± 0.58	4.54 ± 5.78	-1.58 ± 1.78	
054	NGC3198	0.31 ± 0.03	13.74 ± 1.45	-2.68 ± 0.15	1.119	0.35 ± 0.03	13.87 ± 1.54	-2.68 ± 0.16	1.081
055	NGC3949	0.20 ± 0.07	14.47 ± 4.26	-2.74 ± 0.42	2.160	1.62 ± 0.56	73.91 ± 38.44	-2.37 ± 0.79	1.615
056	NGC6015	0.14 ± 0.01	15.96 ± 3.97	-2.82 ± 0.34	7.830	0.12 ± 0.02	24.39 ± 12.56	-3.18 ± 0.71	7.821
057	NGC3917	0.33 ± 0.04	19.89 ± 4.52	-3.04 ± 0.33	3.331	1.14 ± 0.21	6.12 ± 0.92	-2.00 ± 0.22	1.413
058	NGC4085	0.40 ± 0.09	10.70 ± 2.09	-2.40 ± 0.29	15.519	1.98 ± 0.50	3.23 ± 11.62	-1.48 ± 6.63	7.827
059	NGC4389	0.40 ± 0.13	12.07 ± 2.91	-2.66 ± 0.35		1.98 ± 0.41	32.55 ± 17.10	-1.98 ± 0.93	
060	NGC4559	0.23 ± 0.03	9.54 ± 2.92	-2.53 ± 0.42	0.253	1.89 ± 0.53	12.55 ± 4.61	-2.78 ± 0.56	0.105
061	NGC3769	0.20 ± 0.05	11.68 ± 2.74	-2.72 ± 0.32	1.178	0.42 ± 0.23	10.78 ± 3.38	-2.62 ± 0.50	0.985
062	NGC4010	0.41 ± 0.07	14.08 ± 2.67	-2.73 ± 0.28	2.958	1.97 ± 0.46	6.27 ± 3.73	-2.10 ± 1.07	1.613
063	NGC3972	0.34 ± 0.05	12.42 ± 2.40	-2.61 ± 0.28	1.541	0.64 ± 0.27	6.74 ± 8.71	-2.14 ± 2.35	1.243
064	UGC03580	0.33 ± 0.04	9.49 ± 1.53	-2.44 ± 0.23	2.349	0.23 ± 0.07	12.74 ± 3.28	-2.65 ± 0.39	2.347
065	NGC6503	0.16 ± 0.02	8.01 ± 0.88	-2.43 ± 0.15	1.426	0.16 ± 0.04	7.68 ± 0.99	-2.39 ± 0.20	1.411
066	UGC11557	0.35 ± 0.10	11.40 ± 3.81	-2.62 ± 0.50	1.483	1.75 ± 0.51	5.64 ± 16.34	-1.98 ± 5.28	0.605
067	UGC00128	0.22 ± 0.03	17.77 ± 2.79	-3.07 ± 0.24	3.855	0.23 ± 0.03	16.90 ± 3.20	-2.93 ± 0.28	3.796
068	F579-V1	0.15 ± 0.04	8.79 ± 2.62	-2.48 ± 0.41	0.489	0.32 ± 0.32	3.72 ± 3.09	-1.85 ± 1.50	0.217
069	NGC4183	0.16 ± 0.03	11.61 ± 2.46	-2.83 ± 0.29	0.293	0.29 ± 0.11	7.50 ± 2.65	-2.46 ± 0.56	0.193
070	F571-8	0.63 ± 0.09	4.68 ± 1.13	-1.61 ± 0.34	0.998	1.30 ± 0.32	4.54 ± 1.22	-1.58 ± 0.39	0.608
071	NGC2403	0.22 ± 0.01	6.77 ± 0.48	-2.10 ± 0.11	9.178	0.22 ± 0.01	6.86 ± 0.52	-2.07 ± 0.11	9.086
072	UGC06930	0.19 ± 0.05	11.10 ± 2.84	-2.74 ± 0.36	0.631	0.46 ± 0.29	7.23 ± 3.96	-2.37 ± 0.94	0.352
073	F568-3	0.65 ± 0.13	13.02 ± 2.87	-2.55 ± 0.32	1.873	1.70 ± 0.31	7.30 ± 3.00	-2.21 ± 0.67	1.231
074	UGC01230	0.28 ± 0.09	9.45 ± 2.28	-2.48 ± 0.35	1.626	0.64 ± 0.38	7.85 ± 6.86	-2.34 ± 1.41	0.738
075	NGC0247	0.27 ± 0.02	15.38 ± 1.97	-3.07 ± 0.19	1.775	0.27 ± 0.06	16.01 ± 5.00	-3.10 ± 0.49	1.775
076	NGC7793	0.20 ± 0.03	12.73 ± 3.56	-2.92 ± 0.38	0.967	1.98 ± 0.52	3.91 ± 1.99	-2.12 ± 0.90	0.654
077	UGC06917	0.28 ± 0.04	11.18 ± 2.05	-2.71 ± 0.26	1.113	0.85 ± 0.38	5.43 ± 3.16	-2.13 ± 1.05	0.455
078	NGC1003	0.35 ± 0.05	23.58 ± 4.74	-3.32 ± 0.28	2.579	0.15 ± 0.07	78.23 ± 45.59	-4.25 ± 0.81	2.478
079	F574-1	0.31 ± 0.05	10.92 ± 2.13	-2.66 ± 0.28	1.353	0.86 ± 0.26	5.54 ± 1.12	-2.19 ± 0.35	0.229
080	F568-1	0.36 ± 0.08	10.28 ± 2.08	-2.50 ± 0.29	0.810	1.20 ± 0.47	5.25 ± 3.95	-1.84 ± 1.36	0.178
081	UGC06983	0.22 ± 0.04	8.91 ± 1.65	-2.56 ± 0.26	0.853	0.52 ± 0.23	5.86 ± 2.08	-2.19 ± 0.63	0.597
082	UGC05986	0.44 ± 0.05	13.79 ± 2.72	-2.77 ± 0.28	3.504	1.49 ± 0.23	3.81 ± 1.14	-1.67 ± 0.41	0.089
083	NGC0055	0.48 ± 0.05	15.52 ± 1.48	-3.10 ± 0.15	1.221	1.95 ± 0.27	7.33 ± 0.66	-2.54 ± 0.15	0.164
084	ESO116-G012	0.38 ± 0.04	8.22 ± 2.01	-2.38 ± 0.34	1.774	0.97 ± 0.37	5.94 ± 1.76	-2.15 ± 0.44	0.975

Table 3.2 – Continued

SPARC ID	Galaxy Name	α_ϵ	r_s kpc	$\log \rho_s$ [$M_\odot \text{pc}^{-3}$]	χ^2_v	α_ϵ	r_s kpc	$\log \rho_s$ [$M_\odot \text{pc}^{-3}$]	χ^2_v
085	UGC07323	0.38 ± 0.08	9.42 ± 2.86	-2.60 ± 0.43	0.961	0.26 ± 0.54	83.67 ± 82.75	-3.89 ± 1.60	0.453
086	UGC05005	0.36 ± 0.10	12.69 ± 3.44	-2.93 ± 0.39	0.957	1.03 ± 0.50	15.00 ± 20.27	-2.98 ± 2.42	0.016
087	F561-1	0.17 ± 0.07	8.52 ± 2.70	-2.62 ± 0.44		1.75 ± 0.59	3.77 ± 21.01	-2.56 ± 9.61	
088	NGC0024	0.17 ± 0.02	8.34 ± 1.61	-2.53 ± 0.27	0.868	0.32 ± 0.08	3.83 ± 1.09	-1.83 ± 0.48	0.838
089	F568-V1	0.23 ± 0.07	8.15 ± 1.88	-2.46 ± 0.32	0.323	0.65 ± 0.35	5.14 ± 3.70	-1.98 ± 1.28	0.117
090	UGC06628	0.15 ± 0.06	7.86 ± 2.85	-2.58 ± 0.51	0.484	1.63 ± 0.59	1.79 ± 9.06	-1.91 ± 8.90	0.067
091	UGC02455	0.38 ± 0.12	2.61 ± 0.82	-1.59 ± 0.46	6.289	1.85 ± 0.44	21.35 ± 11.54	-1.01 ± 0.85	1.523
092	UGC07089	0.34 ± 0.08	14.11 ± 2.71	-3.12 ± 0.27	0.400	0.23 ± 0.51	162.0 ± 210.5	-4.54 ± 2.00	0.160
093	UGC05999	0.40 ± 0.12	10.98 ± 2.83	-2.76 ± 0.38		1.70 ± 0.49	8.50 ± 8.20	-2.35 ± 1.67	
094	NGC2976	0.53 ± 0.11	9.66 ± 1.77	-2.43 ± 0.26	0.519	1.89 ± 0.48	2.32 ± 12.26	-1.50 ± 9.73	0.337
095	UGC05750	0.37 ± 0.09	13.51 ± 3.78	-3.06 ± 0.39	0.973	1.61 ± 0.49	9.52 ± 5.90	-2.77 ± 1.09	0.088
096	NGC0100	0.40 ± 0.05	8.84 ± 2.52	-2.55 ± 0.40	0.372	1.14 ± 0.43	6.41 ± 6.61	-2.38 ± 1.85	0.130
097	UGC00634	0.39 ± 0.09	11.22 ± 3.18	-2.78 ± 0.40		1.00 ± 0.37	10.35 ± 3.93	-2.62 ± 0.59	
098	F563-V2	0.33 ± 0.08	8.76 ± 2.38	-2.50 ± 0.38	1.446	1.54 ± 0.46	3.76 ± 3.52	-1.64 ± 1.58	0.140
099	NGC5585	0.49 ± 0.05	13.52 ± 1.95	-2.92 ± 0.21	6.758	1.98 ± 0.15	6.80 ± 0.99	-2.41 ± 0.20	4.247
100	NGC0300	0.35 ± 0.05	10.22 ± 2.09	-2.65 ± 0.28	0.533	0.48 ± 0.17	7.78 ± 3.69	-2.46 ± 0.80	0.502
101	UGC06923	0.23 ± 0.07	10.27 ± 2.18	-2.84 ± 0.30		1.83 ± 0.54	3.57 ± 16.68	-2.01 ± 8.61	
102	F574-2	0.17 ± 0.07	8.59 ± 2.99	-2.69 ± 0.47		0.17 ± 0.52	13.5 ± 201.6	-4.88 ± 27.28	
103	UGC07125	0.22 ± 0.03	6.07 ± 2.19	-2.59 ± 0.49	0.730	0.70 ± 0.38	6.46 ± 2.20	-2.78 ± 0.53	0.282
104	UGC07524	0.32 ± 0.04	12.10 ± 1.54	-2.98 ± 0.19	0.495	0.83 ± 0.25	5.55 ± 1.10	-2.42 ± 0.36	0.210
105	UGC06399	0.31 ± 0.06	9.89 ± 1.66	-2.74 ± 0.24	1.149	1.14 ± 0.49	4.64 ± 5.71	-2.13 ± 2.25	0.096
106	UGC07151	0.21 ± 0.03	12.73 ± 2.11	-3.08 ± 0.23	4.428	0.94 ± 0.31	2.47 ± 0.73	-1.84 ± 0.53	2.034
107	F567-2	0.17 ± 0.07	7.26 ± 2.32	-2.55 ± 0.44		1.54 ± 0.56	3.18 ± 11.85	-2.38 ± 6.37	
108	UGC04325	0.19 ± 0.03	6.94 ± 1.76	-2.45 ± 0.35	9.354	0.89 ± 0.23	2.10 ± 0.59	-1.40 ± 0.41	1.414
109	UGC00191	0.25 ± 0.03	6.85 ± 1.86	-2.45 ± 0.38	6.496	0.37 ± 0.06	4.15 ± 1.35	-2.13 ± 0.49	5.146
110	F563-1	0.37 ± 0.08	9.31 ± 2.22	-2.62 ± 0.34	1.148	0.62 ± 0.25	7.56 ± 3.51	-2.31 ± 0.78	0.929
111	F571-V1	0.24 ± 0.09	9.89 ± 2.70	-2.81 ± 0.38	4.005	0.95 ± 0.51	8.27 ± 12.99	-2.65 ± 2.82	0.192
112	UGC07261	0.16 ± 0.05	7.04 ± 2.36	-2.56 ± 0.47	0.094	0.10 ± 0.29	16.25 ± 30.25	-3.40 ± 2.72	0.122
113	UGC10310	0.21 ± 0.05	7.88 ± 2.47	-2.66 ± 0.44	3.113	0.98 ± 0.50	3.27 ± 3.21	-2.07 ± 1.73	0.420
114	UGC02259	0.14 ± 0.03	6.03 ± 1.51	-2.42 ± 0.35	2.099	0.19 ± 0.08	4.52 ± 2.22	-2.18 ± 0.75	1.987
115	F583-4	0.25 ± 0.05	9.55 ± 2.69	-2.83 ± 0.39	0.334	0.14 ± 0.34	88.1 ± 199.2	-4.51 ± 3.23	0.222
116	UGC12732	0.26 ± 0.04	11.04 ± 3.00	-2.96 ± 0.38	0.304	0.23 ± 0.10	16.70 ± 8.66	-3.29 ± 0.81	0.215
117	UGC06818	0.48 ± 0.14	10.60 ± 1.78	-2.83 ± 0.26	6.691	1.93 ± 0.47	9.34 ± 25.83	-2.54 ± 5.09	3.241
118	UGC04499	0.27 ± 0.04	6.91 ± 2.07	-2.56 ± 0.41	1.793	0.86 ± 0.39	4.38 ± 2.75	-2.29 ± 1.07	0.615
119	F563-V1	0.18 ± 0.07	8.57 ± 3.10	-2.81 ± 0.51		1.29 ± 0.57	2.63 ± 39.04	-2.97 ± 27.24	
120	UGC06667	0.36 ± 0.05	9.07 ± 1.28	-2.64 ± 0.21	1.527	0.97 ± 0.34	4.38 ± 1.59	-2.07 ± 0.65	0.150
121	UGC02023	0.22 ± 0.09	7.71 ± 2.81	-2.62 ± 0.51		1.48 ± 0.50	73.94 ± 73.18	-2.51 ± 1.36	
122	UGC04278	0.61 ± 0.10	9.75 ± 2.28	-2.57 ± 0.33	0.821	0.22 ± 0.40	420.6 ± 563.8	-4.56 ± 1.89	0.571
123	UGC12632	0.23 ± 0.04	6.39 ± 1.84	-2.55 ± 0.40	0.414	0.60 ± 0.27	4.68 ± 1.80	-2.35 ± 0.64	0.111
124	UGC08286	0.21 ± 0.02	7.52 ± 1.07	-2.61 ± 0.21	3.118	0.48 ± 0.08	3.41 ± 0.34	-1.94 ± 0.18	1.885
125	UGC07399	0.27 ± 0.03	5.64 ± 1.33	-2.16 ± 0.33	1.448	0.41 ± 0.14	3.36 ± 1.53	-1.72 ± 0.75	1.000
126	NGC4214	0.13 ± 0.03	5.40 ± 1.77	-2.37 ± 0.44	0.755	0.03 ± 0.05	233 ± 5286	-4.83 ± 31.34	0.179
127	UGC05414	0.35 ± 0.07	7.58 ± 2.62	-2.62 ± 0.47		0.87 ± 0.53	4.47 ± 20.39	-2.38 ± 8.39	

Table 3.2 – Continued

SPARC ID	Galaxy Name	α_ϵ	r_s kpc	$\log \rho_s$ [$M_\odot \text{pc}^{-3}$]	χ^2_v	α_ϵ	r_s kpc	$\log \rho_s$ [$M_\odot \text{pc}^{-3}$]	χ^2_v
128	UGC08490	0.15 ± 0.02	4.99 ± 0.97	-2.32 ± 0.27	0.352	0.29 ± 0.07	3.09 ± 0.63	-1.91 ± 0.33	0.116
129	IC2574	0.76 ± 0.06	18.49 ± 1.46	-3.34 ± 0.13	2.395	0.33 ± 0.10	247.1 ± 159.1	-4.51 ± 1.00	2.058
130	UGC06446	0.20 ± 0.03	6.47 ± 1.69	-2.51 ± 0.36	0.311	0.32 ± 0.14	4.45 ± 2.14	-2.21 ± 0.79	0.254
131	F583-1	0.50 ± 0.07	6.95 ± 1.79	-2.43 ± 0.37	0.626	1.17 ± 0.28	6.59 ± 1.66	-2.42 ± 0.36	0.182
132	UGC11820	0.27 ± 0.04	10.88 ± 3.18	-3.09 ± 0.41	4.567	0.07 ± 0.07	971 ± 7034	-6.20 ± 10.28	1.305
133	UGC07690	0.10 ± 0.03	5.88 ± 2.02	-2.62 ± 0.47	4.774	0.66 ± 0.49	1.16 ± 1.15	-1.37 ± 1.57	0.703
134	UGC04305	0.21 ± 0.06	5.32 ± 1.65	-2.31 ± 0.42	2.107	2.00 ± 0.30	1.37 ± 0.41	-1.71 ± 0.50	0.691
135	NGC2915	0.27 ± 0.05	5.16 ± 0.70	-2.24 ± 0.20	0.935	0.71 ± 0.25	3.56 ± 0.80	-1.88 ± 0.41	0.703
136	UGC05716	0.27 ± 0.04	7.88 ± 1.72	-2.77 ± 0.31	3.022	0.36 ± 0.10	7.70 ± 1.95	-2.83 ± 0.41	2.627
137	UGC05829	0.32 ± 0.08	8.03 ± 2.71	-2.78 ± 0.48	0.494	0.24 ± 0.37	26.59 ± 43.42	-3.68 ± 2.77	0.119
138	F565-V2	0.31 ± 0.10	7.53 ± 1.83	-2.66 ± 0.34	5.691	1.26 ± 0.51	6.27 ± 15.90	-2.39 ± 4.65	0.250
139	DDO161	0.43 ± 0.06	6.42 ± 1.97	-2.57 ± 0.43	0.530	1.41 ± 0.36	9.61 ± 2.29	-2.98 ± 0.38	0.248
140	DDO170	0.27 ± 0.04	6.20 ± 2.01	-2.66 ± 0.45	6.112	0.51 ± 0.18	6.09 ± 2.40	-2.68 ± 0.62	4.660
141	NGC1705	0.11 ± 0.02	4.08 ± 0.90	-2.21 ± 0.30	0.230	0.14 ± 0.08	1.74 ± 0.96	-1.51 ± 0.87	0.069
142	UGC05721	0.19 ± 0.03	4.10 ± 0.98	-2.11 ± 0.33	1.444	0.58 ± 0.18	1.97 ± 0.75	-1.45 ± 0.53	0.525
143	UGC08837	0.58 ± 0.14	13.66 ± 1.55	-3.23 ± 0.18	3.579	1.60 ± 0.43	63.09 ± 31.96	-2.82 ± 0.92	0.999
144	UGC07603	0.28 ± 0.04	5.68 ± 1.44	-2.46 ± 0.35	1.781	1.08 ± 0.37	2.07 ± 0.92	-1.69 ± 0.72	0.356
145	UGC00891	0.47 ± 0.06	5.22 ± 1.48	-2.33 ± 0.40		1.15 ± 0.45	6.31 ± 4.73	-2.58 ± 1.35	
146	UGC01281	0.47 ± 0.07	9.60 ± 0.83	-2.88 ± 0.15	0.367	1.98 ± 0.48	3.15 ± 4.38	-2.11 ± 2.56	0.033
147	UGC09992	0.14 ± 0.05	5.01 ± 1.87	-2.50 ± 0.52		0.06 ± 0.63	1.65 ± 11.86	-2.40 ± 13.19	
148	D512-2	0.18 ± 0.06	4.74 ± 1.71	-2.58 ± 0.51		1.10 ± 0.51	1.90 ± 13.10	-2.13 ± 12.72	
149	UGC00731	0.28 ± 0.04	5.89 ± 1.48	-2.53 ± 0.35	0.278	0.41 ± 0.13	5.26 ± 1.92	-2.47 ± 0.59	0.129
150	UGC08550	0.18 ± 0.02	6.12 ± 1.96	-2.71 ± 0.44	1.568	0.38 ± 0.16	3.25 ± 1.39	-2.24 ± 0.71	0.884
151	UGC07608	0.30 ± 0.10	6.04 ± 2.10	-2.56 ± 0.49	2.181	1.09 ± 0.49	3.96 ± 14.82	-2.13 ± 6.86	0.270
152	NGC2366	0.40 ± 0.04	8.91 ± 1.00	-2.99 ± 0.17	2.151	1.98 ± 0.19	2.76 ± 0.22	-2.13 ± 0.13	0.247
153	NGC4068	0.36 ± 0.11	8.89 ± 1.83	-2.95 ± 0.29		1.52 ± 0.47	33.88 ± 25.76	-2.49 ± 1.37	
154	UGC05918	0.20 ± 0.05	5.31 ± 1.99	-2.67 ± 0.52	0.427	0.58 ± 0.43	2.84 ± 2.95	-2.32 ± 1.86	0.114
155	D631-7	0.83 ± 0.11	9.43 ± 0.70	-2.81 ± 0.13	1.309	1.95 ± 0.38	5.63 ± 3.61	-2.48 ± 1.18	0.684
156	NGC3109	0.74 ± 0.06	8.62 ± 0.72	-2.68 ± 0.14	0.297	1.13 ± 0.33	5.74 ± 3.50	-2.43 ± 1.11	0.213
157	UGCA281	0.23 ± 0.05	8.63 ± 1.28	-3.06 ± 0.21	2.236	0.77 ± 0.32	0.94 ± 4.74	-1.69 ± 9.26	0.689
158	DDO168	0.65 ± 0.08	6.79 ± 0.76	-2.45 ± 0.17	9.147	1.99 ± 0.20	2.85 ± 0.39	-1.93 ± 0.23	4.972
159	DDO064	0.31 ± 0.08	6.14 ± 2.02	-2.68 ± 0.46	0.811	1.85 ± 0.51	1.84 ± 15.32	-1.86 ± 15.30	0.458
160	PGC51017	0.58 ± 0.16	19.01 ± 3.18	-3.83 ± 0.24		1.90 ± 0.44	1714 ± 3592	-4.94 ± 3.75	
161	UGCA442	0.37 ± 0.04	7.75 ± 1.06	-2.86 ± 0.20	2.831	0.81 ± 0.36	4.36 ± 1.61	-2.42 ± 0.67	1.441
162	UGC07866	0.22 ± 0.07	7.51 ± 1.74	-2.99 ± 0.32	1.031	0.26 ± 0.56	9.25 ± 37.37	-3.35 ± 7.40	0.253
163	UGC07232	0.25 ± 0.09	4.73 ± 0.75	-2.43 ± 0.24		1.34 ± 0.48	20.67 ± 12.56	-1.56 ± 1.09	
164	UGC07559	0.32 ± 0.09	10.32 ± 1.46	-3.28 ± 0.21	2.163	1.80 ± 0.54	1.91 ± 23.29	-2.29 ± 22.47	0.380
165	NGC6789	0.25 ± 0.09	3.42 ± 0.65	-2.04 ± 0.28		0.34 ± 0.51	48.76 ± 28.83	-2.44 ± 1.03	
166	KK98-251	0.49 ± 0.09	5.16 ± 1.84	-2.56 ± 0.50	1.008	1.90 ± 0.51	3.07 ± 27.87	-2.53 ± 16.73	0.342
167	UGC05764	0.49 ± 0.12	2.43 ± 0.46	-1.38 ± 0.29	7.613	0.95 ± 0.15	1.60 ± 0.36	-1.62 ± 0.33	4.022
168	CamB	0.60 ± 0.16	10.12 ± 1.53	-3.25 ± 0.22	4.784	1.81 ± 0.41	63.95 ± 32.46	-2.78 ± 0.91	4.026
169	ESO444-G084	0.34 ± 0.05	4.56 ± 0.92	-2.33 ± 0.28	0.974	0.30 ± 0.15	6.68 ± 4.89	-2.59 ± 1.23	0.495
170	DDO154	0.49 ± 0.04	5.59 ± 0.45	-2.71 ± 0.13	6.029	1.21 ± 0.16	3.44 ± 0.22	-2.35 ± 0.11	0.838

Table 3.2 – Continued

SPARC ID	Galaxy Name	α_ϵ	r_s kpc	$\log \rho_s$ [$M_\odot \text{pc}^{-3}$]	χ^2_ν	α_ϵ	r_s kpc	$\log \rho_s$ [$M_\odot \text{pc}^{-3}$]	χ^2_ν
171	UGC07577	0.47 ± 0.13	11.69 ± 1.77	-3.49 ± 0.22	1.569	1.36 ± 0.48	79.42 ± 53.12	-3.27 ± 1.15	0.293
172	D564-8	0.35 ± 0.08	9.28 ± 1.74	-3.32 ± 0.26		1.70 ± 0.51	2.17 ± 20.47	-2.49 ± 17.41	
173	NGC3741	0.40 ± 0.05	6.80 ± 0.61	-2.88 ± 0.14	0.635	0.13 ± 0.11	118.2 ± 232.5	-4.82 ± 2.76	0.444
174	UGC04483	0.23 ± 0.05	5.52 ± 0.90	-3.02 ± 0.23	1.937	0.56 ± 0.24	0.97 ± 4.15	-1.94 ± 7.86	0.973
175	UGCA444	0.29 ± 0.05	5.60 ± 0.61	-2.95 ± 0.17	0.115	0.11 ± 0.19	478 ± 4305	-5.70 ± 12.84	0.063

Table 3.3: Same as Table 3.2, but for the DC14 profile.

SPARC ID	Galaxy Name	$\log(\frac{m_*}{M_{\text{halo}}})$	r_s kpc	$\log \rho_s$ [$M_{\odot} \text{ pc}^{-3}$]	χ^2_v	$\log(\frac{m_*}{M_{\text{halo}}})$	r_s kpc	$\log \rho_s$ [$M_{\odot} \text{ pc}^{-3}$]	χ^2_v
001	UGC02487	-0.97	36.05 ± 9.72	-2.23 ± 0.36	5.532	-0.92	40.82 ± 25.72	-2.23 ± 0.62	5.499
002	UGC02885	-1.45	58.54 ± 13.83	-2.77 ± 0.33	1.005	-1.43	80.95 ± 31.30	-3.01 ± 0.40	1.015
003	NGC6195	-2.10	112.40 ± 21.97	-3.20 ± 0.32	2.148	-1.68	95.51 ± 27.76	-3.25 ± 0.40	2.047
004	UGC11455	-1.77	82.43 ± 15.28	-3.07 ± 0.29	4.829	-1.76	85.45 ± 17.57	-3.10 ± 0.24	4.832
005	NGC5371	-0.94	7.38 ± 1.04	-1.03 ± 0.19	2.904	-0.96	5.32 ± 1.06	-0.73 ± 0.20	2.710
006	NGC2955	-1.30	23.83 ± 6.57	-1.89 ± 0.37	3.399	-1.30	9.78 ± 3.04	-0.92 ± 0.33	2.754
007	NGC0801	-1.05	53.41 ± 14.71	-2.79 ± 0.37	8.979	-1.51	283.4 ± 136.6	-4.15 ± 0.52	6.771
008	ESO563-G021	-1.94	110.58 ± 15.80	-3.10 ± 0.21	17.875	-1.89	113.16 ± 18.77	-3.14 ± 0.19	17.879
009	UGC09133	-1.14	37.26 ± 5.98	-2.41 ± 0.22	7.082	-1.07	47.82 ± 9.36	-2.59 ± 0.21	7.064
010	UGC02953	-1.31	20.59 ± 3.71	-1.77 ± 0.24	5.822	-1.32	15.71 ± 3.00	-1.54 ± 0.20	5.798
011	NGC7331	-1.49	33.34 ± 4.73	-2.50 ± 0.19	0.812	-1.50	30.45 ± 5.20	-2.42 ± 0.18	0.801
012	NGC3992	-1.20	30.00 ± 8.13	-2.13 ± 0.36	1.261	-1.08	17.60 ± 8.02	-1.68 ± 0.45	0.694
013	NGC6674	-2.05	234.24 ± 70.76	-3.81 ± 0.47	1.766	-1.81	381.7 ± 259.9	-4.21 ± 0.73	1.460
014	NGC5985	-1.30	16.04 ± 3.18	-1.43 ± 0.26	2.869	-1.71	2.65 ± 0.54	-0.26 ± 0.21	2.043
015	NGC2841	-1.38	60.37 ± 10.79	-2.76 ± 0.24	1.420	-1.37	71.07 ± 16.02	-2.88 ± 0.23	1.415
016	IC4202	-2.20	1.90 ± 0.10	-0.21 ± 0.07	5.551	-2.26	1.92 ± 0.04	-0.22 ± 0.02	5.076
017	NGC5005	-1.52	40.00 ± 16.74	-2.65 ± 0.69	0.154	-1.68	24.75 ± 14.39	-2.18 ± 0.81	0.092
018	NGC5907	-1.17	14.76 ± 3.09	-1.62 ± 0.27	4.513	-1.24	9.96 ± 1.68	-1.23 ± 0.17	4.077
019	UGC05253	-1.50	6.49 ± 0.95	-1.09 ± 0.22	2.578	-1.61	2.41 ± 0.36	-0.37 ± 0.19	2.004
020	NGC5055	-1.37	8.13 ± 0.83	-1.34 ± 0.14	2.988	-1.39	7.24 ± 0.80	-1.22 ± 0.13	3.031
021	NGC2998	-1.30	23.94 ± 5.09	-2.06 ± 0.28	1.367	-1.30	19.06 ± 7.26	-1.85 ± 0.38	1.202
022	UGC11914	-2.24	36.54 ± 6.60	-2.17 ± 0.29	0.670	-2.59	31.95 ± 5.78	-1.88 ± 0.22	0.605
023	NGC3953	-1.30	28.88 ± 22.45	-2.25 ± 1.37	1.133	-1.01	15.71 ± 26.94	-1.83 ± 1.72	0.699
024	UGC12506	-1.30	23.28 ± 4.67	-1.92 ± 0.27	0.250	-1.34	12.54 ± 3.93	-1.47 ± 0.31	0.189
025	NGC0891	-1.45	11.69 ± 1.64	-1.67 ± 0.19	4.777	-1.45	7.50 ± 1.42	-1.29 ± 0.19	3.738
026	UGC06614	-1.68	44.99 ± 11.01	-2.85 ± 0.35	0.250	-1.68	38.44 ± 16.43	-2.69 ± 0.44	0.197
027	UGC02916	-1.13	2.94 ± 0.42	-0.13 ± 0.21	5.890	-0.26	1.15 ± 0.09	0.53 ± 0.12	3.748
028	UGC03205	-1.29	23.21 ± 6.47	-2.03 ± 0.37	3.203	-1.37	5.62 ± 2.05	-0.89 ± 0.37	3.007
029	NGC5033	-1.37	8.76 ± 1.93	-1.31 ± 0.29	4.505	-1.53	3.38 ± 0.65	-0.65 ± 0.19	3.830
030	NGC4088	-1.72	41.02 ± 13.68	-2.94 ± 0.56	0.628	-2.27	49.85 ± 19.79	-2.82 ± 0.59	0.614
031	NGC4157	-1.70	42.86 ± 11.22	-2.91 ± 0.43	0.452	-1.67	41.95 ± 17.10	-2.89 ± 0.59	0.461
032	UGC03546	-1.36	21.01 ± 5.26	-2.13 ± 0.34	1.132	-1.40	7.26 ± 2.19	-1.27 ± 0.31	1.063
033	UGC06787	-1.86	146.65 ± 68.42	-3.55 ± 0.62	17.836	-1.81	181.45 ± 77.29	-3.72 ± 0.42	17.635
034	NGC4051	-1.35	25.54 ± 17.48	-2.45 ± 1.22	2.256	-0.75	17.66 ± 59.64	-2.29 ± 3.44	2.032
035	NGC4217	-1.65	19.64 ± 4.28	-2.30 ± 0.31	3.081	-1.94	1.31 ± 0.22	-0.11 ± 0.18	1.865
036	NGC3521	-1.73	35.55 ± 8.73	-2.67 ± 0.39	0.244	-1.88	29.17 ± 12.21	-2.47 ± 0.62	0.230
037	NGC2903	-1.45	3.97 ± 0.86	-0.82 ± 0.29	7.024	-1.67	1.31 ± 0.08	0.04 ± 0.08	5.465
038	NGC2683	-1.16	22.88 ± 6.34	-2.22 ± 0.37	2.341	-1.01	8.98 ± 5.54	-1.42 ± 0.61	1.920
039	NGC4013	-1.71	50.21 ± 7.95	-3.05 ± 0.24	0.813	-1.70	50.29 ± 8.58	-3.05 ± 0.20	0.807
040	NGC7814	-1.44	16.41 ± 2.55	-1.95 ± 0.21	0.604	-1.42	11.53 ± 2.29	-1.63 ± 0.20	0.542
041	UGC06786	-1.50	15.37 ± 2.66	-1.89 ± 0.23	0.952	-1.57	7.63 ± 1.40	-1.34 ± 0.19	0.844
042	NGC3877	-1.39	16.31 ± 4.59	-2.13 ± 0.37	7.276	-1.96	1.23 ± 0.24	-0.14 ± 0.21	2.059
043	NGC0289	-1.34	28.19 ± 7.19	-2.48 ± 0.35	2.078	-1.24	46.44 ± 27.24	-2.86 ± 0.59	1.977

Table 3.3 – Continued

SPARC ID	Galaxy Name	$\log(\frac{m_\star}{M_{\text{halo}}})$	r_s kpc	$\log \rho_s$ [$M_\odot \text{ pc}^{-3}$]	χ^2_ν	$\log(\frac{m_\star}{M_{\text{halo}}})$	r_s kpc	$\log \rho_s$ [$M_\odot \text{ pc}^{-3}$]	χ^2_ν
044	NGC1090	-1.43	25.89 ± 8.20	-2.56 ± 0.42	3.154	-1.98	1.21 ± 0.13	-0.14 ± 0.12	0.923
045	NGC3726	-1.89	56.42 ± 17.52	-3.16 ± 0.53	2.550	-2.06	61.70 ± 26.80	-3.15 ± 0.66	2.494
046	UGC09037	-1.72	18.79 ± 3.51	-2.44 ± 0.27	1.710	-1.77	12.39 ± 3.41	-2.09 ± 0.29	1.324
047	NGC6946	-1.46	25.55 ± 5.59	-2.55 ± 0.31	1.745	-1.46	20.19 ± 5.04	-2.35 ± 0.27	1.754
048	NGC4100	-1.28	22.11 ± 5.38	-2.18 ± 0.32	1.335	-1.23	16.05 ± 6.77	-1.91 ± 0.42	1.311
049	NGC3893	-1.48	19.10 ± 4.37	-2.27 ± 0.32	1.862	-1.49	9.11 ± 4.98	-1.63 ± 0.55	1.152
050	UGC06973	-1.75	6.33 ± 1.09	-1.44 ± 0.25	4.375	-1.85	3.15 ± 0.91	-0.86 ± 0.33	1.765
051	ESO079-G014	-1.66	28.84 ± 7.86	-2.63 ± 0.38	3.859	-2.28	2.28 ± 0.65	-0.64 ± 0.30	0.950
052	UGC08699	-1.42	28.46 ± 6.22	-2.56 ± 0.31	0.724	-1.42	29.33 ± 9.75	-2.58 ± 0.35	0.723
053	NGC4138	-1.31	20.84 ± 7.31	-2.22 ± 0.55	6.718	-1.03	5.47 ± 5.87	-1.08 ± 1.06	5.267
054	NGC3198	-1.50	10.32 ± 1.86	-1.91 ± 0.24	1.551	-1.62	5.53 ± 1.14	-1.43 ± 0.21	1.242
055	NGC3949	-1.44	19.39 ± 6.07	-2.45 ± 0.46	1.731	-2.71	23.30 ± 11.05	-2.00 ± 0.67	0.852
056	NGC6015	-1.37	22.51 ± 5.41	-2.43 ± 0.32	8.256	-1.37	23.60 ± 10.06	-2.47 ± 0.42	8.259
057	NGC3917	-1.63	33.86 ± 11.19	-2.97 ± 0.54	3.270	-2.19	2.00 ± 0.56	-0.76 ± 0.28	1.518
058	NGC4085	-1.61	12.79 ± 3.41	-2.28 ± 0.37	13.690	-2.05	7.05 ± 6.30	-1.65 ± 1.40	6.989
059	NGC4389	-1.67	13.38 ± 3.79	-2.55 ± 0.39	23.928	-2.70	9.50 ± 4.38	-1.69 ± 0.63	8.280
060	NGC4559	-1.55	14.20 ± 3.81	-2.42 ± 0.36	0.320	-1.64	5.90 ± 2.54	-1.72 ± 0.44	0.212
061	NGC3769	-1.52	12.73 ± 2.84	-2.30 ± 0.30	1.205	-1.57	7.74 ± 3.00	-1.90 ± 0.39	0.837
062	NGC4010	-1.71	14.48 ± 3.23	-2.39 ± 0.32	2.847	-1.85	9.46 ± 4.77	-2.04 ± 0.71	2.285
063	NGC3972	-1.62	14.04 ± 3.48	-2.33 ± 0.34	2.040	-1.78	6.80 ± 2.70	-1.75 ± 0.50	1.194
064	UGC03580	-1.82	8.82 ± 1.28	-2.08 ± 0.20	2.496	-1.87	6.65 ± 1.09	-1.83 ± 0.18	2.471
065	NGC6503	-1.53	6.66 ± 0.57	-1.78 ± 0.11	1.597	-1.54	5.94 ± 0.54	-1.69 ± 0.09	1.555
066	UGC11557	-1.72	13.35 ± 4.20	-2.62 ± 0.47	1.393	-2.31	4.29 ± 3.70	-1.08 ± 1.17	0.518
067	UGC00128	-1.49	17.35 ± 3.01	-2.56 ± 0.24	3.896	-1.50	16.65 ± 3.83	-2.53 ± 0.24	3.908
068	F579-V1	-1.36	11.61 ± 3.47	-2.10 ± 0.40	0.620	-1.59	3.02 ± 2.03	-0.93 ± 0.73	0.207
069	NGC4183	-1.43	13.26 ± 3.68	-2.35 ± 0.37	0.245	-1.48	7.63 ± 3.65	-1.93 ± 0.47	0.208
070	F571-8	-2.26	6.98 ± 1.07	-1.80 ± 0.21	2.306	-2.62	2.67 ± 0.74	-0.94 ± 0.28	0.480
071	NGC2403	-1.65	6.62 ± 0.36	-1.77 ± 0.08	10.258	-1.65	6.40 ± 0.36	-1.73 ± 0.07	10.247
072	UGC06930	-1.53	12.25 ± 3.45	-2.40 ± 0.38	0.634	-1.61	6.12 ± 3.69	-1.80 ± 0.62	0.330
073	F568-3	-1.84	12.44 ± 3.07	-2.54 ± 0.35	2.582	-2.48	5.58 ± 1.64	-1.30 ± 0.38	1.043
074	UGC01230	-1.56	10.71 ± 3.07	-2.30 ± 0.39	1.683	-2.30	3.57 ± 2.21	-0.98 ± 0.86	0.321
075	NGC0247	-1.59	11.03 ± 2.01	-2.37 ± 0.25	1.892	-1.62	8.93 ± 1.73	-2.22 ± 0.20	1.895
076	NGC7793	-1.64	13.45 ± 2.85	-2.61 ± 0.29	0.892	-1.55	10.82 ± 8.35	-2.42 ± 0.91	0.892
077	UGC06917	-1.65	9.89 ± 2.22	-2.24 ± 0.30	1.028	-1.77	5.18 ± 1.62	-1.74 ± 0.32	0.581
078	NGC1003	-1.75	21.67 ± 3.63	-2.91 ± 0.23	2.640	-1.74	24.31 ± 5.29	-3.00 ± 0.22	2.638
079	F574-1	-1.68	7.84 ± 1.73	-2.10 ± 0.30	1.387	-1.89	4.30 ± 1.69	-1.53 ± 0.43	0.532
080	F568-1	-1.68	9.73 ± 2.35	-2.27 ± 0.33	0.912	-2.10	4.20 ± 1.94	-1.33 ± 0.55	0.221
081	UGC06983	-1.59	8.89 ± 2.09	-2.14 ± 0.31	0.792	-1.74	4.11 ± 1.17	-1.54 ± 0.29	0.580
082	UGC05986	-1.78	9.76 ± 2.99	-2.17 ± 0.42	3.583	-2.36	1.34 ± 0.29	-0.58 ± 0.22	1.305
083	NGC0055	-1.96	7.91 ± 0.87	-2.31 ± 0.15	0.773	-1.99	7.55 ± 0.90	-2.27 ± 0.13	0.705
084	ESO116-G012	-1.80	7.97 ± 1.72	-2.09 ± 0.29	1.447	-2.03	2.96 ± 0.99	-1.29 ± 0.34	0.839
085	UGC07323	-1.79	12.00 ± 3.27	-2.57 ± 0.37	0.578	-1.98	7.84 ± 10.00	-2.17 ± 2.00	0.314
086	UGC05005	-1.88	12.52 ± 3.10	-2.73 ± 0.34	0.137	-2.02	11.91 ± 13.90	-2.58 ± 1.58	0.040

Table 3.3 – Continued

SPARC ID	Galaxy Name	$\log(\frac{m_\star}{M_{\text{halo}}})$	r_s kpc	$\log \rho_s$ [$M_\odot \text{ pc}^{-3}$]	χ^2_ν	$\log(\frac{m_\star}{M_{\text{halo}}})$	r_s kpc	$\log \rho_s$ [$M_\odot \text{ pc}^{-3}$]	χ^2_ν
087	F561-1	-1.76	11.06 ± 3.25	-2.56 ± 0.40	3.947	-0.96	9.50 ± 51.41	-2.53 ± 5.87	1.562
088	NGC0024	-1.55	10.18 ± 2.18	-2.22 ± 0.30	0.572	-1.76	1.97 ± 0.44	-0.88 ± 0.22	0.759
089	F568-V1	-1.67	7.41 ± 1.85	-2.09 ± 0.34	0.403	-1.97	3.31 ± 1.96	-1.28 ± 0.72	0.087
090	UGC06628	-1.74	12.69 ± 3.98	-2.66 ± 0.43	2.023	-0.80	2.74 ± 6.42	-1.46 ± 3.01	0.308
091	UGC02455	-2.20	5.19 ± 1.40	-2.15 ± 0.37	7.381	-3.06	1.15 ± 0.49	-0.60 ± 0.57	2.622
092	UGC07089	-1.86	10.69 ± 2.24	-2.58 ± 0.29	0.173	-1.94	10.88 ± 15.68	-2.55 ± 2.29	0.128
093	UGC05999	-1.89	10.16 ± 2.56	-2.57 ± 0.35		-2.48	6.72 ± 4.76	-1.78 ± 1.02	
094	NGC2976	-1.83	11.38 ± 3.31	-2.59 ± 0.39	0.778	-2.51	5.15 ± 2.10	-1.45 ± 0.57	0.398
095	UGC05750	-1.90	10.62 ± 2.57	-2.61 ± 0.33	0.575	-2.03	8.52 ± 4.43	-2.39 ± 0.55	0.428
096	NGC0100	-1.87	9.09 ± 2.13	-2.35 ± 0.32	0.376	-2.05	3.62 ± 2.24	-1.63 ± 0.66	0.176
097	UGC00634	-1.87	10.57 ± 2.53	-2.56 ± 0.33		-2.18	6.47 ± 3.30	-2.01 ± 0.55	
098	F563-V2	-1.73	9.91 ± 2.82	-2.42 ± 0.38	1.221	-2.34	2.54 ± 1.40	-0.90 ± 0.76	0.291
099	NGC5585	-1.90	7.32 ± 1.21	-2.20 ± 0.22	5.819	-1.96	5.30 ± 1.07	-1.93 ± 0.21	5.704
100	NGC0300	-1.79	8.55 ± 2.05	-2.37 ± 0.32	0.573	-1.89	4.91 ± 1.57	-1.83 ± 0.34	0.502
101	UGC06923	-1.81	8.49 ± 1.90	-2.32 ± 0.30	3.998	-1.89	4.74 ± 8.59	-1.85 ± 2.89	2.485
102	F574-2	-1.93	12.19 ± 3.41	-2.78 ± 0.38		-0.27	238 ± 30222	-5.62 ± 128.17	
103	UGC07125	-1.78	7.99 ± 3.11	-2.54 ± 0.52	1.613	-1.81	3.77 ± 1.68	-1.97 ± 0.44	0.269
104	UGC07524	-1.85	5.42 ± 0.75	-2.03 ± 0.19	0.319	-1.87	4.81 ± 0.72	-1.96 ± 0.16	0.265
105	UGC06399	-1.82	7.52 ± 1.61	-2.21 ± 0.29	0.505	-1.95	4.26 ± 1.20	-1.77 ± 0.30	0.294
106	UGC07151	-1.73	11.26 ± 1.91	-2.57 ± 0.24	2.581	-1.62	4.51 ± 1.64	-1.88 ± 0.42	3.506
107	F567-2	-1.91	9.62 ± 2.75	-2.57 ± 0.38		-1.72	4.01 ± 9.18	-1.83 ± 3.21	
108	UGC04325	-1.51	7.36 ± 2.41	-2.03 ± 0.44	6.207	-2.19	0.80 ± 0.16	-0.32 ± 0.23	0.802
109	UGC00191	-1.60	9.17 ± 3.23	-2.32 ± 0.47	4.856	-1.80	2.66 ± 0.88	-1.44 ± 0.35	4.111
110	F563-1	-1.88	7.50 ± 1.72	-2.27 ± 0.31	0.994	-2.39	3.44 ± 1.36	-1.40 ± 0.48	0.683
111	F571-V1	-1.97	8.95 ± 2.23	-2.55 ± 0.34	0.491	-2.07	6.19 ± 7.25	-2.15 ± 1.54	0.183
112	UGC07261	-1.87	12.46 ± 3.84	-2.78 ± 0.42	2.804	-1.54	3.12 ± 4.28	-1.61 ± 1.50	0.192
113	UGC10310	-1.76	9.56 ± 2.96	-2.47 ± 0.42	3.126	-1.85	2.55 ± 2.08	-1.46 ± 0.85	0.612
114	UGC02259	-1.48	7.65 ± 2.40	-2.08 ± 0.42	2.641	-1.63	2.55 ± 1.03	-1.31 ± 0.40	1.783
115	F583-4	-1.89	10.39 ± 2.66	-2.63 ± 0.35	0.528	-1.73	5.63 ± 7.44	-2.20 ± 1.93	0.253
116	UGC12732	-1.73	9.70 ± 2.12	-2.48 ± 0.30	0.316	-1.68	7.87 ± 2.66	-2.41 ± 0.36	0.180
117	UGC06818	-2.11	6.92 ± 1.21	-2.31 ± 0.24	4.143	-2.70	8.37 ± 3.40	-2.16 ± 0.59	2.245
118	UGC04499	-1.81	9.16 ± 2.65	-2.51 ± 0.39	1.962	-2.01	2.53 ± 1.71	-1.52 ± 0.67	0.462
119	F563-V1	-2.20	11.65 ± 3.19	-2.96 ± 0.37	4.856	-0.29	11.2 ± 130.1	-3.48 ± 12.70	1.137
120	UGC06667	-1.94	4.92 ± 0.78	-1.91 ± 0.22	0.544	-2.11	3.24 ± 0.67	-1.58 ± 0.21	0.206
121	UGC02023	-2.08	9.30 ± 2.66	-2.65 ± 0.39		-2.74	7.13 ± 9.38	-1.93 ± 1.73	
122	UGC04278	-2.05	7.97 ± 1.40	-2.31 ± 0.24	0.845	-3.48	23.59 ± 12.69	-2.42 ± 0.61	0.506
123	UGC12632	-1.84	5.48 ± 1.35	-2.10 ± 0.33	0.457	-1.91	2.96 ± 1.54	-1.68 ± 0.51	0.092
124	UGC08286	-1.96	2.10 ± 0.34	-1.25 ± 0.21	1.578	-1.98	1.89 ± 0.19	-1.17 ± 0.10	1.399
125	UGC07399	-1.74	5.70 ± 1.24	-1.89 ± 0.29	1.238	-2.00	1.89 ± 0.65	-1.01 ± 0.34	0.863
126	NGC4214	-2.10	6.96 ± 1.09	-2.41 ± 0.22	1.328	-1.73	3.63 ± 5.23	-1.90 ± 1.94	1.088
127	UGC05414	-2.00	8.73 ± 2.07	-2.52 ± 0.32	0.583	-2.03	4.75 ± 6.86	-2.06 ± 2.21	0.424
128	UGC08490	-1.64	6.06 ± 1.70	-2.10 ± 0.37	0.348	-1.75	1.95 ± 0.46	-1.19 ± 0.24	0.150
129	IC2574	-2.33	9.69 ± 0.75	-2.68 ± 0.12	2.443	-3.14	22.47 ± 3.23	-2.84 ± 0.19	2.171

Table 3.3 – Continued

SPARC ID	Galaxy Name	$\log(\frac{m_\star}{M_{\text{halo}}})$	r_s kpc	$\log \rho_s$ [$M_\odot \text{ pc}^{-3}$]	χ^2_ν	$\log(\frac{m_\star}{M_{\text{halo}}})$	r_s kpc	$\log \rho_s$ [$M_\odot \text{ pc}^{-3}$]	χ^2_ν
130	UGC06446	-1.72	6.49 ± 1.87	-2.15 ± 0.39	0.611	-1.84	2.74 ± 1.09	-1.50 ± 0.40	0.287
131	F583-1	-2.13	5.68 ± 1.00	-2.14 ± 0.24	0.390	-2.42	3.51 ± 1.05	-1.70 ± 0.31	0.184
132	UGC11820	-1.84	13.50 ± 2.81	-2.86 ± 0.29	2.873	-1.77	17.80 ± 6.41	-3.14 ± 0.40	2.534
133	UGC07690	-1.98	11.68 ± 2.62	-2.80 ± 0.31	2.045	-1.47	1.19 ± 0.85	-0.89 ± 0.75	0.940
134	UGC04305	-2.10	17.20 ± 3.70	-3.24 ± 0.29	2.119	-2.38	1.05 ± 0.39	-0.43 ± 0.49	0.924
135	NGC2915	-2.26	2.47 ± 0.30	-1.43 ± 0.16	0.758	-2.39	1.85 ± 0.27	-1.13 ± 0.16	0.526
136	UGC05716	-1.86	6.60 ± 0.96	-2.29 ± 0.21	2.433	-1.79	5.48 ± 1.02	-2.32 ± 0.21	2.123
137	UGC05829	-2.10	7.12 ± 1.80	-2.44 ± 0.35	0.513	-4.93	1270 ± 22004	-4.83 ± 17.58	0.128
138	F565-V2	-2.19	6.22 ± 1.22	-2.31 ± 0.27	0.423	-2.60	4.42 ± 4.32	-1.88 ± 1.50	0.127
139	DDO161	-2.30	7.39 ± 1.34	-2.57 ± 0.25	0.257	-2.33	6.91 ± 1.84	-2.51 ± 0.27	0.250
140	DDO170	-2.19	4.65 ± 1.03	-2.16 ± 0.31	3.184	-2.38	2.57 ± 1.27	-1.73 ± 0.49	2.469
141	NGC1705	-1.88	4.23 ± 0.70	-1.82 ± 0.23	0.905	-1.79	0.79 ± 0.17	-0.47 ± 0.22	0.388
142	UGC05721	-1.84	3.29 ± 0.81	-1.61 ± 0.33	1.012	-2.09	1.04 ± 0.27	-0.68 ± 0.26	0.441
143	UGC08837	-2.37	6.15 ± 0.77	-2.42 ± 0.18	1.647	-2.71	7.72 ± 2.31	-2.39 ± 0.44	1.182
144	UGC07603	-2.03	6.04 ± 1.28	-2.26 ± 0.29	1.558	-2.28	1.13 ± 0.41	-0.97 ± 0.36	0.268
145	UGC00891	-2.32	6.68 ± 1.32	-2.45 ± 0.27		-2.51	4.43 ± 1.85	-2.08 ± 0.43	
146	UGC01281	-2.40	3.62 ± 0.38	-1.93 ± 0.16	0.216	-2.33	3.07 ± 1.15	-1.84 ± 0.58	0.165
147	UGC09992	-2.40	8.65 ± 2.38	-2.80 ± 0.38		-1.08	1.39 ± 3.59	-1.31 ± 3.65	
148	D512-2	-2.23	8.25 ± 2.19	-2.67 ± 0.36		-1.74	2.53 ± 8.43	-1.99 ± 5.23	
149	UGC00731	-2.16	3.40 ± 0.52	-1.87 ± 0.21	0.684	-2.05	2.94 ± 1.06	-1.78 ± 0.35	0.281
150	UGC08550	-1.95	9.42 ± 1.61	-2.68 ± 0.24	1.621	-1.90	1.88 ± 0.73	-1.50 ± 0.39	0.822
151	UGC07608	-2.34	6.41 ± 1.77	-2.48 ± 0.37	0.831	-2.54	2.64 ± 2.88	-1.60 ± 1.63	0.178
152	NGC2366	-2.47	2.40 ± 0.25	-1.74 ± 0.15	0.877	-2.36	2.22 ± 0.25	-1.75 ± 0.13	0.781
153	NGC4068	-2.50	4.92 ± 1.00	-2.31 ± 0.28	2.088	-2.76	4.49 ± 2.62	-2.04 ± 0.85	1.259
154	UGC05918	-2.27	6.34 ± 1.85	-2.47 ± 0.39	4.396	-1.89	1.95 ± 1.53	-1.74 ± 0.84	0.082
155	D631-7	-2.71	4.31 ± 0.31	-2.13 ± 0.11	2.052	-2.98	5.68 ± 0.83	-2.18 ± 0.20	1.431
156	NGC3109	-2.59	4.02 ± 0.29	-1.99 ± 0.11	0.290	-2.88	4.50 ± 0.61	-1.96 ± 0.19	0.194
157	UGCA281	-2.32	3.74 ± 0.73	-1.95 ± 0.27	1.521	-1.74	1.38 ± 6.15	-1.52 ± 7.21	0.848
158	DDO168	-2.60	2.95 ± 0.29	-1.79 ± 0.14	7.005	-2.73	2.79 ± 0.42	-1.65 ± 0.20	6.119
159	DDO064	-2.36	5.18 ± 1.26	-2.28 ± 0.33	0.613	-2.35	1.77 ± 2.23	-1.54 ± 1.96	0.413
160	PGC51017	-2.66	11.04 ± 1.99	-3.17 ± 0.25	12.634	-0.71	4.60 ± 12.08	-3.10 ± 4.07	7.186
161	UGCA442	-2.61	2.80 ± 0.29	-1.85 ± 0.15	1.367	-2.58	2.54 ± 0.35	-1.76 ± 0.16	1.119
162	UGC07866	-2.62	4.65 ± 0.89	-2.31 ± 0.26	1.261	-1.78	1.67 ± 7.74	-1.86 ± 7.50	0.108
163	UGC07232	-2.50	5.23 ± 3.11	-2.37 ± 0.78		-2.81	1.33 ± 0.71	-0.98 ± 0.79	
164	UGC07559	-2.69	4.33 ± 0.62	-2.27 ± 0.20	0.922	-2.16	2.39 ± 4.13	-2.10 ± 2.76	0.360
165	NGC6789	-2.48	6.41 ± 3.32	-2.56 ± 0.68		-3.11	1.17 ± 0.61	-0.57 ± 0.72	
166	KK98-251	-2.65	5.96 ± 1.41	-2.57 ± 0.32	0.397	-2.48	3.41 ± 2.30	-2.28 ± 0.94	0.399
167	UGC05764	-2.46	1.55 ± 0.22	-1.23 ± 0.20	4.245	-2.47	0.93 ± 0.33	-0.96 ± 0.49	4.051
168	CamB	-2.93	5.02 ± 0.78	-2.54 ± 0.22	4.371	-2.71	3.88 ± 1.35	-2.48 ± 0.49	4.255
169	ESO444-G084	-2.64	2.81 ± 0.67	-1.89 ± 0.32	5.044	-4.10	32.76 ± 32.92	-2.96 ± 1.51	1.949
170	DDO154	-2.87	2.51 ± 0.14	-1.86 ± 0.08	1.621	-2.84	2.44 ± 0.14	-1.84 ± 0.07	1.655
171	UGC07577	-2.97	6.14 ± 1.08	-2.73 ± 0.24	0.289	-2.71	5.43 ± 4.02	-2.81 ± 1.10	0.232
172	D564-8	-3.01	4.44 ± 0.57	-2.44 ± 0.19	2.976	-2.38	1.98 ± 1.75	-2.17 ± 1.37	0.332

Table 3.3 – Continued

SPARC ID	Galaxy Name	$\log(\frac{m_\star}{M_{\text{halo}}})$	r_s kpc	$\log \rho_s$ [$M_\odot \text{ pc}^{-3}$]	χ^2_v	$\log(\frac{m_\star}{M_{\text{halo}}})$	r_s kpc	$\log \rho_s$ [$M_\odot \text{ pc}^{-3}$]	χ^2_v
173	NGC3741	-3.01	2.88 ± 0.23	-1.93 ± 0.12	0.871	-4.11	31.55 ± 15.48	-3.22 ± 0.70	0.430
174	UGC04483	-3.22	2.79 ± 0.38	-1.99 ± 0.20	3.645	-2.23	0.51 ± 4.29	-1.19 ± 13.61	0.510
175	UGCA444	-3.36	2.45 ± 0.28	-1.87 ± 0.17	0.171	-6.49	1571 ± 4891	-5.01 ± 3.17	0.065

Chapter 4

The Halo Mass Function of Late-type Galaxies from H I kinematics

4.1 Abstract

We present an empirical method to measure the halo mass function (HMF) of galaxies. We determine the relation between the HI line-width from single-dish observations and the dark matter halo mass (M_{200}) inferred from rotation curve fits in the SPARC database, then we apply this relation to galaxies from the HI Parkes All Sky Survey (HIPASS) to derive the HMF. This empirical HMF is well fit by a Schechter function, and matches that expected in Λ CDM over the range $10^{10.5} < M_{200} < 10^{12} M_{\odot}$. More massive halos must be poor in neutral gas to maintain consistency with the power law predicted by Λ CDM. We detect no discrepancy at low masses. The lowest halo mass probed by HIPASS, however, is just greater than the mass scale where the Local Group missing satellite problem sets in. The integrated mass density associated with the dark matter halos of HI-detected galaxies sums to $\Omega_{\text{m,gal}} \approx 0.03$ over the probed mass range.

4.2 Introduction

The standard Λ Cold Dark Matter (Λ CDM) model predicts the abundance of dark matter (DM) halos, which is quantified by the halo mass function (HMF) $\psi(M_{\text{halo}})$, i.e., the number density of halos at a given halo mass. The analytic prediction (Press & Schechter 1974b) for $\psi(M_{\text{halo}})$ is reproduced by N-body simulations of structure formation (Warren et al. 2006; Boylan-Kolchin et al. 2009). However, it is a challenge to compare the predicted HMF to observations since halo masses are hard to measure for individual galaxies, much less for a large sample.

Quantities accessible to observation include the luminosity and velocity functions of galaxies. These quantify the number density of galaxies as a function of luminosity and rotation speed, respectively. By adopting some prescription to estimate the mass-to-light ratios of stellar populations, the luminosity function can be transformed into the Stellar Mass Function (SMF). A simple comparison between the observed SMF and the Λ CDM prediction can be made by scaling the HMF by the cosmic baryonic fraction $f_b \approx 0.15$. This reveals a discrepancy at both high and low masses: the predicted HMF is a power law (since Λ CDM is scale-free), while the observed SMF is a Schechter function with a characteristic scale at $M_\star \simeq 10^{10.5} M_\odot$. This implies a non-linear variation of the stellar mass with halo mass that is attributed to feedback processes (Bullock & Boylan-Kolchin 2017). Abundance matching (e.g., Behroozi et al. 2010; Moster et al. 2013) quantifies this variation by requiring a correspondence between the observed number density of galaxies and the expected number density of dark matter halos as a function of mass.

An independent approach is to consider the velocity function (VF) of galaxies, which probes more directly the galaxy potential well. Theoretically, the VF of galaxies can be constructed considering the maximum rotation velocity of DM halos ($V_{\text{max}}^{\text{DM}}$). Observationally, blind HI surveys with single-dish radio telescopes provide the spatially integrated HI line-width (W_{HI}), which is a proxy for twice the rotation velocity of galaxies. The VF from HI surveys is well-described by a modified Schechter function and differs from the one predicted in Λ CDM via $V_{\text{max}}^{\text{DM}}$ (e.g., Zwaan et al. 2010; Papastergis et al. 2011) with possible implications for cosmology and the nature of DM (Zavala et al. 2009; Klypin et al. 2015; Schneider et al. 2017; Schneider & Trujillo-Gomez 2018). The comparison between theory and observations, however, is complex because the relation between $V_{\text{max}}^{\text{DM}}$ and W_{HI}

may be strongly non-linear (e.g., Brook & Shankar 2016; Macciò et al. 2016; Brooks et al. 2017; Chauhan et al. 2019; Dutton et al. 2019).

In this letter, we present a new empirical method to directly measure the HMF of galaxies. We use 168 late-type galaxies from the Spitzer Photometry & Accurate Rotation Curves (SPARC) database (Lelli et al. 2016a) to determine the relation between the HI line width from single-dish observations and the halo mass from rotation-curve fits. This provides a tool to estimate halo masses from HI line widths, and thereby translate the VF into the HMF. We apply this method to galaxies from the HI Parkes All Sky Survey (HIPASS) catalogue (Meyer et al. 2004) and provide the first direct comparison between the predicted and measured HMFs.

4.3 Data

4.3.1 The HIPASS Galaxy Sample

We use the sample of 1388 late-type galaxies with optical IDs and inclination larger than 45° (Zwaan et al. 2010) selected from the HI Parkes All Sky Survey (HIPASS) galaxy catalogue (Meyer et al. 2004). Zwaan et al. (2004) show that the completeness of this sample is 99% at a peak flux of 84 mJy and at an integrated flux of 9.4 Jy km s^{-1} . This enables the measurement of galaxy abundance once the volume correction is appropriately taken into account. Zwaan et al. (2010) use these data to measure the VF. We utilize these same data to measure the HMF, using an effective conversion between HI line width and DM halo mass.

4.3.2 SPARC Rotation Curve Fits

The SPARC sample (Lelli et al. 2016a) has measurements of rotation curves from spatially resolved interferometric data as well as HI line widths spatially unresolved single-dish observations (Lelli et al. 2019). It includes 175 late-type galaxies with HI/H α rotation curves traced to large radii, which constrain galaxy dynamical masses. This provides a way to explore the correlation between HI line width and DM halo mass.

Li et al. (2019) fit SPARC rotation curves using two simulation-motivated halo profiles, the Einasto (Einasto 1965; Navarro et al. 2004) and DC14 (Di Cintio et al. 2014a) profiles. These fits provide an estimate of the halo mass M_{200} defined at the mass enclosed within an overdensity 200 times the critical density of the Universe. The fits were made imposing as priors the Λ CDM halo mass–concentration relation (Dutton & Macciò 2014) and the stellar mass–halo mass relation (Moster et al. 2013). We discuss the role of the latter in section 4.5.

For reference, we also fit the commonly used NFW profile (Navarro et al. 1996b) and derive halo masses following the same procedure, although it is well known that the NFW profile does not provide satisfactory fits to the rotation curves (Katz et al. 2017). The halo masses for the NFW profile thereby are less reliable than for the other profiles.

4.3.3 The Single-Dish H I Line Widths

The H I line widths for the SPARC galaxies are collected by Lelli et al. (2019), mainly from the Extragalactic Distance Database (Tully et al. 2009) but also from other references (e.g., Springob et al. 2005; Huchtmeier & Richter 1989). In total, 168 out of 175 galaxies have the line-width measurements at 20% of the peak flux density, i.e., W_{P20} . To translate W_{P20} to the W_{P50} used by the HIPASS team (Zwaan et al. 2010), we adopt the conversion established by Courtois et al. (2009),

$$W_{P50} = W_{P20} - 26 \text{ km/s.} \quad (4.1)$$

This relation has an rms scatter of 21 km/s, which we propagate into the uncertainty in W_{P50} . Although W_{P20} is also available in the HIPASS survey, Zwaan et al. (2010) use W_{P50} because it is less sensitive to noise in the H I spectra. Thus, we adopt the same approach of Zwaan et al. (2010) for the HIPASS galaxies and simply convert W_{P20} into W_{P50} for the SPARC galaxies.

The measured line widths are projected along the line of sight. To recover the intrinsic widths, one has to correct the measurements for inclinations via $W_{P50}^i = W_{P50}/\sin i$. Optically defined inclinations have been extensively used for this purpose, since single-dish surveys cannot resolve the H I distribution. Following the standard procedure (Zwaan et al.

2010), we calculate optical inclinations for the SPARC galaxies according to

$$\cos^2 i = \frac{q^2 - q_0^2}{1 - q_0^2}, \quad (4.2)$$

where q is the axial ratio and $q_0 = 0.2$ accounts for the thickness of stellar disks. We measure the axial ratio from the outer isophotes of the [3.6] images based on those ellipses whose values differ from their mean by less than 20%. SPARC galaxies have well measured kinematic inclinations, but we use the optical inclinations for internal consistency with HIPASS. The results are insensitive to the choice of which inclination we use.

4.4 Results

4.4.1 The Halo Mass–Line Width Correlation

In Figure 4.1, we plot halo mass, M_{200} , against line width, $W_{P50}^i/2$. A strong correlation between M_{200} and $W_{P50}^i/2$ is apparent for each halo model. We use the Gaussian Process Regression (GPR) from the open python package *scikit – learn* (Pedregosa et al. 2011) to capture the mean relation (solid lines in Figure 4.1). The shaded areas show the estimated standard deviations smoothed by the GPR algorithm.

This correlation has a well understood physical background. Roughly speaking, the inclination-corrected HI line widths correspond to twice the rotation velocities since the SPARC galaxies are rotationally supported. The rotation velocity in the outer galaxy regions is mostly driven by the DM halo, thus one expects a correlation between W_{50} and M_{200} . We can thus assign a halo mass to galaxies based on their much more readily measured line width. This enables us to map the HIPASS VF into any variable that correlates with line width.

4.4.2 Stellar Mass Function

To validate our method, we first derive the stellar mass function, which can be directly checked using the extensive measurements made with optical surveys (e.g., Moffett et al. 2016; Wright et al. 2017; Jones et al. 2018). To calculate the stellar masses of the SPARC

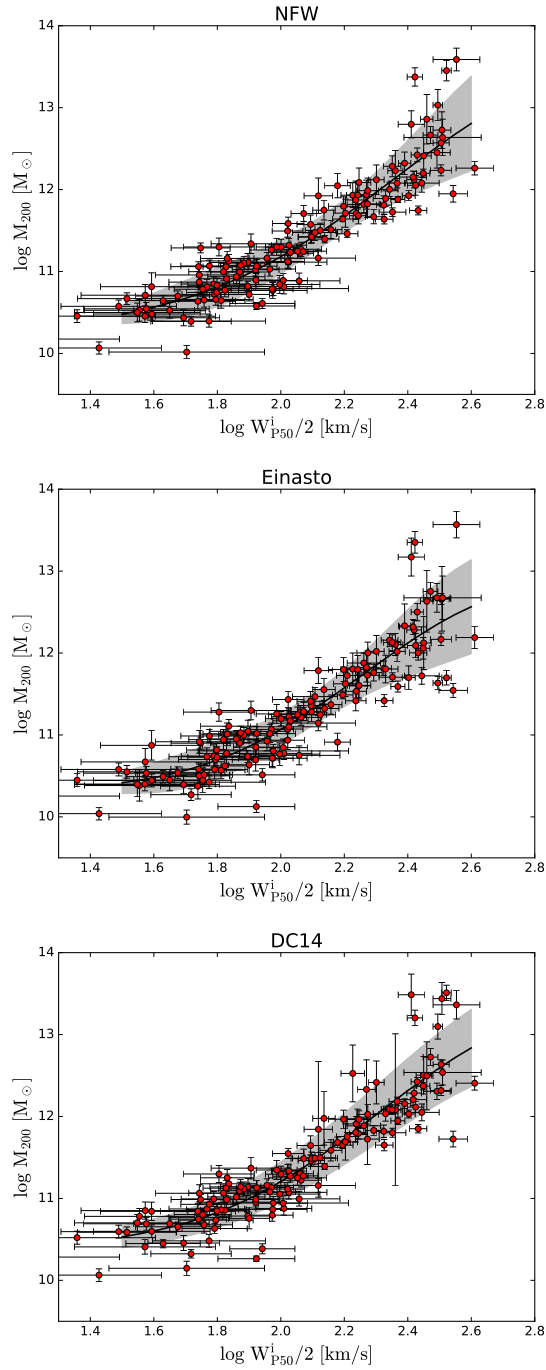


Figure 4.1 Correlations between halo mass, M_{200} , and inclination corrected HI-line widths, $W_{p50}^i/2$, for SPARC galaxies. Halo masses are calculated from rotation-curve fits using the NFW (top), Einasto (middle), and DC14 (bottom) profiles. Solid lines are the best fits using the Gaussian Process Regression (GPR) algorithm and the shaded regions represent the GPR smoothed standard deviations.

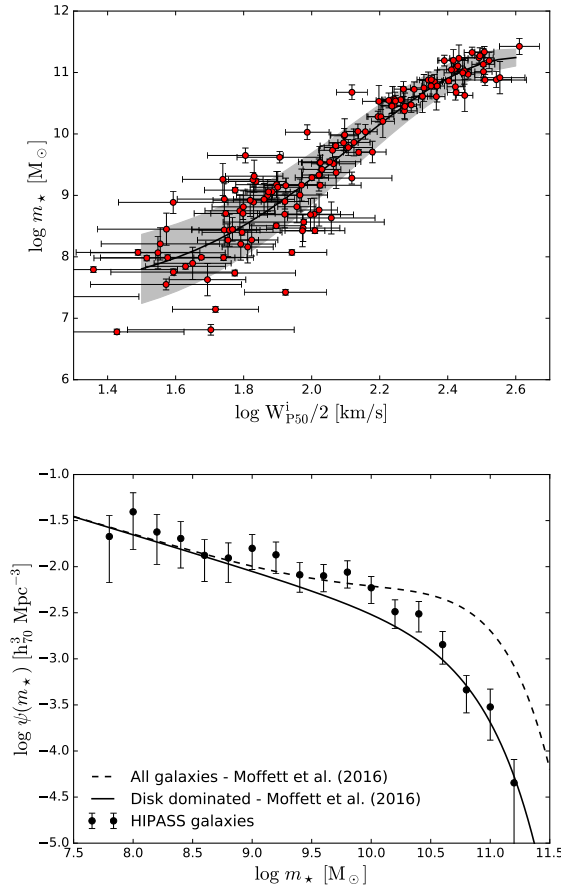


Figure 4.2 Top: same as Figure 4.1, but for the stellar masses of SPARC galaxies assuming $\Upsilon_{\text{disk}} = 0.5$ and $\Upsilon_{\text{bul}} = 0.7$. Bottom: the stellar mass function (points) measured by applying our method to HIPASS galaxies (Meyer et al. 2004; Zwaan et al. 2010). The stellar mass function for galaxies in the GAMA survey (Moffett et al. 2016) is shown as the dashed line. This includes gas poor early type galaxies; the SMF of disk type galaxies (solid line) is a better match to the SMF we derive from HIPASS, as expected.

galaxies, we adopt as fiducial values the [3.6] stellar mass-to-light ratios $\Upsilon_{\text{disk}} = 0.5$ and $\Upsilon_{\text{bul}} = 0.7$ (McGaugh et al. 2016b). The SPARC galaxies show a strong correlation between $\log m_{\star}$ and $\log W_{P50}^i/2$ as expected from the Tully & Fisher (1977) relation (see the left panel of Figure 4.2). We then use the best GPR fit to derive the stellar masses for each individual HIPASS galaxy from their HI line widths.

The effective volume V_{eff} for each HIPASS galaxy is derived using a bicariate stepwise maximum likelihood technique (Zwaan et al. 2004). After binning the data, we sum the values of $\frac{1}{V_{\text{eff}}}$ for galaxies within each bin following Zwaan et al. (2010). This gives the

stellar mass function. There are two sources for the uncertainties: one from the poisson distribution which is given by the square root of the summation of V_{eff}^{-2} , and the other one from the scatter of the $W_{\text{p50}}^i/2 - m_{\star}$ relation. To account for the latter, we add Gaussian noise (the standard deviation of the Gaussian noise is given by the scatter of the $W_{\text{p50}}^i/2 - m_{\star}$ relation) to the estimated stellar mass for each HIPASS galaxy and measure a new SMF. After 10000 random iterations, we calculate the standard deviations of 10000 HMFs and add them to the poisson errors in quadrature.

The result is plotted in Figure 4.2 together with the SMF measured by Moffett et al. (2016) from the Galaxy and Mass Assembly survey (Liske et al. 2015). Moffett et al. (2016) measured the SMFs for different morphologies. Disk dominated galaxies contain most of the cold gas in galaxies, so make the most direct comparison to H I-selected HIPASS galaxies. Figure 4.2 shows a satisfactory agreement between these two measurements covering the available mass range. This confirms that our method can measure a mass function, and match one that is independently measured by a completely different type of survey.

4.4.3 Halo Mass Function

Using the best GPR fits shown in Figure 4.1, we derived the halo masses of the HIPASS galaxies for the three profiles. Summing the values of V_{eff}^{-1} within each halo mass bin, we obtain the halo mass functions. We estimate the uncertainties using the same method as for the stellar mass function.

The HMFs for the NFW, Einasto, and DC14 profiles are shown in Figure 4.3. The bins are set to avoid being only partially covered by the data. They are similar in shape, given the similar $W_{\text{p50}}^i/2 - M_{200}$ correlations for the three halo profiles. The HMFs are well fit by the modified Schechter function,

$$\psi(M_{200}) = \psi_{\star} \left(\frac{M_{200}}{M_{\star}} \right)^{\alpha+1} \exp \left(- \frac{M_{200}}{M_{\star}} \right) \ln 10. \quad (4.3)$$

The corresponding parameters are listed in Table 4.1.

The integral of the Schechter function gives the mass density of DM associated with

Table 4.1. The best-fit parameters of the modified Schechter function for the NFW, Einasto and DC14 profiles.

Model	$\psi_{\star} \times 10^3$	$\log M_{\star}/M_{\odot}$	α	$\Omega_{\text{m,gal}}$
NFW	4.44 ± 0.84	11.86 ± 0.03	-1.57 ± 0.08	0.031
Einasto	3.93 ± 1.09	11.76 ± 0.05	-1.66 ± 0.10	0.023
DC14	3.60 ± 0.57	11.94 ± 0.02	-1.64 ± 0.06	0.034

Note. — $\Omega_{\text{m,gal}}$ is the integrated dark-matter mass density.

galaxies detected in HI:

$$\rho_{\text{DM}} = \psi_{\star} M_{\star} \left[\Gamma\left(\alpha + 2, \frac{M_{\text{up}}}{M_{\star}}\right) - \Gamma\left(\alpha + 2, \frac{M_{\text{low}}}{M_{\star}}\right) \right], \quad (4.4)$$

where $\Gamma(\alpha + 2, x) = \int_0^x x^{\alpha+1} e^{-x} dx$ is the incomplete Gamma function, and M_{up} and M_{low} are the upper and lower limits of the integrating masses, respectively. We calculate $\Omega_{\text{m,gal}} = \rho_{\text{DM}}/\rho_{\text{crit}}$ in the mass range between $10^{10.5}$ and $10^{12.5} M_{\odot}$. We find that the DM mass density in HI-detected galaxies is only about a tenth of the cosmic DM density in the probed mass range, as shown in Table 4.1. Even if we integrate the best-fit Schechter function from zero to infinity, the DM mass density is still smaller than 0.04. This suggests that most DM in the universe is not bound to HI-rich galaxies.

The empirical HMF that we derive is in reasonable agreement with theoretical expectations from Λ CDM for all halo types (Fig. 4.3). This holds at intermediate and low halo masses down to $\sim 10^{10.5} M_{\odot}$. Galaxies with lower masses are generally not observed in current, single-dish surveys (Papastergis et al. 2013; Guo et al. 2017) and hence are missing in the HIPASS sample.

A halo mass of $10^{10.5} M_{\odot}$ corresponds to a stellar mass of $\sim 10^8 M_{\odot}$. This is typical of low-mass dwarf Irregulars in the field, which are usually gas rich, often having more gas than stars (McGaugh et al. 2017). Consequently, this stellar mass may correspond to a wide range of baryonic masses (the sum of stars and gas). Though low mass, these galaxies are more massive than the satellite galaxies of the Local Group. Consequently, we may

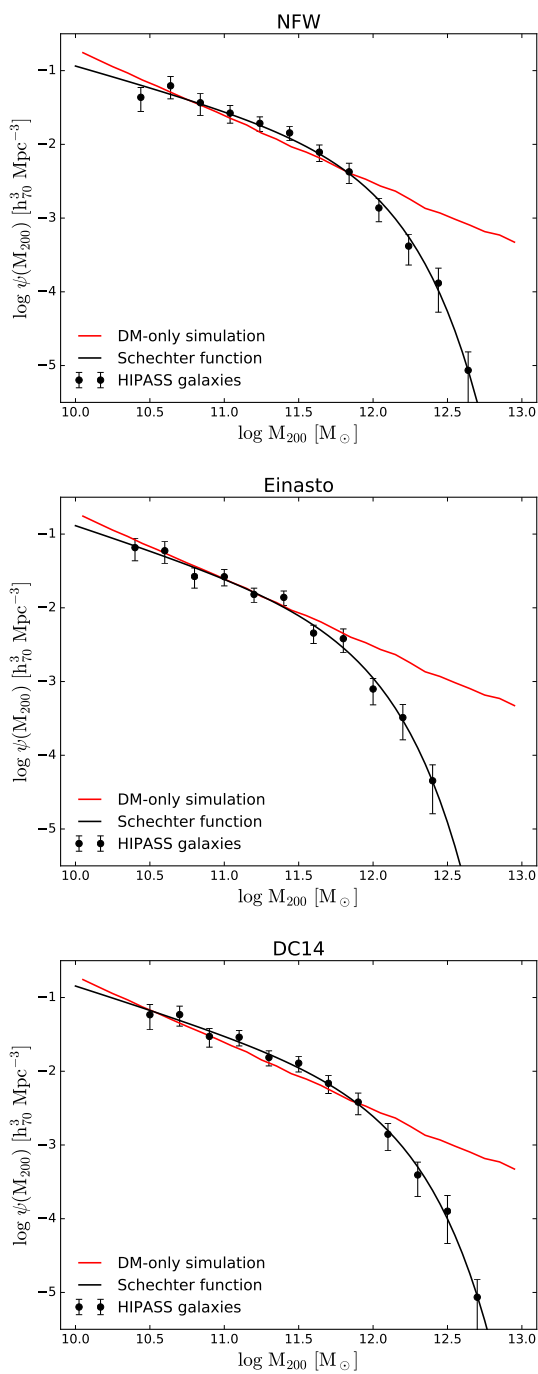


Figure 4.3 The halo mass functions measured using the HIPASS galaxies (Meyer et al. 2004; Zwaan et al. 2010) for the NFW (top), Einasto (middle) and DC14 (bottom) profiles. Solid black lines are the best-fit modified Schechter functions. Red lines represent the prediction of DM-only simulations (Springel et al. 2018a; Nelson et al. 2019).

not have reached the regime where the missing satellite problem takes hold (Tikhonov & Klypin 2009; Bullock & Boylan-Kolchin 2017).

At high masses, the VF of HIPASS galaxies truncates sharply above $W_{P50} > 200$ km/s (Figure 1 of Zwaan et al. 2010). Consequently, our empirical HMF shows a corresponding cut-off above $M_{200} = 10^{12} M_{\odot}$, comparable to the mass of the Milky Way. Intriguingly, the ALFALFA survey finds more high-widths galaxies than HIPASS and its VF truncates at slightly larger values of $W_{P50} > 300$ km/s (Papastergis et al. 2011). Thus, the ALFALFA data must still imply a cut-off in the empirical HMF, albeit at slightly larger halo masses. This may seem problematic compared to the predicted halo mass function, which continues as a power law. However, the sharp cut-off in the observed HMF does not preclude the existence of more massive halos, provided that they are HI poor. Early-type galaxies fit this description, and fill out the top end of the stellar mass function in Fig. 4.2. Further tests will require careful interrogation of hydrodynamical simulations that select mock galaxies in a way that matches the HIPASS survey. This is beyond the scope of the present work, so it remains an open question whether the current generation of simulations is consistent with these observations.

4.5 Discussion and conclusion

In this paper, we present an empirical method to derive the halo mass function of galaxies. We first determine the correlation between HI line width and DM halo mass as determined from rotation curve fits utilizing the NFW, Einasto, and DC14 halo models. We use this correlation to assign halo masses to galaxies detected in the HIPASS HI survey. It is then possible to map the observed velocity function to the actual halo mass function.

We detect no analog to the missing satellite problem down to a halo mass of $10^{10.5} M_{\odot}$. However, our halo mass function only spans two dex in halo mass compared with the much larger range in the stellar mass function. This is due to the nonlinear stellar mass–halo mass relation (see Moster et al. 2013). It suggests that

$$\log M_{\star} \propto (\beta + 1) \log M_{200}, \quad (4.5)$$

at $M_{200} < M_1 = 10^{11.59} M_{\odot}$, where $\beta = 1.376$. As such, if the HIPASS galaxies span 4

dex in stellar mass, their halo masses span only $4/(\beta + 1) = 1.7$ dex. This nonlinearity compresses an approximately flat observed VF (Zwaan et al. 2010) into a less extended, more steeply rising HMF.

The stellar mass–halo mass relation of abundance matching was imposed as a prior in fitting the SPARC rotation curves. On the one hand, this is appropriate to the extent that abundance matching has become an essential aspect of the Λ CDM paradigm. On the other hand, the correlation between halo mass and HI line width is less clear if we do not impose the stellar mass–halo mass relation as a prior. If instead we were to make the natural assumption that $M_{200} \sim W_{50}^3$ (Posti et al. 2019b), the low-mass end of the HMF would be shallower than predicted. Abundance matching thus plays a key role in reproducing the predicted halo abundance at intermediate and low halo mass.

Accepting the abundance-matching prior on halo masses obtained from rotation curve fits, we find good agreement between the predicted and measured halo mass functions at intermediate and low halo masses down to $10^{10.5} M_{\odot}$. Below this mass limit, there is a hint of a discrepancy in the field analogous to the missing satellite problem. To explore if this is a genuine problem requires pressing the mass limit of blind HI surveys to lower masses. This will be possible with large interferometric HI surveys with the SKA and its pathfinders.

4.6 Appendix A¹: Optical inclinations vs. kinematic inclinations

In order to be consistent with the measurements of the HIPASS sample, we have used optical inclinations to correct the HI line widths of the SPARC galaxies, although they have well-measured kinematic inclinations from spatially resolved HI data. The estimation of optical inclinations is based on the eccentricity of outer isophotes at [3.6]. We use the surface brightness profiles to determine the edges of the SPARC galaxies, as shown in the bottom panels of Figure 4.4. The eccentricity profiles of most SPARC galaxies become flat at the edges, such as UGC06787, while some galaxies show continuously decreasing eccentricities, for example UGC05918. Starting from the most outer point of each SPARC galaxy determined from its surface brightness profile, we move inward and select all these points which differ from the mean eccentricity no more than 20%. We then estimate the mean eccentricity based on these selected points. Axial ratio $q = (1 - e)$ is then used to calculate optical inclination according to equation 4.2. The resultant optical inclinations are plotted against kinematic ones as tabulated in the SPARC database in Figure 4.5. There is a large scatter around the line of unity, indicating that optical inclinations can be largely uncertain.

To check the effect of the assumed inclinations on the final HMF, we also build $M_{200}-W_{\text{HI}}$ relations using the best-fit kinematic inclinations for the NFW, Einasto and DC14 models. We stress that the kinematic inclinations are not those tabulated in the original SPARC database, but from our rotation curve fits (see Li et al. 2020). They are hence halo-profile dependent. We investigate the correlations between $\log(M_{200})$ and $\log(W_{\text{HI}}^2/2)$ in the left panels of Figure 4.6. For all the three halo profiles, they present tighter correlations with less outliers than using optical inclinations. This is also suggested in Figure 4.5, since there is no systematic difference between optical and kinematic inclinations.

Following the same procedure, we measure the halo mass functions using the HIPASS galaxy sample for the NFW, Einasto and DC14 profiles (see the right panels in Figure 4.6). The measured halo mass functions resemble those measured using optical inclinations: they are well-fit by the Schechter function, and consistent with DM-only simulations at

¹This appendix is not in the published paper.

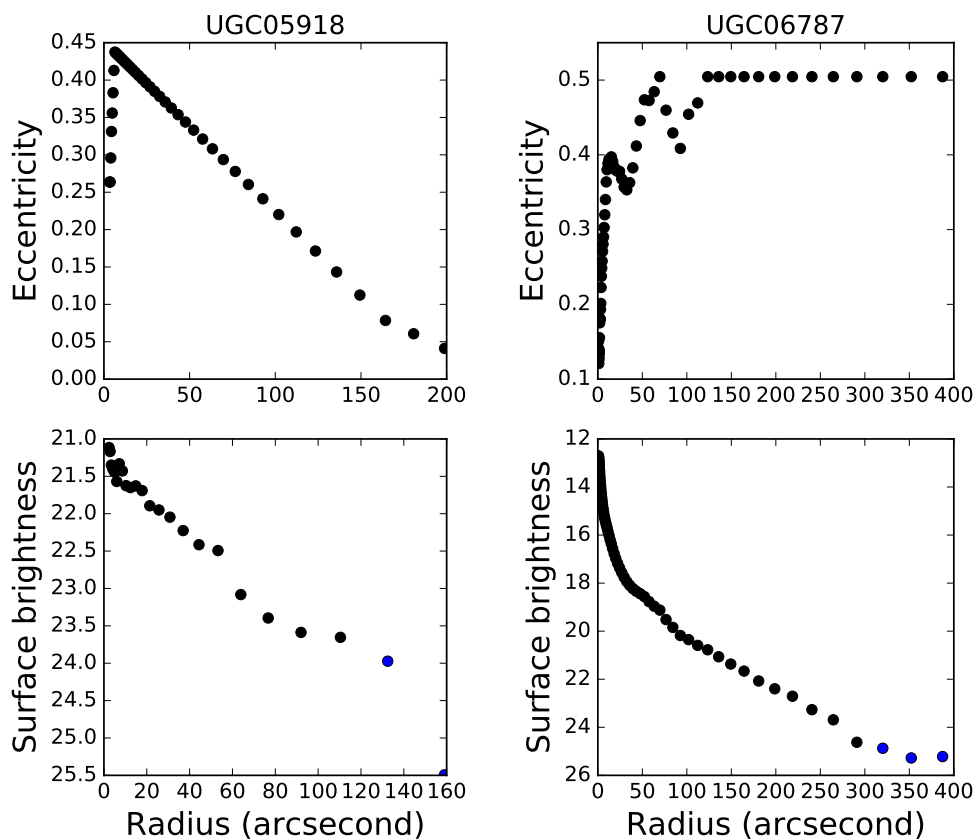


Figure 4.4 The eccentricity (top) and surface brightness (bottom) profiles for two example galaxies, UGC05918 (left) and UGC06787 (right). Surface brightness is measured at [3.6] in units of mag arcsec^{-2} . Blue points are beyond the fiducial galaxy edges, being affected by the sky background.

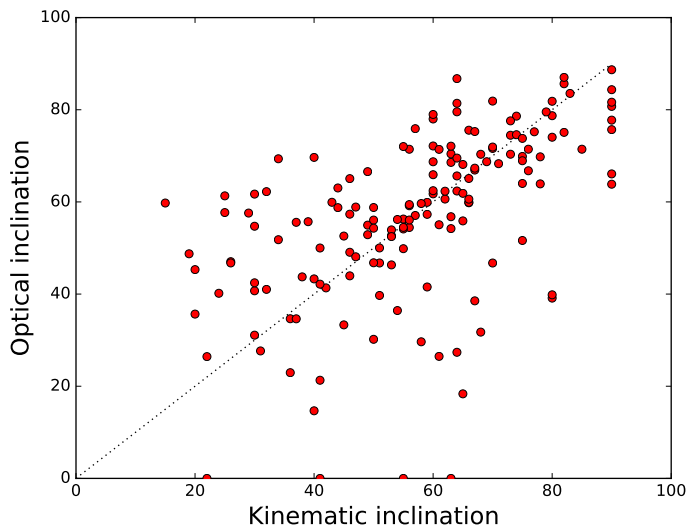


Figure 4.5 Optical inclinations vs. kinematic inclinations for the SPARC galaxies. The two methods give significantly different inclination estimations indicated by the large scatter around the line of unity (dotted line).

low and intermediate halo masses, but significantly differ from the expectations at high halo mass end. We hence conclude that the measured halo mass function is insensitive to which inclination we use, but optical inclinations are preferred for internal self-consistency and to have realistic errors on the final HMF.

4.7 Appendix B²: Comparing the measured halo mass functions with IllustrisTNG simulations

We have shown that our measured halo mass functions are significantly lower than the predictions of DM-only simulations at the high mass end. It is hence of great interests to investigate if baryonic physics can compensate this discrepancy. We analyze the output of IllustrisTNG simulations (Marinacci et al. 2018; Nelson et al. 2018; Pillepich et al. 2018; Naiman et al. 2018; Springel et al. 2018b), in which feedback from both supernovae and active galactic nuclei (AGN) have been implemented and improved to achieve a sufficient suppression of star formation (Weinberger et al. 2017). Among the three set of available

²This appendix is not in the published paper.

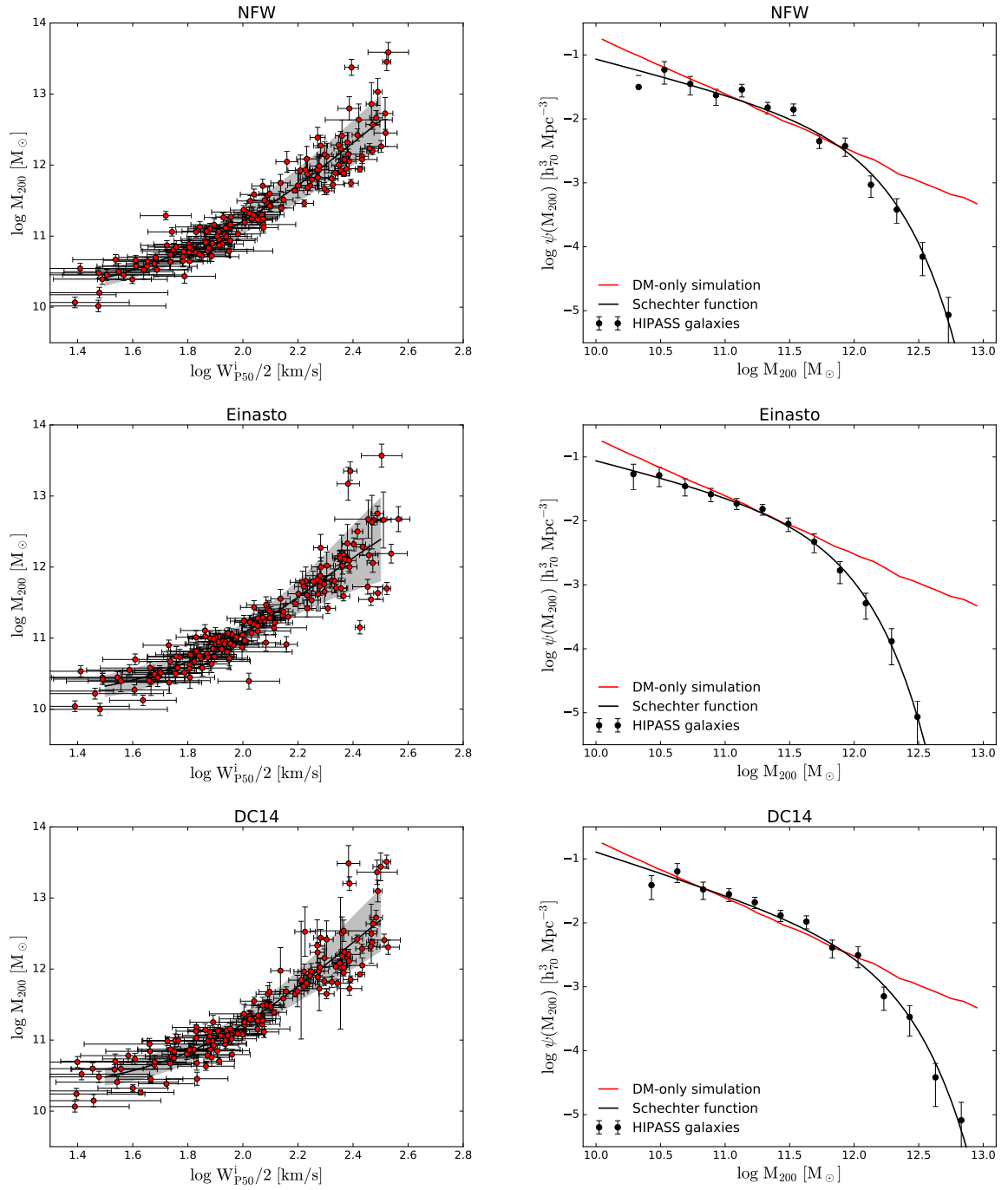


Figure 4.6 The $\log M_{200}$ - $\log W_{p50}^i/2$ relation (left) and the measured HMF (right) with $W_{p50}^i/2$ corrected for kinematic inclinations.

simulations (TNG50, TNG100, TNG300), we use the output of TNG100, since it covers a comparable range of DM halo masses.

HIPASS galaxies are HI selected, since the HI flux has to be large enough to be observable. To carry out a strict comparison, one has to model the same selection process by putting an observer into the simulation box and select the galaxies with HI flux larger than some cutoff value within the observational beam of the telescope. This requires a substantial efforts. For a preliminary investigation, we use gas fraction, $f_g = m_{\text{gas}}/(m_{\text{gas}} + m_{\star})$, instead of flux as the selection criterion. In Figure 4.7, we show the expected abundance of DM halos with $f_g > 0.1$ in TNG100 simulations. With this selection criterion, the expected HMF is still significantly higher than the measured one at high mass end. We hence adopt a more strict selection criterion $f_g > 0.4$. This excludes more galaxies and leads to a lower halo abundance both at high and intermediate halo masses. The overall shape seems impossible to reproduce since the abundance of gas-poor DM halos do not drop as rapidly as in the Schechter function.

The simple selection using gas fraction is not a substitute of gas flux, since the former neglects the effect of distance. More distant galaxies have to have higher gas fractions compared to nearby galaxies with the same baryonic masses in order to be observed. Thus, using gas flux as selection criterion is equivalent to using distance dependent gas fraction. We expect to carry out this investigate and make a more solid comparison between observations and simulations in future modeling in detail the selection effect of HIPASS data.

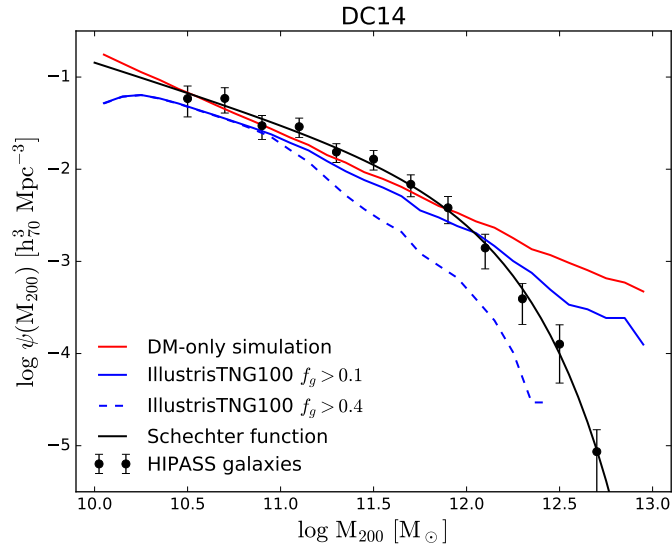


Figure 4.7 The halo mass function measured using the HIPASS galaxies (Meyer et al. 2004; Zwaan et al. 2010) for the DC14 profile compared with the prediction of simulations. Solid black lines are the best-fit modified Schechter functions. Red lines represent the prediction of DM-only simulations (Springel et al. 2018a; Nelson et al. 2019). Blue solid and dashed lines are the prediction of Illustris TNG100 simulations (Marinacci et al. 2018; Nelson et al. 2018; Pillepich et al. 2018; Naiman et al. 2018; Springel et al. 2018b) with the halo selection criterion $f_g > 0.1$ and $f_g > 0.4$, respectively, where the gas fraction is $f_g = m_{\text{HI}}/(m_{\text{HI}} + m_{\star})$.

Chapter 5

Adiabatic Compression of Dark Matter Halos

5.1 Abstract

Traditionally, when fitting rotation curves of disk galaxies, baryons and dark matter (DM) halos are treated as separate, independent, static components. In reality, the two components are dynamically coupled: the final DM configuration differs from its primordial initial condition, and depends on the details of the final distribution of baryons. We compute the impact of adiabatic compression on primordial NFW halos for the observed baryonic mass distributions of SPARC galaxies. We find that adiabatic compression significantly increases the DM contribution to rotation curves, often causing a conflict with the data. This effect exacerbates the core-cusp problem in low-mass galaxies, and is even more pronounced in high-mass spirals in which baryonic feedback is inefficient. We develop a new method that simultaneously fits rotation curves and compresses primordial halos. This method results in DM halos that are in dynamic equilibrium with the baryonic distributions that they host. We apply this method to the SPARC galaxies, and find that the primordial halos are systematically less massive than previously thought. The ultimate density distribution of these DM halos is specific to each galaxy: commonly used analytic approximations (like the NFW halo) are not adequate to describe real galaxies.

5.2 Introduction

Rotation curves are a key tool to infer the structure of dark matter (DM) halos for rotationally supported galaxies. Traditional rotation curve fitting simply assumes some analytic density profile for the DM halo which contains several parameters (generally a scale radius r_s and a characteristic volume density ρ_s and possibly some additional shape parameters). For the assumed density profile, one can easily calculate the halo circular velocity in the disk plane, and add it quadratically with baryonic contributions to match observed rotation curves. This way, DM halos and baryonic matter are treated separately and independently. This neglects the gravitational interactions between them.

To properly take the interactions into account, one has to simulate the evolution of DM halos. Recent simulations of galaxy formation have extensively implemented baryonic effects. One of the motivations for introducing baryonic physics is to address the core-cusp problem: DM-only simulations predict cuspy halos (Moore 1994; Navarro et al. 1996a, 1997), while observed DM halos have relatively flat density profiles towards galactic centers (Walter et al. 2008; de Blok et al. 2008; Oh et al. 2011). It is thought that baryonic processes such as supernova explosions (e.g. Di Cintio et al. 2014a) and repeated star formation (Read et al. 2016a,b) can drive energetic outflows, which reduce the inner DM density to turn central cusps into cores. These feedback effects, however, are competing with baryonic contraction (Blumenthal et al. 1986; Gnedin et al. 2004; Chan et al. 2015): as baryons settle into and collapse in the centers of DM halos, DM halos are expected to become more concentrated due to the baryonic gravitational pull. Gnedin et al. (2004) studied the cooling of gas in the inner regions of DM halos using cosmological simulations, and found that the dissipation of gas indeed compresses DM halos, resulting in steeper radial density profiles. Using the FIRE (Feedback In Realistic Environments) simulations, Chan et al. (2015) investigated the dependence of the inner slopes of DM halo profiles on halo mass. The results show that halo profiles are shallower at $M_{\text{halo}} \sim 10^{10}$ - $10^{11} M_{\odot}$, where baryonic feedback is relatively strong. Di Cintio et al. (2014a) and Dekel et al. (2017) express the dependence in terms of the ratios of stellar-to-halo masses (see also Freundlich et al. 2020; Lazar et al. 2020) as a result of the two competing baryonic processes.

These cosmological simulations clearly show the importance of baryonic effects. However, it remains unclear which one of the two processes (expansion or compression) is

dominant in actual, observed galaxies, as these simulations do not fit real galaxies. The study of halo compression of real galaxies has been pioneered by Sellwood & McGaugh (2005), which take DM halos and baryonic distributions as input, and let DM halos to evolve and stabilize as baryonic material condenses to form realistic galaxies within them. Sellwood & McGaugh (2005) applied this method to five example galaxies with extended HI rotation curves from Sanders & McGaugh (2002). The stellar disks of these five galaxies are assumed to be exponential with two adjustable parameters, total mass and disk scale length. By selecting appropriate parameters manually, Sellwood & McGaugh (2005) provide satisfactory fits to the observed rotation curves.

Here we apply Sellwood’s method to the SPARC dataset of 175 late-type galaxies (Lelli et al. 2016a), and investigate the effect of halo compression in a statistical sense. The SPARC galaxies have Spitzer photometry at [3.6], which provides solid estimates for stellar mass distributions, hence we do not need to assume exponential disks. We first test the compression code on the best-fit, static NFW halos for the SPARC galaxies (Li et al. 2020). This quantifies the amplitude of compression that is implicitly ignored by the traditional approach. If this effect is substantial, the compressed NFW halos may not be able to fit the observed rotation curves any more. In order to obtain stable DM halos and satisfactory fits to rotation curves at the same time, we develop a new method, fitting rotation curves while simulating the adiabatic contraction of DM halos.

In Section 3, we introduce Sellwood’s compression code, including the algorithm of adiabatic compression and initial setup. We show the results of compression and best-fit compressed halos in Section 4, followed by a brief discussion in the concluding Section 5.

5.3 Compression code and input

5.3.1 The compression algorithm

The purpose of the compression code is to create the compressed halos that are in equilibrium with embedded baryonic distributions. Halo compression is treated as an adiabatic process, which can be modeled using adiabatic invariants of particles orbits (Eggen et al. 1962). This was shown to be a good approximation in a hierarchical Λ CDM cosmogony by Choi et al. (2006). Blumenthal et al. (1986) proposed a popular form of the adiabatic con-

traction model, which assumes homogeneous contraction, circular particle orbits for DM particles, and conserves angular momentum only. As a result, random motions of particles are neglected, and spherical shells contract in radius but do not cross each other.

Young (1980) proposed a different algorithm incorporating random motions. He found that spherical mass distributions with an isotropic distribution function are less compressed than that with circular orbits only. Young’s method conserves both angular momentum (azimuthal action) and radial action, while in general adiabatic process conserves all three actions. The third action is essentially zero and hence ignored due to the assumption of spherical symmetry. This assumption has been tested using N-body simulations (Jesseit et al. 2002; Sellwood & McGaugh 2005), and is found to be highly accurate while being computationally less expensive.

The compression code we use implements Young’s algorithm. It is a subprogram of Sellwood’s *Galaxy* N-body simulation code (Sellwood 2014). The compression code works directly on gravitational potential profile $\Phi(r)$, density profile $\rho(r)$, and distribution function $f(E, L)$. It starts with a single DM halo, and adds baryonic mass gradually. The addition of baryons is reflected in the change of gravitational potential $\Phi(r)$. The central idea of Young’s method is to update distribution function $f(E, L)$ based on the new $\Phi(r)$ using adiabatic invariants. After a small fraction of baryons is added, the specific energy E and the distribution function f are changed to E' and f' , respectively, but the number of DM particles are conserved,

$$f'(E', L) = f(E, L). \quad (5.1)$$

The new $E' = E'(E, L)$ can be calculated by equating the radial action $J'_r(E', L) = J_r(E, L)$, or any function of adiabatic invariants, and the value of $f'(E', L)$ is hence directly determined.

The process can be specified as following:

1. Determine the initial total gravitational potential $\Phi_0(r)$ and distribution function $f_0(E_0, L)$ of DM halos from the initial DM density profile $\rho_0(r)$;
2. Add baryons and update the gravitational potential profile $\Phi_n(r) = \Phi_{n-1}(r) + \Phi_{\text{bar}}(r)$;
3. Update the distribution function using the adiabatic invariants following the change of gravitational potential;

4. Update DM density profile $\rho_n(r)$ based on the new distribution function and gravitational potential.

The procedure is iterated until the solution converges. In contrast to computationally expensive N-body simulations, it takes only a couple of minutes to stabilize a DM halo. The rapid convergence provides a key benefit: we can explore different inputs, and find best initial condition for the primordial (pre-compressed) halo that results in a final, compressed, dynamically stable DM halo that fits the rotation curve data.

5.3.2 Input of compression

The compression program requires as input the surface density profiles of stellar disks, bulges, and gas, as well as initial DM halos. In this work, we use homogenized HI surface density profiles culled from the literature (Lelli et al. in prep.) as well as new, unpublished mass models that are over-sampled at high resolution by interpolating the stellar and HI density profiles with a spline. For six galaxies, HI density profiles are not available and are removed from our analysis. During the compression process, baryonic distributions are added gradually until reach the input surface density, and DM halos evolve in response to the gradually increased gravitational potential. The addition of baryonic mass is artificially implemented, independent on DM halos. In reality, both baryons and DM change their initial density distributions due to their mutual and self gravitational interactions. The baryonic distribution, however, is also affected by non-gravitational physical processes such as gas flows, gas heating and cooling, star formation, and stellar feedback, requiring full hydrodynamic simulations. Instead of simulating the entire evolution of a realistic galaxy, here we ask a simpler, basic question: how much can the DM distribution change from the initial NFW profile in response to the formation of a baryonic disk if gravity is the dominant player?

The initial DM halos are assumed to be spherical and isotropic. We use the NFW profile (Navarro et al. 1996a),

$$\rho = \frac{\rho_s}{\left(\frac{r}{r_s}\right)\left[1 + \left(\frac{r}{r_s}\right)\right]^2}, \quad (5.2)$$

since it is widely accepted to be the correct primordial form before baryonic physics settles in (see for example Di Cintio et al. 2014a; Read et al. 2016a). The associated particle

distribution function is given by numerically solving Eddington’s formula (section 4.3 in Binney & Tremaine 2008). The DM density profile for different galaxies are specified by two halo parameters: $M_s = 4\pi\rho_s r_s^3$, and r_s , which are taken as input in the compression code.

The initial NFW halos of the SPARC galaxies are from Li et al. (2020). We use the results imposing Λ CDM priors. The Spitzer photometry at [3.6] and the Λ CDM priors break the disk-halo degeneracy (van Albada et al. 1985) and the degeneracy between halo parameters. The resultant DM halos are hence well determined. The derived characteristic volume density ρ_s and scale radius r_s for each galaxy are tabulated in the SPARC database, from which M_s can be easily calculated. Though the uncertainties on these parameters are also given, we cannot propagate them into the final predicted rotation curves through compression because of the need of iteratively compute every possible halo configuration. The point of this first step is simply to explore the magnitude of the compression for galaxies with large varieties.

5.4 Results

5.4.1 Compressing the static, best-fit NFW halos

As a first step, we run compression for 169 SPARC galaxies to test the code performance on the best-fit, static NFW halos from Li et al. (2020). To illustrate the effect of halo compression, we show two example galaxies, NGC2903 and UGC06786, in Figure 5.1. Both galaxies are large spirals with high-quality rotation curves (quality flag Q=1), and their distances are determined using the light curves of Type Ia Supernovae. In Li et al. (2020), we show that the NFW profile provides good fits to their rotation curves. Therefore, they are ideal examples to illustrate the basic effect of adiabatic compression.

In Figure 5.1, we show the contribution of each baryonic component from Li et al. (2020), which remains invariant during compression. The compressed DM halos of these two galaxies show higher velocity profiles than uncompressed ones. This leads to the total rotation curves to overshoot the observed ones. The compression effect is more important at small radii, where the rotation curves rise more steeply. Even before compression, the NFW profile is too cuspy to fit the inner regions of many rotation curves. Therefore, the

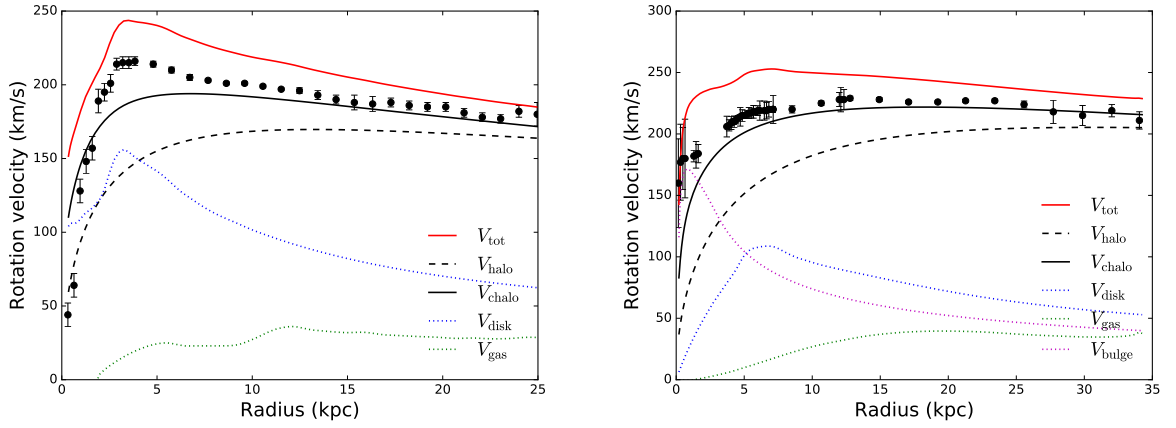


Figure 5.1 Example galaxies NGC2903 (left) and UGC06786 (right) with compressed halos. Green, blue, and purple dotted lines are the contributions of gas, stellar disk, and bulges, respectively. Dashed black lines represent the best-fit NFW halos from Li et al. (2020), while solid black lines indicate the compressed halos. Red solid lines are the total contributions after compression, which are higher than the observed rotation curves as a result of the effect of compression. This illustrates the magnitude of the effect that has been neglected in previous rotation curve fits.

adiabatic contraction further intensifies the core-cusp problem.

As mentioned earlier, baryonic feedback is thought to be able to reduce the inner density of DM halos. Since the compression code does not include baryonic physics, we cannot model baryonic feedback as cosmological simulations do. But how efficient feedback is depends on the stellar-to-halo mass (SHM) ratio due to the competition between stellar feedback and adiabatic contraction. In Li et al. (2020), we show that the halo masses of NGC2903 and UGC06786 are $10^{11.64} M_{\odot}$ and $10^{12.08} M_{\odot}$, respectively. Using their best-fit stellar-to-mass ratios, we calculate their SHM ratios: $\log(m_{\star}/M_{200}) = -1.30$ for NGC2903, and $\log(m_{\star}/M_{200}) = -1.56$ for UGC06786. At these SHM ratios, Di Cintio et al. (2014a) and Lazar et al. (2020) find that core formation of DM halos is less efficient, and the cuspy NFW profile is essentially recovered. As such, the adiabatic contraction is the dominant process, so that baryonic feedback cannot erase the cuspy DM halos.

In order to investigate the compression effect in a statistical sense, we plot the reduced χ^2 ,

$$\chi_v^2 = \frac{\chi^2}{N - f}, \quad \chi^2 = \sum_R \frac{[V_{\text{obs}}(R) - V_{\text{tot}}(R)]^2}{(\delta V_{\text{obs}})^2}, \quad (5.3)$$

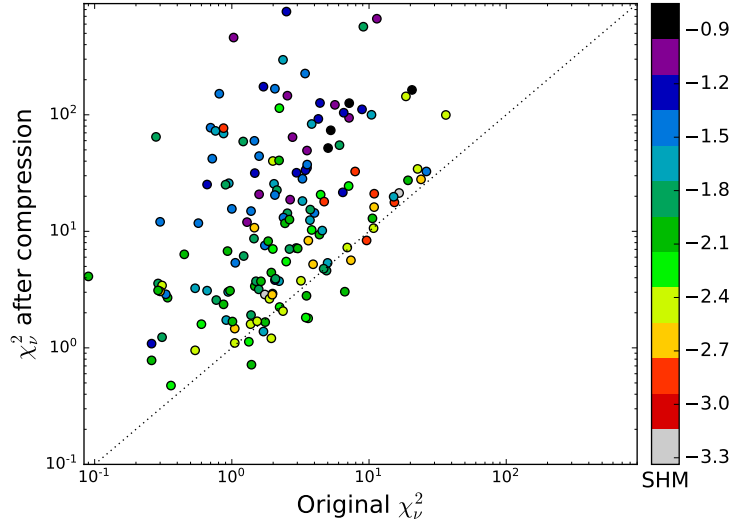


Figure 5.2 The reduced χ_v^2 after compression are plotted against their values prior to compressions from Li et al. (2020). The dotted line is the line of unity. Galaxies are color-coded by their SHM values, i.e. $\log(m_\star/M_{200})$. The increase in χ_v^2 illustrates how significant the compression is, and that an unmodified NFW halo is not an adequate description of real galaxies.

after halo compression against their tabulated values in Li et al. (2020) in Figure 5.2. Notice the difference in the definitions of χ_v^2 in this work: the degree of freedom $f = 0$, since we do not fit rotation curves but simply compress DM halos and compare with observations. This leads to a few galaxies with χ_v^2 after compression lower than those without compression. Apart from that, the vast majority of the galaxies show much larger χ_v^2 than those without compression, as expected. In general, Figure 5.2 shows that halo compression is a non-negligible effect when fitting rotation curves from low-mass dwarfs to high-mass spirals.

We color-code galaxies according to their SHM ratios, which reflect how efficient their stellar feedback could be. There seems to be a trend: galaxies with higher SHM ratios tend to have worse fit quality compared with uncompressed halos. This is because more massive galaxies compress their host halos more significantly due to stronger gravitational pull. The efficiency of halo compression depends on the SHM ratios monotonically, in contrast to baryonic feedback, which shows a peak efficiency at $\log(m_\star/M_{200}) \sim -2.5$ (Di Cintio et al. 2014a,b). This reveals the version of the core-cusp problem at $\log(m_\star/M_{200}) > -2.5$, where stellar feedback starts declining while adiabatic compression continues intensifying.

5.4.2 Fitting compressed halos

Although fitting static DM halos to rotation curves provide important insights to rotation curves, the deduced DM halos are generally not a proper representation of the Λ CDM expectation since the gravitational effect of baryons is neglected. DM-only simulations predict a universal NFW halo that is prior to compression and any baryonic feedback, while what contributes to observed rotation curves is the post-compression halo. The compression simulations build a bridge connecting the pre-compression halos to post-compression rotation curves. We hence develop a new method by introducing the compression procedure into rotation curve fits.

We start from some initial guess on the parameters of the primordial halos, such as those tabulated in Li et al. (2020), and run the compression simulation. We then test the compressed halos with observed rotation curves and calculate the χ^2 . To find the best initial halo parameters, we have to iterate the process many times with different inputs. For convenience, we introduce a fit-quality feedback to let the code automatically search for the best parameters. As a start, we fit only one parameter, M_s . Since we aim to minimize χ^2 , the fit-quality feedback can be chosen as the derivative of χ^2 ,

$$d\chi^2 = \sum_R \frac{[V_{\text{obs}}(R) - V_{\text{tot}}(R)]}{(\delta V_{\text{obs}})^2} \left(-2 \frac{dV_{\text{tot}}(R)}{dM_s}\right) dM_s. \quad (5.4)$$

Since $\frac{dV_{\text{tot}}}{dM_s}$ is positive, the sign of $d\chi^2$ entirely depends on $\sum_R \frac{[V_{\text{obs}}(R) - V_{\text{tot}}(R)]}{(\delta V_{\text{obs}})^2}$. The code calculates this quantity after each run of compression, and decides to increase or decrease M_s based on its sign for next run. Thanks to the rapid convergence of the compression code, it takes less than half an hour to fit one galaxy. We have tested this algorithm using different halo parameters, and find the resultant DM halos are insensitive to initial parameters.

In Figure 5.3, we show the fitting results of NGC2903 and UGC06786. As expected, the fits are drastically improved with respect to Figure 5.1 by decreasing M_s . However, the overall shapes are still in contrast with data. Notably, the inner regions of the rotation curves are significantly higher than the data. This is the classic signature of the core-cusp problem in low-mass galaxies, and the adiabatic compression makes it evident even in high-mass galaxies. Massive galaxies generally have fast rising rotation curves at small radii, leaving room for cuspy NFW halos. This makes the core-cusp problem less serious. How-

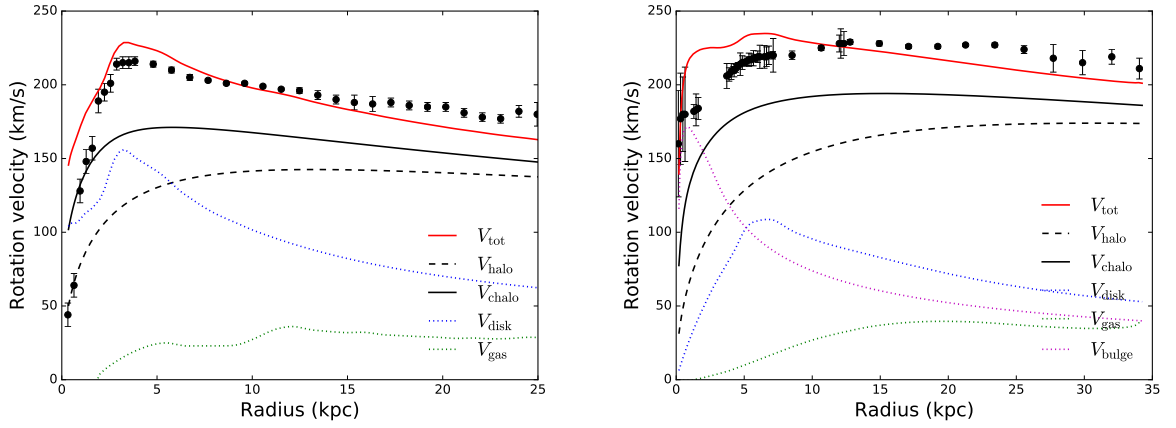


Figure 5.3 Same as Figure 5.1 but with $M_s = 4\pi\rho_s r_s^3$ optimized. For both galaxies, M_s are tuned down to compensate the compression effect.

ever, being massive also implies suffering stronger adiabatic compression, which makes the inner halo too cuspy to be accommodated by observed rotation curves. To alleviate this discrepancy, the normalization factor M_s has to be decreased, which, however, also decreases the DM density at large radii. As a result, the overall shape is in serious contrast to the observed rotation curves.

Note that we only fit one halo parameter while halo profiles are specified by two parameters. By fixing scale radius r_s , we are actually fitting the characteristic volume density ρ_s given $M_s = 4\pi\rho_s r_s^3$. Adding r_s as a fitting parameter would make the fits better somehow, since the central density of DM halos can be reduced by increasing r_s . However, given DM halos are significantly compressed as shown by the solid and dashed lines in Figure 5.3, scale radius has to be increased dramatically to counteract the compression effect. Otherwise, the fast decreasing baryonic contributions would drive the total rotation curves to fall rapidly at large radii, in contrast to the data. The larger scale radius would cause problem in the concentration-halo mass relation that is imposed as part of the Λ CDM priors in our static rotation curve fits in Chapter 2.

In Figure 5.4, we plot the optimized M_s against their original values. For the vast majority of the SPARC galaxies, M_s are systematically tuned down in response to halo compression. The optimized M_s are not randomly distributed, but clustered along but beneath the line of unity with a shallower slope. The DM halo mass M_{200} is related to the

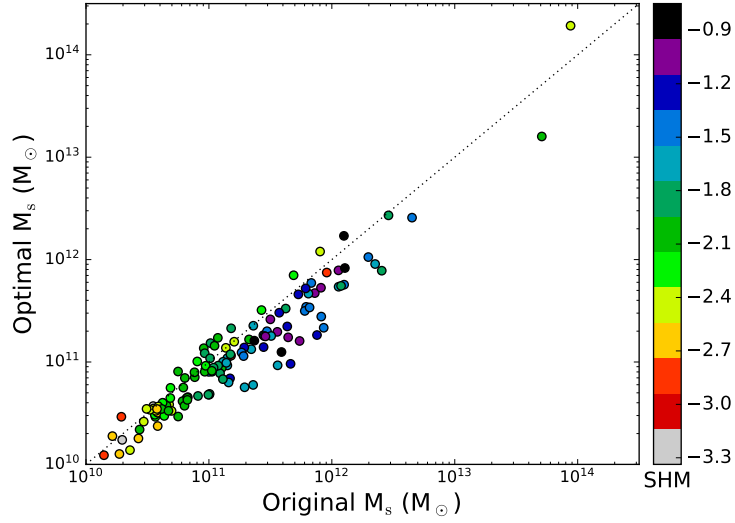


Figure 5.4 The optimal $M_s = 4\pi\rho_s r_s^3$ are plotted against their original values from Li et al. (2020). Galaxies are color-coded by their SHM values, i.e. $\log(m_*/M_{200})$, which are correlated with M_s .

characteristic mass M_s by

$$M_{200} = M_s \left[\ln(1 + C_{200}) - \frac{C_{200}}{1 + C_{200}} \right], \quad (5.5)$$

where the concentration C_{200} is between (3, 20) for most of the SPARC galaxies (Li et al. 2020). Therefore, M_s is a good representative of M_{200} . Figure 5.4 implies that the primordial NFW halos must be less massive and span relatively smaller range than we previously thought. More massive DM halos accrete more baryons, which in turn contract more DM particles in and form more massive galaxies. The initial universal NFW halo is modified specifically for each individual galaxy, dependent on the detailed baryonic distributions. This leads the ultimate DM halos to presents a large diversity.

A few galaxies show higher optimized M_s . This happens because we used galaxy distance and disk inclination as free parameters in the static halo fits (Li et al. 2020), while they are fixed to the fiducial SPARC values in the compressed halos fits presented here. Thus, it can occasionally happen that the static halo fits pushing distance and inclination to higher and lower values than the initial ones, respectively, leading to small M_s .

5.5 Conclusion

In this Chapter, we study the effects of adiabatic contraction of the DM halos of the SPARC galaxies. By compressing the best-fit NFW halos from classic, static halo fits to rotation curves from Li et al. (2020), we find that adiabatic contraction is important at all masses, and more profound at high-mass galaxies. The compressed halos make larger contributions to rotation curves, generally in serious contrast with the data. This leads to the core-cusp problem at high-mass galaxies, where baryonic feedback is inefficient, motivating the development of a new technique to include adiabatic compression during rotation curve fitting. Our new method highlights that the core-cusp problem do not occur only in low-mass galaxies but also in high-mass ones: when the primordial NFW halos are compressed by the baryonic gravitational pull, they become even denser, not longer able to fit the rotation curves of high-mass spiral galaxies. Our compression simulations do not include baryonic feedback, which might be able to alleviate the high central concentration problem. However, this must occur in high-mass galaxies, where supernova feedback is expected to be less efficient than in low-mass galaxies (Di Cintio et al. 2014a). Therefore, any new mechanism that aims to solve the core-cusp problem, has to be efficient and universal enough to be applied to galaxies with a large diversity in stellar mass.

Chapter 6

Fitting the Radial Acceleration Relation to Individual SPARC Galaxies

6.1 Abstract

Galaxies follow a tight radial acceleration relation (RAR): the acceleration observed at every radius correlates with that expected from the distribution of baryons. We use the Markov chain Monte Carlo method to fit the mean RAR to 175 individual galaxies in the SPARC database, marginalizing over stellar mass-to-light ratio (Υ_*), galaxy distance, and disk inclination. Acceptable fits with astrophysically reasonable parameters are found for the vast majority of galaxies. The residuals around these fits have an rms scatter of only 0.057 dex ($\sim 13\%$). This is in agreement with the predictions of modified Newtonian dynamics (MOND). We further consider a generalized version of the RAR that, unlike MOND, permits galaxy-to-galaxy variation in the critical acceleration scale. The fits are not improved with this additional freedom: there is no credible indication of variation in the critical acceleration scale. The data are consistent with the action of a single effective force law. The apparent universality of the acceleration scale and the small residual scatter are key to understanding galaxies.

6.2 Introduction

Since the discovery of the flat rotation curves of disk galaxies (Bosma 1978; Rubin et al. 1978), the mass discrepancy problem has been widely explored. The baryonic Tully-Fisher relation (BTFR Tully & Fisher 1977; McGaugh et al. 2000; Lelli et al. 2016b) was established as the link between the flat rotation velocity V_f and the baryonic mass for late-type galaxies. The definition of mass discrepancy at each radius, $M_{\text{tot}}/M_{\text{bar}} \simeq V_{\text{obs}}^2/V_{\text{bar}}^2$, makes it possible to study the “local” relation between the rotation curve shape and the baryonic mass distribution, which lead to the mass discrepancy-acceleration relation (McGaugh 2004b).

In order to explore the mass discrepancy-acceleration relation further, Lelli et al. (2016a) built the *Spitzer* Photometry and Accurate Rotation Curves (SPARC) database: a sample of 175 disk galaxies with homogeneous [3.6] surface photometry and high-quality HI/H α rotation curves, spanning a wide range in morphological types (S0 to Irr), stellar masses (5 dex), surface brightnesses (4 dex), and gas fractions. Using the SPARC database, McGaugh et al. (2016b) established the radial acceleration relation (RAR), in which the observed acceleration ($g_{\text{obs}} = V_{\text{obs}}^2/R$) tightly correlates with the baryonic one (g_{bar}). The $g_{\text{obs}}-g_{\text{bar}}$ plane has a major advantage over the mass discrepancy-acceleration relation: the two quantities and the corresponding errors are fully independent, thus observed and expected scatters can be easily computed without additional complications from covariances between the measurements. Furthermore, Lelli et al. (2017b) extend the galaxy sample to include 25 early-type galaxies and 62 dwarf spheroidals, finding that they follow the same relation as late-type galaxies within the uncertainties.

Assuming that the stellar mass-to-light ratio Υ_{\star} does not vary strongly at [3.6] (McGaugh 2014, 2015; Meidt et al. 2014; Schombert & McGaugh 2014), it is found that the RAR has an observed rms scatter of only 0.13 dex (McGaugh et al. 2016b; Lelli et al. 2017b). This is largely driven by uncertainties on galaxy distance and disk inclination, as well as possible galaxy-to-galaxy variations in the value of Υ_{\star} . Hence, the intrinsic scatter around the RAR must be even smaller.

Given that late-type galaxies statistically satisfy the RAR, we can explore its intrinsic scatter by fitting individual galaxies and marginalizing over Υ_{\star} , galaxy distance (D), and disk inclination (i). This is equivalent to rotation curve fits in modified Newtonian dynam-

ics (MOND, Milgrom 1983), but our aim here is to measure the intrinsic scatter around the RAR from a purely empirical perspective. Moreover, differently from classic MOND studies (e.g., Sanders & McGaugh 2002), we impose priors on Υ_{\star} , D , and i based on the observational uncertainties. These “free” parameters are treated as global quantities for each galaxy, whereas the RAR involves local quantities measured at each radius. Hence, there is no guarantee that adjusting those parameters within the errors can result in satisfactory individual fits for each and every galaxy or decrease the empirical scatter around the mean relation.

In section 2, we describe our fitting method, which is a Markov chain Monte Carlo (MCMC) simulation. In section 3, we show the fitted individual galaxies and their posterior distribution. The distributions of adjusted parameters are also presented. In section 4, the RAR and its residuals are described. We also check the resulting BTFR. We generalize the RAR to consider possible galaxy-to-galaxy variation in the critical acceleration scale in section 5. In section 6, we summarize our results and discuss the general implication of the extremely small rms scatter (0.057 dex) of our best-fitting relation.

6.3 Method

6.3.1 Parameter dependence

Based on Spitzer [3.6] images and total HI maps from the SPARC database, one can calculate the acceleration due to the baryonic mass distribution at every radius,

$$g_{\text{bar}}(R) = (\Upsilon_{\text{disk}} V_{\text{disk}}^2 + \Upsilon_{\text{bul}} V_{\text{bul}}^2 + V_{\text{gas}}^2)/R, \quad (6.1)$$

where Υ_{disk} and Υ_{bul} are the stellar mass-to-light ratios for the disk and bulge, respectively. Similarly, the observed acceleration can be calculated directly from the observed velocity V_{obs} ,

$$g_{\text{obs}}(R) = \frac{V_{\text{obs}}^2}{R}. \quad (6.2)$$

According to the RAR (McGaugh & Schombert 2014; McGaugh et al. 2016b; Lelli et al. 2017b), the expected total acceleration g_{tot} strongly correlates with that expected from bary-

onic distributions g_{bar} ,

$$g_{\text{tot}}(R) = \frac{g_{\text{bar}}}{1 - e^{-\sqrt{g_{\text{bar}}/g_{\ddagger}}}}, \quad (6.3)$$

where $g_{\ddagger} = 1.20 \times 10^{-10} \text{ m s}^{-2}$. Thus, one can compare the observed acceleration with the expected one.

A constant value of Υ_{\star} for all galaxies is able to statistically establish the RAR, but some scatter must have been introduced since Υ_{\star} should vary from galaxy to galaxy. An inappropriate Υ_{\star} can lead to systematic offsets from the RAR for individual objects. Specifically, Υ_{disk} and Υ_{bulge} affect g_{bar} according to Equation 6.1.

Uncertainties in galaxy distance affect the radius (R) and the baryonic components of the rotation curve (V_k). With D being adjusted to D' , R and V_k transform as

$$R' = R \frac{D'}{D}; \quad V'_k = V_k \sqrt{\frac{D'}{D}} \quad (6.4)$$

where k denotes disk, bulge or gas. Therefore, g_{bar} does not depend on distance. Instead, g_{obs} goes as D^{-1} because the observed rotation velocity (V_{obs}) and its error (δV_{obs}) are inferred from the line-of-sight velocity which is distance independent.

In the SPARC database, galaxy distances are estimated using five different methods (see Lelli et al. 2016a for details): (1) the Hubble flow corrected for Virgo-centric infall (97 galaxies), (2) the tip of the red giant branch (TRGB) method (45 galaxies), (3) the magnitude-period relation of Cepheids (3 galaxies), (4) membership to the Ursa Major cluster of galaxies (28 galaxies), and (5) supernovae (SN) light curves (2 galaxies). The first method is the least accurate because the systemic velocity (redshift) of a galaxy may be largely affected by peculiar flows in the nearby Universe. The other methods have accuracies ranging between 5% and 15%. Table I in McGaugh et al. (2016b) shows that errors on galaxy distance are the main source of scatter on the RAR.

Uncertainties in disk inclination are another important source of scatter. When the disk inclination i is adjusted to i' , V_{obs} and δV_{obs} transform as

$$V'_{\text{obs}} = V_{\text{obs}} \frac{\sin(i)}{\sin(i')}; \quad \delta V'_{\text{obs}} = \delta V_{\text{obs}} \frac{\sin(i)}{\sin(i')}. \quad (6.5)$$

Hence, g_{obs} has a further dependence on disk inclination. Clearly, the correction becomes very large for face-on galaxies with small inclination. We also note that several galaxies

have warped HI disks: the inclination angle systematically varies with radius. While warps are taken into account in deriving rotation curves (e.g., NGC 5055 from Battaglia et al. 2006), here we treat the inclination as a single global parameter for each galaxy.

6.3.2 MCMC simulation

To fit individual galaxies, we used *emcee* (Foreman-Mackey et al. 2013) to map the posterior distribution of the parameter set: the stellar mass-to-light ratio, galaxy distance, and disk inclination. Following standard procedures, we imposed Gaussian priors on Υ_{\star} , D , and i . The priors were centered around the assumed values in SPARC and have standard deviations given by the observational errors for D and i and the scatter expected from stellar population models for Υ_{\star} (e.g., Bell & de Jong 2001b). Hence, Υ_{\star} , D , and i are not entirely free parameters: the MCMC simulation is searching for an optimal solution within a realistic region of the parameter space. Specifically, we imposed $\Upsilon_{\text{disk}} = 0.5$ and $\Upsilon_{\text{bulge}} = 0.7 M_{\odot}/L_{\odot}$ with a standard deviation of 0.1 dex. We adopted a fixed mass-to-light conversion for the gas unlike what Swaters et al. (2012) did. We also required that the parameters remain physical and positive definite: $\Upsilon_{\star} > 0$, $D > 0$ Mpc, and $0^{\circ} < i < 90^{\circ}$.

We used the standard affine-invariant ensemble sampler in *emcee* and initialized the MCMC chains with 200 random walkers. We ran 500 burnt-in iterations and then ran the simulation to more than five autocorrelation times. We checked that the acceptance fractions for all galaxies are in the range (0.1, 0.7). To achieve the acceptance fraction, we set the size of the stretch move $a = 2$.

We record the parameter set corresponding to the maximum probability and calculate the reduced χ^2 ,

$$\chi_v^2 = \sum_R \frac{[g_{\text{obs}}(R) - g_{\text{tot}}(R)]^2 / \sigma_{g_{\text{obs}}}^2}{N - f}, \quad (6.6)$$

where $\sigma_{g_{\text{obs}}} = 2V_{\text{obs}} \times \frac{\delta V_{\text{obs}}}{R}$ is the uncertainty in the observed acceleration, N the number of data points, and f the degrees of freedom, for every galaxy.

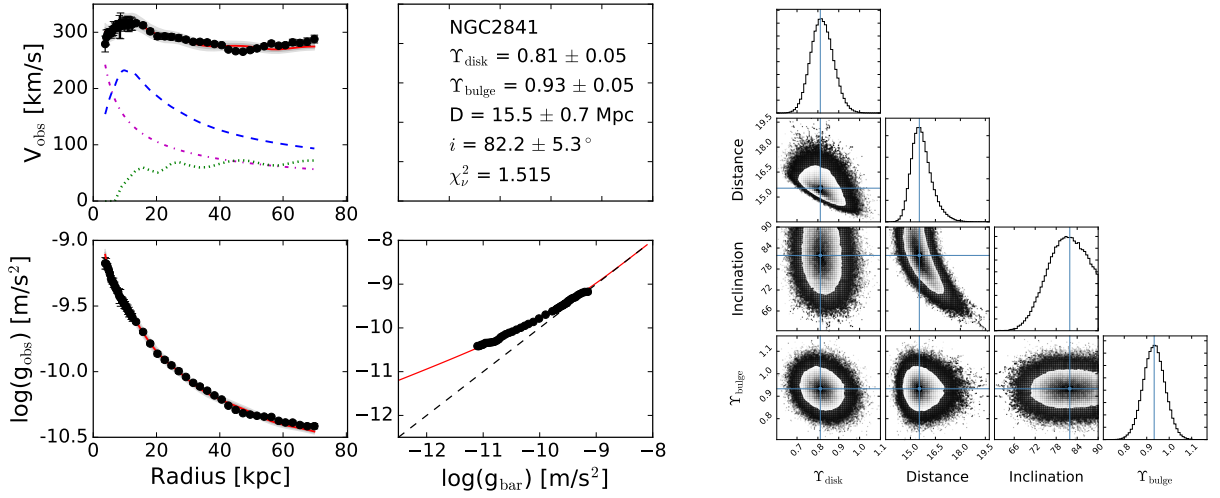


Figure 6.1 Example of MCMC fits (*left*) and the corresponding posterior distribution (*right*). In the left panels, the points with error bars are the observed rotation curves $V_{\text{obs}}(R)$ or corresponding accelerations $V_{\text{obs}}^2(R)/R$. In the rotation curve panel, each baryonic component is presented: purple dash-dotted line for the bulge, blue dashed line for the disk, and green dotted line for the gas. The red solid line is the fitted rotation curve. The dark gray and light gray bands show the 68% and 95% confidence regions, respectively, considering the posterior distribution of Υ_{\star} ; they do not include additional uncertainties on i and D . In the acceleration panels, the red solid line represents the mean RAR to which we fit. In the right panels, the blue cross indicates the parameter set corresponding to the maximum posterior probability. The complete figure set (175 images) is shown in the appendix.

6.4 Fitting individual galaxies

6.4.1 Fit results

By fitting individual galaxies to the RAR, the stellar mass-to-light ratio, the galaxy distance and the disk inclination are optimized. In particular, we note that the RAR may be used as a distance indicator in analogy to the BTFR. The former relation is more demanding in terms of data quality, but has the advantage of using the full shape of the rotation curve and the baryonic mass profile instead of merely using the flat rotation velocity and total baryonic mass that go into the BTFR.

Figure 6.1 shows an example of an MCMC fit for a star-dominated spiral galaxy (NGC 2841). This object has historically been regarded as a problematic case for MOND (Begeman et al. 1991; Gentile et al. 2011), but a good fit is obtained allowing for uncertainties in distance

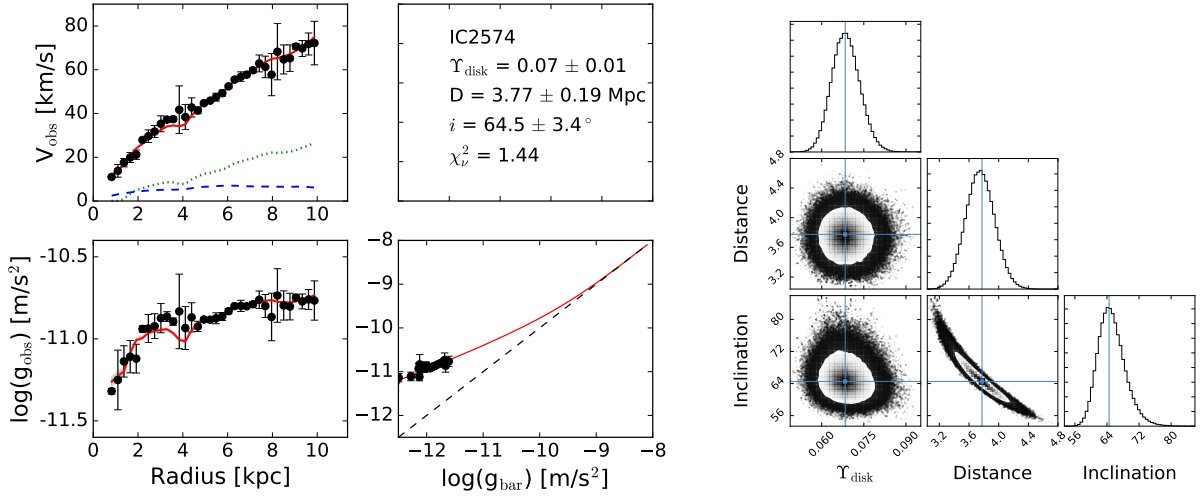


Figure 6.2 Same as Figure 6.2 but for the gas-dominated dwarf galaxy IC 2574.

and inclination within 1σ . The values of Υ_{disk} and Υ_{bulge} are relatively high but not unreasonable for such a massive, metal-rich galaxy. Similar figures are available for all SPARC galaxies.

Figure 6.2 illustrates the MCMC fit of a gas-dominated dwarf galaxy (IC 2574). This object is often considered a problematic case for Λ CDM because it has a large core extending over ~ 8 kpc (e.g., Oman et al. 2015). Moreover, Navarro et al. (2017) claimed that this galaxy strongly deviates from the RAR (their Figure 3). We find an excellent fit for IC 2574 after adjusting its distance and inclination by $1 \sigma_D$ and $1.5 \sigma_i$, respectively. The adjusted mass-to-light ratio is rather low ($\Upsilon_{\text{disk}} = 0.07 M_{\odot}/L_{\odot}$), perhaps uncomfortably so. This object is also present in the THINGS database (de Blok et al. 2008), where the rotation curve is consistent with but slightly higher than that adopted here. If we apply the same MCMC technique to the THINGS data, we find a good fit with $\Upsilon_{\star} = 0.25 M_{\odot}/L_{\odot}$, illustrating the sensitivity of this parameter to even small changes in the rotation curve.

We stress that for gas-rich dwarfs, the vast majority of the rotation curve is explained by the gas contribution with very little room for adjustment. Rather than be overly concerned with the exact value of Υ_{\star} in such gas-dominated galaxies, it is amazing that this procedure works at all: Υ_{\star} has little power to affect the overall fit, while D and i are constrained by their priors to be consistent with the observed values. Gas-dominated galaxies are more prediction than fit: given the observed gas distribution and the RAR, the rotation curve must

be what it is. The fitting parameters provide only minor tweaks to the basic prediction.

In general, the fits to most galaxies are good. The mass-to-light ratios are generally consistent with the expectations of stellar population synthesis. It is rare that either D or i are adjusted outside of their observational uncertainties. We maintain the same fitting function (equation 6.3) for all 175 galaxies.

While most fits are visually good, they may occasionally have poor values of χ^2 . These usually occur when one or a few individual velocity measurements have tiny error bars. The discrepancy of these points from the fit is small in an absolute sense, but still impacts χ^2 . It is likely that in some cases the errors are slightly underestimated. For example, the potential contribution of non-circular motions may have been understated and the velocities may not exactly trace the underlying gravitational potential. In general, these fits are as good as possible: one cannot do better with a dark matter halo fit. The Navarro-Frenk-White (NFW) halo fit to NGC 2841 (Katz et al. 2017) looks indistinguishable from that in Fig. 6.1: the two extra fit parameters available with a dark matter fit do not alter the shape of the continuous line that best approximates the data. We therefore consider fits of this type to be good even if χ^2 is larger than unity.

In about 10% of the cases, however, the fits are genuinely poor. Poor fits generally happen for rotation curves of lowest quality. For the sake of completeness, we fit all 175 galaxies in the SPARC database, but we did not expect to find good fits for galaxies with quality flag $Q = 3$ (e.g., NGC 4389, UGC 2455, UGC 4305) where the gas kinematics is likely out of equilibrium (see Lelli et al. 2016b, for details). Some poor fits are also found for galaxies with $Q = 1$ (e.g., D631-7, F571-8, and IC 4202) and $Q = 2$ (e.g., Cam B, DDO 168, and NGC 2915). This may happen for several reasons: (i) the errors on D and i may be slightly underestimated, hence the priors place strong constraints that then contribute more to the probability function and preclude somewhat better fits, (ii) there may be features in the rotation curves that do not trace the smooth gravitational potential but are due to large-scale non-circular motions, and (iii) these galaxies may have unusual dust content that affects the shape of the [3.6] luminosity profile and the calculation of g_{bar} (this may be particularly important for edge-on systems such as IC 4202 and F571-8). In the specific case of D631-7, the gas contribution was computed assuming a purely exponential distribution since the HI surface density profile was not available (see Lelli

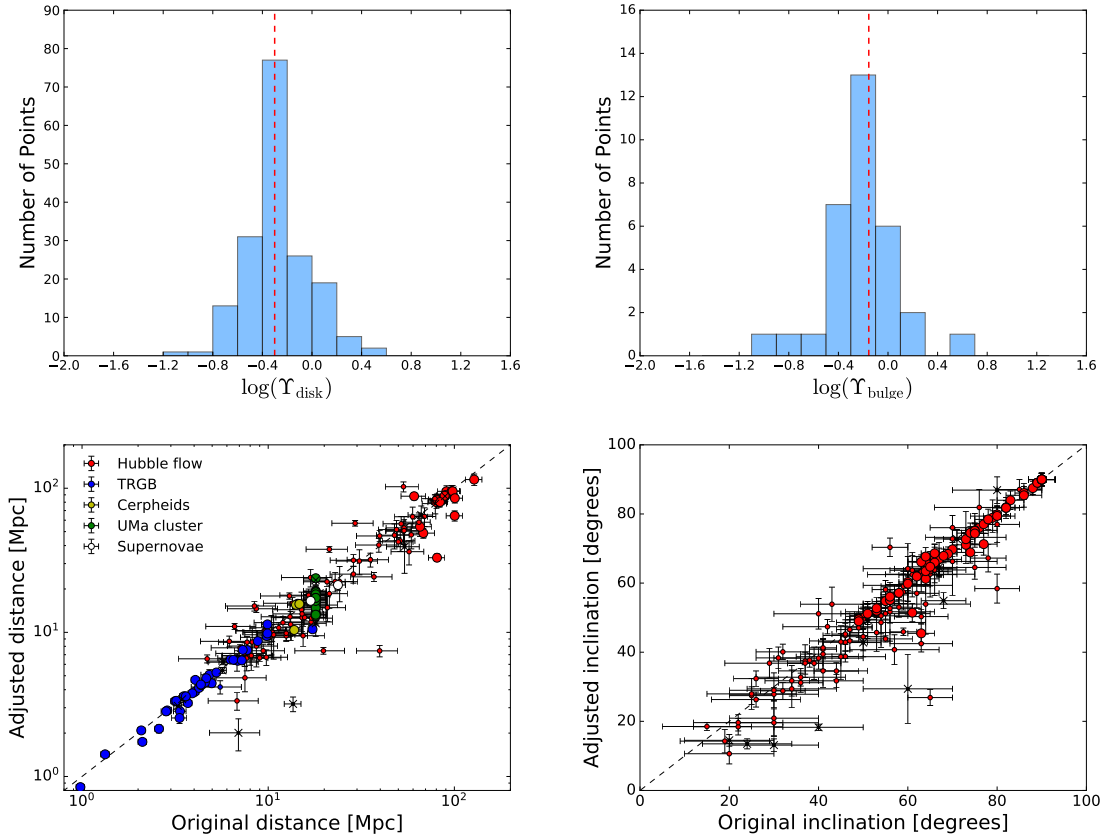


Figure 6.3 Distributions of fitted parameters. The top panels show the histograms of the optimized Υ_{disk} (top left) and Υ_{bulge} (top right). The vertical dashed lines represent the values of 0.5 (disk) and 0.7 (bulge) adopted in McGaugh et al. (2016b). In the bottom panels, the optimal galaxy distance (bottom left) and disk inclination (bottom right) are plotted against their original values. The dashed line is the line of unity. Different methods of measuring distance are indicated by different colors. Large and small symbols correspond to data with an accuracy higher and lower than 15% for distance and 5% for inclination, respectively, based on observational errors as tabulated in SPARC. Crosses indicate galaxies with the low-quality rotation curves ($Q=3$, see Lelli et al. 2016a). A few other outliers are discussed in the text.

et al. 2016). Since the RAR is very sensitive to the precise baryonic distribution, even small deviations from an exponential profile may lead to a poor fit in such a gas-dominated galaxy. In general, we consider it likely that lower quality data lead to lower quality fits. Having $\sim 10\%$ of such cases seems an inevitable occurrence in any astronomical database built from many diverse rotation curve studies such as SPARC (Lelli et al. 2016a). It would be strange if there were no such cases.

6.4.2 Distributions of adjusted parameters

Figure 6.3 shows the distributions of the optimized parameters. The top panels show histograms of Υ_{\star} . The dashed lines indicate $\Upsilon_{\text{disk}} = 0.5 M_{\odot}/L_{\odot}$ and $\Upsilon_{\text{bulge}} = 0.7 M_{\odot}/L_{\odot}$ adopted in McGaugh et al. (2016b) and Lelli et al. (2017b). The optimized stellar mass-to-light ratios are tightly distributed around these values. The median values of Υ_{disk} and Υ_{bulge} are 0.50 and 0.67, respectively. By and large, the best-fit stellar mass-to-light ratios are consistent with the expectations of stellar population synthesis models (Schombert & McGaugh 2014; Meidt et al. 2014; McGaugh 2014; Norris et al. 2016).

Adjusted distances and inclinations are also shown in Figure 6.3 (bottom panels). Galaxies with a low-quality flag in SPARC ($Q=3$, see Lelli et al. 2016a) typically prefer smaller values of D and i with respect to their original values (see black crosses in the figure). After removing these low-quality data, the distributions of D and i are fairly symmetric around the line of unity indicating that there are no major systematics. Hubble flow distances are the least certain and show the largest variation between measured and best-fit distance. More accurate methods (Cepheids, TRGB) show less variation, as expected.

A few galaxies show significant deviations ($> 1 \sigma_D$) from the optimized ones. For example, PGC51017 (with a TRGB distance) is a starburst dwarf galaxy where the rotation curve clearly does not trace the equilibrium gravitational potential (Lelli et al. 2014), thus it is not surprising that the distance is pushed to unphysical values in order to obtain a good fit. This rotation curve has a low-quality flag in SPARC ($Q=3$) and is only included here for the sake of completeness. Another example is NGC3198, which is sometimes regarded as a problematic case for MOND (Gentile et al. 2011, 2013). The MCMC method finds a good fit with $D = 10.4 \pm 0.4$ Mpc, which is consistent with the Cepheid-based distance (13.8 ± 1.4 Mpc) within 2σ .

Table in the appendix lists the optimal parameters and reduced χ^2 for each galaxy in order of declining luminosity. The errors on the fitting parameters are estimated from their posterior distributions using the “std” output in GetDist. These errors are generally smaller than those in the SPARC database because of the combined constraints from the Gaussian priors and the likelihood function.

6.5 Galaxy scaling relations

6.5.1 Radial acceleration relation

The RAR and its residuals, $\log(g_{\text{obs}}) - \log(g_{\text{tot}})$, are plotted in Figure 6.4. To compare them with previous results (McGaugh et al. 2016b; Lelli et al. 2017b), the same selection criteria were adopted: we removed 10 face-on galaxies with $i < 30^\circ$ and 12 galaxies with asymmetric rotation curves that do not trace the equilibrium gravitational potential ($Q = 3$). We also required a minimum precision of 10% in observational velocity ($\delta V_{\text{obs}}/V_{\text{obs}} < 0.1$). This retains 2694 data points out of 3163.

After Υ_* , D , and i were adjusted within the errors, the RAR was extremely tight and had an rms scatter of 0.057 dex. We fit the histogram of the residuals with a Gaussian function (the dashed line in the right panel of Figure 6.4): the fit is acceptable, but there are broad symmetric wings in the residuals that are not captured by a single Gaussian function. Hence, we fit a double Gaussian function. The double Gaussian function substantially improves the fit and fully describes the residual distribution with standard deviations of 0.062 dex and 0.020 dex. The mean values μ are consistent with zero.

Interestingly, the errors on the rotation velocities are not expected to be Gaussian because they are obtained by summing two different contributors (see Swaters et al. 2009; Lelli et al. 2016a): the formal error from fitting the whole disk (driven by data quality and random non-circular motions) and the difference between velocities in the approaching and receding sides of the galaxy (representing global asymmetries and kinematic lopsidedness). The success of the double Gaussian fit suggests that the two Gaussian components perhaps probe these two different sources of errors and hence dominate the total residual scatter over all other possible error sources.

The small residual scatter leaves very little room for any intrinsic scatter because (1) the observational errors in the rotation velocities are not negligible, driving errors in g_{obs} , and (2) there could be additional sources of errors in g_{bar} like the detailed 3D geometry of baryons and possible radial variations in Υ_* . Considering these error sources, the intrinsic scatter in the RAR must be smaller than 0.057 dex.

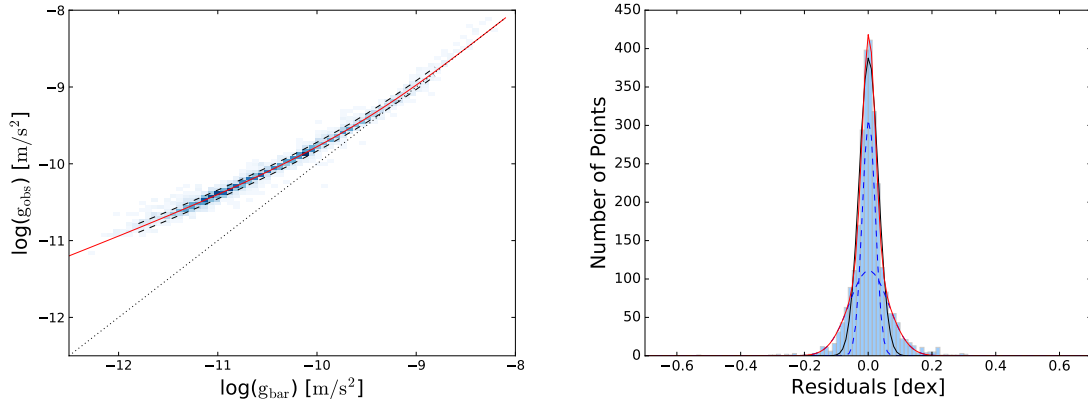


Figure 6.4 RAR (*left*) and the residuals (*right*) with Υ_{\star} , D , and i optimized by the MCMC method. In the left panel, the red solid line represents the mean RAR from Equation 6.3. The black dotted line is the line of unity. 2694 individual data points from 153 SPARC galaxies are represented by the blue color-scale. Black dashed lines show the rms scatter. In the right panel, the histogram of the residuals is fit with both single (black solid line) and double (red solid line) Gaussian functions. Blue dashed lines show the two components of the double Gaussian function.

6.5.2 Baryonic Tully-Fisher relation

The BTFR relates the total baryonic masses of galaxies to their flat rotation velocity. In some sense, this is the asymptotic version of the RAR at large radii (see Sect. 7.1 of Lelli et al. 2017b for details). For $R \rightarrow \infty$, g_{bar} becomes small and Eq. 6.3 gives $g_{\text{obs}} \simeq \sqrt{g_{\text{bar}} g_{\dagger}}$ by Taylor expansion. Since $g_{\text{obs}} = V_{\text{f}}^2/R$ and $g_{\text{bar}} \simeq GM_{\text{bar}}/R^2$, the radial dependence cancels out and we are left with $V_{\text{f}}^4 \propto M_{\text{bar}}$. Thus, a BTFR with slope 4 is built into eq. 6.3.

Here, we fit the BTFR directly to check how well we recover the behavior required by eq. 6.3. In addition to the slope specified by the asymptotic limit of the RAR, we also expect the BTFR to be tighter after fitting Υ_{\star} , D , and i to the RAR. However, this does not necessarily have to happen since the BTFR only considers the flat rotation velocity (V_{f}) and the total baryonic mass (M_{b}), whereas we fit the whole shape of the rotation curve using the full baryonic mass profile. We adopted the same selection criteria as described in Sect. 6.5.1 and removed the galaxies that did not reach a flat rotation velocity as defined by Lelli et al. (2016b). This retained 123 galaxies out of 175 (5 more galaxies with the latest version of SPARC relative to Lelli et al. 2016b).

Figure 6.5 shows a tight BTFR. We used the LTS_LINEFIT program (Cappellari et al.

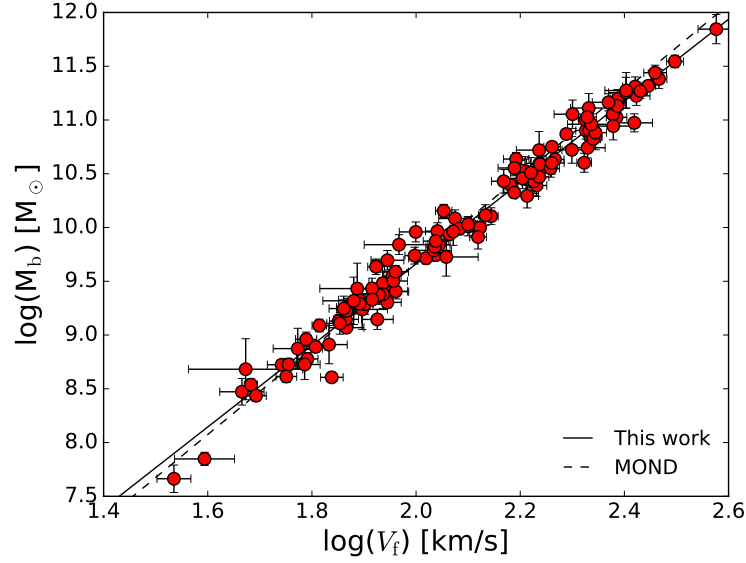


Figure 6.5 Baryonic Tully-Fisher relation with Υ_* , D , and i optimized (red points). The solid line illustrates the fitted BTFR. For reference, the dashed line shows the prediction of MOND: $\log(M_b) = 4 \log(V_f) + \log[X/(a_0 G)]$.

2013) to fit the linear relation

$$\log(M_b) = n \log(V_f) + \log(A). \quad (6.7)$$

LTS_LINEFIT considers errors in both variables and estimates n and A together with the intrinsic scatter around the linear relation. The errors on V_f and M_b were calculated using equations 3 and 5 of Lelli et al. (2016b), but we treated disk and bulge separately. These equations consider the errors on Υ_{disk} , Υ_{bulge} , i , and D , which were estimated from the posterior distributions of the MCMC fits. We also corrected observed quantities such as luminosity and flat rotation velocity according to the adjusted D and i . The fitting results are summarized in Table 6.1. To enable a direct comparison with Lelli et al. (2016b), we also show the case where D and i were kept fixed to the SPARC values and the mass-to-light ratio was constant for all galaxies, but we improved compared to Lelli et al. (2016b) by considering disk ($\Upsilon_* = 0.5$) and bulge ($\Upsilon_* = 0.7$) separately. In this case, the errors on D and i were taken from the SPARC database, while the errors on Υ_{disk} and Υ_{bulge} were assumed to be 0.11 dex for all galaxies. We find a slightly steeper slope than Lelli

Table 6.1 BTFR: The fitted parameters and scatter.

Case	Slope (n)	log(A)	Intrinsic scatter	rms scatter
Constant Υ_\star	3.81 ± 0.08	2.17 ± 0.17	0.108 ± 0.024	0.234
Free Υ_\star, D, i	3.79 ± 0.05	2.08 ± 0.10	0.035 ± 0.019	0.127

et al. (2016b) because bulges have higher mass-to-light ratios than disks and are more common in massive galaxies, increasing M_b at the top end of the relation. Except for this small difference, our results are entirely consistent with those of Lelli et al. (2016b) for the constant Υ_\star case.

The estimated intrinsic scatter of the BTFR is rather small. We estimate a conservative upper limit on the intrinsic scatter as the best-fit value (0.035 dex) plus 3σ (the error on the estimated intrinsic scatter). This gives $\sigma_{\text{intr}} < 0.1$ dex. Satisfying this bound provides a strong constraint on galaxy formation models (e.g., Desmond 2017b).

The fitted slope of the BTFR is close to 3.8 in both cases. Formally, this differs from 4.0 by $\sim 4\sigma$, although slopes consistent with 4 are obtained when we weight the data by the gas fraction (Lelli et al. 2016b). Given that the functional form of Eq. 6.3 guarantees a BTFR with a slope of 4, this discrepancy is puzzling.

Several effects may cause the difference. One is simply that there are uncertainties in the mass-to-light ratios estimated from our fits. This adds scatter to the data, which inevitably lowers the fitted slope.

A more subtle concern is that the measured value of V_f is not quite the same as that implicit in Equation 6.3. We measure V_f in the outer parts of extended rotation curves, and can do so consistently and robustly. However, Equation 6.3 only guarantees a BTFR slope of 4 with V_f in the limit of zero acceleration, or infinite distance from the galaxy. The measurements are made at finite radii. The definition of V_f in Lelli et al. (2016b) (their equation 2) requires measured rotation curves to be flat to within 5%, but there may be some small slope within that limit. It is well known (e.g., Verheijen 2001) that bright galaxies have rotation curves that tend to decline toward V_f , while those of faint galaxies tend to rise toward V_f . It is conceivable that this effect causes a slight systematic variation in the measured V_f with mass that acts to lower the slope. That is to say, the value of V_f we measure empirically may not reach the flat velocity sufficiently well that is implied by the limit $g_{\text{bar}} \rightarrow 0$ assumed in the derivation above.

The geometry of disk galaxies may also have an impact: a thin disk rotates faster than the equivalent spherical distribution (Binney & Tremaine 1987). This is quantified by the factor X that appears in the normalization of the MOND prediction for the BTFR: $A = X/(a_0G)$. The factor $X \rightarrow 1$ as $R \rightarrow \infty$, but on average, $\langle X \rangle = 0.8$ (McGaugh 2005) at the finite radii observed in spiral galaxies. We have assumed that X is the same for all galaxies, but it is conceivable that disk thickness varies with mass so that X is a weak function thereof. This might also affect the slope.

Regardless of which of these effects dominates, it is clear that the slope of the BTFR is steep. It is not 3.0 as one might reasonably assume in Λ CDM (e.g., Mo et al. 1998), nor is it 3.5 (e.g., Bell & de Jong 2001b), as might be expected after adiabatic compression (Bullock et al. 2001). The difference (or lack thereof) between 3.8 and 4.0 may be the limit of what we can hope to discern with astronomical data. The limit is not due to the data themselves, but to systematic effects.

6.6 Does the critical acceleration scale g_{\dagger} vary?

In the previous analysis we have assumed that g_{\dagger} is constant for all galaxies. The small scatter observed around the RAR (McGaugh et al. 2016b; Lelli et al. 2017b) already demonstrates that this is very nearly the case. However, the answer to the question of whether the value of g_{\dagger} is truly constant can be used to distinguish between a scaling relation and a law of nature.

As a further check on this point, we fit all galaxies again, treating g_{\dagger} as an additional free parameter. We made fits with both a flat prior (for the range $0 \leq g_{\dagger} \leq 10^{-9} \text{ m s}^{-2}$) and a Gaussian prior (with $g_{\dagger} = 1.20 \pm 0.02 \text{ m s}^{-2}$: McGaugh et al. 2016b; Lelli et al. 2017b). The cumulative distributions of reduced χ^2 of these fits are shown along with that for fixed g_{\dagger} in Figure 6.6.

Allowing g_{\dagger} to vary from galaxy to galaxy does not improve the fits. In the case of the flat prior, the cumulative distribution of reduced χ^2 is practically indistinguishable from the case of fixed g_{\dagger} , despite the additional freedom. In the case of a Gaussian prior, the reduced χ^2 is even slightly worse because essentially the same fit is recovered (for a similar total χ^2), but the extra parameter increases the number of degrees of freedom, increasing

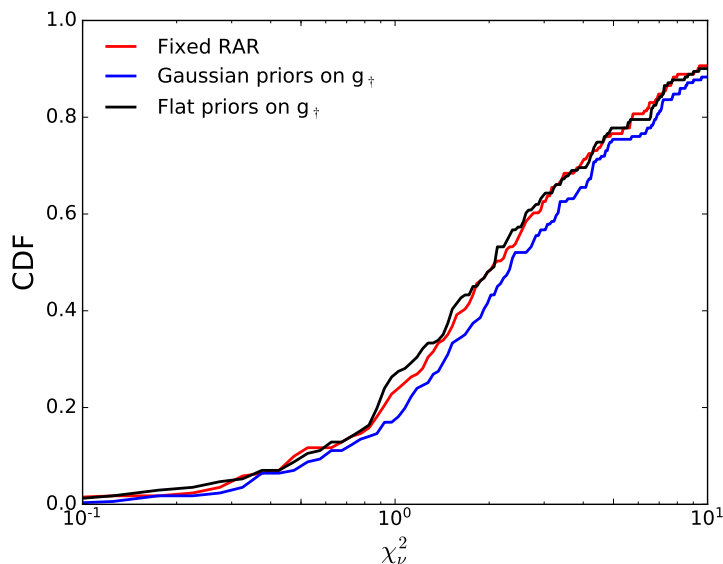


Figure 6.6 Cumulative distributions of reduced χ^2 for fixed g_{\ddagger} fits (red line) and variable g_{\ddagger} fits using flat (black line) and Gaussian priors (blue line).

the reduced χ^2 . The fits are not meaningfully improved by allowing g_{\ddagger} to vary.

The resulting rms scatter remains nearly invariant: 0.054 dex and 0.057 dex when using the flat prior and the Gaussian prior on g_{\ddagger} , respectively. This indicates that the remaining rms scatter is dominated by observational uncertainties on rotation curves and possible intrinsic scatter. As a practical matter, there is no room to accommodate substantial variation in g_{\ddagger} .

We show the distributions of best-fit g_{\ddagger} in Figure 6.7 for both flat and Gaussian priors. The flat prior leads to a wide distribution of g_{\ddagger} , while a Gaussian prior results in a tight distribution around its fiducial value. The Gaussian prior indeed results in a distribution so close to a fixed g_{\ddagger} , with a width smaller than the standard deviation imposed by the prior, that it appears as a δ -function on a scale that accommodates the wide distribution of the flat prior. That the apparent distribution of g_{\ddagger} is so large in the case of the flat prior is indicative of parameter degeneracy: changes in g_{\ddagger} can be compensated for by changes in the mass-to-light ratio (or the nuisance parameters) so that both may vary in an unphysical way to achieve trivial gains in χ^2 .

Adjusting the value of g_{\ddagger} improves neither the fits nor the rms scatter. The data are consistent with the same value for all galaxies. There is no need to invoke variable g_{\ddagger} (cf.

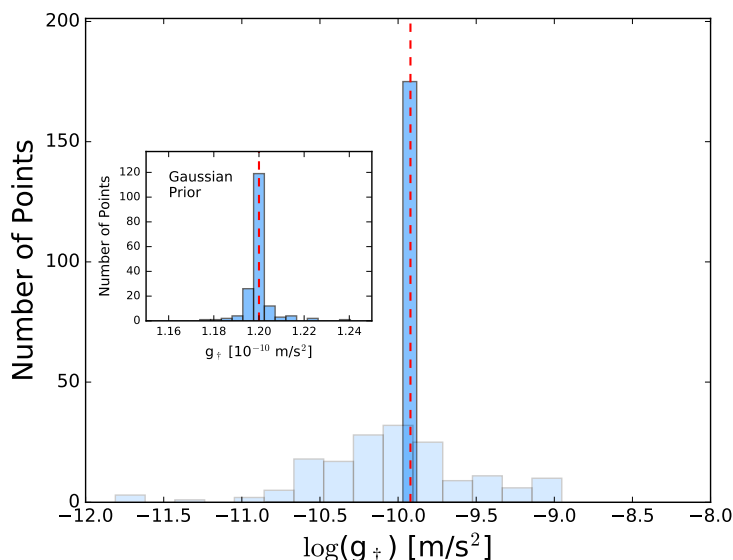


Figure 6.7 Distribution of optimal g_{\dagger} imposing a flat (light blue) and Gaussian (dark blue) prior. The red dashed line marks our fiducial value $1.2 \times 10^{-10} \text{ m/s}^2$. The inset shows the Gaussian prior alone, zoomed in and switched to a linear scale to resolve the distribution. Note the vast difference in scales: the flat prior results in a broad range of g_{\dagger} (although with no improvement in χ^2 , as seen in Figure 6.6), while the Gaussian prior effectively returns a constant g_{\dagger} .

Bottema & Pestaña 2015). To do so would violate the law of parsimony (Occam’s razor).

6.7 Discussion and conclusion

By fitting individual galaxies with the MCMC method, we showed that the intrinsic scatter of the RAR is extremely small. The baryonic matter distribution can reproduce the rotation curve very well, and vice versa.

The tightness of the RAR provides a challenge for the standard Λ CDM cosmology. Recent studies claim that the RAR is a natural product of galaxy formation in Λ CDM (Keller & Wadsley 2017; Ludlow et al. 2017), but none of these studies have properly taken into account observational effects when comparing theory and observations. There are two major issues: (1) general confusion between the concepts of observed and intrinsic scatter, and (2) oversampling of simulated rotation curves. Keller & Wadsley (2017) analyzed 32 galaxies from the MUGS2 “zoom-in” hydrodynamic simulations and argued that the dis-

sipative collapse of baryons can result in a relation with a scatter of 0.06 dex. Similarly, Ludlow et al. (2017) analyzed a suite of simulated galaxies from the EAGLE project and found a relation with a scatter of 0.09 dex. However, these values cannot be compared with the observed scatter because (1) measurement errors are not added to the simulated galaxies and are not properly propagated, and (2) the simulated rotation curves are not sampled with the same number of resolution elements as in the observations. Both effects can significantly underpredict the scatter expected from cosmological simulations. Oversampling the same error-free simulated galaxy over and over can artificially decrease the expected scatter around the mean relation.

In contrast, Desmond (2017a) took both radial sampling and observational errors into account (see also Di Cintio & Lelli 2016). Desmond (2017a) found that fiducial Λ CDM models significantly overpredict the observed scatter around the mass discrepancy-acceleration relation by $\sim 3.5 \sigma$. This discrepancy remains even if one assumes a perfect 1:1 relation between halo mass and stellar mass of galaxies with no scatter. Hence, this problem seems to be due to the stochastic hierarchical formation of DM halos, independent of baryonic physics.

The detailed shape of the RAR is also important. Ludlow et al. (2017) fit the Equation 6.3 to their simulated galaxies, but found a value of $g_{\dagger} = 2.6 \times 10^{-10} \text{ m s}^{-2}$ instead of $g_{\dagger} = 1.2 \pm 0.02 \times 10^{-10} \text{ m s}^{-2}$. This is a 70σ discrepancy. Recently, Tenneti et al. (2018) analyzed galaxies from the MassiveBlack-II simulation. They also found a correlation between g_{tot} and g_{bar} , but this is better fit by a power law with a width of ~ 0.1 dex rather than by Equation 3. Hence, the detailed properties of the RAR (shape and scatter) remain an open issue for Λ CDM models of galaxy formation.

We here reported an rms scatter of 0.057 dex after marginalizing over the uncertainties due to mass-to-light ratio, galaxy distance, and disk inclination. This observed scatter is a hard upper limit to the intrinsic scatter since the errors on the observed velocities are non-negligible. This is hard to understand in a Λ CDM scenario since the diverse formation histories of galaxies must necessarily introduce some scatter on the relation, as demonstrated by the existing cosmological simulations.

In order to reconcile the conundrum that the standard cold dark matter faces, some new dark sectors have been proposed, such as dipolar DM particles subjected to gravitational

polarization (Blanchet & Le Tiec 2008, 2009), dark fluids (Zhao & Li 2010; Khoury 2015), dissipative DM particles (Chashchina et al. 2017), or fifth forces (Burrage et al. 2017). To be viable, such hypotheses must explain the shape, amplitude, and negligible scatter of the RAR. The coupling between the baryonic matter and dark matter must be rather strong to explain these observations.

On the other hand, the tight RAR could be easily understood in MOND (Milgrom 1983). MOND dictates that the equations of motions become scale-invariant at accelerations $a < a_0$, where a_0 corresponds to g_{\ddagger} in Equation 6.3 (Milgrom 2009). Thus, Equation 6.3 is related to the interpolation function $\nu(g_{\text{bar}}/a_0)$ of MOND. The scale invariance can be achieved in two ways: modified gravity (MG) by changing the Poisson equation (Bekenstein & Milgrom 1984; Milgrom 2010), and modified inertia (MI) by changing the Second Law of Newton (Milgrom 1994). MI requires the relation $g_{\text{obs}} = \nu(g_{\text{bar}}/a_0)g_{\text{bar}}$ to be true for circular orbits, leading to zero intrinsic scatter in the RAR of rotating disk galaxies (Milgrom 1994). MG requires the system to be spherically symmetric to hold precisely to the acceleration relation (Bekenstein & Milgrom 1984). Thus, the predicted g_{tot} of disk galaxies can show subtle differences in MG (Brada & Milgrom 1995; Milgrom 2012), and some non-zero intrinsic scatter could be introduced. Our results suggest a preference for the MI theory.

Other modified gravity theories such as emergent gravity could also potentially explain the RAR (Verlinde 2017). However, Lelli et al. (2017a) shows that the RAR predicted by this theory has significant intrinsic scatter and the residuals should correlate with radius, which contradicts the data.

The extremely small intrinsic scatter of the RAR provides a tool for testing various theories of modified gravity or dark matter. It also provides key insights toward the path for finally solving the “dark matter problem”.

6.8 Appendix A¹: Flat priors vs. physically motivated priors in MCMC simulations

In Section 6.6, I show the distributions of best-fit g_{\dagger} imposing both flat priors and strong Gaussian priors. These two priors lead to significantly different distributions of g_{\dagger} . Though we have stressed the importance of using Gaussian priors, some authors have used flat priors with hard boundaries to argue against a constant acceleration scale (e.g. see Rodrigues et al. 2018). Their argument is simple: since we impose a strong Gaussian prior, it is expected that we get an almost constant g_{\dagger} , i.e. the result is imposed artificially rather than naturally shows up from the data. More generally speaking, flat priors have been given higher priority by many astronomers (see the statistics in Tak et al. 2018), since they do not introduce artificial selections. In fact, artificial selection has been extensively applied in physics. For example, many physical equations have multiple solutions. Physicists simply take the physical solution while ignore the nonphysical ones. This kind of selection is made based on the understanding of physical phenomenon, which is not always automatically implemented in mathematical equations.

The MCMC simulation with flat priors is similar to multiple-solution equations. When fitting parameters are let free totally, the resultant posterior distributions often show strong degeneracies, which means there are multiple solutions corresponding to nearly the same fit quality. The resultant probability distribution may not be well defined if improper priors are imposed as warned by Tak et al. (2018). It requires us to pick the physically reasonable solutions, since MCMC would simply select the solution based on the slight difference in the ill-defined probability function. It is difficult to pick a reasonable solution from infinite ones. The simplest way is to impose a physically motivated prior, which implements our physical understandings, so that MCMC can return right solutions. The philosophy is then to check if the imposed priors result in the same likelihood, i.e. fit quality, as flat priors. If not, either the prior or the model itself is problematic.

Figure 6.6 shows that the fit quality is nearly the same imposing Gaussian or flat priors on g_{\dagger} . It implies that constant g_{\dagger} is indeed one of the solutions when imposing flat priors, and automatically selected by MCMC due to the imposed prior. However, one should keep

¹This appendix is not in the published paper.

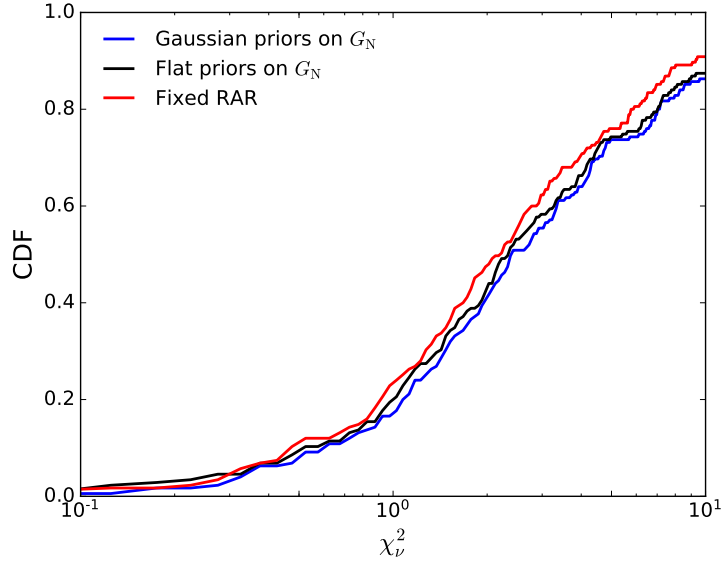


Figure 6.8 Cumulative distributions of reduced χ^2 for fixed G_N fits (red line) and variable G_N fits using flat (black line) and Gaussian priors (blue line).

in mind that we do not prove g_{\ddagger} must be but can be a constant.

To demonstrate how badly flat priors could mislead us, I add Newtonian constant of gravitation $G_N = 4.3 \times 10^{-6} \text{ kpc km}^2 \text{ s}^{-2} \text{ M}_{\odot}^{-1}$, as a fitting parameter instead of g_{\ddagger} , together with stellar mass-to-light ratio, galaxy distance, disk inclination. This test is hence similar to that shown in Section 6.6. The only difference is that g_{\ddagger} is replaced with G_N . I impose on G_N both flat prior within $(10^{-8}, 10^{-4}) \text{ kpc km}^2 \text{ s}^{-2} \text{ M}_{\odot}^{-1}$, and Gaussian prior with a standard deviation of $0.2 \times 10^{-6} \text{ kpc km}^2 \text{ s}^{-2} \text{ M}_{\odot}^{-1}$. The cumulative distributions of reduced χ^2_v for both priors are shown in Figure 6.8. The two priors lead to nearly the same fit quality, but slightly worse than the fixed RAR due to more fitting parameters. It implies there is no added value to vary G_N from galaxy to galaxy. However, the resultant distributions of G_N are significantly different (see Figure 6.9). The Gaussian prior recovers a constant G_N , while the flat prior gives a wide distribution spanning ~ 3 dex. Therefore, if one believes the results from imposing flat prior, there would be a problem called "Absence of a fundamental gravitational constant in galaxies" (similar to Rodrigues et al. 2018), which would rule out Newtonian gravity.

One potential defect in the above test is that the RAR is not a law as solid as Newtonian Gravity, the latter has been proved accurately in solar system. To carry out a more robust

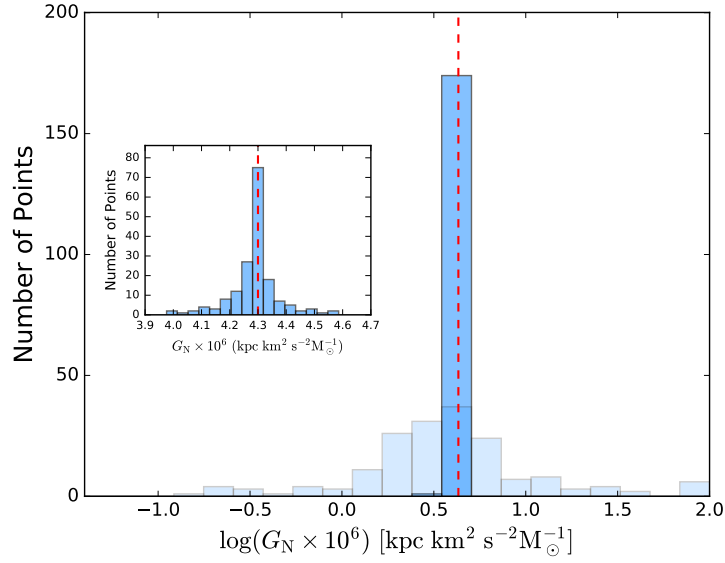


Figure 6.9 Distribution of optimal G_N imposing a flat (light blue) and Gaussian (dark blue) prior. The red dashed line marks the fiducial value $4.3 \times 10^{-6} \text{ kpc km}^2 \text{ s}^{-2} M_{\odot}^{-1}$. The inset shows the Gaussian prior alone, zoomed in and switched to a linear scale to resolve the distribution. Note the vast difference in scales: the flat prior results in a broad range of G_N (although with no improvement in χ^2 , as seen in Figure 6.8), while the Gaussian prior effectively returns a constant G_N .

test, one needs to investigate exoplanets where Newtonian gravity applies. However, one can simply use the solar system assuming the distance of each solar planet is uncertain within some range. If G_N is allowed to vary from planet to planet, any deviation in distance from the true value would be compensated by varying G_N . This would lead to a wide distribution of G_N . But if one fixes G_N , Newtonian Gravity can describe all solar planets with reasonable distance determinations.

To summarize, flat priors in MCMC simulations can show the maximum ability of a model in fitting data. But one has to be aware of that they often overfit data with unreliable parameter estimations. Physically motivated priors implement our physical understandings and hence provide solid estimations of parameters. Its success depends on how reliable the priors are. Therefore, one needs to check the resultant distributions of fitting parameters as well as fit quality.

6.9 Appendix B: Rotation curve fits and best-fit parameters

In this Section, I tabulate the best-fit parameter using the radial acceleration relation (fixed g_{\ddagger} and G_N) as well as the rotation curve fits of 175 galaxies. The RAR fits and the posterior distributions are available in the published paper Li et al. (2018) and the SPARC website ².

²astroweb.case.edu/SPARC

Table 6.2: Maximum posterior parameters and reduced χ^2 of individual rotation curve fits to the RAR. $L_{[3.6]}$, D_0 and i_0 are the original luminosity, distance, and inclination from the SPARC database. Galaxies are ordered by decreasing luminosity.

SPARC ID	Galaxy name	$\log(L_{[3.6]})$ (L_\odot)	Υ_{disk} (M_\odot/L_\odot)	Υ_{bulge} (M_\odot/L_\odot)	Distance (Mpc)	D/D ₀	Inclination (deg.)	i/i_0	χ^2_ν
001	UGC02487	11.69	1.83 ± 0.20	0.91 ± 0.18	63.7 ± 9.4	0.92	31.2 ± 2.8	0.87	4.482
002	UGC02885	11.61	0.45 ± 0.06	0.97 ± 0.08	82.7 ± 5.5	1.03	64.7 ± 3.4	1.01	0.858
003	NGC6195	11.59	0.32 ± 0.06	0.85 ± 0.07	115 ± 11	0.90	57.0 ± 4.2	0.92	2.258
004	UGC11455	11.57	0.38 ± 0.04	...	84.7 ± 5.4	1.08	90.0 ± 0.6	1.00	6.545
005	NGC5371	11.53	3.30 ± 0.29	...	7.44 ± 0.68	0.19	52.7 ± 2.0	0.99	10.156
006	NGC2955	11.50	0.37 ± 0.06	0.84 ± 0.08	95.3 ± 8.9	0.97	52.7 ± 4.3	0.94	3.906
007	NGC0801	11.49	1.33 ± 0.12	...	33.0 ± 2.0	0.41	79.9 ± 1.0	1.00	7.753
008	ESO563-G021	11.49	0.43 ± 0.04	...	88.0 ± 4.9	1.45	84.0 ± 2.7	1.01	28.836
009	UGC09133	11.45	1.64 ± 0.06	1.10 ± 0.02	36.3 ± 6.9	0.64	45.7 ± 5.4	0.86	6.937
010	UGC02953	11.41	0.61 ± 0.01	0.62 ± 0.01	18.1 ± 1.9	1.10	50.4 ± 3.5	1.01	5.661
011	NGC7331	11.40	0.32 ± 0.02	0.60 ± 0.12	15.7 ± 0.6	1.07	75.3 ± 2.0	1.00	1.289
012	NGC3992	11.36	0.76 ± 0.10	...	21.3 ± 1.7	0.90	55.1 ± 1.9	0.98	3.465
013	NGC6674	11.33	0.95 ± 0.11	1.30 ± 0.45	43.2 ± 6.8	0.84	50.5 ± 5.2	0.94	10.638
014	NGC5985	11.32	0.63 ± 0.10	3.32 ± 0.30	46.7 ± 4.1	1.18	60.3 ± 2.0	1.01	6.974
015	NGC2841	11.27	0.81 ± 0.05	0.93 ± 0.05	15.5 ± 0.6	1.10	81.9 ± 5.2	1.08	1.515
016	IC4202	11.25	1.60 ± 0.19	0.34 ± 0.04	64.4 ± 5.2	0.64	90.0 ± 0.6	1.00	41.908
017	NGC5005	11.25	0.54 ± 0.07	0.56 ± 0.07	16.6 ± 1.3	0.98	67.9 ± 2.0	1.00	0.091
018	NGC5907	11.24	1.08 ± 0.07	...	10.5 ± 0.4	0.61	87.5 ± 1.8	0.99	7.730
019	UGC05253	11.23	0.63 ± 0.05	0.69 ± 0.03	22.5 ± 3.5	0.98	36.8 ± 3.2	1.00	4.747
020	NGC5055	11.18	0.56 ± 0.01	...	9.83 ± 0.30	0.99	43.8 ± 0.9	0.80	7.415
021	NGC2998	11.18	0.82 ± 0.10	...	48.8 ± 3.8	0.72	57.2 ± 2.0	0.99	2.940
022	UGC11914	11.18	0.22 ± 0.03	0.48 ± 0.04	24.0 ± 3.4	1.42	38.4 ± 3.1	1.24	1.731
023	NGC3953	11.15	0.59 ± 0.10	...	16.0 ± 1.8	0.89	61.9 ± 1.0	1.00	3.424
024	UGC12506	11.14	1.12 ± 0.16	...	85.3 ± 6.3	0.85	85.4 ± 3.4	0.99	1.981
025	NGC0891	11.14	0.33 ± 0.02	0.40 ± 0.05	11.4 ± 0.4	1.15	90.0 ± 0.6	1.00	7.368
026	UGC06614	11.09	0.51 ± 0.12	0.50 ± 0.09	88.6 ± 8.8	1.00	32.8 ± 2.6	0.91	1.164
027	UGC02916	11.09	1.57 ± 0.24	0.73 ± 0.06	54.1 ± 7.9	0.83	44.5 ± 4.1	0.89	11.652
028	UGC03205	11.06	0.73 ± 0.06	1.32 ± 0.07	42.5 ± 3.1	0.85	66.2 ± 3.9	0.99	4.196
029	NGC5033	11.04	1.03 ± 0.08	0.43 ± 0.06	12.7 ± 0.5	0.81	65.9 ± 1.0	1.00	8.024
030	NGC4088	11.03	0.40 ± 0.07	...	13.4 ± 1.3	0.74	68.4 ± 2.0	0.99	0.664
031	NGC4157	11.02	0.43 ± 0.06	0.64 ± 0.15	15.7 ± 1.3	0.87	81.7 ± 3.0	1.00	0.720

Table 6.2 – Continued

SPARC ID	Galaxy name	$\log(L_{[3.6]})$ (L_{\odot})	Υ_{disk} (M_{\odot}/L_{\odot})	Υ_{bulge} (M_{\odot}/L_{\odot})	Distance (Mpc)	D/D ₀	Inclination (deg.)	i/i_0	χ^2_{ν}
032	UGC03546	11.01	0.68 ± 0.08	0.51 ± 0.04	25.4 ± 3.4	0.88	54.1 ± 4.5	0.98	0.907
033	UGC06787	10.99	0.45 ± 0.04	0.28 ± 0.01	37.7 ± 1.8	1.77	68.6 ± 2.7	1.04	20.814
034	NGC4051	10.98	0.45 ± 0.09	...	15.3 ± 1.9	0.85	47.1 ± 2.8	0.96	2.491
035	NGC4217	10.93	1.17 ± 0.20	0.17 ± 0.02	18.2 ± 1.5	1.01	86.1 ± 1.9	1.00	3.171
036	NGC3521	10.93	0.46 ± 0.05	...	8.54 ± 0.83	1.11	75.3 ± 4.9	1.00	0.510
037	NGC2903	10.91	0.21 ± 0.01	...	11.0 ± 0.5	1.67	67.6 ± 2.8	1.02	20.637
038	NGC2683	10.91	0.55 ± 0.06	0.73 ± 0.18	9.44 ± 0.46	0.96	77.0 ± 5.2	0.96	3.370
039	NGC4013	10.90	0.35 ± 0.05	0.79 ± 0.17	18.1 ± 1.0	1.01	89.0 ± 0.8	1.00	1.807
040	NGC7814	10.87	1.17 ± 0.12	0.52 ± 0.04	15.8 ± 0.6	1.10	90.0 ± 0.6	1.00	1.334
041	UGC06786	10.87	0.27 ± 0.02	0.34 ± 0.01	57.2 ± 2.6	1.95	67.7 ± 2.6	1.06	1.389
042	NGC3877	10.86	0.40 ± 0.07	...	16.8 ± 1.7	0.93	76.0 ± 1.0	1.00	10.221
043	NGC0289	10.86	0.92 ± 0.09	...	14.8 ± 2.9	0.71	42.9 ± 4.7	0.93	2.132
044	NGC1090	10.86	0.74 ± 0.07	...	24.3 ± 1.8	0.66	63.5 ± 3.0	0.99	2.778
045	NGC3726	10.85	0.47 ± 0.07	...	13.8 ± 1.3	0.77	52.0 ± 2.0	0.98	2.982
046	UGC09037	10.84	0.20 ± 0.02	...	80.2 ± 5.9	0.96	63.3 ± 4.1	0.97	2.259
047	NGC6946	10.82	0.64 ± 0.05	0.71 ± 0.04	4.18 ± 0.44	0.76	37.7 ± 2.0	0.99	1.525
048	NGC4100	10.77	0.76 ± 0.10	...	15.0 ± 1.2	0.83	72.7 ± 2.0	1.00	1.658
049	NGC3893	10.77	0.45 ± 0.06	...	19.4 ± 1.7	1.08	49.5 ± 1.9	1.01	0.997
050	UGC06973	10.73	0.17 ± 0.02	0.39 ± 0.07	23.0 ± 1.6	1.28	72.7 ± 2.8	1.02	15.579
051	ESO079-G014	10.71	0.50 ± 0.09	...	31.6 ± 3.0	1.10	79.4 ± 4.7	1.00	4.334
052	UGC08699	10.70	0.63 ± 0.10	0.70 ± 0.05	40.4 ± 4.4	1.03	73.2 ± 7.5	1.00	0.989
053	NGC4138	10.64	0.55 ± 0.11	0.69 ± 0.17	17.9 ± 1.8	0.99	53.0 ± 2.8	1.00	2.492
054	NGC3198	10.58	0.77 ± 0.03	...	10.4 ± 0.4	0.75	71.1 ± 3.1	0.97	2.057
055	NGC3949	10.58	0.44 ± 0.07	...	17.3 ± 1.9	0.96	54.8 ± 2.0	1.00	0.547
056	NGC6015	10.51	1.12 ± 0.06	...	11.8 ± 0.6	0.69	59.8 ± 2.0	1.00	10.873
057	NGC3917	10.34	0.55 ± 0.09	...	16.9 ± 1.5	0.94	78.9 ± 2.0	1.00	4.603
058	NGC4085	10.34	0.35 ± 0.06	...	16.8 ± 1.8	0.93	81.9 ± 2.0	1.00	9.088
059	NGC4389	10.33	0.30 ± 0.07	...	11.6 ± 2.2	0.64	42.8 ± 4.1	0.86	9.313
060	NGC4559	10.29	0.52 ± 0.06	...	6.66 ± 0.36	0.74	67.0 ± 1.0	1.00	0.496
061	NGC3769	10.27	0.41 ± 0.07	...	16.2 ± 1.3	0.90	69.8 ± 2.0	1.00	0.949
062	NGC4010	10.24	0.36 ± 0.07	...	18.2 ± 1.5	1.01	89.0 ± 0.8	1.00	2.741
063	NGC3972	10.16	0.50 ± 0.08	...	19.2 ± 1.7	1.07	77.0 ± 1.0	1.00	2.074
064	UGC03580	10.12	0.29 ± 0.02	0.11 ± 0.01	22.4 ± 1.6	1.08	63.4 ± 3.8	1.01	2.291

Table 6.2 – Continued

SPARC ID	Galaxy name	$\log(L_{[3.6]})$ (L_{\odot})	Υ_{disk} (M_{\odot}/L_{\odot})	Υ_{bulge} (M_{\odot}/L_{\odot})	Distance (Mpc)	D/D ₀	Inclination (deg.)	i/i_0	χ^2_v
065	NGC6503	10.11	0.45 ± 0.02	...	6.47 ± 0.16	1.03	74.6 ± 1.8	1.01	2.979
066	UGC11557	10.08	0.42 ± 0.11	...	22.5 ± 6.2	0.93	19.6 ± 4.0	0.65	3.175
067	UGC00128	10.08	2.49 ± 0.12	...	58.1 ± 9.3	0.90	40.7 ± 4.3	0.71	6.254
068	F579-V1	10.07	0.63 ± 0.14	...	89.6 ± 8.9	1.00	26.3 ± 2.2	1.01	2.559
069	NGC4183	10.03	0.79 ± 0.14	...	13.0 ± 0.9	0.72	81.8 ± 2.0	1.00	1.132
070	F571-8	10.01	0.11 ± 0.02	...	102 ± 8	1.92	87.1 ± 2.9	1.02	41.610
071	NGC2403	10.00	0.51 ± 0.01	...	3.33 ± 0.11	1.05	66.1 ± 2.1	1.05	14.142
072	UGC06930	9.95	0.63 ± 0.13	...	17.3 ± 2.3	0.96	28.8 ± 2.5	0.90	1.233
073	F568-3	9.92	0.41 ± 0.09	...	82.1 ± 8.1	1.00	38.3 ± 3.2	0.96	3.064
074	UGC01230	9.88	0.72 ± 0.17	...	53.1 ± 10.6	0.99	18.4 ± 2.4	0.84	2.951
075	NGC0247	9.87	0.78 ± 0.08	...	3.23 ± 0.16	0.87	68.9 ± 3.1	0.93	3.060
076	NGC7793	9.85	0.55 ± 0.09	...	3.60 ± 0.18	1.00	43.3 ± 2.9	0.92	1.013
077	UGC06917	9.83	0.54 ± 0.09	...	18.4 ± 1.5	1.02	56.1 ± 1.9	1.00	1.315
078	NGC1003	9.83	0.37 ± 0.03	...	10.8 ± 0.9	0.94	66.9 ± 4.9	1.00	4.669
079	F574-1	9.82	0.71 ± 0.13	...	95.7 ± 8.7	0.99	62.6 ± 6.6	0.96	2.501
080	F568-1	9.80	0.61 ± 0.13	...	95.2 ± 8.8	1.05	32.4 ± 2.2	1.24	1.287
081	UGC06983	9.72	0.77 ± 0.11	...	17.3 ± 1.2	0.96	49.0 ± 1.0	1.00	1.392
082	UGC05986	9.67	0.31 ± 0.04	...	14.6 ± 0.8	1.69	90.0 ± 1.8	1.00	3.997
083	NGC0055	9.67	0.19 ± 0.03	...	1.74 ± 0.07	0.82	71.3 ± 3.2	0.93	1.579
084	ESO116-G012	9.63	0.35 ± 0.04	...	17.9 ± 0.9	1.38	74.5 ± 2.9	1.01	2.444
085	UGC07323	9.61	0.41 ± 0.09	...	6.87 ± 0.96	0.86	46.5 ± 3.0	0.99	0.660
086	UGC05005	9.61	0.45 ± 0.10	...	50.8 ± 10.1	0.95	34.6 ± 4.8	0.84	0.315
087	F561-1	9.61	0.52 ± 0.13	...	65.2 ± 10.1	0.98	13.5 ± 1.4	0.56	1.564
088	NGC0024	9.59	1.01 ± 0.11	...	7.55 ± 0.32	1.03	66.1 ± 2.6	1.03	0.850
089	F568-V1	9.58	0.81 ± 0.16	...	83.7 ± 7.4	1.04	51.1 ± 4.4	1.28	1.042
090	UGC06628	9.57	0.52 ± 0.13	...	14.4 ± 4.7	0.95	10.6 ± 2.9	0.53	0.851
091	UGC02455	9.56	0.33 ± 0.09	...	2.01 ± 0.50	0.29	49.3 ± 5.3	0.97	6.549
092	UGC07089	9.55	0.36 ± 0.08	...	13.3 ± 1.2	0.74	79.4 ± 3.1	0.99	0.426
093	UGC05999	9.53	0.48 ± 0.11	...	47.2 ± 9.3	0.99	19.6 ± 2.4	0.89	5.693
094	NGC2976	9.53	0.35 ± 0.08	...	3.58 ± 0.18	1.00	62.5 ± 6.4	1.02	1.730
095	UGC05750	9.52	0.48 ± 0.11	...	47.5 ± 9.6	0.81	53.9 ± 8.7	0.84	1.352
096	NGC0100	9.51	0.28 ± 0.06	...	15.9 ± 1.5	1.18	89.0 ± 0.8	1.00	1.286
097	UGC00634	9.48	0.49 ± 0.09	...	31.3 ± 6.2	1.01	37.4 ± 4.7	1.01	2.425

Table 6.2 – Continued

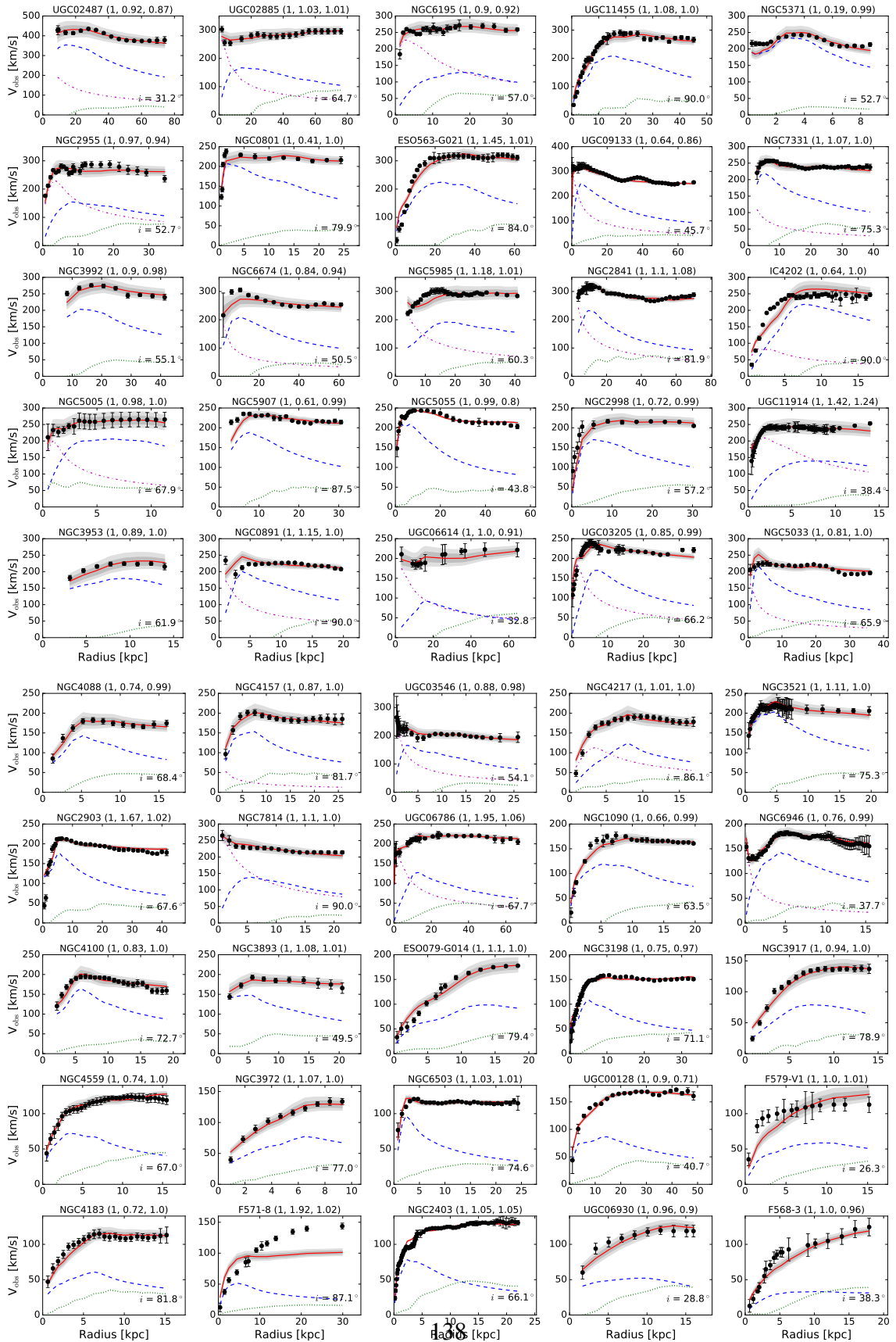
SPARC ID	Galaxy name	$\log(L_{[3.6]})$ (L_{\odot})	Υ_{disk} (M_{\odot}/L_{\odot})	Υ_{bulge} (M_{\odot}/L_{\odot})	Distance (Mpc)	D/D ₀	Inclination (deg.)	i/i_0	χ^2_{ν}
098	F563-V2	9.48	0.59 ± 0.14	...	63.4 ± 10.5	1.06	36.8 ± 4.3	1.27	0.991
099	NGC5585	9.47	0.22 ± 0.01	...	7.81 ± 0.46	1.11	51.2 ± 1.9	1.00	6.817
100	NGC0300	9.47	0.40 ± 0.05	...	2.09 ± 0.10	1.00	47.4 ± 2.1	1.13	0.906
101	UGC06923	9.46	0.42 ± 0.09	...	16.5 ± 1.5	0.92	64.7 ± 2.0	1.00	1.624
102	F574-2	9.46	0.49 ± 0.12	...	88.1 ± 9.0	0.99	13.1 ± 1.8	0.44	0.092
103	UGC07125	9.43	0.92 ± 0.15	...	7.45 ± 0.40	0.38	89.9 ± 1.8	1.00	1.599
104	UGC07524	9.39	0.79 ± 0.12	...	4.50 ± 0.23	0.95	38.8 ± 1.6	0.84	1.839
105	UGC06399	9.36	0.53 ± 0.10	...	19.0 ± 1.5	1.05	75.1 ± 2.0	1.00	0.520
106	UGC07151	9.36	0.50 ± 0.05	...	6.35 ± 0.28	0.92	90.0 ± 2.0	1.00	3.751
107	F567-2	9.33	0.56 ± 0.13	...	78.2 ± 11.8	0.99	14.5 ± 1.7	0.73	2.204
108	UGC04325	9.31	0.94 ± 0.19	...	10.2 ± 1.4	1.07	41.3 ± 2.7	1.01	9.429
109	UGC00191	9.30	1.10 ± 0.13	...	12.5 ± 2.5	0.73	43.0 ± 4.7	0.96	3.842
110	F563-1	9.28	0.56 ± 0.12	...	51.7 ± 8.2	1.06	27.4 ± 2.5	1.10	1.499
111	F571-V1	9.27	0.50 ± 0.12	...	80.0 ± 8.0	1.00	27.8 ± 2.0	0.93	0.288
112	UGC07261	9.24	0.56 ± 0.12	...	12.8 ± 3.4	0.98	29.0 ± 5.0	0.97	0.827
113	UGC10310	9.24	0.62 ± 0.14	...	13.4 ± 3.3	0.88	31.7 ± 4.4	0.93	1.762
114	UGC02259	9.24	1.14 ± 0.19	...	10.0 ± 1.3	0.95	40.9 ± 2.8	1.00	7.221
115	F583-4	9.23	0.48 ± 0.11	...	50.3 ± 8.8	0.94	51.2 ± 7.0	0.93	0.134
116	UGC12732	9.22	1.07 ± 0.14	...	11.4 ± 2.6	0.86	36.8 ± 4.7	0.94	0.496
117	UGC06818	9.20	0.29 ± 0.06	...	14.8 ± 1.6	0.82	74.3 ± 3.1	0.99	5.387
118	UGC04499	9.19	0.51 ± 0.10	...	9.85 ± 1.06	0.79	49.5 ± 3.0	0.99	1.776
119	F563-V1	9.19	0.48 ± 0.12	...	39.3 ± 13.6	0.73	29.4 ± 10.0	0.49	0.875
120	UGC06667	9.15	1.00 ± 0.20	...	23.8 ± 1.3	1.32	89.0 ± 0.8	1.00	5.357
121	UGC02023	9.12	0.49 ± 0.12	...	10.0 ± 3.1	0.96	14.3 ± 3.4	0.75	1.147
122	UGC04278	9.12	0.53 ± 0.07	...	10.3 ± 0.7	1.08	89.9 ± 1.8	1.00	2.597
123	UGC12632	9.11	1.08 ± 0.19	...	6.72 ± 0.84	0.69	45.2 ± 3.0	0.98	1.803
124	UGC08286	9.10	1.05 ± 0.07	...	6.45 ± 0.18	0.99	90.0 ± 1.8	1.00	2.637
125	UGC07399	9.06	0.59 ± 0.10	...	15.2 ± 1.2	1.81	58.1 ± 2.6	1.06	1.895
126	NGC4214	9.06	0.46 ± 0.11	...	2.87 ± 0.14	1.00	18.5 ± 1.2	1.23	1.062
127	UGC05414	9.05	0.41 ± 0.09	...	7.45 ± 0.82	0.79	54.6 ± 3.0	0.99	1.299
128	UGC08490	9.01	0.86 ± 0.11	...	4.81 ± 0.35	1.03	50.7 ± 2.4	1.01	0.337
129	IC2574	9.01	0.07 ± 0.00	...	3.78 ± 0.19	0.97	64.5 ± 3.4	0.86	1.440
130	UGC06446	8.99	1.04 ± 0.17	...	11.7 ± 1.2	0.97	50.9 ± 2.9	1.00	0.996

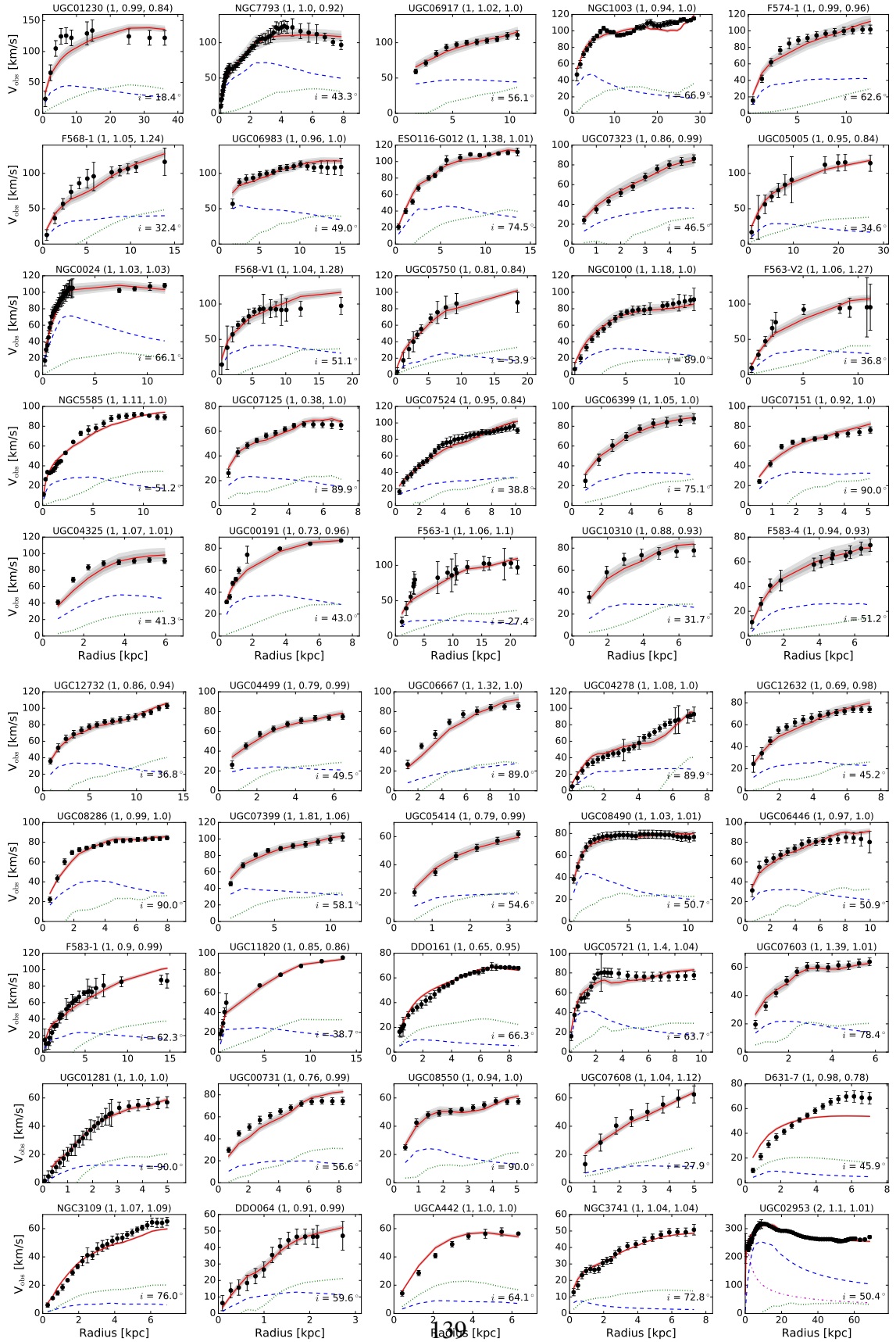
Table 6.2 – Continued

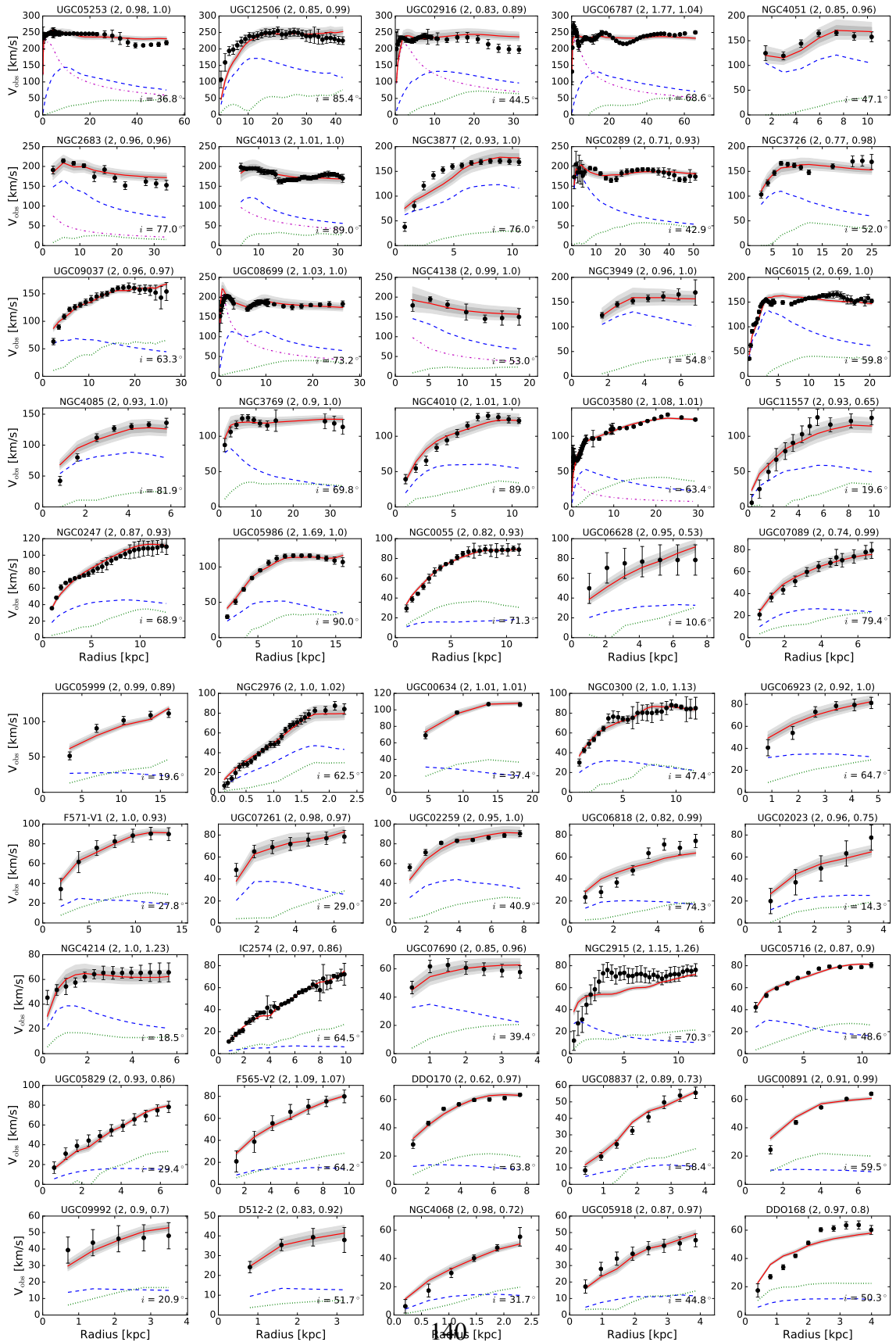
SPARC ID	Galaxy name	$\log(L_{[3.6]})$ (L_{\odot})	Υ_{disk} (M_{\odot}/L_{\odot})	Υ_{bulge} (M_{\odot}/L_{\odot})	Distance (Mpc)	D/D ₀	Inclination (deg.)	i/i_0	χ^2_{ν}
131	F583-1	8.99	0.91 ± 0.14	...	31.9 ± 3.5	0.90	62.3 ± 4.9	0.99	2.663
132	UGC11820	8.99	1.01 ± 0.11	...	15.5 ± 4.2	0.85	38.7 ± 6.7	0.86	1.988
133	UGC07690	8.93	0.60 ± 0.13	...	6.90 ± 1.44	0.85	39.4 ± 4.4	0.96	1.525
134	UGC04305	8.87	0.71 ± 0.16	...	3.44 ± 0.17	1.00	18.3 ± 0.9	0.46	2.024
135	NGC2915	8.81	0.32 ± 0.05	...	4.68 ± 0.17	1.15	70.3 ± 2.7	1.26	4.017
136	UGC05716	8.77	1.41 ± 0.07	...	18.6 ± 4.0	0.87	48.6 ± 7.2	0.90	5.664
137	UGC05829	8.75	0.60 ± 0.14	...	8.03 ± 2.28	0.93	29.4 ± 5.5	0.86	0.454
138	F565-V2	8.75	0.50 ± 0.12	...	56.7 ± 6.9	1.09	64.2 ± 7.2	1.07	0.474
139	DDO161	8.74	0.23 ± 0.04	...	4.84 ± 0.97	0.65	66.3 ± 9.8	0.95	1.468
140	DDO170	8.73	0.79 ± 0.15	...	9.48 ± 1.47	0.62	63.8 ± 7.3	0.97	4.917
141	NGC1705	8.73	1.22 ± 0.13	...	6.23 ± 0.26	1.09	86.9 ± 3.8	1.09	0.373
142	UGC05721	8.73	0.62 ± 0.08	...	8.66 ± 0.75	1.40	63.7 ± 4.3	1.04	1.824
143	UGC08837	8.70	0.20 ± 0.03	...	6.39 ± 0.38	0.89	58.4 ± 4.2	0.73	2.349
144	UGC07603	8.58	0.34 ± 0.06	...	6.55 ± 0.42	1.39	78.4 ± 3.0	1.01	1.772
145	UGC00891	8.57	0.32 ± 0.07	...	9.24 ± 0.99	0.91	59.5 ± 4.8	0.99	25.160
146	UGC01281	8.55	0.39 ± 0.06	...	5.27 ± 0.20	1.00	90.0 ± 0.6	1.00	0.244
147	UGC09992	8.53	0.51 ± 0.13	...	9.62 ± 3.11	0.90	20.9 ± 5.1	0.70	1.076
148	D512-2	8.51	0.48 ± 0.12	...	12.7 ± 3.1	0.83	51.7 ± 8.5	0.92	0.370
149	UGC00731	8.51	2.39 ± 0.45	...	9.45 ± 0.79	0.76	56.6 ± 3.0	0.99	6.415
150	UGC08550	8.46	0.74 ± 0.11	...	6.32 ± 0.32	0.94	90.0 ± 1.8	1.00	1.552
151	UGC07608	8.42	0.48 ± 0.12	...	8.57 ± 2.12	1.04	27.9 ± 4.5	1.12	0.734
152	NGC2366	8.37	0.24 ± 0.03	...	3.09 ± 0.16	0.95	54.9 ± 2.3	0.81	1.934
153	NGC4068	8.37	0.38 ± 0.09	...	4.30 ± 0.22	0.98	31.7 ± 1.9	0.72	2.519
154	UGC05918	8.37	0.54 ± 0.13	...	6.63 ± 1.22	0.87	44.8 ± 4.5	0.97	0.936
155	D631-7	8.29	0.20 ± 0.04	...	7.53 ± 0.18	0.98	45.9 ± 1.1	0.78	15.872
156	NGC3109	8.29	0.21 ± 0.04	...	1.43 ± 0.05	1.07	76.0 ± 3.5	1.09	4.133
157	UGCA281	8.29	0.37 ± 0.06	...	5.45 ± 0.26	0.96	64.5 ± 2.8	0.96	0.469
158	DDO168	8.28	0.46 ± 0.11	...	4.12 ± 0.21	0.97	50.3 ± 2.1	0.80	19.714
159	DDO064	8.20	0.48 ± 0.11	...	6.21 ± 0.83	0.91	59.6 ± 4.8	0.99	0.334
160	PGC51017	8.19	0.44 ± 0.10	...	3.19 ± 0.37	0.23	63.4 ± 3.3	0.96	4.567
161	UGCA442	8.15	0.44 ± 0.10	...	4.35 ± 0.20	1.00	64.1 ± 3.2	1.00	7.650
162	UGC07866	8.09	0.45 ± 0.11	...	4.48 ± 0.23	0.98	34.5 ± 2.4	0.79	0.260
163	UGC07232	8.05	0.46 ± 0.09	...	2.83 ± 0.16	1.00	59.1 ± 4.2	1.00	6.169

Table 6.2 – Continued

SPARC ID	Galaxy name	$\log(L_{[3.6]})$ (L_{\odot})	Υ_{disk} (M_{\odot}/L_{\odot})	Υ_{bulge} (M_{\odot}/L_{\odot})	Distance (Mpc)	D/D ₀	Inclination (deg.)	i/i_0	χ^2_{ν}
164	UGC07559	8.04	0.31 ± 0.06	...	4.43 ± 0.24	0.89	51.4 ± 2.6	0.84	2.602
165	NGC6789	8.00	0.60 ± 0.14	...	3.60 ± 0.17	1.02	53.9 ± 4.9	1.25	5.904
166	KK98-251	7.93	0.44 ± 0.10	...	3.35 ± 0.47	0.49	57.4 ± 5.2	0.97	1.227
167	UGC05764	7.93	3.83 ± 0.50	...	7.14 ± 1.32	0.96	59.3 ± 8.3	0.99	16.177
168	CamB	7.88	0.34 ± 0.08	...	2.83 ± 0.30	0.84	26.9 ± 2.3	0.41	5.758
169	ESO444-G084	7.85	0.42 ± 0.09	...	5.08 ± 0.43	1.05	40.1 ± 2.2	1.25	3.253
170	DDO154	7.72	0.19 ± 0.03	...	3.87 ± 0.16	0.96	61.2 ± 2.1	0.96	3.482
171	UGC07577	7.65	0.24 ± 0.05	...	2.14 ± 0.14	0.83	45.5 ± 2.7	0.72	5.794
172	D564-8	7.52	0.40 ± 0.09	...	8.69 ± 0.28	0.99	42.5 ± 2.4	0.67	3.160
173	NGC3741	7.45	0.31 ± 0.05	...	3.35 ± 0.12	1.04	72.8 ± 3.1	1.04	0.767
174	UGC04483	7.11	0.43 ± 0.10	...	2.55 ± 0.22	0.76	53.0 ± 2.9	0.91	0.869
175	UGCA444	7.08	0.49 ± 0.12	...	0.84 ± 0.04	0.86	67.2 ± 4.0	0.86	0.330







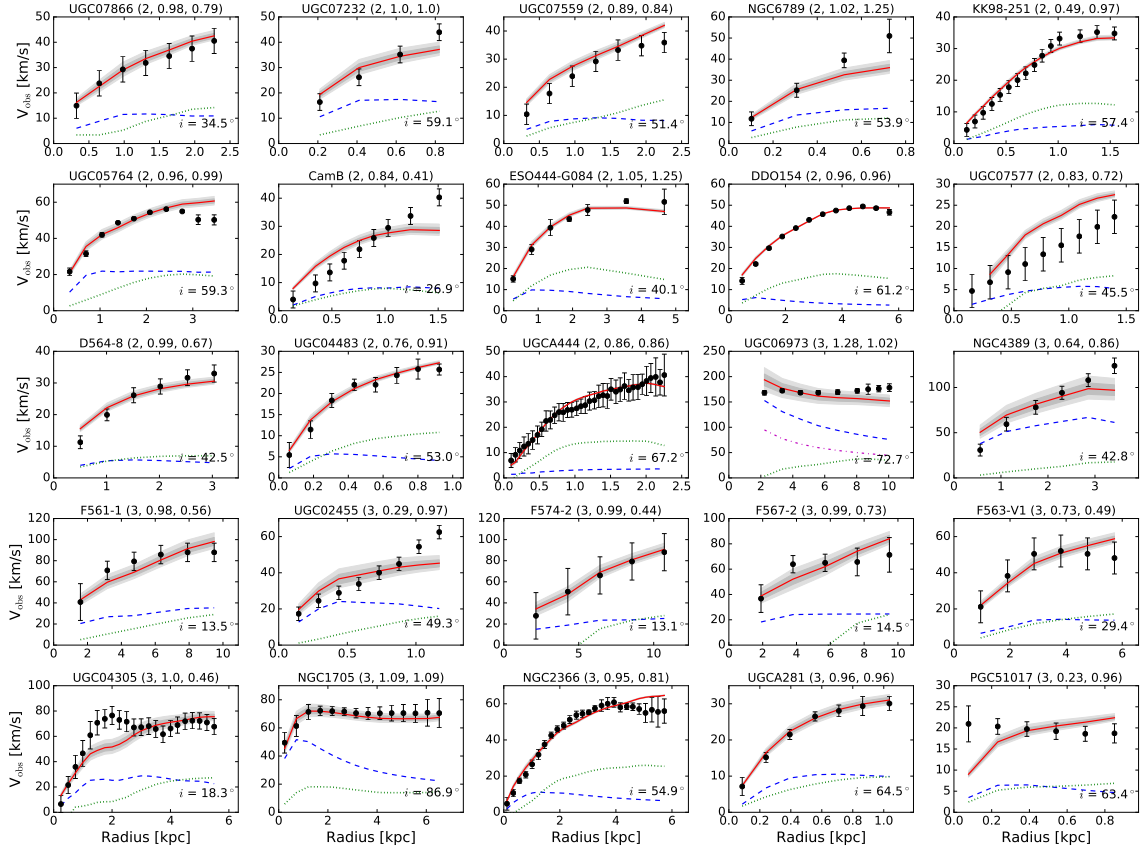


Figure 6.10 Rotation curve fits of 175 SPARC galaxies using the radial acceleration relation. Galaxies are listed in the order of decreasing luminosity and quality flag Q (refer to Lelli et al. 2016a). Green dotted, blue dashed, and purple dot-dashed represent gas, disk, bulge contributions, respectively. Red solid lines are the total contributions. Dark and light gray bands show 1σ and 2σ confidence regions. The three numbers in the title regions indicate quality flag Q , the ratios of best-fit distances and inclinations to the tabulated values in the SPARC dataset, respectively. The optimized inclination for each galaxy is shown within the figure panel.

Chapter 7

Summary and Outlook

7.1 Summarizing major results

In this dissertation, I presented a series of studies into the mass discrepancy problem along the lines of both cold dark matter model and Modified Newtonian Dynamics. Previous studies on rotationally supported galaxies were limited to small samples, less robust mass modelings, and low-resolution rotation curves. I used 175 late-type galaxies from the SPARC database, which have *Spitzer* photometry at [3.6] and accurate HI rotation curves. I am hence able to strictly and systematically test these two hypothesis in a statistical sense.

To test the cold dark matter assumption, I investigate seven halo profiles, including pseudo-isothermal, Burkert, Navarro-Frenk-White, Einasto, Di Cintio et al. (2014a, DC14), cored-NFW (Read et al. 2016a), and Lucky13, by fitting the SPARC rotation curves using a Markov Chain Monte Carlo method. I find that the empirical cored profiles generally provide better fits to the SPARC rotation curves than the cuspy NFW profile does, confirming the core-cusp problem with high statistical significance in a large galaxy sample. Core formation from baryonic feedback can largely fix this problem, as the DC14 and cored-NFW profiles do a better job in fitting rotation curves. The stellar-to-halo mass correlation is well recovered for all the halo profiles once imposed as a prior, while the concentration-halo mass relation is hardly reproduced in detail by any profile.

Fitting rotation curves provides the first direct test of the assumed DM halo models. One then needs to investigate the detailed properties of the resultant DM halos, and compare them with cosmological simulations as a consistency check. I first explore the correlations

between DM halos and stellar disks, spanning ~ 5 dex in luminosity. It turns out that the characteristic volume density ρ_s of DM halos is constant with galaxy luminosity, while the scale radius linearly correlates with galaxy luminosity in logarithmic scale. This implies that their product $\rho_s \cdot r_s$ is correlated with galaxy luminosity as well, contrary to previous works (e.g. Kormendy & Freeman 2016). These different results are largely driven by the different methods of breaking the disk-halo degeneracy, as well as the different priors on DM halo parameters. Given the *Spitzer* photometry provides more solid modelings of the stellar mass distribution and simulation-motivated priors are better understood, the constant characteristic volume density of DM halos serves as a test bed for future simulations, which can generate a varieties of DM halos spanning large range in halo mass.

Besides the properties of DM halos, I also investigate their abundance as this is a key prediction of the standard CDM model. This is quantified by the DM halo mass function (HMF), i.e. the halo number density per unit mass. The direct measurement of the HMF has been a challenge in astronomical observations, since it requires the determination of DM halo masses for a large sample of galaxies. The SPARC rotation curve fits provide a way to explore the relation between DM halo masses and HI line width. The latter is easy to measure for statistically significant galaxy samples, as it does not require galaxies to be spatially resolved. I take the HIPASS galaxies from Zwaan et al. (2004) and estimate their halo masses based on their HI line widths using the established relation from the SPARC rotation curves. This enables me to measure the HMF of disk galaxies. The measured HMF is consistent with the prediction of DM-only simulations at intermediate and low halo masses. However, the lowest halo mass I probed is above the masses of dwarf satellite galaxies in the Local Group, hence I cannot investigate the missing satellite problem using the given data. At high halo masses, the measured HMF is significantly lower than predicted. High-mass halos must be HI poor to maintain consistency with Λ CDM. A simple implementation of HI selection effects improve the data-theory comparison, but the overall shape of the HMF is still not well reproduced. Carefully modeling the selection process in observations is required when selecting simulated halos in order to make a fair comparison with simulations.

One effect that has mostly been neglected when fitting rotation curves is the adiabatic contraction of DM halos due to baryonic mass distributions. This is an important effect

because it could lead to DM halos that are unable to exist in reality. I then simulate the evolution of the derived DM halos of the SPARC galaxies starting from the initial NFW halos. The compressed halos turn out to contribute more to rotation curves even for those galaxies with insufficient baryonic feedbacks, especially in the inner regions of galaxies. This implies that the compressed halos have significantly higher central density, intensifying the core-cusp problem. Therefore, the NFW profile cannot be the density profile of DM halos in reality. I propose a new method of fitting rotation curves that combines traditional fitting procedure and halo compression. This method can result in DM halos that are in dynamical equilibrium with embedded baryonic mass distributions. I test this method using the SPARC galaxies.

On the side of modified gravity, I apply the well established radial acceleration relation (RAR) to individual SPARC galaxies. The RAR is an empirical, statistical relation. To be a feasible realization of modified Newtonian Dynamics, it has to hold for individual galaxies, have small or zero intrinsic scatter (contingent on modified gravity or modified inertia), and present a universal acceleration scale. By marginalizing over stellar mass-to-light ratio, galaxy distance, and disk inclination, I fit the RAR to individual SPARC galaxies, and find it provides satisfactory fits to the vast majority of the SPARC rotation curves. After removing the scatter due to the variation of stellar mass-to-light ratios, and the uncertainties on galaxy distance and disk inclinations, the RAR turns out to have an rms scatter of 0.057 dex. This is comparable to the scatter due to the observational uncertainties on rotation curves (e.g. McGaugh et al. 2016b). This implies that the intrinsic scatter must be extremely small, presenting a preference for modified inertia. I also test the universality of the critical acceleration scale in the RAR by adding it as a free parameter, imposing both flat and Gaussian priors. I find these two priors result in essentially the same fit qualities, though the resulting distributions of the acceleration scale are significantly different: the Gaussian prior indeed recovers the constant acceleration scale, while the flat prior leads to a wide distribution. Therefore, there is no need to vary the acceleration scale from galaxy to galaxy. There exists a universal acceleration scale for rotationally supported galaxies. I prove from three perspectives that the RAR is a viable realization of modified Newtonian Dynamics in disk galaxies.

In summary, cold dark matter model can describe the dynamics of rotating galaxies,

but suffers from some severe challenges. Baryonic feedback seems to be able to alleviate the core-cusp problem, but the adiabatic compression effect intensifies it significantly. The newly established constant volume density is yet to be tested by simulations. The mismatch of the HMF at high halo masses between measurements and simulations remains a problem and requires a careful treatment of HI selection effects. In contrast, MOND can fit rotation curves of late-type galaxies with less introduced degree of freedoms, and it causes almost no problems in galactic scale.

7.2 Prospective work

The systematic study of the dynamics of rotationally supported galaxies show a preference of MOND. However, a comprehensive evaluation would also require systematic studies on galaxy-cluster and cosmological scales, since a successful model has to be able to explain all related observations. As such, it is an obvious extension to my PhD work to test the dark matter properties and the RAR established in galaxies to galaxy clusters.

Galaxy clusters are the largest gravitational binding systems. In spite of the undoubted importance, the studies of galaxy clusters have been relatively limited and less conclusive with respect to galaxies due to observational difficulties and the fact that galaxy clusters are less abundant than galaxies. Thanks to Chandra and XMM-Newton, more and more clusters have been observed in X-rays, with spatially resolved gas surface brightness profiles (e.g. Evans et al. 2010). It is hence imaginable to build a large sample of galaxy clusters, with both X-ray gas mass profile and dynamical mass profile, similar to the SPARC database.

Since clusters are gas dominated (Laganá et al. 2013), X-ray gas is a good estimate to the total baryonic mass, and it can be derived by deprojecting surface brightness profile. Recent development in gravitational lensing has been able to measure spatially resolved dynamical mass profile of galaxy clusters (e.g. Postman et al. 2012; Umetsu et al. 2016), given that galaxy clusters are powerful gravitational lenses (Kneib & Natarajan 2011). One can also derive dynamic mass profile from X-ray gas profile by assuming hydrostatic equilibrium. This method could lead to a systematic bias as large as 40% (Schellenberger & Reiprich 2017). Member galaxies of clusters can also be used as tracers of gravitational

potential, as a considerable number of member galaxies have been identified and spectroscopically confirmed for many clusters.

Therefore, exploring the RAR and the nature of dark matter using spatially resolved galaxy clusters is a prospect and entirely feasible project. It is also an essential step to carry out a comprehensive evaluation onto the two hypothesis towards the dark matter problem.

Bibliography

- Abdo, A. A., Ackermann, M., Ajello, M., et al. 2010, *ApJ*, 712, 147
- Ackermann, M., Ajello, M., Albert, A., et al. 2013, *Phys. Rev. D*, 88, 082002
- Ackermann, M., Albert, A., Anderson, B., et al. 2015, *Phys. Rev. Lett.*, 115, 231301
- Ackermann, M., Albert, A., Baldini, L., et al. 2012, *ApJ*, 747, 121
- Adams, J. J., Simon, J. D., Fabricius, M. H., et al. 2014, *ApJ*, 789, 63
- Afonso, C., Albert, J. N., Andersen, J., et al. 2003, *A&A*, 400, 951
- Afshordi, N., McDonald, P., & Spergel, D. N. 2003, *ApJ*, 594, L71
- Albert, A., Anderson, B., Bechtol, K., et al. 2017, *ApJ*, 834, 110
- Alcock, C., Allsman, R. A., Alves, D. R., et al. 2000, *ApJ*, 542, 281
- Angus, G. W., Famaey, B., & Buote, D. A. 2008, *MNRAS*, 387, 1470
- Aoki, W., Barklem, P. S., Beers, T. C., et al. 2009, *ApJ*, 698, 1803
- Aprile, E., Aalbers, J., Agostini, F., et al. 2017, *Phys. Rev. Lett.*, 119, 181301
- Aprile, E., Arisaka, K., Arneodo, F., et al. 2011a, *Phys. Rev. Lett.*, 107, 131302
- Aprile, E., Arisaka, K., Arneodo, F., et al. 2011b, *Phys. Rev. D*, 84, 061101
- Aprile, E., Arisaka, K., Arneodo, F., et al. 2010, *Phys. Rev. Lett.*, 105, 131302
- Arcadi, G., Dutra, M., Ghosh, P., et al. 2018, *European Physical Journal C*, 78, 203

Audren, B., Lesgourgues, J., Mangano, G., Serpico, P. D., & Tram, T. 2014, JCAP, 2014, 028

Aver, E., Olive, K. A., & Skillman, E. D. 2015, JCAP, 2015, 011

Babcock, H. W. 1939, Lick Observatory Bulletin, 498, 41

Babul, A. & Rees, M. J. 1992, MNRAS, 255, 346

Bai, Y., Fox, P. J., & Harnik, R. 2010, Journal of High Energy Physics, 2010, 48

Baltz, E. A. 2004, arXiv e-prints, astro

Baring, M. G., Ghosh, T., Queiroz, F. S., & Sinha, K. 2016, Phys. Rev. D, 93, 103009

Battaglia, G., Fraternali, F., Oosterloo, T., & Sancisi, R. 2006, A&A, 447, 49

Begeman, K. G. 1987, PhD thesis, -

Begeman, K. G., Broeils, A. H., & Sanders, R. H. 1991, MNRAS, 249, 523

Behroozi, P. S., Conroy, C., & Wechsler, R. H. 2010, ApJ, 717, 379

Bekenstein, J. & Milgrom, M. 1984, ApJ, 286, 7

Bekenstein, J. D. 2004, Phys. Rev. D, 70, 083509

Bell, E. F. & de Jong, R. S. 2001a, ApJ, 550, 212

Bell, E. F. & de Jong, R. S. 2001b, ApJ, 550, 212

Benson, A. J., Farahi, A., Cole, S., et al. 2013, MNRAS, 428, 1774

Binggeli, B., Sandage, A., & Tammann, G. A. 1985, AJ, 90, 1681

Binney, J. & Tremaine, S. 1987, Galactic dynamics

Binney, J. & Tremaine, S. 2008, Galactic Dynamics: Second Edition

Blanchet, L. & Le Tiec, A. 2008, Phys. Rev. D, 78, 024031

Blanchet, L. & Le Tiec, A. 2009, Phys. Rev. D, 80, 023524

Blumenthal, G. R., Faber, S. M., Flores, R., & Primack, J. R. 1986, *ApJ*, 301, 27

Bosma, A. 1978, PhD thesis, PhD Thesis, Groningen Univ., (1978)

Bosma, A. 1981, *AJ*, 86, 1825

Bothun, G. D., Aaronson, M., Schommer, B., et al. 1985, *ApJS*, 57, 423

Bottema, R. & Pestaña, J. L. G. 2015, *MNRAS*, 448, 2566

Boylan-Kolchin, M., Bullock, J. S., & Kaplinghat, M. 2011, *MNRAS*, 415, L40

Boylan-Kolchin, M., Bullock, J. S., & Kaplinghat, M. 2012, *MNRAS*, 422, 1203

Boylan-Kolchin, M., Springel, V., White, S. D. M., Jenkins, A., & Lemson, G. 2009, *MNRAS*, 398, 1150

Brada, R. & Milgrom, M. 1995, *MNRAS*, 276, 453

Brook, C. B. & Shankar, F. 2016, *MNRAS*, 455, 3841

Brooks, A. M., Papastergis, E., Christensen, C. R., et al. 2017, *ApJ*, 850, 97

Bull, P., Akrami, Y., Adamek, J., et al. 2016, *Physics of the Dark Universe*, 12, 56

Bullock, J. S. & Boylan-Kolchin, M. 2017, *ARA&A*, 55, 343

Bullock, J. S., Kolatt, T. S., Sigad, Y., et al. 2001, *MNRAS*, 321, 559

Bullock, J. S., Kravtsov, A. V., & Weinberg, D. H. 2000, *ApJ*, 539, 517

Burkert, A. 1995, *ApJ*, 447, L25

Burrage, C., Copeland, E. J., & Millington, P. 2017, *Phys. Rev. D*, 95, 064050

Cappellari, M., Scott, N., Alatalo, K., et al. 2013, *MNRAS*, 432, 1709

Carlson, E. D., Machacek, M. E., & Hall, L. J. 1992, *ApJ*, 398, 43

Chan, T. K., Kereš, D., Oñorbe, J., et al. 2015, *MNRAS*, 454, 2981

Charmousis, C., Copeland, E. J., Padilla, A., & Saffin, P. M. 2012, *Phys. Rev. Lett.*, 108, 051101

Chashchina, O., Foot, R., & Silagadze, Z. 2017, *Phys. Rev. D*, 95, 023009

Chauhan, G., Lagos, C. d. P., Obreschkow, D., et al. 2019, *MNRAS*, 488, 5898

Chemin, L., de Blok, W. J. G., & Mamon, G. A. 2011, *AJ*, 142, 109

Choi, E., Naab, T., Ostriker, J. P., Johansson, P. H., & Moster, B. P. 2014, *MNRAS*, 442, 440

Choi, J.-H., Lu, Y., Mo, H. J., & Weinberg, M. D. 2006, *MNRAS*, 372, 1869

Clowe, D., Bradač, M., Gonzalez, A. H., et al. 2006, *ApJ*, 648, L109

Conn, A. R., Lewis, G. F., Ibata, R. A., et al. 2013, *ApJ*, 766, 120

Cooke, R. J., Pettini, M., Jorgenson, R. A., Murphy, M. T., & Steidel, C. C. 2014, *ApJ*, 781, 31

Courtois, H. M., Tully, R. B., Fisher, J. R., et al. 2009, *AJ*, 138, 1938

Cybert, R. H., Fields, B. D., Olive, K. A., & Yeh, T.-H. 2016, *Reviews of Modern Physics*, 88, 015004

de Blok, W. J. G. & Bosma, A. 2002, *A&A*, 385, 816

de Blok, W. J. G. & McGaugh, S. S. 1996, *ApJ*, 469, L89

de Blok, W. J. G. & McGaugh, S. S. 1997, *MNRAS*, 290, 533

de Blok, W. J. G., McGaugh, S. S., Bosma, A., & Rubin, V. C. 2001, *ApJ*, 552, L23

de Blok, W. J. G., Walter, F., Brinks, E., et al. 2008, *AJ*, 136, 2648

de Rham, C. & Gabadadze, G. 2010, *Phys. Rev. D*, 82, 044020

de Rham, C., Gabadadze, G., & Tolley, A. J. 2011, *Phys. Rev. Lett.*, 106, 231101

Debattista, V. P. & Sellwood, J. A. 2000, *ApJ*, 543, 704

Debuhr, J., Quataert, E., Ma, C.-P., & Hopkins, P. 2010, MNRAS, 406, L55

Dekel, A., Ishai, G., Dutton, A. A., & Maccio, A. V. 2017, MNRAS, 468, 1005

Desmond, H. 2017a, MNRAS, 464, 4160

Desmond, H. 2017b, MNRAS, 472, L35

Di Cintio, A., Brook, C. B., Dutton, A. A., et al. 2014a, MNRAS, 441, 2986

Di Cintio, A., Brook, C. B., Macciò, A. V., et al. 2014b, MNRAS, 437, 415

Di Cintio, A. & Lelli, F. 2016, MNRAS, 456, L127

Di Matteo, T., Springel, V., & Hernquist, L. 2005, Nature, 433, 604

Diemand, J., Kuhlen, M., Madau, P., et al. 2008, Nature, 454, 735

Dodelson, S. 2011, International Journal of Modern Physics D, 20, 2749

Donato, F., Gentile, G., Salucci, P., et al. 2009, MNRAS, 397, 1169

Drlica-Wagner, A., Bechtol, K., Rykoff, E. S., et al. 2015, ApJ, 813, 109

Dutton, A. A. & Macciò, A. V. 2014, MNRAS, 441, 3359

Dutton, A. A., Obreja, A., & Macciò, A. V. 2019, MNRAS, 482, 5606

Eder, J. A. & Schombert, J. M. 2000, ApJS, 131, 47

Efstathiou, G. 1992, MNRAS, 256, 43P

Eggen, O. J., Lynden-Bell, D., & Sandage, A. R. 1962, ApJ, 136, 748

Einasto, J. 1965, Trudy Astrofizicheskogo Instituta Alma-Ata, 5, 87

Eisenstein, D. J. & Hu, W. 1998, ApJ, 496, 605

Eisenstein, D. J., Zehavi, I., Hogg, D. W., et al. 2005, ApJ, 633, 560

Emsellem, E., Renaud, F., Bournaud, F., et al. 2015, MNRAS, 446, 2468

Evans, I. N., Primini, F. A., Glotfelty, K. J., et al. 2010, *ApJS*, 189, 37

Famaey, B. & Binney, J. 2005, *MNRAS*, 363, 603

Feng, J. L. 2010, *Non-WIMP candidates*, ed. G. Bertone, 190

Fitts, A., Boylan-Kolchin, M., Elbert, O. D., et al. 2017, *MNRAS*, 471, 3547

Flores, R. A. & Primack, J. R. 1994, *ApJ*, 427, L1

Foreman-Mackey, D., Hogg, D. W., Lang, D., & Goodman, J. 2013, *PASP*, 125, 306

Freundlich, J., Jiang, F., Dekel, A., et al. 2020, arXiv e-prints, arXiv:2004.08395

Gentile, G., Famaey, B., & de Blok, W. J. G. 2011, *A&A*, 527, A76

Gentile, G., Józsa, G. I. G., Serra, P., et al. 2013, *A&A*, 554, A125

Gnedin, O. Y., Kravtsov, A. V., Klypin, A. A., & Nagai, D. 2004, *ApJ*, 616, 16

Goodman, J., Ibe, M., Rajaraman, A., et al. 2010, *Phys. Rev. D*, 82, 116010

Goodman, J., Ibe, M., Rajaraman, A., et al. 2011, *Physics Letters B*, 695, 185

Governato, F., Brook, C., Mayer, L., et al. 2010, *Nature*, 463, 203

Governato, F., Zolotov, A., Pontzen, A., et al. 2012, *MNRAS*, 422, 1231

Gunn, J. E. & Gott, J. Richard, I. 1972, *ApJ*, 176, 1

Guo, H., Li, C., Zheng, Z., et al. 2017, *ApJ*, 846, 61

Hansen, M., Langæble, K., & Sannino, F. 2015, *Phys. Rev. D*, 92, 075036

Hernquist, L. 1990, *ApJ*, 356, 359

Hinshaw, G., Weiland, J. L., Hill, R. S., et al. 2009, *ApJS*, 180, 225

Hochberg, Y., Kuflik, E., Volansky, T., & Wacker, J. G. 2014, arXiv e-prints, arXiv:1402.5143

Hopkins, P. F., Hernquist, L., Cox, T. J., et al. 2006, *ApJS*, 163, 1

- Hu, W., Barkana, R., & Gruzinov, A. 2000, *Phys. Rev. Lett.*, 85, 1158
- Huchtmeier, W. K. & Richter, O.-G. 1989, *A General Catalog of HI Observations of Galaxies. The Reference Catalog.*, 350
- Ibata, R. A., Lewis, G. F., Conn, A. R., et al. 2013, *Nature*, 493, 62
- Ikeuchi, S. 1986, *Ap&SS*, 118, 509
- Jesseit, R., Naab, T., & Burkert, A. 2002, *ApJ*, 571, L89
- Jones, M. G., Papastergis, E., Pandya, V., et al. 2018, *A&A*, 614, A21
- Katz, H., Lelli, F., McGaugh, S. S., et al. 2017, *MNRAS*, 466, 1648
- Keller, B. W. & Wadsley, J. W. 2017, *ApJ*, 835, L17
- Kennedy, R., Frenk, C., Cole, S., & Benson, A. 2014, *MNRAS*, 442, 2487
- Kent, S. M. 1987, *AJ*, 93, 816
- Khoury, J. 2015, *Phys. Rev. D*, 91, 024022
- Klypin, A., Karachentsev, I., Makarov, D., & Nasonova, O. 2015, *MNRAS*, 454, 1798
- Klypin, A., Kravtsov, A. V., Valenzuela, O., & Prada, F. 1999, *ApJ*, 522, 82
- Knebe, A. & Gibson, B. K. 2004, *MNRAS*, 347, 1055
- Kneib, J.-P. & Natarajan, P. 2011, *A&A Rev.*, 19, 47
- Komatsu, E., Dunkley, J., Nolta, M. R., et al. 2009, *ApJS*, 180, 330
- Komatsu, E., Smith, K. M., Dunkley, J., et al. 2011, *ApJS*, 192, 18
- Koposov, S. E., Yoo, J., Rix, H.-W., et al. 2009, *ApJ*, 696, 2179
- Kormendy, J. & Freeman, K. C. 2004, in *IAU Symposium, Vol. 220, Dark Matter in Galaxies*, ed. S. Ryder, D. Pisano, M. Walker, & K. Freeman, 377
- Kormendy, J. & Freeman, K. C. 2016, *ApJ*, 817, 84

Korsaga, M., Amram, P., Carignan, C., & Epinat, B. 2019a, MNRAS, 482, 154

Korsaga, M., Carignan, C., Amram, P., Epinat, B., & Jarrett, T. H. 2018, MNRAS, 478, 50

Korsaga, M., Epinat, B., Amram, P., et al. 2019b, MNRAS, 490, 2977

Kowalski, M., Rubin, D., Aldering, G., et al. 2008, ApJ, 686, 749

Kravtsov, A. V., Gnedin, O. Y., & Klypin, A. A. 2004, ApJ, 609, 482

Kroupa, P. 2001, MNRAS, 322, 231

Kroupa, P., Theis, C., & Boily, C. M. 2005, A&A, 431, 517

Kunkel, W. E. & Demers, S. 1976, in *The Galaxy and the Local Group*, Vol. 182, 241

Kusenko, A. & Rosenberg, L. J. 2013, arXiv e-prints, arXiv:1310.8642

Laganá, T. F., Martinet, N., Durret, F., et al. 2013, A&A, 555, A66

Lazar, A., Bullock, J. S., Boylan-Kolchin, M., et al. 2020, arXiv e-prints, arXiv:2004.10817

Lelli, F., McGaugh, S. S., & Schombert, J. M. 2016a, AJ, 152, 157

Lelli, F., McGaugh, S. S., & Schombert, J. M. 2016b, ApJ, 816, L14

Lelli, F., McGaugh, S. S., & Schombert, J. M. 2017a, MNRAS, 468, L68

Lelli, F., McGaugh, S. S., Schombert, J. M., Desmond, H., & Katz, H. 2019, MNRAS, 484, 3267

Lelli, F., McGaugh, S. S., Schombert, J. M., & Pawlowski, M. S. 2017b, ApJ, 836, 152

Lelli, F., Verheijen, M., & Fraternali, F. 2014, A&A, 566, A71

Li, P., Lelli, F., McGaugh, S., & Schombert, J. 2018, A&A, 615, A3

Li, P., Lelli, F., McGaugh, S., & Schombert, J. 2020, ApJS, 247, 31

Li, P., Lelli, F., McGaugh, S. S., Starkman, N., & Schombert, J. M. 2019, MNRAS, 482, 5106

Liske, J., Baldry, I. K., Driver, S. P., et al. 2015, MNRAS, 452, 2087

Lovell, M. R., Frenk, C. S., Eke, V. R., et al. 2014, MNRAS, 439, 300

Lu, B.-Q. & Zong, H.-S. 2016, Phys. Rev. D, 93, 103517

Ludlow, A. D., Benítez-Llambay, A., Schaller, M., et al. 2017, Phys. Rev. Lett., 118, 161103

Lynden-Bell, D. 1976, MNRAS, 174, 695

Macciò, A. V., Dutton, A. A., & van den Bosch, F. C. 2008, MNRAS, 391, 1940

Macciò, A. V., Udrescu, S. M., Dutton, A. A., et al. 2016, MNRAS, 463, L69

Mambrini, Y., Profumo, S., & Queiroz, F. S. 2016, Physics Letters B, 760, 807

Mamon, G. A. & Łokas, E. L. 2005, MNRAS, 362, 95

Marinacci, F., Vogelsberger, M., Pakmor, R., et al. 2018, MNRAS, 480, 5113

Mateo, M. L. 1998, ARA&A, 36, 435

Matthews, L. D., van Driel, W., & Gallagher, J. S., I. 1998, AJ, 116, 1169

McGaugh, S. 1999, in American Institute of Physics Conference Series, Vol. 470, After the Dark Ages: When Galaxies were Young (the Universe at $2 < Z < 5$), ed. S. Holt & E. Smith, 72–76

McGaugh, S. 2014, Galaxies, 2, 601

McGaugh, S. S. 2004a, ApJ, 611, 26

McGaugh, S. S. 2004b, ApJ, 609, 652

McGaugh, S. S. 2005, ApJ, 632, 859

McGaugh, S. S. 2012, AJ, 143, 40

McGaugh, S. S. 2015, Canadian Journal of Physics, 93, 250

McGaugh, S. S. & de Blok, W. J. G. 1998a, ApJ, 499, 41

McGaugh, S. S. & de Blok, W. J. G. 1998b, ApJ, 499, 41

McGaugh, S. S., Lelli, F., & Schombert, J. M. 2016a, Phys. Rev. Lett., 117, 201101

McGaugh, S. S., Lelli, F., & Schombert, J. M. 2016b, Physical Review Letters, 117, 201101

McGaugh, S. S., Rubin, V. C., & de Blok, W. J. G. 2001, AJ, 122, 2381

McGaugh, S. S. & Schombert, J. M. 2014, AJ, 148, 77

McGaugh, S. S., Schombert, J. M., Bothun, G. D., & de Blok, W. J. G. 2000, ApJ, 533, L99

McGaugh, S. S., Schombert, J. M., de Blok, W. J. G., & Zagursky, M. J. 2010, ApJ, 708, L14

McGaugh, S. S., Schombert, J. M., & Lelli, F. 2017, ApJ, 851, 22

McGaugh, S. S. & Wolf, J. 2010, ApJ, 722, 248

Meidt, S. E., Schinnerer, E., van de Ven, G., et al. 2014, ApJ, 788, 144

Merritt, D., Graham, A. W., Moore, B., Diemand, J., & Terzić, B. 2006, AJ, 132, 2685

Merritt, D., Navarro, J. F., Ludlow, A., & Jenkins, A. 2005, ApJ, 624, L85

Metz, M., Kroupa, P., & Jerjen, H. 2007, MNRAS, 374, 1125

Meyer, M. J., Zwaan, M. A., Webster, R. L., et al. 2004, MNRAS, 350, 1195

Mihos, J. C. & Hernquist, L. 1996, ApJ, 464, 641

Milgrom, M. 1983, ApJ, 270, 365

Milgrom, M. 1994, Annals of Physics, 229, 384

Milgrom, M. 2009, ApJ, 698, 1630

Milgrom, M. 2010, MNRAS, 403, 886

Milgrom, M. 2012, *Phys. Rev. Lett.*, 109, 251103

Mo, H. J., Mao, S., & White, S. D. M. 1998, *MNRAS*, 295, 319

Moffett, A. J., Ingarfield, S. A., Driver, S. P., et al. 2016, *MNRAS*, 457, 1308

Mohr, J. J., Evrard, A. E., Fabricant, D. G., & Geller, M. J. 1995, *ApJ*, 447, 8

Moore, B. 1993, *ApJ*, 413, L93

Moore, B. 1994, *Nature*, 370, 629

Moore, B., Ghigna, S., Governato, F., et al. 1999, *ApJ*, 524, L19

Moster, B. P., Naab, T., & White, S. D. M. 2013, *MNRAS*, 428, 3121

Müller, O., Pawłowski, M. S., Jerjen, H., & Lelli, F. 2018, *Science*, 359, 534

Naiman, J. P., Pillepich, A., Springel, V., et al. 2018, *MNRAS*, 477, 1206

Natarajan, P., Chadayammuri, U., Jauzac, M., et al. 2017, *MNRAS*, 468, 1962

Navarro, J. F., Benítez-Llambay, A., Fattahi, A., et al. 2017, *MNRAS*, 471, 1841

Navarro, J. F., Eke, V. R., & Frenk, C. S. 1996a, *MNRAS*, 283, L72

Navarro, J. F., Frenk, C. S., & White, S. D. M. 1996b, *ApJ*, 462, 563

Navarro, J. F., Frenk, C. S., & White, S. D. M. 1997, *ApJ*, 490, 493

Navarro, J. F., Hayashi, E., Power, C., et al. 2004, *MNRAS*, 349, 1039

Navarro, J. F., Ludlow, A., Springel, V., et al. 2010, *MNRAS*, 402, 21

Nelson, D., Pillepich, A., Springel, V., et al. 2018, *MNRAS*, 475, 624

Nelson, D., Springel, V., Pillepich, A., et al. 2019, *Computational Astrophysics and Cosmology*, 6, 2

Norris, M. A., Van de Ven, G., Schinnerer, E., et al. 2016, *ApJ*, 832, 198

Oehm, W., Thies, I., & Kroupa, P. 2017, *MNRAS*, 467, 273

Oh, S.-H., Brook, C., Governato, F., et al. 2011, *AJ*, 142, 24

Oh, S.-H., Hunter, D. A., Brinks, E., et al. 2015, *AJ*, 149, 180

Okamoto, T. & Frenk, C. S. 2009, *MNRAS*, 399, L174

Oman, K. A., Navarro, J. F., Fattahi, A., et al. 2015, *MNRAS*, 452, 3650

Oort, J. H. 1932, *Bull. Astron. Inst. Netherlands*, 6, 249

Overduin, J. M. & Wesson, P. S. 2004, *Phys. Rep.*, 402, 267

Papastergis, E., Giovanelli, R., Haynes, M. P., Rodríguez-Puebla, A., & Jones, M. G. 2013, *ApJ*, 776, 43

Papastergis, E., Martin, A. M., Giovanelli, R., & Haynes, M. P. 2011, *ApJ*, 739, 38

Papastergis, E. & Ponomareva, A. A. 2017, *A&A*, 601, A1

Pawlowski, M. S. & Kroupa, P. 2013, *MNRAS*, 435, 2116

Pawlowski, M. S. & McGaugh, S. S. 2014, *ApJ*, 789, L24

Pawlowski, M. S., McGaugh, S. S., & Jerjen, H. 2015, *MNRAS*, 453, 1047

Pedregosa, F., Varoquaux, G., Gramfort, A., et al. 2011, *Journal of Machine Learning Research*, 12, 2825

Perlmutter, S., Aldering, G., Goldhaber, G., et al. 1999, *ApJ*, 517, 565

Persic, M., Salucci, P., & Stel, F. 1996, *MNRAS*, 281, 27

Pildis, R. A., Schombert, J. M., & Eder, A. 1997, *ApJ*, 481, 157

Pillepich, A., Nelson, D., Hernquist, L., et al. 2018, *MNRAS*, 475, 648

Planck Collaboration, Ade, P. A. R., Aghanim, N., et al. 2014, *A&A*, 571, A15

Planck Collaboration, Ade, P. A. R., Aghanim, N., et al. 2016, *A&A*, 594, A13

Portinari, L., Sommer-Larsen, J., & Tantalo, R. 2004, *MNRAS*, 347, 691

- Posti, L., Fraternali, F., & Marasco, A. 2019a, *A&A*, 626, A56
- Posti, L., Marasco, A., Fraternali, F., & Famaey, B. 2019b, *A&A*, 629, A59
- Postman, M., Coe, D., Benítez, N., et al. 2012, *ApJS*, 199, 25
- Press, W. H. & Schechter, P. 1974a, *ApJ*, 187, 425
- Press, W. H. & Schechter, P. 1974b, *ApJ*, 187, 425
- Queiroz, F. S. & Sinha, K. 2014, *Physics Letters B*, 735, 69
- Quinn, T., Katz, N., & Efstathiou, G. 1996, *MNRAS*, 278, L49
- Rajaraman, A., Shepherd, W., Tait, T. M. P., & Wijangco, A. M. 2011, *Phys. Rev. D*, 84, 095013
- Read, J. I., Agertz, O., & Collins, M. L. M. 2016a, *MNRAS*, 459, 2573
- Read, J. I., Iorio, G., Agertz, O., & Fraternali, F. 2016b, *MNRAS*, 462, 3628
- Read, J. I. & Trentham, N. 2005, *Philosophical Transactions of the Royal Society of London Series A*, 363, 2693
- Rees, M. J. 1986, *MNRAS*, 218, 25P
- Refregier, A. 2003, *ARA&A*, 41, 645
- Ricotti, M. & Gnedin, N. Y. 2005, *ApJ*, 629, 259
- Riess, A. G., Macri, L. M., Hoffmann, S. L., et al. 2016, *ApJ*, 826, 56
- Rix, H.-W. & Lake, G. 1993, *ApJ*, 417, L1
- Rodrigues, D. C., Marra, V., del Popolo, A., & Davari, Z. 2018, *Nature Astronomy*, 2, 668
- Rubin, V. C., Ford, Jr., W. K., & Thonnard, N. 1978, *ApJ*, 225, L107
- Sakai, S. 1999, in *IAU Symposium, Vol. 183, Cosmological Parameters and the Evolution of the Universe*, ed. K. Sato, 48

- Sanders, R. H. 1998, MNRAS, 296, 1009
- Sanders, R. H. 2001, ApJ, 560, 1
- Sanders, R. H. 2003, MNRAS, 342, 901
- Sanders, R. H. & McGaugh, S. S. 2002, ARA&A, 40, 263
- Schechter, P. L. 2002, in Lighthouses of the Universe: The Most Luminous Celestial Objects and Their Use for Cosmology, ed. M. Gilfanov, R. Sunyaev, & E. Churazov, 3
- Schellenberger, G. & Reiprich, T. H. 2017, MNRAS, 469, 3738
- Schneider, A. & Trujillo-Gomez, S. 2018, MNRAS, 475, 4809
- Schneider, A., Trujillo-Gomez, S., Papastergis, E., Reed, D. S., & Lake, G. 2017, MNRAS, 470, 1542
- Schombert, J. & McGaugh, S. 2014, PASA, 31, e036
- Schombert, J., McGaugh, S., & Lelli, F. 2019, MNRAS, 483, 1496
- Sellwood, J. A. 2014, arXiv e-prints, arXiv:1406.6606
- Sellwood, J. A. & McGaugh, S. S. 2005, ApJ, 634, 70
- Shapiro, P. R., Giroux, M. L., & Babul, A. 1994, ApJ, 427, 25
- Sheth, R. K., Mo, H. J., & Tormen, G. 2001, MNRAS, 323, 1
- Slatyer, T. R. & Wu, C.-L. 2017, Phys. Rev. D, 95, 023010
- Sorce, J. G., Courtois, H. M., Tully, R. B., et al. 2013, ApJ, 765, 94
- Spano, M., Marcelin, M., Amram, P., et al. 2008, MNRAS, 383, 297
- Spergel, D. N. & Steinhardt, P. J. 2000, Phys. Rev. Lett., 84, 3760
- Springel, V., Di Matteo, T., & Hernquist, L. 2005, MNRAS, 361, 776
- Springel, V., Pakmor, R., Pillepich, A., et al. 2018a, MNRAS, 475, 676

Springel, V., Pakmor, R., Pillepich, A., et al. 2018b, MNRAS, 475, 676

Springel, V., Wang, J., Vogelsberger, M., et al. 2008, MNRAS, 391, 1685

Springob, C. M., Haynes, M. P., Giovanelli, R., & Kent, B. R. 2005, ApJS, 160, 149

Starkman, N., Lelli, F., McGaugh, S., & Schombert, J. 2018, MNRAS, 480, 2292

Stinson, G. S., Bailin, J., Couchman, H., et al. 2010, MNRAS, 408, 812

Swaters, R. A., Sancisi, R., van Albada, T. S., & van der Hulst, J. M. 2009, A&A, 493, 871

Swaters, R. A., Sancisi, R., van der Hulst, J. M., & van Albada, T. S. 2012, MNRAS, 425, 2299

't Hooft, G. 1976, Phys. Rev. D, 14, 3432

Tak, H., Ghosh, S. K., & Ellis, J. A. 2018, MNRAS, 481, 277

Tan, A., Xiao, M., Cui, X., et al. 2016, Phys. Rev. Lett., 117, 121303

Taylor, A. N., Dye, S., Broadhurst, T. J., Benítez, N., & van Kampen, E. 1998, ApJ, 501, 539

Tenneti, A., Mao, Y.-Y., Croft, R. A. C., et al. 2018, MNRAS, 474, 3125

Thoul, A. A. & Weinberg, D. H. 1996, ApJ, 465, 608

Tikhonov, A. V. & Klypin, A. 2009, MNRAS, 395, 1915

Tissera, P. B., White, S. D. M., Pedrosa, S., & Scannapieco, C. 2010, MNRAS, 406, 922

Tisserand, P., Le Guillou, L., Afonso, C., et al. 2007, A&A, 469, 387

Tremaine, S. & Gunn, J. E. 1979, Phys. Rev. Lett., 42, 407

Tully, R. B., Courtois, H. M., & Sorce, J. G. 2016, AJ, 152, 50

Tully, R. B. & Fisher, J. R. 1977, A&A, 54, 661

Tully, R. B., Libeskind, N. I., Karachentsev, I. D., et al. 2015, ApJ, 802, L25

Tully, R. B., Rizzi, L., Shaya, E. J., et al. 2009, *AJ*, 138, 323

Umetsu, K., Zitrin, A., Gruen, D., et al. 2016, *ApJ*, 821, 116

van Albada, T. S., Bahcall, J. N., Begeman, K., & Sancisi, R. 1985, *ApJ*, 295, 305

Verheijen, M. A. W. 1997, PhD thesis, -

Verheijen, M. A. W. 2001, *ApJ*, 563, 694

Verheijen, M. A. W. & Sancisi, R. 2001, *A&A*, 370, 765

Verlinde, E. 2017, *SciPost Physics*, 2, 016

Walter, F., Brinks, E., de Blok, W. J. G., et al. 2008, *AJ*, 136, 2563

Warren, M. S., Abazajian, K., Holz, D. E., & Teodoro, L. 2006, *ApJ*, 646, 881

Weinberger, R., Springel, V., Hernquist, L., et al. 2017, *MNRAS*, 465, 3291

Wright, A. H., Robotham, A. S. G., Driver, S. P., et al. 2017, *MNRAS*, 470, 283

Wyżkowski, Ł., Kozłowski, S., Skowron, J., et al. 2011, *MNRAS*, 413, 493

Young, P. 1980, *ApJ*, 242, 1232

Zavala, J., Jing, Y. P., Faltenbacher, A., et al. 2009, *ApJ*, 700, 1779

Zhao, H. 1996, *MNRAS*, 278, 488

Zhao, H. & Li, B. 2010, *ApJ*, 712, 130

Zhao, H. S. & Famaey, B. 2006, *ApJ*, 638, L9

Zwaan, M. A., Meyer, M. J., & Staveley-Smith, L. 2010, *MNRAS*, 403, 1969

Zwaan, M. A., Meyer, M. J., Webster, R. L., et al. 2004, *MNRAS*, 350, 1210

Zwicky, F. 1937, *ApJ*, 86, 217